

Enabling Deep Region Specific Optical Measurements in a Diffusive Medium with Near-Infrared Spectroscopy

A dissertation submitted by
Giles Blaney
in partial fulfillment of the
requirements for the degree of
Doctor of Philosophy in
Biomedical Engineering

Department of Biomedical Engineering
Tufts University, School of Engineering
Medford, MA USA

May 2022

Compiled: April 18, 2022

Committee: Professor Sergio Fantini (Advisor), Professor Srivalleesha Mallidi,
Professor Shuchin Aeron, & Professor Steven Jacques

The full cosmos consists of the physical stuff and consciousness. Take away consciousness and it's only dust; add consciousness and you get things, ideas, and time.

- Neal Stephenson, *Anathem*

Abstract

One of the chief issues with typical near-infrared spectroscopy measurements on the surface of a diffuse medium is the dominance of signal from superficial parts of the medium. When applied to non-invasive measurements of the brain, this leads to a confound from the scalp and skull tissue. The main thread of this work is to minimize this issue by developing measurements that are more specific to deep regions. The centerpiece of this work is the development of the dual-slope technique which is preferentially sensitive to deep regions and is nearly insensitive to various instrumental and motion artifacts. The first part of this work focuses on preferentially deep measurements. This starts with studying different source-detector distances. Then dual-slope itself is introduced, which is then extended to diffuse optical imaging. In this first part we conclude that dual-slope has promise due to its preferentially deep sensitivity, lack of reliance on calibration, and suppression of artifacts. The second part utilizes the methods developed in the first part on measurements of hemodynamic oscillations on the human brain. Here we conclude that the data is consistent with blood flow dominated dynamics in the brain and blood volume dominated dynamics in the scalp. Finally, the calibration-free aspect of dual-slope is applied to absolute broadband spectroscopy, and we conclude that measurements of absolute properties on a heterogeneous medium behave in complex and unexpected ways, which may even be wavelength dependent. This work provides a demonstration of the various benefits of dual-slope, guiding various directions of its development.

Contents

Title Page	i
Abstract	iii
Contents	v
Acronyms	xi
Symbols	xiii
Equipment, Materials, & Software	xv
Preface	xvii
Organization of this Work	xix
A Brief Introduction to Frequency-Domain Near-Infrared Spectroscopy	xxi
I Preferentially Deep Measurements	1
1 Motivation for Seeking Deep Measurements	3
2 Short versus Long Source-Detector Distances	5
2.1 Sensitivity Profiles	5
2.1.1 Single-Distance Sensitivity	5
2.1.2 Single-Slope Sensitivity	6
2.2 Multi-Distance Measurement on the Human Brain	7
2.2.1 Methods Used in Multi-Distance Work	7
2.2.1.A Summary of Experimental Parameters	7
2.2.1.B Analysis Overview	8
2.2.2 Summary of Multi-Distance Results	8
3 Introduction to Dual-Slope	13
3.1 Overview of the Dual-Slope Method	13
3.2 Advantages of Dual-Slope	14
3.2.1 Suppression of Artifacts and Drifts	14
3.2.1.A Derivation of Dual-Slope Artifact Cancellation	14

3.2.1.B	Example of Dual-Slope Artifact Cancellation	16
3.2.2	Preferentially Deep Sensitivity	17
3.2.2.A	Dual-Slope Sensitivity Profile	17
3.2.2.B	Quantitative Comparison of Sensitivity for Dual-Slope and Other Data-Types	18
3.2.2.B.a	Sensitivity Maps	18
3.2.2.B.b	Sensitivity Curves	19
3.3	Discussion of the Dual-Slope Method	20
3.3.1	Considerations on the Noise of the Two Data Types, Intensity and Phase	20
3.3.2	Possible Enhancements of the Dual Slope Method	21
4	Point Measurements with Dual-Slope	23
4.1	Methods Used in Point Dual-Slope Work	23
4.1.1	Summary of Experimental Parameters	23
4.1.2	Analysis Overview	23
4.2	Summary of Point Dual-Slope Results	25
4.2.1	Dual-Slope Phasor Simulations	25
4.2.2	First <i>In Vivo</i> Dual-Slope Results	27
5	Dual-Slope Imaging	29
5.1	Design of a Dual-Slope Imaging Array	29
5.1.1	Discovering Dual-Slope Sets	29
5.1.2	Refining a Dual-Slope Array	31
5.2	Image Reconstruction	33
5.2.1	The Sensitivity Matrix	33
5.2.2	The Moore-Penrose Inverse	34
5.2.3	Evaluation of a Imaging System Using the Moore-Penrose Inverse	35
5.2.3.A	Maps Evaluating Array Performance	35
5.2.3.A.a	Reconstruction and Cross-Talk Maps	35
5.2.3.A.b	Resolution and Localization Maps	36
5.2.3.B	Condition Number	38
5.2.3.C	Singular Value Decomposition and Singular Vectors	39
5.3	Constructing a Dual-Slope Array	40
5.3.1	Fiber Array Design	41
5.3.2	Fiber Array Construction Methods	42
5.3.3	Head-Cap Design	43
5.3.4	Example Dual-Slope Imaging Arrays	43
5.3.4.A	The Circular Array	43
5.3.4.A.a	Physical Realization of Circular Array	44
5.3.4.B	The Hexagonal Array	45
5.3.4.B.a	Physical Realization of Hexagonal Array	46
5.4	Dual-Slope Imaging Results	48
5.4.1	Dual-Slope Imaging on Phantoms	48
5.4.2	<i>In Vivo</i> Dual-Slope Imaging	51
5.4.2.A	Dual-Slope Imaging of Muscle	51
5.4.2.B	Dual-Slope Imaging of Brain	54

II Cerebral Hemodynamics	65
6 Introduction to Wavelet Coherent Hemodynamics Spectroscopy	67
6.1 Hemodynamic Oscillations	67
6.2 Determination of Hemodynamic Phasors with Wavelet	68
6.3 Meanings of Select Phasors and Vectors	69
7 Test for Significant Coherence	71
7.1 Applications for a Significant Coherence Test	71
7.2 The Coherence Threshold Time-Frequency Map	71
7.3 Methods for Creating the Coherence Threshold Map	72
7.3.0.A Simple Threshold Determination	73
7.3.0.B Memory Efficient Algorithm for Coherence Threshold Determination	73
7.3.0.B.a Summary of Memory Efficient Algorithm	73
7.3.0.B.b Initialization	76
7.3.0.B.c Adding Samples	76
7.3.0.B.d Shifting Elements	76
7.3.1 Testing the Memory Efficient Algorithm	77
7.3.1.A Testing with Constructed Distributions	77
7.3.1.B Application of Wavelet Coherence Analysis	77
7.3.2 Discussion of the Memory Efficient Algorithm	78
7.3.2.A Values of the Number of Coherence Samples Taken and Kept	79
7.3.2.B Applicability of the Algorithm	79
7.3.2.C Considerations and Limitations of the Algorithm	80
8 In-Vivo Cerebral Hemodynamics	87
8.1 Overview Coherent Hemodynamics Spectroscopy Results	87
8.2 Multi-Distance Studies	87
8.2.1 Only Considering Cuff Oscillations and Single-Distance Intensities	88
8.2.1.A Summary of Single-Distance Multi-Distance Cuff Oscillation Results	88
8.2.1.A.a Total-Hemoglobin versus Arterial Blood Pressure Phasor Ratio Vector	89
8.2.1.A.b Deoxy-Hemoglobin versus Oxy-Hemoglobin Phasor Ratio Vector	92
8.2.1.B Discussion of Single-Distance Multi-Distance Cuff Oscillations	92
8.2.2 Considering Various Oscillations with Frequency-Domain Data-Types	94
8.2.2.A Summary of Frequency-Domain Multi-Distance Oscillation Results	94
8.2.2.A.a Absolute Optical Properties	94
8.2.2.A.b Coherence Between Arterial Blood Pressure and One of Oxy-hemoglobin, Deoxy-hemoglobin, or Total-Hemoglobin	94
8.2.2.A.c Deoxy-Hemoglobin and Oxy-Hemoglobin Phasor Ratio as a Function of Source-Detector Distance for Different Measurement Methods	96
8.2.2.A.d Deoxy-Hemoglobin and Oxy-Hemoglobin Phasor Ratio Measured at Long Source-Detector Distances with Different Methods	97
8.2.2.B Discussion of Frequency-Domain Multi-Distance Oscillations	98
8.3 Dual-Slope Study	100

8.3.1	Summary of First Frequency-Domain Dual-Slope Oscillation Results	100
8.3.1.A	Phase and Amplitude Relationships of Total-Hemoglobin and Arterial Blood Pressure During Systemic Oscillations for Different Measurement Methods	100
8.3.1.B	Phase and Amplitude Relationships of Deoxy-Hemoglobin and Oxy-Hemoglobin During Systemic Arterial Blood Pressure Oscillations for Different Measurement Methods	100
8.3.2	Discussion Frequency-Domain Dual-Slope Oscillations	101
8.3.2.A	A Greater Amplitude Ratio of Deoxy-Hemoglobin versus Oxy-Hemoglobin in the Brain Suggests a Smaller Blood Volume Change	102
III	Calibration-Free Spectroscopy	105
9	Dual-Slope Based Absolute Broadband-Spectroscopy	107
9.1	Motivation for Dual-Slope Based Spectroscopy	107
9.2	Techniques, Experiments, and Absolute Absorption Retrieval	108
9.2.1	Techniques	108
9.2.1.A	Frequency-Domain Multi-Distance Near-Infrared Spectroscopy	108
9.2.1.B	Continuous-Wave Dual-Slope Broadband Diffuse Reflectance Spectroscopy	108
9.2.2	Validation Experiments	110
9.2.3	Retrieval of Absolute Absorption Spectra	111
9.3	Results from Validation Experiment	111
9.4	Discussion of Dual-Slope Broadband Spectroscopy Validation	113
9.4.1	The Milk and Water Absorption Spectrum	113
9.4.2	Comparing Frequency-Domain and Continuous-Wave Retrieved Absorption .	113
9.4.3	The Additions of Dye to the Phantom	114
9.5	Summary of Dual-Slope Broadband Diffuse Reflectance Spectroscopy Validation	115
10	Absolute Absorption Spectroscopy of Tissue	117
10.1	<i>In-Vivo</i> Absolute Absorption Measurements of Muscle	117
10.1.1	<i>In-Vivo</i> Muscle Measurement Procedure	117
10.1.2	From Absolute Absorption to Absolute Chromophore Concentrations	118
10.1.2.A	Effective Homogeneous Chromophore Fits	119
10.1.2.B	Effective Two-Layer Chromophore Fits	119
10.1.3	<i>In-Vivo</i> Spectral Results	120
10.1.3.A	Absolute Effective Absorption Spectra Recovered <i>In-Vivo</i>	120
10.1.3.B	Recovered Effective Homogeneous Chromophores	121
10.1.3.C	Pseudo-Recovered Effective Two-Layered Chromophores and Two-Layer Modeling	123
10.1.4	Discussion of <i>In-Vivo</i> Spectral Results	126
10.1.4.A	Heterogeneity as the Origin of the Absorption Background	126
10.1.4.B	Other Possible Origins of the Absorption Background	128
10.1.4.C	Meaning of Spectrally Obtained Effective Concentrations	129
10.2	<i>In-Silico</i> Spectra of Two-Layer Tissue	131
10.2.1	Motivation to Understand the Partial Volume Effect	131
10.2.2	Description of Two-Layer Simulations	132

10.2.2.A	Simulation Parameters	132
10.2.2.B	Simulation Procedure for Recovered Effective Absolute Properties .	132
10.2.2.C	Sensitivity in a Two-Layer Medium	133
10.2.3	<i>In-Silico</i> Results for a Two-Layer Model and Effective Homogeneous Recovery	134
10.2.3.A	Recovery of Effective Homogeneous Absolute Values	134
10.2.3.A.a	Baseline Model Two-Layer	134
10.2.3.A.b	Variation of Two-Layer Model Parameters	134
10.2.3.B	Sensitivity to Absorption Parameters in a Two-Layered Medium .	136
10.2.3.B.a	Baseline Model Sensitivities	136
10.2.3.B.b	Variation of Sensitivities as a Result of Varying Two-Layer Model Parameters	137
10.3	Discussion of Two-Layer <i>in-Silico</i> Simulations	141
Appendices		143
A Forward Models		145
A.1	Diffuse Reflectance and Fluence	145
A.1.1	Diffuse Reflectance from A Semi-Infinite Homogeneous Medium	145
A.1.2	Fluence in a Semi-Infinite Homogeneous Medium	147
A.1.3	Diffuse Reflectance from a Layered Cylindrical Medium	147
A.2	Optical Properties	149
A.2.1	Absorption Coefficient	149
A.2.2	Reduced Scattering Coefficient	149
B Measurement of Absolute Optical Properties		155
B.1	Iterative Method	155
B.2	Linear Slopes Method	156
C Measuring Changes in the Absorption Coefficient		163
C.1	Generalized Total Optical Path-Length	163
C.2	Absorption Changes Measured with Single-Distance Intensity or Phase	164
C.3	Absorption Changes Measured with Intensity or Phase Slopes	164
D Recovery of Chromophore Concentrations		169
E Generation of Sensitivity Maps		171
E.1	Generalized Partial Optical Path-Length	171
E.2	Sensitivity to Local Absorption Perturbation	172
E.2.1	Computational Methods to Generate Sensitivity Maps	172
E.3	Extension of Sensitivity to Signal-to-Noise	173
F Simulation of Apparent Measurements		185
F.1	Simulation of Measurements of Dynamic Changes	185
F.2	Simulation of Measurements of Absolute Optical Properties	186
G Phasor Analysis		187
G.1	Wavelet Phasor Analysis	187
G.1.1	Coherent Hemodynamics Spectroscopy Phasor Ratio Vectors	187

H Determination of Coherence	189
H.1 Coherence	189
H.1.1 Wavelet Coherence	189
H.2 Coherence Thresholding	190
H.2.1 Coherent Hemodynamics Spectroscopy Thresholding	190
Postface	191
Current and Future Work	193
Acknowledgments	195
Family	195
Carolyn Blaney	195
Gary Blaney	195
George Blaney	195
John & Virginia Michaud	196
Phillip & Marjorie Blaney	196
Mary Drabik	196
Ernst & Gail von Metzsch	196
Anjelica Molnar-Fenton	197
Mentors and Colleagues	197
Profs. Sergio Fantini & Angelo Sassaroli	197
Cristianne Fernandez, Leon Wang, & Thao Pham	197
Prof. Charles DiMarzio	197
Blair Cochran	198
Funding	198
Bibliography	199

Acronyms

- 2D** 2-dimensional. 43, 50, 72–76, 80
- 3D** 3-dimensional. 38, 40, 43, 44, 50, 73, 74, 76
- 6D** 6-dimensional. 38
- ABP** Arterial Blood Pressure. 4, 8, 9, 23, 26, 67–71, 78, 87–90, 92, 93, 96, 190
- APD** Avalanche Photo-Diode. 108
- AR** Auto-Regulation. 4, 67, 68, 70–72, 78, 87, 89–94, 99
- bDRS** broadband Diffuse Reflectance Spectroscopy. 107–115, 117–119, 131
- BF** Blood-Flow. xxiv, 3, 23, 53, 54, 56, 57, 69–71, 78, 87, 93, 94, 96, 98, 99, 101–103
- BV** Blood-Volume. 23, 69, 87, 89, 90, 92–94, 96, 98, 99, 102, 103
- CCO** Cytochrome-C-Oxidase. 118, 128, 129, 193
- CHS** Coherent Hemodynamics Spectroscopy. 4, 8, 24, 27, 46, 68–72, 78, 80, 87–89, 93, 94, 99, 100, 102, 187, 189, 190, 193
- CNC** Computer Numerical Control. 50
- CNR** Contrast-to-Noise Ratio. 193
- CPU** Central Processing Unit. 31
- CW** Continuous-Wave. xxii, 4, 16, 47, 54, 107, 108, 110–115, 117–120, 128, 130–133, 141, 146, 147, 156, 160, 163, 164, 171
- CWT** Continuous Wavelet Transform. 187, 189
- D** Deoxy-hemoglobin. xxiv, 3, 8, 67, 92, 94, 95, 99, 117–123, 125, 127–132, 149, 169, 170
- DOI** Diffuse Optical Imaging. 48
- DOIT** Diffuse Optical Imaging of Tissue. xix, 197
- DPF** Differential Path-length Factor. 5, 55, 164
- DS** Dual-Slope. xix, 11, 13–27, 29–33, 35, 41, 43–57, 60, 68, 87, 100–103, 107–115, 117–119, 127, 128, 130–132, 141, 155–157, 160, 163, 165, 172, 173, 193
- DSF** Differential Slope Factor. 7, 14, 49, 55, 164, 165, 172
- FD** Frequency-Domain. xxi–xxiv, 4, 7, 9, 10, 13, 14, 16, 20, 21, 23, 27, 47, 48, 54, 72, 87, 94, 100, 107–109, 111–115, 117–120, 125, 128–133, 141, 146, 155–157, 163, 164, 171, 193
- FFF** Fused Filament Fabrication. 43
- fMRI** functional Magnetic Resonance Imaging. 27, 99, 103
- fNIRS** functional Near-InfraRed Spectroscopy. xxiv, 3, 43, 45–48, 51, 54, 57, 68, 103
- FWHM** Full-Width Half-Max. 37, 38, 44, 46, 119, 120, 187
- GRN** Gaussian Random Number. 72, 73, 76, 80
- ICA** Independent Component Analysis. 3, 103
- IQR** Inter-Quartile Range. 95
- IRB** Institutional Review Board. 52, 55, 117
- L** Lipid. 112, 113, 117–125, 127–142, 149, 170

- MD** Multi-Distance. 4, 7, 8, 13, 48, 68, 87, 88, 92, 94, 101, 103, 107–109, 111–115, 117, 130, 155, 156
- MP** Moore-Penrose inverse. 34, 35, 39, 48, 50, 53, 55
- NIH** National Institutes of Health. 198
- NIRS** Near-InfraRed Spectroscopy. xx–xxiv, 3–5, 7, 9, 13, 14, 16, 19, 21, 23, 27, 40, 47, 48, 50, 67, 68, 71, 87, 88, 92, 94, 97, 100, 103, 107–109, 111–115, 117–119, 125, 129, 131, 132, 156, 163, 193
- O** Oxy-hemoglobin. xxiv, 3, 8, 67, 92, 94, 95, 99, 117–123, 125, 127–132, 149, 169, 170
- OD** Outer Diameter. 40, 42
- PDMS** PolyDiMethylSiloxane. 41–44, 47, 48
- Ph.D.** Doctor of Philosophy. xix, 195, 197
- PLA** PolyLactic Acid. 43, 44
- PMT** PhotoMultiplier Tube. 40, 108
- Prof.** Professor. xxi, 197, 198
- RAM** Random Access Memory. 31, 38, 72–75, 78–81
- S** tissue oxygen Saturation. 94, 95, 120–123, 132–142, 149
- SC** Self-Calibrating. 14, 21, 23, 48, 53–55, 107, 108, 117–119, 125, 129, 131, 132, 155, 156
- SD** Single-Distance. 4–7, 9–11, 13–22, 24–27, 29–33, 41, 44, 47, 54–58, 87, 88, 94–103, 107, 130, 163–165, 172, 173, 185
- SEM** Standard-Error of the Mean. 100, 118, 120, 124, 125
- SMA** SubMiniature version A. 40
- SNR** Signal-to-Noise Ratio. 5–7, 17, 20, 21, 43, 118, 173
- SS** Single-Slope. 6, 7, 9–11, 13–22, 24–27, 29–33, 41, 44, 48, 58, 87, 88, 94–102, 156, 163–165, 172, 173
- SVD** Singular Value Decomposition. 34, 39, 40, 46
- T** Total-hemoglobin. 68, 93–95, 102, 103, 120–124, 132–142, 149
- TD** Time-Domain. xxii, 4, 13, 20, 21, 27, 72, 103, 107, 130
- TFA** Transfer-Function Analysis. 71, 72, 78, 80
- TTL** Transistor-Transistor Logic. 109, 110
- UHMW** Ultra High Molecular Weight polyethylene. 41, 42
- USB** Universal Serial Bus. 109, 110
- VO** Venous Occlusion. 51, 53, 54
- W** Water. 44, 94, 110–115, 117–125, 127–142, 149, 170

Symbols

I	Intensity. xxii–xxiv, 5–7, 9, 10, 13, 14, 16–22, 24–27, 45, 47–51, 53, 54, 56, 57, 87, 88, 94–103, 118, 146, 155, 156, 163–165, 171–173, 185	$\ln(\rho^2 I)$ linearized Intensity. 7, 13, 16, 23, 107, 146, 156, 164
R	Reflectance. xxiv, 3, 107, 108, 110, 113, 120, 128, 129, 132, 133, 146–148, 155, 171	Δ localization matrix. 36–38, 44, 46, 62
ΔA	Arterial blood pressure change. 69, 71, 189	Γ resolution matrix. 36–38, 44, 46, 62
ΔD	Deoxy-hemoglobin concentration change. 3, 8, 9, 24, 26, 27, 54–57, 67, 69, 71, 78, 88, 94, 98, 149, 163, 170, 186, 189	$\mathcal{S}^+ \mathcal{S}$ inverse sensitvity matrix multiplied by the original sensitvity matrix. 35–39
ΔO	Oxy-hemoglobin concentration change. 3, 8, 9, 24, 26, 27, 54–57, 67–69, 71, 78, 88, 94, 98, 149, 163, 170, 186, 189	\mathcal{S} matrix of sensitvity to absorptiion change. 33–35, 38–40, 48–50, 53, 55, 171
ΔT	Total-hemoglobin concentration change. 8, 9, 54, 69, 71, 94	\mathcal{A} additive optical artifact. 14–16
ΔD	Oxy-hemoglobin minus Deoxy-hemoglobin concentration change. 69	\mathcal{S} Sensitivity to absorptiion change. 4, 5, 7–10, 17–25, 27, 33, 34, 45, 47, 48, 53, 54, 68, 87, 92, 96, 101–103, 133, 171–174, 185, 186, 193
Φ	fluence rate. xxii, 147, 171	\mathcal{Y} optical data. 13–16, 164, 165, 172, 173
\bar{R}^2	adjusted coefficient of determination. 119, 120, 122–124	\mathfrak{C} Coherence. 68–74, 76–80, 94–97, 102, 187, 189, 190, 193
\hat{F}	blood Flow unit phasor. 69, 70, 94	μ_{eff} effective attenuation coefficient. 107–111, 133, 146, 155
\hat{V}	blood Volume unit phasor. 69, 70	ω angular modulation frequency. xxiv, 145–148, 155, 156, 164, 171
κ	condition number. 35, 38–40, 45, 46	ϕ phase. xxii–xxiv, 4–7, 9–11, 13, 14, 16–27, 43, 45, 47–51, 53, 54, 56, 57, 87, 88, 94–103, 107, 146, 155, 156, 163–165, 171–173, 185, 193
λ	optical wavelength. xxii, xxiii, 3, 8, 15, 25, 40, 54, 94, 107, 108, 110–112, 114, 115, 117–120, 122, 124, 125, 128–130, 132, 133, 142, 149, 150, 169, 170, 186	ρ source-detector distance. xxii, 3–11, 13–23, 27, 29–33, 48, 68, 87, 89–94, 96–101, 107–110, 113, 117, 119, 128–133, 145–148, 155, 156, 163–165, 171–173, 185, 186
$\langle t \rangle$	mean time-of-flight. 4, 20, 27, 103	$\mathfrak{C}(\tilde{D}, \tilde{A})$ Coherence between Deoxy-hemoglobin and Arterial blood pressure phasor. 69, 94, 95, 190

- $\epsilon(\tilde{O}, \tilde{A})$ Coherence between Oxy-hemoglobin and Arterial blood pressure phasor. 69, 94, 95, 190
- $\epsilon(\tilde{T}, \tilde{A})$ Coherence between Total-hemoglobin and Arterial blood pressure phasor. 69, 94, 95, 190
- \vec{C} cross-talk between voxels vector. 35, 36, 38, 44, 46
- $\vec{\mathcal{R}}$ reconstruction of voxels vector. 35, 36, 38, 44, 46
- $\overrightarrow{D/A}$ phasor ratio vector between Deoxy-hemoglobin and Arterial blood pressure phasor. 89, 90
- $\overrightarrow{D/O}$ phasor ratio vector between Deoxy-hemoglobin and Oxy-hemoglobin. 8–10, 24, 25, 27, 68–70, 88, 89, 92–94, 96–102, 187, 188, 190
- $\overrightarrow{O/A}$ phasor ratio vector between Oxy-hemoglobin and Arterial blood pressure phasor. 89, 90
- $\overrightarrow{T/A}$ phasor ratio vector between Total-hemoglobin and Arterial blood pressure phasor. 69, 70, 88–94, 100–103, 187, 188, 190
- \vec{r} position vector. 5, 29, 31–34, 145–147, 155, 163–165, 171–173
- \tilde{A} Arterial blood pressure phasor. 68–70, 87, 89, 91, 94, 187
- \tilde{D} Deoxy-hemoglobin phasor. 8, 24, 25, 67–70, 87, 89, 93, 94, 96, 98, 99, 101, 186, 187
- \tilde{O} Oxy-hemoglobin phasor. 8, 24, 25, 67–70, 87, 89, 93, 94, 96, 98, 99, 101, 186, 187
- \tilde{R} complex Reflectance. 108, 120, 128, 132, 133, 145–148, 151, 155, 163, 171, 172, 186
- \tilde{T} Total-hemoglobin phasor. 69, 70, 87, 89, 91, 93, 94, 102
- $\tilde{\Phi}$ complex fluence rate. 147, 152, 171, 172
- $\tilde{\mu}_{eff}$ complex effective attenuation coefficient. 107–109, 111, 133, 145, 147, 155, 163
- a single scattering albedo. 114
- b reduced scattering power coefficient. 111, 120, 121, 123, 125–127, 132, 133, 135, 137–139, 141, 150
- c speed of light in vacuum. 145–147, 155, 156
- f_{mod} modulation frequency. xxii, 5, 7, 16, 21, 25, 27, 132, 146, 147, 164, 193
- n index of refraction. 5, 25, 51, 133, 145–148, 151, 155, 156
- $\Delta\mu_a$ absorption coefficient change. 3–8, 14, 15, 17, 18, 24, 50, 53–55, 112–114, 133, 149, 163–165, 169–173, 185, 186
- $\Delta\vec{\mu}_a$ vector of absorption coefficient changes. 34–36, 39, 53, 149, 169, 185
- ϵ extinction coefficient. 107, 112–114, 117–119, 133, 149, 170
- $\langle L \rangle$ total optical path-length. 163–165, 171–173
- $\langle \ell \rangle$ partial optical path-length. 171–173, 193
- $\langle \tilde{L} \rangle$ general complex total optical path-length. 14, 163, 164, 166, 171, 172
- $\langle \tilde{\ell} \rangle$ general complex partial optical path-length. 171–174
- E matrix of extinction coefficients. 149, 169, 170
- μ_a absorption coefficient. xxii–xxiv, 3–5, 8, 9, 14, 15, 23, 25, 48, 49, 51–53, 56, 94, 95, 107, 108, 110–115, 117–122, 124–133, 135, 141, 145–149, 155, 156, 163, 169, 173, 186, 193
- μ'_s reduced scattering coefficient. xxii, xxiii, 3–5, 8, 9, 14, 15, 23, 25, 48, 49, 51–53, 56, 95, 107, 108, 111, 113, 119–121, 123, 125–127, 129, 130, 132, 133, 135, 137–139, 141, 145–150, 155, 156, 163, 171, 186, 193
- μ_s scattering coefficient. 114
- μ'_t total reduced attenuation coefficient. 155, 156
- μ_t total attenuation coefficient. 114
- $\vec{\mu}_a$ vector of absorption coefficients. 149, 169, 170

Equipment, Materials, & Software

Arduino Arduino Uno R3 [Ivrea, Italy]. 110

cII Daler-Rowney Calli India-Ink [Bracknell, England]. 41, 48

HAL Avantes AvaLight-HAL-S-Mini [Louisville, CO USA]. 110

HERO Avantes AvaSpec-HERO [Louisville, CO USA]. 110

II Higgins India-Ink [Leeds, MA USA]. 44, 48, 111–115

Imagent ISS Imagent V2 [Champaign, IL USA]. xxiii, 7, 14, 21, 23, 40, 48, 54, 88, 108

LBMB Photonwares 1×2 LBMB [Woburn, MA USA]. 110

MATLAB MathWorks MATrix LABoratory [Natick, MA USA]. 29–31, 36–38, 58–60, 62, 63, 72, 75–77, 79, 80, 82, 85, 119, 151, 152, 156, 157, 160, 166, 169, 170, 172, 174, 185, 187, 189, 190

N7 QCR Solutions NIR746A [Palm City, FL USA]. 110–115

N8 QCR Solutions NIR869A [Palm City, FL USA]. 110–115

silicone Rubber Glass Smooth-On [Macungie, PA USA]. 48

TiO₂ AEE Titanium diOxide powder [Upper Saddle River, NJ USA]. 48

Preface

Organization of this Work

The purpose of this dissertation is two-fold. First, to summarize the work that I have done during my time as a Doctor of Philosophy (Ph.D.) Candidate in the Diffuse Optical Imaging of Tissue (DOIT) lab at Tufts University. Second, to provide a guide for future DOIT lab members to understand the methods that we have utilized during my time in the lab. The dissertation focuses on the first purpose and achieves the second by expanding on some introductions to techniques beyond what exists in published work.

During my approximately 4.5 yr in the DOIT lab I have been able to publish 9 first author articles[1–9] and present 6 times at conferences as first author[10–15]. This dissertation is organized to include all of this work, but due to the amount of content in published articles alone, I have focused on those. Therefore, have opted not to include work that has not made it to publication yet, has only been presented at conferences, or has been the result of collaborations.

Table 1 provides a guide to the dissertation, and shows which of my first-author articles apply to which chapters. Overall the work is organized into three parts and an appendix. Part I is the most important, describing our work to achieve measurements that are preferentially sensitive to deep regions within a diffuse medium; this is centered around Dual-Slope (DS). Part II describes how these measurements have been applied to brain hemodynamics, and our phasor based analysis of those hemodynamics. Part III describes how we have applied the calibration-free advantages of DS to absolute measurement over a broadband spectrum. Finally, Appendices A–H present all of the supporting methods for this work.

Table 1 also guides which chapters would

be more suited for people with different backgrounds. I have split the backgrounds into three categories:

- Novice: One who is in a completely different field *or* an underclassmen undergraduate student.
- Competent: One who is in a closely related field *or* an upperclassmen undergraduate student *or* an underclassmen graduate student.
- Expert: One who is in the same field *or* an upperclassmen graduate student *or* one who has completed their Ph.D. in a closely related field.

These are of course suggestions and the reader may choose to read any section in any order they wish. Links between, and references to, sections are provided whenever possible to explain where one should go for more information on one topic or another.

Table 1: Organization and guide to this dissertation

Page		Recommended for a			Articles
		Novice	Competent	Expert	
NIRS Intro	xxi	Yes	Optional	No	-
Chapter 1	3	Optional	Yes	Optional	-
Chapter 2	5	No	Optional	Yes	[1, 2]
Chapter 3	13	Optional	Yes	Yes	-
Chapter 4	23	No	Optional	Yes	[3]
Chapter 5	29	No	Optional	Yes	[4, 5]
Chapter 6	67	Optional	Yes	Yes	-
Chapter 7	71	No	No	Optional	[6]
Chapter 8	87	No	Optional	Yes	[1-3]
Chapter 9	107	No	Optional	Yes	[7]
Chapter 10	117	No	Optional	Yes	[8, 9]
Appendix	145	No	Optional	Optional	-

Note ¹ Articles refer only to my first-author journal articles that are directly pertinent to that chapter.

Acronyms Near-InfraRed Spectroscopy (NIRS); and Introduction (Intro).

A Brief Introduction to Frequency-Domain Near-Infrared Spectroscopy

To understand what Frequency-Domain (FD) Near-InfraRed Spectroscopy (NIRS) is we must first understand the optically diffuse medium. In an optically diffuse medium light moves about by randomly changing the direction it's traveling. Particles representing packets of light are called photons. The act of these photons randomly changing direction is called scattering. Therefore, one says that an optically diffuse medium is one in which the behavior of photons is mostly described by their scattering. An example of a possible random photon path from scattering can be seen in Figure 1.

In reality many media may be described in this optically diffuse way. For example, a cloud is optically diffuse. In a cloud photons enter, randomly scatter within, then exit. Due to the random scattering of the photons, your eye can not determine where a photons entered the cloud, thus the cloud appears opaque or white. Expanding on this example you may realize that, in general, what is described as an optically diffuse medium is seen as opaque. Examples of this are the aforementioned cloud, a glass of milk, or even biological tissue.

Scattering is not the only thing that may happen to a photon in a diffuse medium. A second common property that a diffuse medium has is absorption. This is when photons die when they interact with the medium. Take a black cup of coffee, this medium is primarily absorbing since photons die off as they travel through the liquid. But black coffee has little scattering since

the photons do not change direction much.^a If the coffee is strong and dark we know that it has high absorption, while if it is light and watery we know it has low absorption. Now imagine we add milk to the coffee, this will make the coffee opaque as we have just added scattering and the photons' directions within the liquid are now randomized. If we add cream instead of milk we may notice the coffee is even more opaque since cream has higher scattering compared to milk.

Both absorption and scattering are probabilistic statements since every time a photon interacts with a piece of the medium there is a some chance that it will be absorbed, scattered, or neither. This is probabilistic because there is chance or probability associated with these events, just like when flipping a coin or rolling a dice. Since these interactions happen billions of times within the medium, the average behavior of the photons becomes rather predictable. In the coin flipping analogy, this is the same as saying that, if you flip a coin billions of times, we can predict that very close to half those times it will come up heads. An example of this predictable average distribution of the photons can be see in Figure 1. This is in some ways amazing since we have stared with random events and can draw predictable conclusions. Focusing on diffusion theory, a theory that describes a optically diffuse medium, this average behavior can be modeled using two optical properties that are associated with the absorption probability and probability of scatter in a random direction. These properties are named

^aCredit for this example goes to Prof. Steven Jacques.

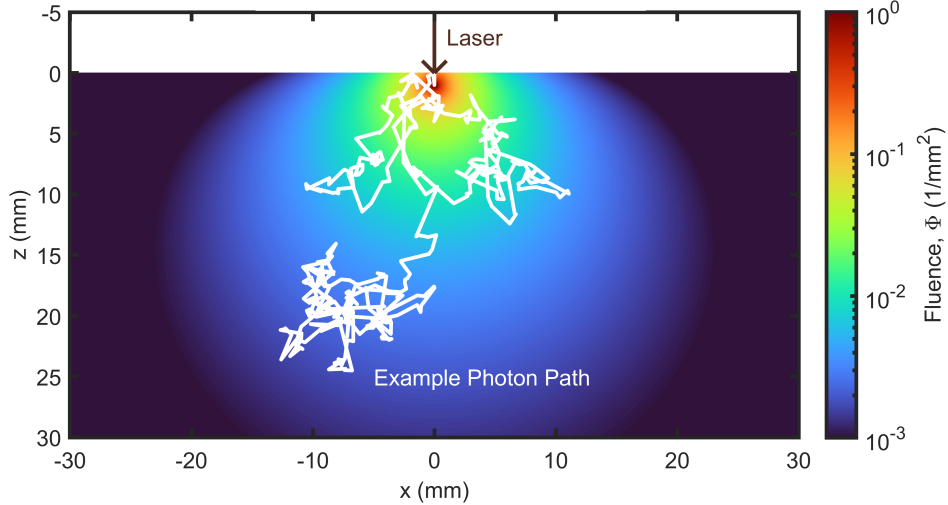


Figure 1: Example distribution of fluence rate (Φ) which may be thought of as photon density produced from the diffusion of many photons. An Example possible path of a single photon is shown as a white line.

the absorption coefficient (μ_a) and the reduced scattering coefficient (μ'_s).

FD NIRS essentially seeks to measure these two properties, that is the μ_a and the μ'_s , to describe a diffuse medium. In general μ_a provides chemical information about the medium, like the strength of the coffee in the above example, and μ'_s provides structural information, like the amount of fat droplets from cream in the coffee. A popular application of NIRS is in the measurement of biological tissues. In this cause μ_a may give us information about concentrations of blood. The μ_a of blood is dependent on the optical wavelength (λ), which can be thought of as the color of the light. A typical dependence of μ_a on λ is shown in Figure 2. NIRS is called Near-InfraRed Spectroscopy because the technique focuses on a range of colors or λ s starting from red and going to near-infrared,^b with the former being visible by the human eye and the latter not. The reason for this choice of λ s is that biological tissue tends to have lower absorption in this range, thus photons can probe further into tissue. In-fact Figure 2 shows the average path before absorption versus λ to show this so-called

optical window of tissue.

Now lets consider how NIRS measurements are physically done. In the most basic sense some source of light is used to inject^c photons into a medium, then that light is detected at some other point at some source-detector distance (ρ).^d The way the source light varies in time describes the flavor of NIRS. This is either Continuous-Wave (CW), FD, or Time-Domain (TD). In the case of CW the source light does not change with time, for FD the brightness or intensity of the light oscillates as a sinusoidal wave,^e and finally TD uses a source with a brief pulse of light. Focusing only on the interpretation of FD, the detected light will have some oscillation amplitude (*id est* Intensity (I)) and some time shift which is called its phase (ϕ) shift. This provides two pieces of information about the behavior of light within the medium which then may be translated into the two desired properties, the μ_a and the μ'_s .

As mentioned above, a notable application of

^cBy inject we simply mean that photons are made to enter the medium, this can be as simple as shining a light at the optical medium.

^dSource-detector distance (ρ) is typically on the order of 10 mm.

^eThe modulation frequency (f_{mod}) is on the order of 100 MHz for Frequency-Domain (FD).

^bThis near-infrared optical wavelength (λ) range is approximately 600 nm to 1000 nm.

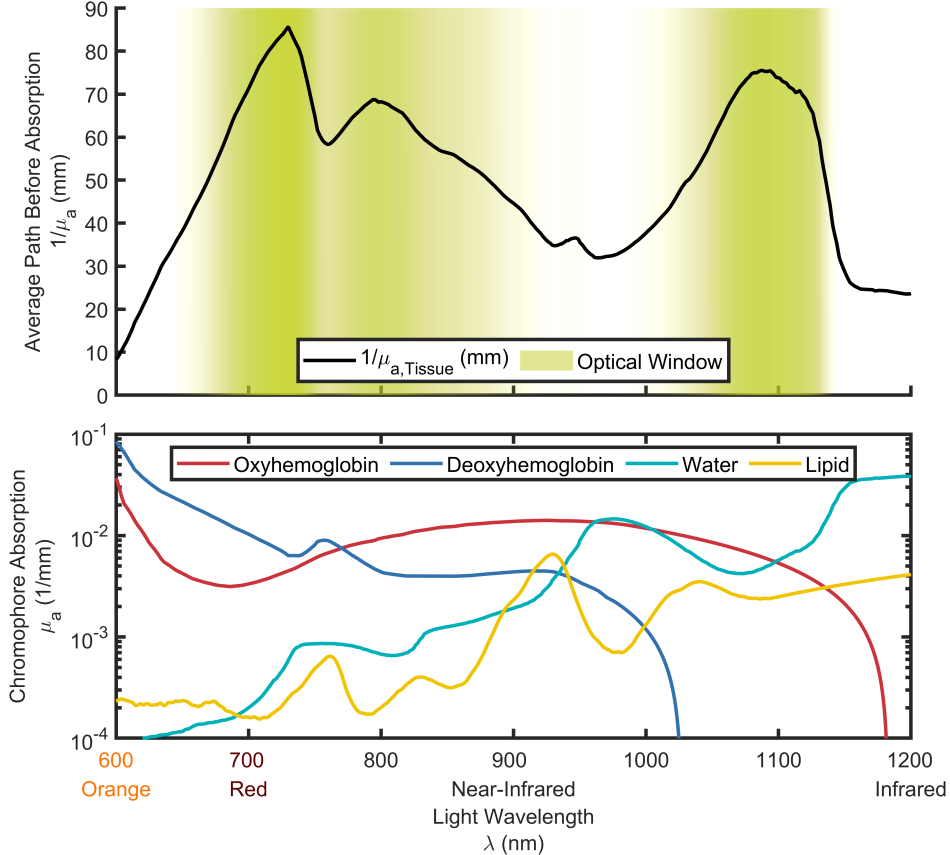


Figure 2: [Top] The average length of a path before a photon is absorbed ($1/\mu_a$) versus optical wavelength (λ) in biological tissue. Long path-lengths allow for deeper light penetration, these regions are so-called optical windows and are shown in green. [Bottom] The typical absorption coefficient (μ_a) versus λ for typical biological chromophores (*id est* absorbers).

diffuse optics and NIRS is on biological tissues [16–18]. However, diffuse optics finds a variety of applications in several other fields of study. In food science [19], it may be applied for inspection [20] or evaluation [21]. In pharmaceutical manufacturing, diffuse optics may join other process analytical technologies, for example to analyze and characterize particles [22] or powders [23]. A few other examples include archaeological soil analysis [24], dendrology (study of wood) [25], and art authentication [26]. In the study of biological tissue, diffuse optics finds applications in basic research, medical diagnostics, and physiological monitoring. Examples include clinical brain monitoring [27], the study of brain activation [28], breast imaging [29], and muscle measurements in sports science [30]. This is by no

means an exhaustive list of the possible applications of NIRS and diffuse optics.

Regardless of application, a laboratory can purchase a commercially available FD NIRS instrument for their research. In this work the ISS Imagent V2 [Champaign, IL USA] (Imagent) was utilized for all FD NIRS experiments. These instruments provide FD measurements at multiple discrete λ s and retrieve the I and ϕ of the detected FD light. Therefore, they can be used either for absolute measurement of optical properties μ_a and μ'_s or dynamic measurements of μ_a which are interpreted as hemodynamics.

We conclude this introduction with a specific example of a FD NIRS experiment applied to the human brain. When a person experiences some visual stimulus, it is expected that the vi-

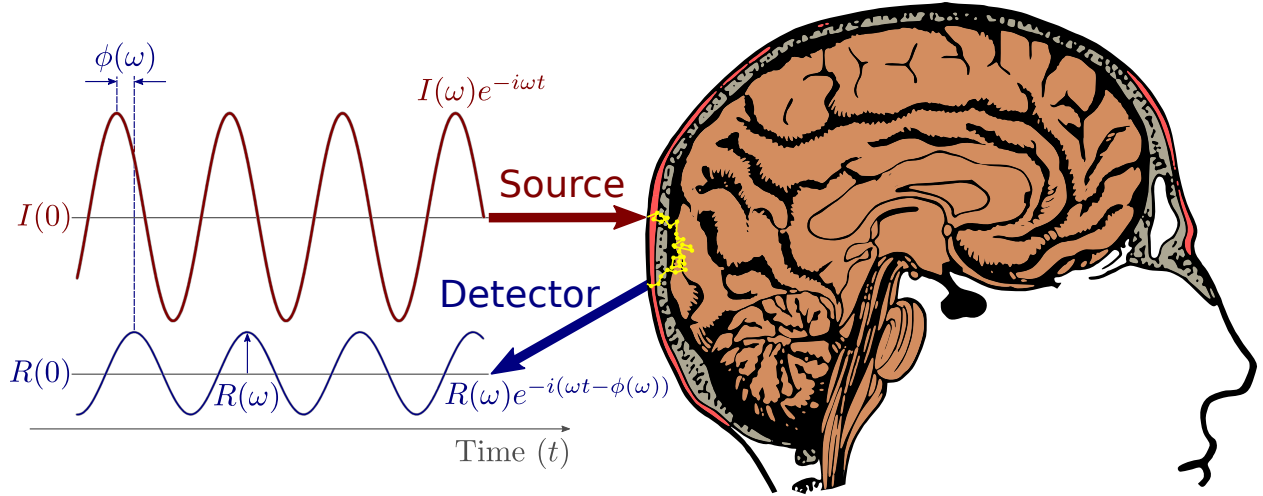


Figure 3: Example of Frequency-Domain Near-Infrared Spectroscopy applied to the human brain. Temporal profile of source light in red and of detected light in blue.

Symbols: Phase (ϕ), angular modulation frequency (ω), source Intensity (I), & detected Reflectance (R)

sual portion of their brain will begin to utilize more oxygen. This causes the body to increase Blood-Flow (BF) to the visual cortex and so that more oxygen may be supplied there. An increase in BF is indicated by an increase in the concentration of Oxy-hemoglobin (O) and a decrease in the concentration of Deoxy-hemoglobin (D). Since these concentrations are connected to μ_a by Figure 2, one may measure this change using FD NIRS. Therefore an experiment may be devised to make these so-called functional Near-Infrared Spectroscopy (fNIRS) measurements as shown in Figure 3. Here sinusoidal light is injected into the subject's head where it diffuses through the brain before being detected. The detected light's phase shift and amplitude is measured and may be converted to optical properties and blood concentrations. Through analysis the changes in O and D may indicate BF and thus brain activity. This example is just one application in which FD NIRS may be used to make measurements on tissue. The following dissertation will discuss details on how to collect and analyze these FD NIRS data, including the case of this example experiment, as well as various other experiments and applications.

Part I

Preferentially Deep Measurements

Chapter 1

Motivation for Seeking Deep Measurements

Near-InfraRed Spectroscopy (**NIRS**) is a measurement technique that has found a variety of applications in the study of highly scattering media. It is capable of measuring the absorption coefficient (μ_a) and reduced scattering coefficient (μ'_s), where the former represents chemical information and the latter represents structural information (see Page [xxi](#)). A key application of these measurements is non-invasive investigation of biological tissues. Examples of biomedical **NIRS** applications include measurements on skeletal muscle [31] to extract Blood-Flow (**BF**) or oxygen consumption, imaging of breast tissue [29] to detect breast cancer, and assessment of cerebral hemodynamics in the brain [32]. When measurement of tissue chromophores such as Oxy-hemoglobin (**O**) and Deoxy-hemoglobin (**D**) is the focus, μ_a becomes the chief property of interest. This is because concentrations of **O** and **D** can be found using Beer's law and μ_a at multiple optical wavelengths (λ_s) (Appendices **A&D**). Furthermore, measurements of hemodynamics may be achieved by measuring absorption coefficient change ($\Delta\mu_a$) and converting to Oxy-hemoglobin concentration change (ΔO) and Deoxy-hemoglobin concentration change (ΔD) which is less demanding than achievement absolute measurement (Appendices **C&D**).

A common implementation of **NIRS** is in the Reflectance (**R**) mode, in which the scattering medium is often modeled by a semi-infinite geometry. In these diffuse **R** measurements, signal contributions from superficial layers may obscure

contributions from deeper portions of the turbid medium. Since the targeted tissue is often below these superficial layers, methods that produce data representative of the deeper region are sought. The importance of addressing these superficial confounding effects has been especially recognized in measurements on the brain [33, 34]. Two such areas include functional Near-InfraRed Spectroscopy (**fNIRS**) [32, 35] for studies of brain activity and cerebral oximetry [36, 37] for clinical applications. In these cases the superficial region is extracerebral tissue (scalp, skull, *dura* mater, *subdural*, *arachnoid*, and *subarachnoid* spaces) through which all detected photons must propagate.

Numerous methods have been proposed to decouple superficial or systemic hemodynamic changes from those specific to the brain [33, 38–41]. One such approach is to collect data at short and long source-detector distance (ρ) separations in conjunction with data processing methods such as Independent Component Analysis (**ICA**) [38], adaptive filtering [39], regression procedures [40], or a least-square algorithm [41]. Alternatively, physiological modeling of hemodynamic and metabolic processes in the scalp and the brain, treated as separate tissue compartments, has been proposed [33]. The vast majority of the methods for superficial hemodynamic decontamination have been introduced for functional brain studies, where one may think that the activated cortical area responds in a unique way, and independent of systemic changes occurring in both extra-cerebral and cerebral tissues. However,

in recent years, more studies have been focusing on induced or spontaneous systemic changes in Arterial Blood Pressure (ABP) for studying micro-circulation integrity and cerebral Auto-Regulation (AR) for which the above decontamination assumptions may no longer be valid. For example systemic changes are observed with Coherent Hemodynamics Spectroscopy (CHS) [42–44], paced breathing [45], and spontaneous low frequency oscillations [46–48]. Further methods to induce cerebral perfusion changes include modulating the fraction of inspired carbon dioxide [49]. The level of success in decoupling the cerebral and scalp hemodynamics contributions to optical signals has been variable, and thus remains a critical issue in the field on non-invasive NIRS. For measurements of the brain, it would be preferable to develop methods that are intrinsically more sensitive to brain tissue by reducing contributions from the scalp and skull, thus avoiding more complicated signal processing techniques. Of course, this result would also be relevant to non-invasive measurements of other tissues (skeletal muscle, breast tissue, *et cetera*) that are located below superficial layers (skin, adipose tissue, *et cetera*).

Such preferentially deep NIRS measurements may be achieved without complex signal processing assumptions by using gradients of optical signals versus ρ instead of measurements between a single source and detector. Such so-called slope based methods have been shown to be weakly sensitive to a uniform superficial layer [50]. Additionally, further advantages can be found in the various temporal domains of NIRS. Most of the commercially available NIRS instruments are based on Continuous-Wave (CW) light emission and optical detection [18]. However, richer information is provided by time-resolved methods in the Frequency-Domain (FD) and Time-Domain (TD), where the light sources are intensity modulated (at a frequency on the order of 100 MHz) or pulsed (with a pulse width on the order of 10 ps), respectively. Time-resolved methods have shown a higher sensitivity to deeper changes in tissues compared to CW methods [27, 51], either in TD through mean time-of-flight ($\langle t \rangle$), higher moments (like the variance), or late time gates

of the photon time-of-flight distribution [42, 52–54], or in FD through phase (ϕ) measurement [51]. Moreover, slope methods based on Multi-Distance (MD) measurements of the first and second moments in TD [54] or ϕ in FD [50, 55–57] have shown to feature a reduced superficial Sensitivity to absorption change (S) in the tissue than Single-Distance (SD) methods.

The issue of NIRS measurements being sensitive to superficial signal is an issue whether the measurement is absolute μ_a and μ'_s or hemodynamics through $\Delta\mu_a$. However, due to the importance and interest of hemodynamic measurements, they will be the primary focus of the following chapters. Therefore, we will seek to investigate various methods for retrieving $\Delta\mu_a$ with the goal of achieving a preferentially deep measurement.

Chapter 2

Short versus Long Source-Detector Distances

2.1 Sensitivity Profiles

One of the most basic methods for probing deeper in a diffuse medium with Near-InfraRed Spectroscopy (NIRS) is to use longer source-detector distance (ρ). This is based on the idea that longer ρ s are sensitive to deeper parts of the medium. If we focus on measurement of absorption coefficient change ($\Delta\mu_a$), we can produce Sensitivity to absorption change (\mathcal{S}) maps as those shown in Blaney *et alia* Journal of Biophotonics (2020) [3]. The methods for doing this are shown in Appendix E. Essentially \mathcal{S} may be interpreted using the following expression:

$$\mathcal{S}_i(\vec{r}_j) = \frac{[\Delta\mu_{a,apparent}]_i}{\Delta\mu_{a,actual}(\vec{r}_j)} \quad (2.1)$$

which, shows the \mathcal{S} of measurement i which measures an apparent absorption change of $[\Delta\mu_{a,apparent}]_i$ when there is an actual absorption change of $\Delta\mu_{a,actual}$ at position \vec{r}_j . \mathcal{S} has the property that when it is spatially summed over the whole medium the result is one,^a meaning the measurement would measure the actual $\Delta\mu_a$ if the change occurred everywhere.

We may go one step further when considering these \mathcal{S} maps by considering the size of the $\Delta\mu_a$ perturbation both in terms of volume and amplitude and the instrumental noise. By doing so the \mathcal{S} maps can be converted to Signal-to-Noise Ratio (SNR) maps. Methods for doing

^aThe sum of Sensitivity to absorption change (\mathcal{S}) over the whole medium is one if the considered perturbation volumes, see Appendix E.

this are explained in Blaney *et alia* Journal of Biophotonics (2020) [3] and Appendix E. Using the SNR maps, one may choose to create Boolean maps showing where the SNR is greater than one. These are the maps shown in this chapter to represent where within a medium a given measurement can measure a given absorption change considering instrumental noise.

The specific parameters used to simulate a semi-infinite homogeneous medium were a absorption coefficient (μ_a) of 0.01 mm^{-1} , reduced scattering coefficient (μ'_s) of 1.2 mm^{-1} and index of refraction (n) of 1.4. The perturbation was considered to be a $\Delta\mu_a$ of 0.003 mm^{-1} and size $10 \text{ mm} \times 10 \text{ mm} \times 2 \text{ mm}$. Instrumental parameters included a modulation frequency (f_{mod}) of 140.625 MHz, Intensity (I) noise of 0.4 %, and phase (ϕ) noise of 0.06° . These parameter values are used in various of our \mathcal{S} maps and simulations both in this chapter and subsequent chapters.

2.1.1 Single-Distance Sensitivity

Single-Distance (SD) measurements obtain changes in either the I or ϕ between a single source and single detector. These changes can then be converted to apparent $\Delta\mu_a$ using the Differential Path-length Factor (DPF) method as shown in Blaney *et alia* Journal of Biophotonics (2020) [3] and Appendix C.

Figure 2.1 shows maps of where the SNR is greater than or equal to 1 from the \mathcal{S} and parameters in Section 2.1. These maps show the profiles for both SDI and SD ϕ with ρ s of 11 mm, 16 mm,

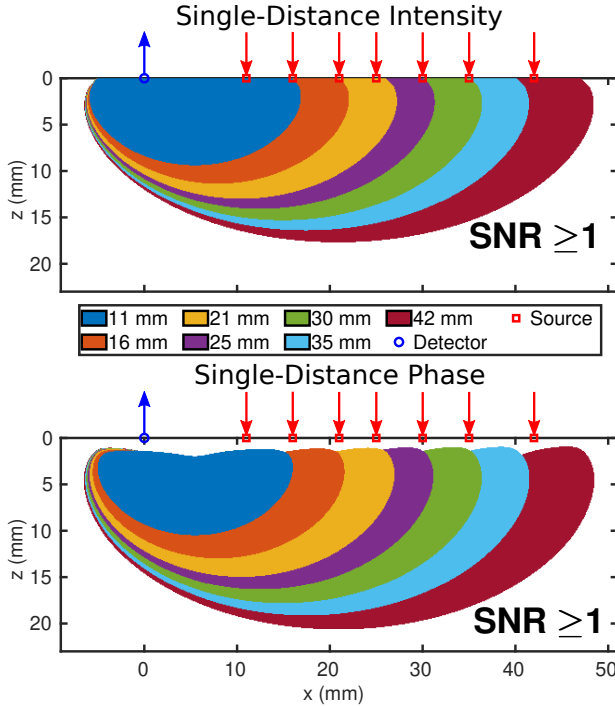


Figure 2.1: Regions where the Signal-to-Noise Ratio (SNR) is ≥ 1 for Single-Distance (SD) measurements at the seven different source-detector distances (ρ_s) of 11 mm, 16 mm, 21 mm, 25 mm, 30 mm, 35 mm and 40 mm. [Top] SD Intensity (I). [Bottom] SD phase (ϕ).

Note 1: Simulation parameters stated in Section 2.1.

Note 2: Simulation methods in Appendix E.

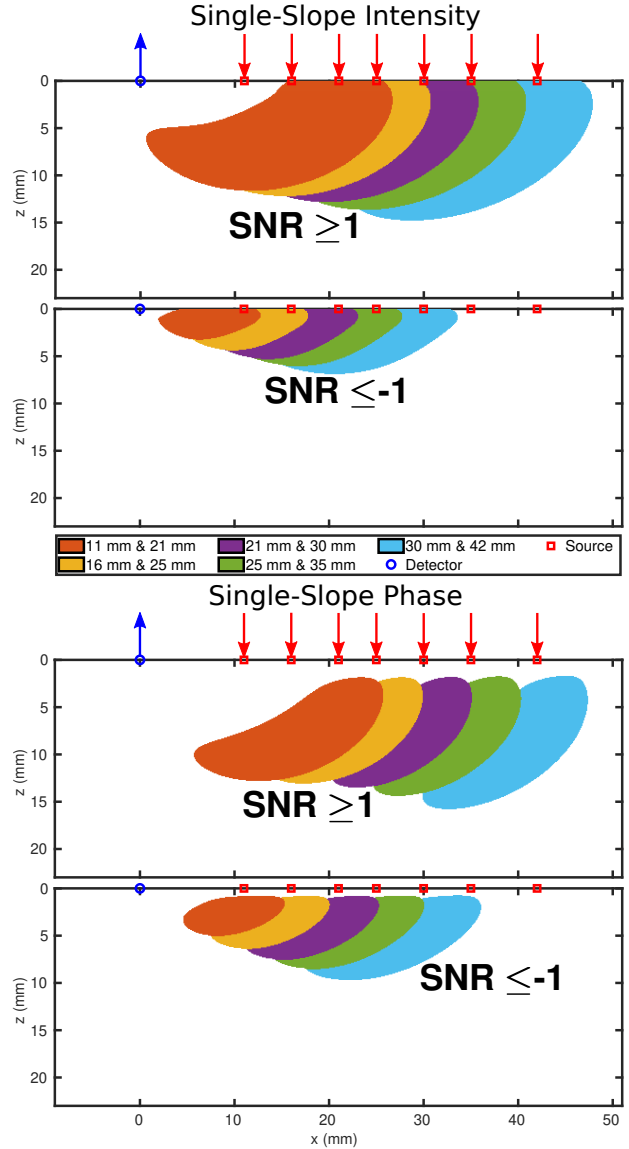


Figure 2.2: Regions where the Signal-to-Noise Ratio (SNR) is ≥ 1 or ≤ -1 for Single-Slope (SS) measurements at the five different source-detector distance (ρ) pairs of 11 mm and 21 mm, 16 mm and 25 mm, 21 mm and 30 mm, 25 mm and 35 mm, and 30 mm and 40 mm. [Top] SS Intensity (I). [Bottom] SS phase (ϕ).

Note 1: Simulation parameters stated in Section 2.1.

Note 2: Simulation methods in Appendix E.

21 mm, 25 mm, 30 mm, 35 mm and 40 mm. This choice of distances was chosen to be the same as the ones for the probe used in Khaksari *et alia* Journal of Biomedical Optics (2018) [1] and Blaney *et alia* Photonics (2019) [2]. This probe is shown in Figure 2.3.

In general, these maps confirm that the typical statements that longer ρ_s and time-resolved measurements such as ϕ probe deeper. One practical limitation should be mentioned in that, at longer ρ , noise is expected to increase; however this ρ dependent noise was not considered in these maps to make visualization easier. For this reason there is a point of diminishing returns at longer ρ which the maps do not express.

2.1.2 Single-Slope Sensitivity

Now moving to Single-Slope (SS) measurements, we consider either I or ϕ measured at more than one ρ to produce one measurement of $\Delta\mu_a$. SS

measures the changes in the slope of either linearized Intensity ($\ln(\rho^2 I)$) or ϕ versus ρ . These changes are then converted to $\Delta\mu_a$ using the Differential Slope Factor (DSF) method described in Blaney *et alia* Journal of Biophotonics (2020) [3] and Appendix C.

Figure 2.2 shows regions where the absolute SNR is greater than or equal to 1 for SS data-types. Again the probe from Blaney *et alia* Photonics (2019) [2] and Figure 2.3 was considered and slopes were created from SD pairs whose ρs differed by approximately 10 mm. S for SS becomes more complex compared to SD since significant portions of the map become negative. The reason for this is the subtraction used to calculate slopes. The physical meaning of negative S is the possibility of measuring the opposite sign $\Delta\mu_a$ than the actual. This should be considered an artifact. To visualize this Figure 2.2 shows two maps for each of the two data-types SS I and SS ϕ . The SNR less than or equal to negative 1 map corresponds to the negative S region.

Overall SS measurements are considered a slight improvement over SD since they effectively subtract measurements from short ρ from the signal. However, as seen in the maps this can induce artifacts by creating a significant negative S region. However, if the $\Delta\mu_a$ within the medium is layered, then SS has a significant advantage over SD since the negative and positive superficial S regions mostly cancel (Figure 3.7) leaving a signal representative of the deep region.

2.2 Multi-Distance Measurement on the Human Brain

Motivated by the expected Sensitivity to absorption change (S) profiles shown in Figures 2.1&2.2 measurements of cerebral hemodynamics were conducted using many source-detector distances (ρs) in Khaksari *et alia* Journal of Biomedical Optics (2018) [1] and Blaney *et alia* Photonics (2019) [2]. The detailed physiological interpretation of those results will be discussed in Part II. Here we will discuss how these works demonstrate the difference between long and

short ρ .

2.2.1 Methods Used in Multi-Distance Work

2.2.1.A Summary of Experimental Parameters

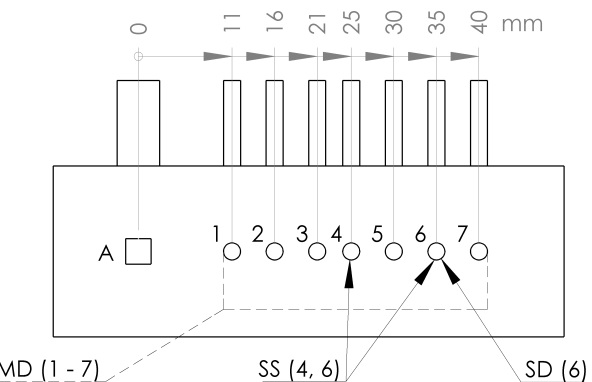


Figure 2.3: Bottom view of a Multi-Distance (MD) optical probe with fiber bundles shown emerging from the top of the drawing. The detector is labeled A and the sources labeled 1 to 7. The full MD set is shown including sources 1 to 7 with source-detector distance (ρ) of 11 mm, 16 mm, 21 mm, 25 mm, 30 mm, 35 mm and 40 mm. An example Single-Slope (SS) set using sources 4 & 7 and an example Single-Distance (SD) set with set source 6 is also shown.

Note 1: This can be found as Figure 1(b) in Blaney *et alia* Photonics (2019) [2].

Note 2: This probe was utilized in Khaksari *et alia* Journal of Biomedical Optics (2018) [1] and Blaney *et alia* Photonics (2019) [2]

Data were collected from 6 healthy human subjects, 3 females and 3 males in Blaney *et alia* Photonics (2019) [2]. Experiments were repeated 10 times on each subject, except Subject 2 for whom measurements were repeated 5 times. Khaksari *et alia* Journal of Biomedical Optics (2018) [1] presented only 1 of these measurement sessions and excluded 1 male subject, while Blaney *et alia* Photonics (2019) [2] presented all data. Frequency-Domain (FD) Near-Infrared Spectroscopy (NIRS) data was collected using an ISS Imagent V2 [Champaign, IL USA] (Imagent) with a modulation frequency

(f_{mod}) of 140.625 MHz and optical wavelengths (λ_s) of 690 nm and 830 nm. 2 optical probes were used (only 1 presented in Khaksari *et alia* Journal of Biomedical Optics (2018) [1]), each featuring one detector fiber bundle and seven pairs of source bundles, with ρ_s of 11 mm, 16 mm, 21 mm, 25 mm, 30 mm, 35 mm and 40 mm (Figure 2.3). The 2 optical probes were placed on the right and left sides of the subject's forehead.^b During the experiment Arterial Blood Pressure (ABP) oscillations were induced at 0.1 Hz using either thigh cuff inflation (Figures 2.4, 8.1, & 4.1) or paced breathing (Figure 8.1). The duration of these oscillations were 3 min in either case. These oscillations will be discussed in more detail in Part II. The full experiment lasted 15 min.

2.2.1.B Analysis Overview

The baseline absorption coefficient (μ_a) and reduced scattering coefficient (μ'_s) were measured using calibrated Multi-Distance (MD) measurements and the linear slopes method in Appendix B. Then using these absolute properties the methods in Appendix C were used to retrieve temporal traces of absorption coefficient change ($\Delta\mu_a$) which where converted to Oxy-hemoglobin concentration change (ΔO) and Deoxy-hemoglobin concentration change (ΔD) using the methods in Appendix D. Finally, Coherent Hemodynamics Spectroscopy (CHS) analysis (discussed in Part II) was achieved using methods in Appendices G&H. For the purposes of this chapter the output of this analysis was phasor ratio vector between Deoxy-hemoglobin and Oxy-hemoglobin (\vec{D}/\vec{O}), or the transfer function between Oxy-hemoglobin (O) and Deoxy-hemoglobin (D) at the oscillation frequency of 0.1 Hz.

To investigate the different S to different regions in tissue, which may have different actual hemodynamic oscillations, data exhibiting these heterogeneities was simulated. Methods for this are explained in Appendix F. Here two layers were simulated with different actual Oxy-

hemoglobin phasor (\vec{O}) and Deoxy-hemoglobin phasor (\vec{D}) and the apparent recovered \vec{D}/\vec{O} retrieved from the simulation for comparison to experimental results.

2.2.2 Summary of Multi-Distance Results

Figure 2.4 shows representative time traces for a MD CHS experiment. This figure results from the protocol in Khaksari *et alia* Journal of Biomedical Optics (2018) [1] and shows the last 2 min of baseline, 3 min of cyclic cuff occlusions, and the first 2 min the end baseline. In this figure, all the signals are filtered with a 0.15 Hz low-pass filter to suppress the cardiac signal. Figure 2.4(a) shows the heart rate, Figure 2.4(b) and Figure 2.4(c) show ABP, Total-hemoglobin concentration change (ΔT), ΔO and ΔD at a ρ of 35 mm, and Figure 2.4(d) and Figure 2.4(e) show ABP, ΔT , ΔO and ΔD at a ρ of 10 mm. The induced oscillations of ABP, ΔT , ΔO and ΔD at 0.1 Hz during cyclic cuff occlusions are clearly visible in Figure 2.4. Already there is some indication of different dynamics at different ρ . However, careful quantitative analysis of these signals requires CHS phasor analysis (Appendices G&H). Figure 2.5 shows the results of such analysis on such dynamic traces.

Figure 2.5 shows average results for the \vec{D}/\vec{O} over ρ for various data-types. To reproduce these experimental results (Figure 2.5(a)(c)) and help interpret them, we used S maps to simulate recovered phasors for a three-layered medium (Appendix F), structured as follows:^c

- A top layer (10 mm thick) featuring arterial volume oscillations represented by $\vec{D} = 0.05\angle 20^\circ \mu\text{M}$ and $\vec{O} = 0.95\angle 20^\circ \mu\text{M}$.
- An intermediate layer (at depths of 10 mm to 15 mm) featuring no hemodynamic oscillations.
- A bottom layer (at depths of 15 mm to 30 mm) featuring blood flow oscillations represented by $\vec{D} = 3.00\angle -180^\circ \mu\text{M}$ and $\vec{O} = 3.00\angle 0^\circ \mu\text{M}$.

^bIn the case Khaksari *et alia* Journal of Biomedical Optics (2018) [1] the 1 probe was placed on the right forehead

^cMotivation for these phasors is found in Part II.

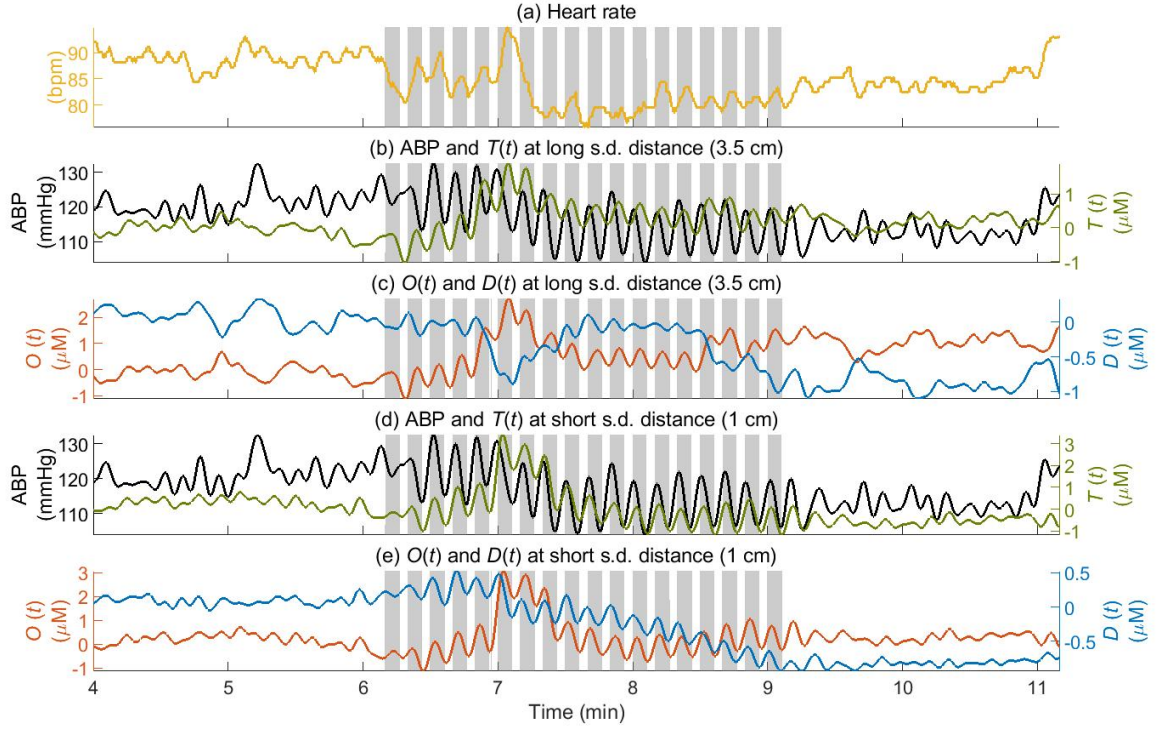


Figure 2.4: Representative time series of the data collected on Subject 1 in Khaksari *et alia* Journal of Biomedical Optics (2018) [1]. (a) Heart rate. (b) Arterial Blood Pressure (ABP) and Total-hemoglobin concentration change (ΔT) at a source-detector distance (ρ) of 35 mm. (c) Oxy-hemoglobin concentration change (ΔO) and Deoxy-hemoglobin concentration change (ΔD) at a ρ of 35 mm. (d) ABP and ΔT at ρ of 10 mm. (e) ΔO and ΔD at a ρ of 10 mm. The shaded areas indicate times of thigh cuff inflation.

Note 1: These results can be found as Figure 3 in Khaksari *et alia* Journal of Biomedical Optics (2018) [1].

The simulation parameters including absolute μ_a and μ'_s can be found in Section 2.1. The simulated phasors are reasonable given the results in both Khaksari *et alia* Journal of Biomedical Optics (2018) [1] and Blaney *et alia* Photonics (2019) [2] as well as Blaney *et alia* Journal of Biophotonics (2020) [3]. This three-layered dynamic medium, which simulates arterial blood volume oscillations in the scalp, no hemodynamic oscillations in the skull, and flow velocity oscillations in the brain, we retrieved the apparent phasors for all of the same measurements done experimentally (Figure 2.5(b)(d)) and were able to largely reproduce our experimental results. From these simulations one may note the significantly greater value of the amplitude of \bar{D}/\bar{O}

for Single-Slope (SS) Intensity (I) and Single-Distance (SD) phase (ϕ) versus SD I at ρs greater than 25 mm, and the shorter ρ range (approximately 15 mm to 20 mm) at which SS I and SD ϕ yield the asymptotic phase value of -180° for \bar{D}/\bar{O} , which is only approached by SD I at approximately 35 mm.

These results in Figure 2.5 provide indications on the different depth-sensitivity of three sets of data collected in non-invasive FD NIRS, namely SD I , SD ϕ , and SS I . It is known that SD I and SD ϕ have different regions of S within tissue, with SD ϕ data probing deeper than SD I , and that SS I affords a reduced S to the most superficial tissue layer (Figures 2.1, 2.2, & 3.7). In Figure 2.5, SD I data shows a trend as the ρ

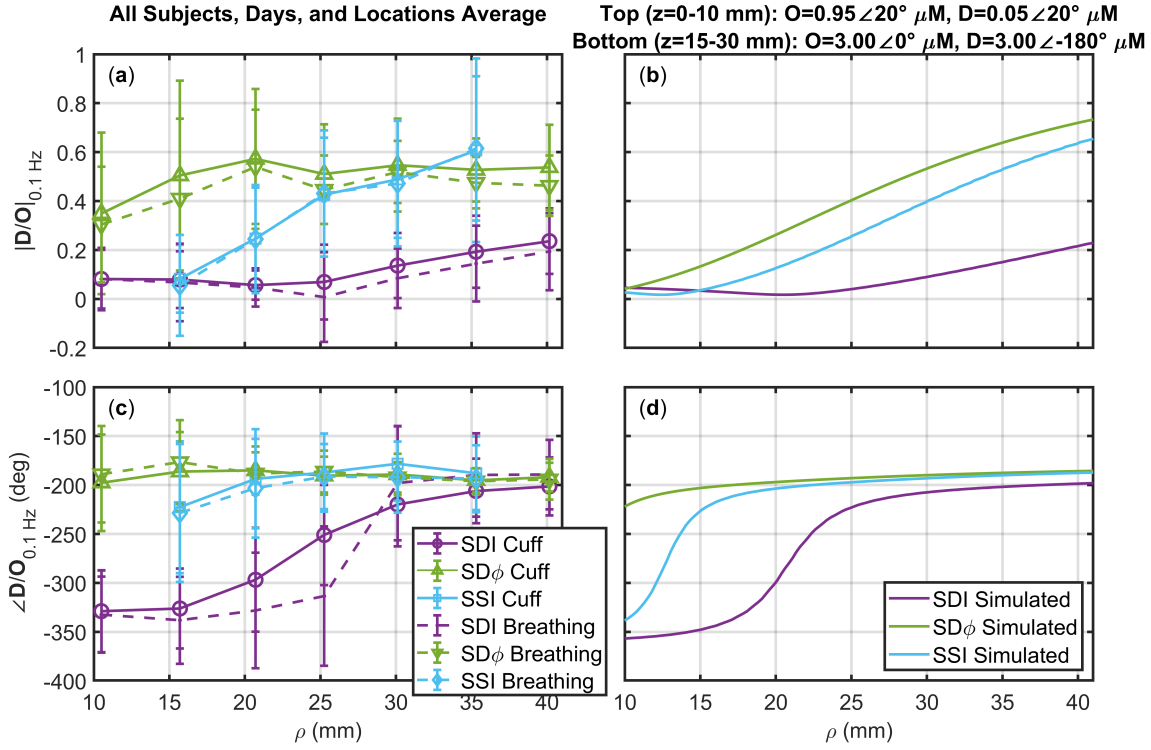


Figure 2.5: Amplitude ((a)&(b)) and phase ((c)&(d)) of phasor ratio vector between Deoxy-hemoglobin and Oxy-hemoglobin ($\overrightarrow{D}/\overrightarrow{O}$) at 0.1 Hz versus source-detector distance (ρ) (Figure 2.3). Experimental data in (a)&(c) represent the average over all subjects, days, and locations for cyclic thigh cuff inflation (Solid Lines) and for paced breathing (Dashed Lines) from Blaney *et alia* Photonics (2019) [2]. Simulation (Appendix F) results in (b)&(d) are for a medium with three-layers of dynamics: top layer from z of 0 mm to 10 mm with $\overrightarrow{D}/\overrightarrow{O} = 0.05 \angle 0^\circ$, intermediate layer from z of 10 mm to 15 mm with no oscillatory hemodynamics, and bottom layer from z of 15 mm to 30 mm with $\overrightarrow{D}/\overrightarrow{O} = 1.00 \angle -180^\circ$ (where z is depth). Three analysis methods are shown Single-Distance (SD) Intensity (I) (Purple), SD Intensity (I) (Green), and Single-Slope (SS) I (Cyan). SS I measurements refer to two sources spaced by approximately 10 mm, plotted such that the plotted ρ is the average of the ρ s of the two sources.

Note 1: Error bars show standard deviation of all analyzed pixels that show significant coherence (Chapter 7) in the wavelet transfer function scalogram (Appendices G&H) across all subjects days and locations.

Note 2: These results can be found as Figure 5 in Blaney *et alia* Photonics (2019) [2].

increases, corresponding to the larger contribution from deeper tissue sensed at greater ρ s. It is therefore expected that the asymptotic value of SD I data at large ρ is more representative of deeper brain tissue, even though it still remains sensitive to extracerebral, superficial tissue. Probably more surprisingly, the SD ϕ data does not show a similar trend with ρ , or at least SD ϕ data appear to reach their asymptotic value at a relatively short distance of about 20 mm. We

assign this behavior to a significantly greater S of SD ϕ data versus SD I data to deeper, cerebral tissue. Similarly, and in this case expectedly, SS I data also shows a greater S to deeper tissue with respect to SD I data. A major advantage of SD ϕ data over SS I data is that it only needs one source-detector pair, but it requires the instrumental complexity of FD technology. The increased noise in ϕ measurements affects even more strongly SS ϕ data, not reported here, than

SD ϕ data because SS is essentially a derivative measurement which typically amplify noise.

The results presented here provide evidence that the pursuit of ϕ and SS data-types was warranted. Therefore, these studies of multiple ρ s [1, 2] motivated us to explore these data-types in more detail and develop further methods utilizing them. The follow chapter will introduce the result of this development, Dual-Slope (DS), and subsequent chapters expand on this novel data-type.

Chapter 3

Introduction to Dual-Slope

3.1 Overview of the Dual-Slope Method

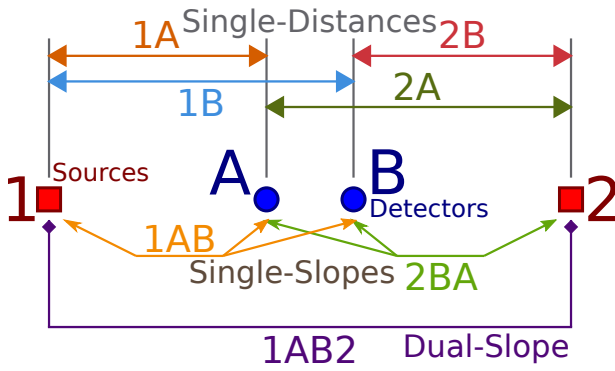


Figure 3.1: Example linear-symmetric Dual-Slope (DS) set. Sources shown in red and numbered 1 and 2. Detectors shown in blue and lettered A and B. Single-Distance (SD) short sets are 1A and 2B, and long sets are 1B and 2A. Common source Single-Slope (SS) sets are 1AB and 2BA (See Note 1). Finally the DS set comprises all optodes and is named 1AB2.

Note 1: Common detector SS sets A12 and B21 are also present, but are redundant with the common source sets shown.

Note 2: This configuration is typically implemented with source-detector distances (ρ s) of 25 mm and 35 mm, that is 1A and 2B are 25 mm and 1B and 2A are 35 mm

To address the issue of superficial sensitivity and seek preferentially deep sensitivity we developed the Dual-Slope (DS) method for Near InfraRed Spectroscopy (NIRS)[3, 58, 59]. This was inspired by our Multi-Distance (MD) studies[1, 2] which showed promise in Single-Slope (SS) and phase (ϕ) data-types. We developed

DS for Frequency-Domain (FD), however a similar technique for Time-Domain (TD) was also developed simultaneously[60].

DS relies on the averaging of two measurements of the slope of some optical data (\mathcal{Y}) versus source-detector distance (ρ). An example of a typical DS optode configuration is shown in Figure 3.1. In FD NIRS, \mathcal{Y} may be the ϕ or the linearized Intensity ($\ln(\rho^2 I)$)^a of the detected light signal which is measured between a single source and one detector. This measurement between one source and one detector is dubbed Single-Distance (SD). Using data at multiple ρ s, the slopes of ϕ or $\ln(\rho^2 I)$ ^b versus ρ can be measured. These slope measurements can be achieved with either a single detector and multiple sources or multiple detectors and a single source. Both cases are referred to as SS measurements which were discussed in Chapter 2.^c

These SS or DS measurements of the slope of $\ln(\rho^2 I)$ or ϕ versus ρ can be measured as the change of the slope from some baseline value of the slope. This is done since the goal of these measurements is not a reconstruction of absolute optical properties, but instead, measurements

^aThe data-type linearized Intensity ($\ln(\rho^2 I)$) is referred to as just Intensity (I) in most cases.

^bTo first approximation linearized Intensity ($\ln(\rho^2 I)$) and phase (ϕ) are linear versus source-detector distance (ρ) in the semi-infinite homogeneous medium (Appendices A&B).

^cFor simplicity of explanation we assume that each Single-Slope (SS) is only made of two Single-Distance (SD) measurements, however, in general one may consider SS measurements using more than two SD. Additionally, we will assume that a SS comprises only 1 source or 1 detector but this is strictly not true since the actual requirements are geometrical[5, 58].

of absorption coefficient change ($\Delta\mu_a$) from a baseline value. Conversion of these changes in slope into $\Delta\mu_a$ is done by introducing a Differential Slope Factor (DSF), which can be calculated using absolute optical properties or generalized optical path-lengths which come from the general complex total optical path-length ($\langle \tilde{L} \rangle$). This method is explained in detail in Blaney *et alia* Journal of Biophotonics (2020) [3] and Appendix C.

A DS measurement is achieved by averaging 2 SSs^d under the following *requirements*[5, 59]:^e

1. A DS set is made of two^d SSs named SS1 & SS2, which share sources or detectors but not both.
2. The difference between the ρ s for both SSs must be the same, thus $|\rho_{SD2} - \rho_{SD1}|_{SS1} = |\rho_{SD2} - \rho_{SD1}|_{SS2}$.^c
3. The detector for the shorter SD measurement in SS1 must be the same detector for the longer SD measurement in SS2.^e

When designing DS sets, the above *requirements* must be met. But, in addition to these *requirements*, there are also two practical *constraints*[5, 59].^f

1. All ρ s should be between 20 mm to 40 mm.^g
2. The difference between the ρ s ($\Delta\rho$) for the SSs should be in the range 10 mm to 20 mm.^h

^dStrictly speaking a Dual-Slope (DS) may be made by averaging more than 2 Single-Slopes (SSs), however for simplicity our discussion will assume there are two SSs in a DS set.

^eThe following description of *requirements* assumes each Single-Slope (SS) is made of 1 source and 2 detectors for simplicity.^{c&d}

^fThese *constraints* are based on Near-InfraRed Spectroscopy (NIRS) instrumental limitation and specific values correspond to the ISS Imagent V2 [Champaign, IL USA] (Imagent).

^gThe lower limit of source-detector distance (ρ) is to achieve preferentially deep sensitivity and the upper limit is governed by detector noise or source power.

^hThe lower end limit on the difference in source-detector distance (ρ) is limited by measurement noise and the upper limit is due to detector dynamic range.

Given these *requirements* and *constraints* many different DS sets may be designed[5, 59]. However, when point measurements were sought, such as in Blaney *et alia* Journal of Biophotonics (2020) [3] which is discussed in the next chapter, the so-called linear-symmetric set in Figure 3.1 was chosen. Typical ρ s for this type of set are 25 mm and 35 mm. More complex sets were utilized when DS was expanded into imaging in Blaney *et alia* Optics Letters (2020) [4] and Blaney *et alia* Review of Scientific Instruments (2020) [5], this will be discussed in Chapter 5.

3.2 Advantages of Dual-Slope

3.2.1 Suppression of Artifacts and Drifts

3.2.1.A Derivation of Dual-Slope Artifact Cancellation

The Dual-Slope (DS) arrangement was inspired by the Self-Calibrating (SC) approach which was developed for achieving calibration-free measurements of absolute optical properties in Frequency-Domain (FD) Near-InfraRed Spectroscopy (NIRS)[61]. SC does not require calibration because instrumental coupling factors is canceled out in analysis. The difference between DS and SC is that SC was developed to use both Intensity (I) and phase (ϕ) in FD while DS may use just one or the other. Additionally, DS focuses on absorption coefficient change ($\Delta\mu_a$) while SC focuses on absolute absorption coefficient (μ_a) and reduced scattering coefficient (μ'_s). Regardless of the differences, DS has all of the same insensitivity to coupling as SC.

The full derivation showing artifact cancellation is in the original SC and DS publications[58, 61], but a simplified and less general version is shown here to highlight this advantage of DS. First, lets consider the optode arrangement shown in Figure 3.1 and some optical data (\mathcal{Y}). \mathcal{Y} is measured by all the Single-Distances (SDs), but for each SD set the theoretical \mathcal{Y} ($SD\mathcal{Y}_{theo}$) is added to some additive optical artifacts ($\mathcal{A}s$) to yield the measured \mathcal{Y} ($SD\mathcal{Y}_{meas}$).

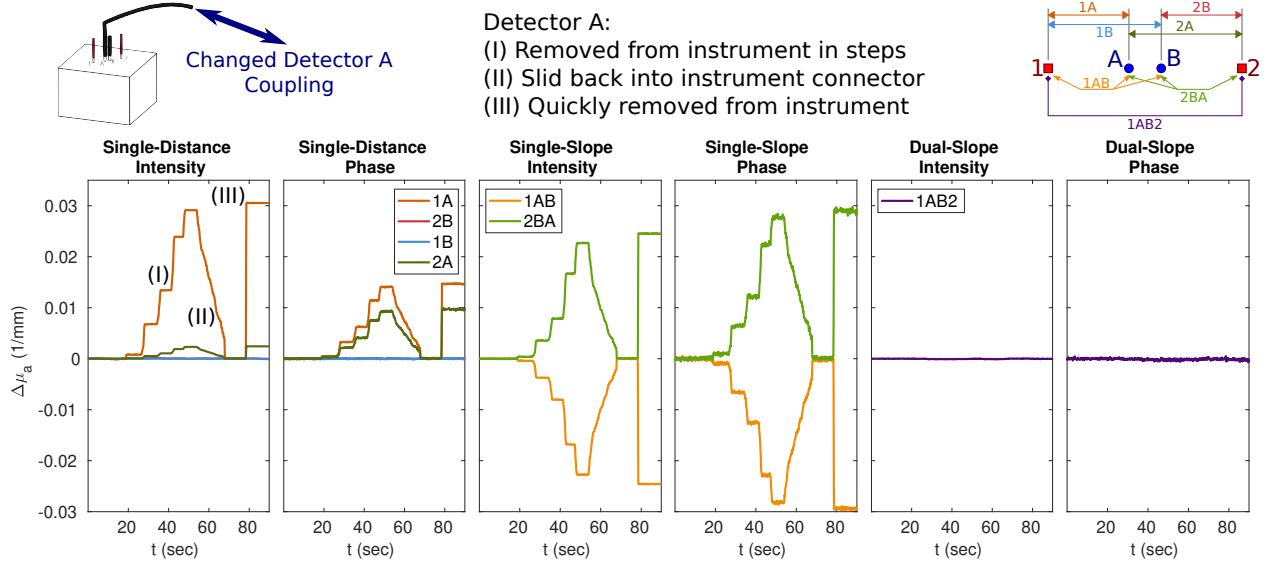


Figure 3.2: Demonstration of a Dual-Slope (DS) set's ability to cancel artifacts when the detector A fiber was removed and replaced from the instrument. The set used two source-detector distances (ρ_s) of 25 mm and two ρ_s of 35 mm. The optical wavelength (λ) was 690 nm, for which the phantom had a absorption coefficient (μ_a) of 0.017 mm^{-1} and a reduced scattering coefficient (μ'_s) of 0.43 mm^{-1} . Note 1: This figure can be found as Figure 3 in Blaney *et alia* (2022) [13].

There is a unique A for each optode, therefore we have:

$$\text{SDY}_{1A,\text{meas}} = \text{SDY}_{1A,\text{theo}} + A_1 + A_A \quad (3.1)$$

$$\text{SDY}_{1B,\text{meas}} = \text{SDY}_{1B,\text{theo}} + A_1 + A_B \quad (3.2)$$

$$\text{SDY}_{2A,\text{meas}} = \text{SDY}_{2A,\text{theo}} + A_2 + A_A \quad (3.3)$$

$$\text{SDY}_{2B,\text{meas}} = \text{SDY}_{2B,\text{theo}} + A_2 + A_B \quad (3.4)$$

where SD \mathcal{Y} is the \mathcal{Y} data for the designated SD set (*exempli gratia* 1A) which is either measured (*meas*) or theoretical (*theo*). Here we note that the theoretical is what we want, but, measured is what we have. As is the measured can not be separated from artifacts.ⁱ

ⁱIf the additive optical artifact (A) is constant in time and Single-Distance (SD) is used for dynamic measurements against a baseline, the artifacts do cancel out when finding absorption coefficient change ($\Delta\mu_a$) (Appendix C). However, it is typically not reasonable to assume that the A 's are constant in time.

Now lets consider the Single-Slopes (SSs) in Figure 3.1. SS measures the slope of \mathcal{Y} versus source-detector distance (ρ). Considering that SS uses the SD from Equations 3.1 to 3.4 as the dependent variable, we have:

$$\begin{aligned} \text{SSY}_{1AB,\text{meas}} &= \frac{\text{SDY}_{1B,\text{meas}} - \text{SDY}_{1A,\text{meas}}}{\rho_{1B} - \rho_{1A}} \\ &= \left[(\text{SDY}_{1B,\text{theo}} + A_1 + A_B) \right. \\ &\quad \left. - (\text{SDY}_{1A,\text{theo}} + A_1 + A_A) \right] \div [\rho_{1B} - \rho_{1A}] \\ &= \frac{\text{SDY}_{1B,\text{theo}} - \text{SDY}_{1A,\text{theo}} + A_B - A_A}{\rho_{1B} - \rho_{1A}} \end{aligned} \quad (3.5)$$

$$\begin{aligned} \text{SSY}_{2BA,\text{meas}} &= \frac{\text{SDY}_{2A,\text{meas}} - \text{SDY}_{2B,\text{meas}}}{\rho_{2A} - \rho_{2B}} \\ &= \left[(\text{SDY}_{2A,\text{theo}} + A_2 + A_A) \right. \\ &\quad \left. - (\text{SDY}_{2B,\text{theo}} + A_2 + A_B) \right] \div [\rho_{2A} - \rho_{2B}] \\ &= \frac{\text{SDY}_{2A,\text{theo}} - \text{SDY}_{2B,\text{theo}} + A_A - A_B}{\rho_{2A} - \rho_{2B}} \end{aligned} \quad (3.6)$$

Then realizing that the theoretical SS is the slope

formed by the theoretical **SDs** we get:

$$\text{SSY}_{1\text{AB},\text{meas}} = \text{SSY}_{1\text{AB},\text{theo}} + \frac{\mathcal{A}_B - \mathcal{A}_A}{\rho_{1B} - \rho_{1A}} \quad (3.7)$$

$$\text{SSY}_{2\text{BA},\text{meas}} = \text{SSY}_{2\text{BA},\text{theo}} + \frac{\mathcal{A}_A - \mathcal{A}_B}{\rho_{2A} - \rho_{2B}} \quad (3.8)$$

Notice now that the \mathcal{A} from the 2 sources has canceled out thus these **SS** measurements are only effected by artifacts from the detectors.^j

Finally, we can consider the **DS** set in Figure 3.1 which is the average of the two **SSs**:

$$\begin{aligned} & \text{DSY}_{1\text{AB2},\text{meas}} \\ &= \frac{\text{SSY}_{1\text{AB},\text{meas}} + \text{SSY}_{2\text{BA},\text{meas}}}{2} \\ &= \left[\left(\text{SSY}_{1\text{AB},\text{theo}} + \frac{\mathcal{A}_B - \mathcal{A}_A}{\rho_{1B} - \rho_{1A}} \right) \right. \\ & \quad \left. + \left(\text{SSY}_{2\text{BA},\text{theo}} + \frac{\mathcal{A}_A - \mathcal{A}_B}{\rho_{2A} - \rho_{2B}} \right) \right] \div 2 \end{aligned} \quad (3.9)$$

Now recall the **DS requirement** that the difference between the ρ s for both **SSs** must be the same, so:

$$\rho_{1B} - \rho_{1A} = \rho_{2A} - \rho_{2B} = \Delta\rho_{1\text{AB2}} \quad (3.10)$$

therefore:

$$\begin{aligned} & \text{DSY}_{1\text{AB2},\text{meas}} \\ &= \left[\left(\text{SSY}_{1\text{AB},\text{theo}} + \frac{\mathcal{A}_B - \mathcal{A}_A}{\Delta\rho_{1\text{AB2}}} \right) \right. \\ & \quad \left. + \left(\text{SSY}_{2\text{BA},\text{theo}} + \frac{\mathcal{A}_A - \mathcal{A}_B}{\Delta\rho_{1\text{AB2}}} \right) \right] \div 2 \\ &= \frac{\text{SSY}_{1\text{AB},\text{theo}} + \text{SSY}_{2\text{BA},\text{theo}}}{2} \end{aligned} \quad (3.11)$$

and finally realizing that the theoretical **DS** is the average of the theoretical **SSs**:

$$\text{DSY}_{1\text{AB2},\text{meas}} = \text{DSY}_{1\text{AB2},\text{theo}} \quad (3.12)$$

^jCommon source Single-Slopes (**SSs**), like **1AB** and **2BA**, cancel out the source artifacts while common detector, like **A12** and **B21**, cancel out the detector artifacts (Figure 3.1).

So the measured **DS** is the same as the theoretical, thus **DS** is not effected by artifacts.^k But this is only true for additive optical artifact (\mathcal{A}), so we should discuss how valid of a type of artifact this is.

In FD **DS** measurements, \mathcal{Y} is either linearized Intensity ($\ln(\rho^2 I)$) or ϕ . So lets consider what an additive effect would mean. For $\ln(\rho^2 I)$ this would be a multiplicative artifact on I , which is in-fact a reasonable type of artifact. Thus, artifacts that **DS** can cancel include:

- Detector gain changes or factors.
- Source power changes or factors.
- Optode coupling efficiency, both changes and absolute.

However, a artifact that **DS** can not cancel is an additive one to I which may occur if background light changes. However, since most FD NIRS instruments only are sensitive to light at their modulation frequency (f_{mod}), this is likely not a concern. Background light would be a concern for Continuous-Wave (CW), however. Thinking of ϕ artifacts, an additive artifact which **DS** can cancel would be a time delay which is likely the most common type of phase artifact. **DS** can not cancel multiplicative factors on the ϕ which may be caused by the instrumental clock artifacts, but these types of artifacts are less likely to occur. Therefore, was can conclude that **DS** is nearly insensitive to artifacts, instrumental factors or changes, coupling changes, and other drifts described by \mathcal{A} in typical FD NIRS experimental conditions.

3.2.1.B Example of Dual-Slope Artifact Cancellation

To demonstrate these **DS** in-sensitivities to artifacts an experiment was conducted using the

^kDual-Slope (**DS**) not being effected by additive optical artifacts (\mathcal{As}) is dependent on \mathcal{A} not changing while one DS measurement is made. This is not strictly true since some time multiplexing must occur. Thus, in practice **DS** is insensitive to \mathcal{As} which change on a time scale slower than the multiplexing period. Since this period is often on the scale of 10 ms, there is effectively complete artifact cancellation in physiological experiments.

DS geometry shown in Figure 3.1 with symmetric short and long ρ_s of 25 mm and 35 mm. Figure 3.2 shows the results of this experiment with data analyzed to find $\Delta\mu_a$ using the methods in Appendix C. In this case the fiber for detector A was removed from the instrument in steps, then slid back into place, and finally pulled out. SD measurements that included detector A (*id est* 1A and 2A) were heavily effected, measuring an increase in $\Delta\mu_a$ due to the decrease in I or ϕ . Both SS measurements were effected but in opposite ways since detector A either comprised the short or the long arm for the 2 slopes. For example, considering SS set 1AB, SD set 1A comprised the short arm which experienced a decrease in signal which increased the SS's measurement of slope thus, appearing as a decrease $\Delta\mu_a$.^l Finally, for DS set 1AB2 little to no change in $\Delta\mu_a$ was observed despite the large induced artifact. This is because DS set 1AB2 is in fact the average of SS sets 1AB and 2BA which where effected in opposite ways by said artifact. Therefore, we have confirmed that DS can successfully suppress artifacts these artifacts. The same suppression would be true for source artifacts, coupling artifacts with the tissue, and instrumental drifts.

3.2.2 Preferentially Deep Sensitivity

3.2.2.A Dual-Slope Sensitivity Profile

Expanding on Figures 2.1&2.2, Figure 3.3 shows the same type of regions where the Signal-to-Noise Ratio (SNR) is greater than or equal to 1 from the parameters in Section 2.1, but now for DS. Particularly, this is the linear-symmetric DS set shown in Figure 3.1 with ρ_s of 25 mm and 35 mm. These profiles (Figure 3.3) immediately show the second advantage of DS of data-types such as SD and SS. This being preferentially deep sensitivity. The methods for creating these Sensitivity to absorption change (S) profiles can be found in Appendix E.

It is common to refer to the profiles for SD shown in Figure 2.1 as *bananas*, therefore we opted to refer to the profiles for DS in Figure 3.3

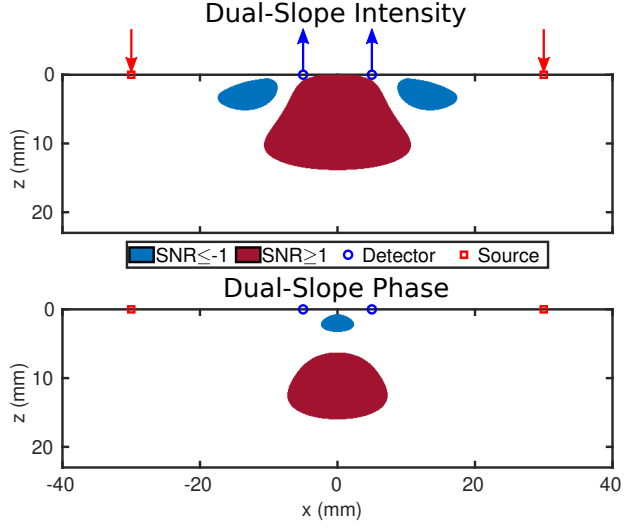


Figure 3.3: Regions where the Signal-to-Noise Ratio (SNR) is ≥ 1 or ≤ -1 for Dual-Slope (DS) measurements using the geometry shown in Figure 3.1 with source-detector distances (ρ_s) of 25 mm and 35 mm. [Top] DS Intensity (I). [Bottom] DS phase (ϕ).

Note 1: Simulation parameters stated in Section 2.1.

Note 2: Simulation methods are found in Appendix E.

as *nuts*. This naming scheme led to the fantastic title of Fantini *et alia* Journal of Innovative Optical Health Sciences (2019) [59] of “Transformational Change in the Field of Diffuse Optics: From Going Bananas to Going Nuts”. Comparing *bananas* to *nuts* one can see that a *banana* has significant regions near the surface, thus has significant superficial contribution. This is not the case for *nuts* where most of the region is localized relatively deep. One must be careful to not say that the *nut* or DS S is deeper however, since the lowest extent of the *bananas* are at approximately the same depth as the *nut*. DS really has the advantage of having preferentially deep S , or suppressing superficial.

This advantage is even more pronounced in DS ϕ where the *nut* is deeper has no part touching the surface unlike DS I . However, DS ϕ has the disadvantage of increased noise compared to I making the SNR lower overall. Additionally, both DS I and DS ϕ have regions of negative S . This is shown as the SNR being less than or equal

^lThe same reasoning is true for Single-Slope (SS) set 2BA but with the long leg changing.

to -1 . These may make data interpretation difficult and create artifacts. This will be explored more in the following sections. However, overall, the negative \mathcal{S} is not a significant concern for DS^m since it is small and almost entirely cancels out with large layer shaped perturbations (Figure 3.7).

3.2.2.B Quantitative Comparison of Sensitivity for Dual-Slope and Other Data-Types

3.2.2.B.a Sensitivity Maps The value of \mathcal{S} can be interpreted by Equation 2.1 which shows it as the ratio between the apparent measured $\Delta\mu_a$ and the actual $\Delta\mu_a$ of some localized perturbation. The methods for creating these maps are discussed in Blaney *et alia* Journal of Biophotonics (2020) [3] and Appendix E. For detailed examination and comparison of the \mathcal{S} maps the actual values for \mathcal{S} are plotted for each of the data-types within the DS set shown in Figure 3.1 with ρ_s of 25 mm and 35 mm (Figures 3.4,3.5,&3.6). For these simulations the same properties as Section 2.1 were used.

Figures 3.4,3.5,&3.6 show these quantitative \mathcal{S} maps all on the same color-scale and approximately on the length scale. This is to allow comparison between them. The color-map is chosen so that the features for every map type are visible. Since for some maps the \mathcal{S} has a large difference from others, the highly negative or highly positive values are shown as solid black or white, respectively. It is worth noting that the sum of an \mathcal{S} map is one as long as the perturbations are simulated without overlap (Appendix E). In these maps overlap is used to smooth the visualization, however, in general the same intuition about the sum being the same applies.ⁿ The intuition being that, overall, there is more positive than negative \mathcal{S} . Thus, if there is large negative

^mDespite the negative Sensitivity to absorption change (\mathcal{S}) of Dual-Slope (DS) not being a significant concern, it is a significant concern for Single-Slope (SS) where the negative region is large and can create complicated and confusing recovered data.

ⁿThe amount of perturbation overlap is governed by the perturbation size (Appendix E) specified in Section 2.1.

\mathcal{S} in one region there will be large positive \mathcal{S} in another to compensate. Also, if the region of sensitivity is large it will have a lower value since it is spread out, this is compared to a small region such as is the case for short versus long ρ .

First, lets focus on the SD \mathcal{S} maps in Figure 3.4. In general you can see that as the region of sensitivity increases in size the actual value decreases, this is due to the aforementioned normalization of the sum of \mathcal{S} . For this reason going from short to long ρ_s means overall lower values of local \mathcal{S} . Thus, the actual shape of the region is what should really be focused on. For example, in the case of SD I the \mathcal{S} is the strongest right near the surface underneath the optodes. This is actually the opposite of what we want, as it means SD measurements represent superficial perturbations, preferentially. Next looking at SD ϕ we see that the \mathcal{S} is more spread, but also deeper. Therefore, SD ϕ may already have what we want, preferentially deep sensitivity. However, ϕ does have negative \mathcal{S} near the surface which could make data difficult to interpret.^o

Next, we may focus on the SS \mathcal{S} maps in Figure 3.5. One may naïvely think SS is a good idea since it effectively subtracts information from a short ρ which represents superficial $\Delta\mu_a$. However, as soon as one looks at the maps it can be seen that SS is problematic. This is because it exhibits large regions of negative \mathcal{S} and correspondingly large regions of positive \mathcal{S} to compensate. This could lead to very confusing data since one does not know if the measured perturbation was in the negative or positive region. Additionally, one can not argue that the sensitivity is preferentially deep as SS shows significant \mathcal{S} close to the detectors. Furthermore, such extreme values of sensitivity are not desirable since a small perturbation in a particular place may dominate the measurement when one really wants to measure a smaller amplitude but more spatially spread perturbation. A final argument against SS is that it amplifies the noise beyond what is present in SD measurements since it is effectively a type of

^oA negative Sensitivity to absorption change (\mathcal{S}) representing the opposite direction absorption coefficient change ($\Delta\mu_a$) being measured from the actual, a true increase measured as a decrease for example.

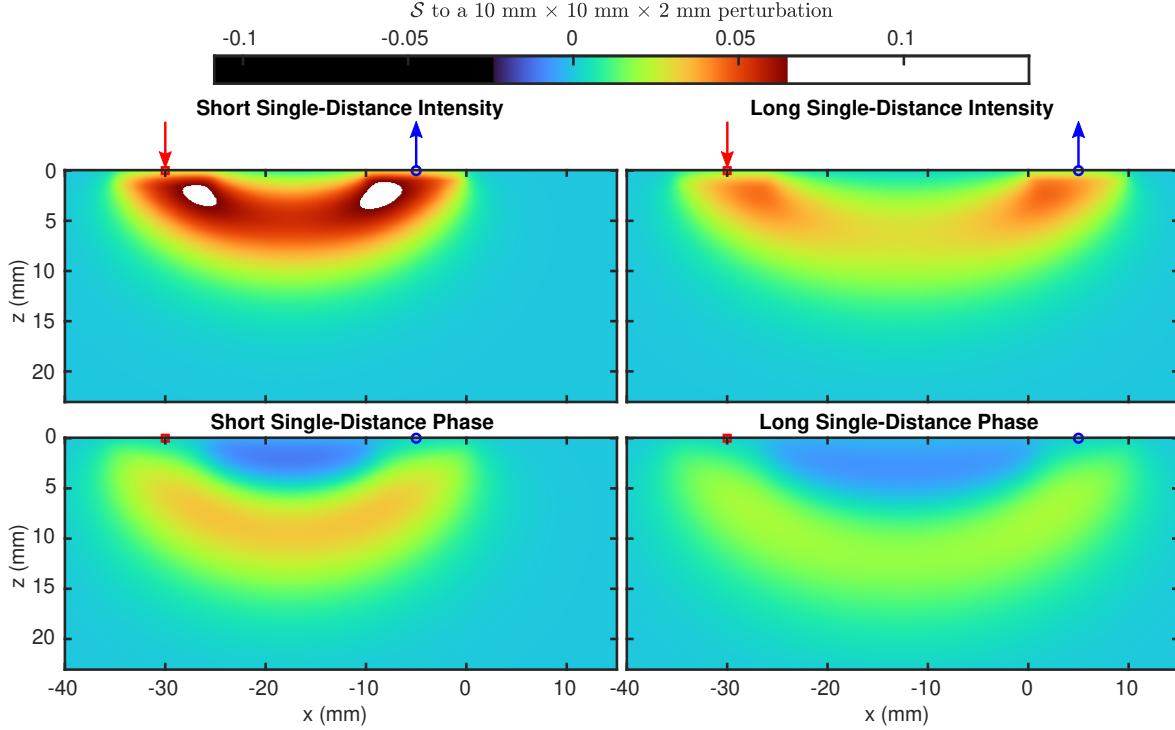


Figure 3.4: Maps of Single-Distance (SD) Sensitivity to absorption change (\mathcal{S}) for a long (1B) and a short (1A) distance in the Dual-Slope (DS) set shown in Figure 3.1. [Top] SD Intensity (I). [Bottom] SD phase (ϕ). [Left] The short source-detector distance (ρ) of 25 mm. [Right] The long ρ of 35 mm.

Note 1: Simulation parameters stated in Section 2.1.

Note 2: This figure is on the same scale as Figures 3.5&3.6.

Note 3: Simulation methods are found in Appendix E.

derivative measure. Therefore, we argue that SS measurements should be avoided.

Finally, moving to DS in Figure 3.6 we immediately see the centralized *nut* which localizes the sensitivity below the detectors. In both DS I and ϕ the superficial sensitivity is mostly removed compared to what was seen in SS and even SD. For ϕ this is most striking since the *nut* really is localized deep. I , however, still exhibits some superficial sensitivity in the center. On the negative side, DS does exhibit negative \mathcal{S} regions. These are not as strong as those seen in SS and are rather weak particularly for DS ϕ . Furthermore, these regions become less of a concern when larger perturbations are considered which cancel with neighboring positive sensitivity, which will be shown in the next section (Figure 3.7). Overall, these results reinforce the advantage of DS's preferentially deep sensitivity.

3.2.2.B.b Sensitivity Curves When biological tissue is measured with NIRS the tissue generally has an overall layered structure. For example scalp, then skull, then brain in cerebral measurements. For this reason it is also helpful to examine \mathcal{S} curves where the perturbations considered are not localized in the lateral directions but instead layers. Figure 3.7 shows this where the upper plot is the \mathcal{S} to a thin layer at different depths and the lower plot is the \mathcal{S} to the bottom layer of the medium if the medium is split in half at a given depth.^p Since layered perturbations are considered here DS and SS are the same and these curves are labeled as DS in

^pThe curves in the bottom panel of Figure 3.7 must approach 1 as z approaches 0. This is because when z is 0 the Sensitivity to absorption change (\mathcal{S}) is to the whole medium, which is 1 (Appendix E).

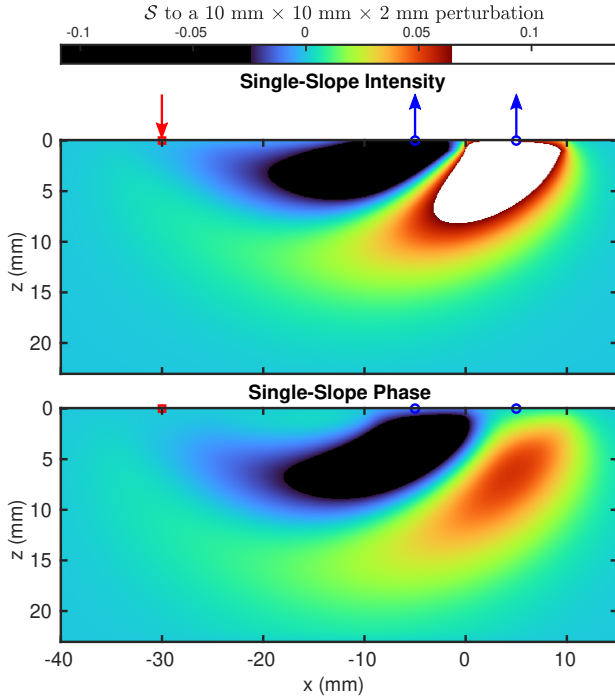


Figure 3.5: Maps of Single-Slope (SS) Sensitivity to absorption change (\mathcal{S}) for a set (1AB) in the Dual-Slope (DS) set shown in Figure 3.1 utilizing source-detector distances (ρ_{s}) of 25 mm and 35 mm. [Top] SS Intensity (I). [Bottom] SS phase (ϕ).

Note 1: Simulation parameters stated in Section 2.1.
Note 2: This figure is on the same scale as Figures 3.4&3.6.

Note 3: Simulation methods are found in Appendix E.

the figure.^q

Now that layered perturbations are considered (Figure 3.7) the issue of negative \mathcal{S} is for the most part gone. This makes the curves rather easy to interpret. Since we desire preferentially deep sensitive a peak at larger z in the upper panel of Figure 3.7 and an overall higher curve in the lower panel of Figure 3.7 is desired. The curve that exhibits this the most strongly is DS ϕ and unsurprisingly the shorter SD I is the worse. Another interesting result in Figure 3.7 is that

^qDual-Slope (DS) and Single-Slope (SS) being the same in the layered case leads to some interesting interpretations of results. This being that if one measures different signals from the two SS in a DS probe there must be some lateral heterogeneity, or instrumental artifacts.

the short SD ϕ and the DS I are almost the same. This is impressive evidence that ϕ is a data-type worth pursuing since even at ρ of 25 mm it can measure about as deep as DS I .

3.3 Discussion of the Dual-Slope Method

The overall conclusion of this chapter is that Dual-Slope (DS) and particularly DS phase (ϕ) exhibits two advantages:

- Insensitivity to artifacts.
- Preferentially deep sensitivity.

The former advantage is rather robust and will be true in most cases, however the later advantage of sensitivity may be more fickle. This is because all of the Sensitivity to absorption change (\mathcal{S}) profiles (Figures 2.1,2.2,&3.3), maps (Figures 3.4,3.5,&3.6), and curves (Figure 3.7) depend on the simulated diffuse optical medium. The one used here and stated in Section 2.1 is typical for biological tissue[2, 3, 17] however there is room for variation in the model of the medium. For example the medium simulated was the semi-infinite homogeneous with extrapolated boundary condition (Appendices A&E)[3, 58], but a better model is likely a layered[8] or even more heterogeneous medium. There is some indication that these maps will change in these complex scenarios but the general conclusions are expected to remain the same.

3.3.1 Considerations on the Noise of the Two Data Types, Intensity and Phase

The main disadvantage of ϕ measurements is their higher noise compared to Intensity (I) measurements. This can be seen in the Signal-to-Noise Ratio (SNR) maps presented in Figures 2.1,2.2,&3.3 whose methods are in Appendix E. Works have presented ϕ [56] in Frequency-Domain (FD) or mean time-of-flight ($\langle t \rangle$) and variance[42, 53, 54] in Time-Domain (TD) with a relatively large noise. This is

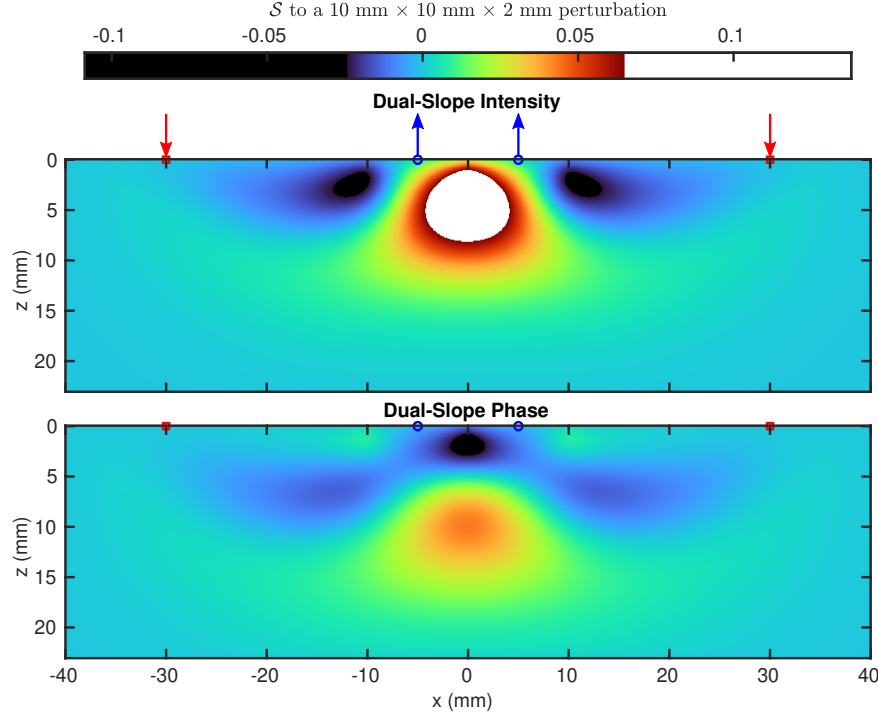


Figure 3.6: Maps of Dual-Slope (DS) Sensitivity to absorption change (S) for the set (1AB2) in Figure 3.1 utilizing source-detector distances (ps) of 25 mm and 35 mm. [Top] DS Intensity (I). [Bottom] DS phase (ϕ).

Note 1: Simulation parameters stated in Section 2.1.

Note 2: This figure is on the same scale as Figures 3.4&3.5.

Note 3: Simulation methods are found in Appendix E.

also seen in our representative time traces (Figures 4.3,5.24,&8.1), particularly in Single-Slope (SS) which suffers from greater noise with respect to Single-Distance (SD) and DS (Appendix E). However, there is room for improvement, for example by identifying optimal modulation frequency (f_{mod}). In fact, a previous TD study looked at the SNR of ϕ as a function of f_{mod} [62] and showed that higher f_{mod} s (higher than the 140.625 MHz used here) may offer a better SNR for ϕ .

Furthermore, there are possible noise improvements that can be pursued in our ISS Imagent V2 [Champaign, IL USA] (Imagent) FD Near-InfraRed Spectroscopy (NIRS) instrument. First, the acquisition time or the duty cycle of the measurements we use in a time-multiplexed scheme may be increased. Second, due to the time multiplexing of our instrument, data from

different sources are not acquired simultaneously. Therefore, the ideal cancellation of noise is not achieved as described in the Self-Calibrating (SC) approach[61]. Addressing these issues by using a different multiplexing scheme or frequency encoding would be a first step to improving the SNR for ϕ measurements.

3.3.2 Possible Enhancements of the Dual Slope Method

A number of aspects of the DS method may be optimized or further developed to enhance performance in terms of SNR and depth S , and to develop imaging capabilities. For example, as mentioned above, one may identify an optimal f_{mod} to achieve a best compromise between SNR and depth of maximal S . One may also consider potential advantages of using multiple f_{mod} s. Furthermore, we have shown that multi-

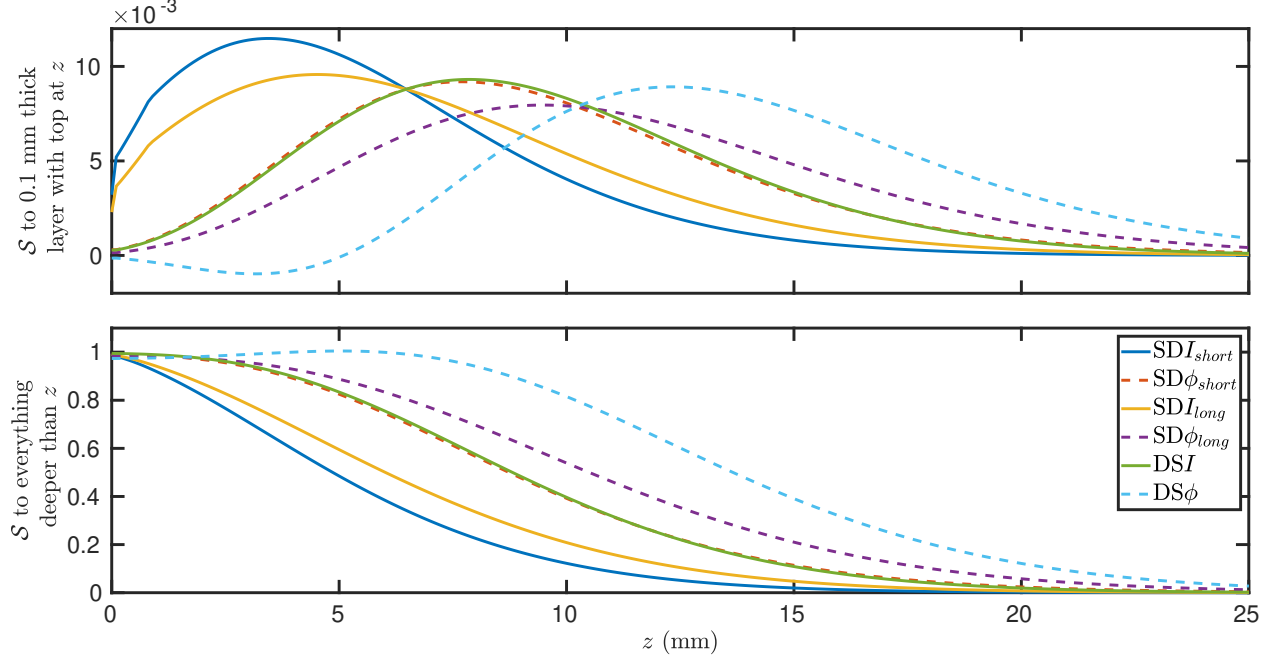


Figure 3.7: Curves of the Sensitivity to absorption change (\mathcal{S}) to layered perturbations extending in all x and y for the Dual-Slope (DS) set shown in Figure 3.1. Solid lines show Intensity (I) data-types and dashed lines show phase (ϕ) data-types. The short Single-Distance (SD) has a source-detector distance (ρ) of 25 mm and the long SD has a ρ of 35 mm. [Top] \mathcal{S} to a thin layer with top at z . [Bottom] \mathcal{S} to a layer extending from z to ∞ .^p

Note 1: Simulation parameters except the perturbation size are stated in Section 2.1.

Note 2: Simulation methods are found in Appendix E.

Note 3: Single-Slope (SS) is not shown here since SS and DS have the same \mathcal{S} to layered perturbations.^q

ple (more than 2) source-detector distances (ρ s) may be used in each SS measurement[58] and this may be advantageous in some applications. Finally, the DS method may be a basis for imaging applications, for example by employing an array of sources and detectors that features a number of partially overlapping DS regions of sensitivity. In-fact this imaging application has been under development and will be discussed in the following Chapter 5.

Chapter 4

Point Measurements with Dual-Slope

4.1 Methods Used in Point Dual-Slope Work

4.1.1 Summary of Experimental Parameters

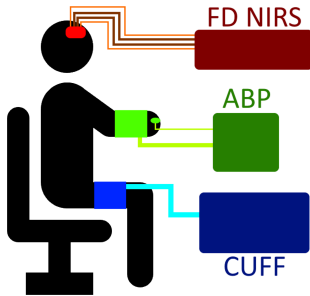


Figure 4.1: Diagram of experimental setup showing a seated subject with the Frequency-Domain (FD) Near-Infrared Spectroscopy (NIRS) [Red] probe, a finger plethysmography probe measuring Arterial Blood Pressure (ABP) [Green], and a pneumatic thigh cuff [Blue] inflation system. Note 1: This setup can be found as Figure 1 in Blaney *et alia* Journal of Biophotonics (2020) [3].

The first *in vivo* Dual-Slope (DS) experiments utilized point measurements.^a These results were published in Blaney *et alia* Journal of Biophotonics (2020) [3]. In this case, data were collected from 4 healthy human subjects, 3 females and 1 male. Frequency-Domain (FD) Near-Infrared Spectroscopy (NIRS) data was collected using the ISS Imagent V2 [Champaign, IL USA] (Imagent) whose parameters are stated

^aPoint measurement meaning, a temporal trace was acquired for each Dual-Slope (DS) set, and no sort of image reconstruction was done.

in Section 2.2.1.A. One DS probe was used with the arrangement shown in Figure 3.1 with source-detector distances (ρ_s) of 25 mm and 35 mm. During the experiment Arterial Blood Pressure (ABP) oscillations were induced at 0.1 Hz using either thigh cuff inflation (Figure 4.1). The duration of the oscillation was 3 min. These oscillations will be discussed in more detail in Part II. This full experiment lasted 6 min.

4.1.2 Analysis Overview

The work in Blaney *et alia* Journal of Biophotonics (2020) [3] also utilized the methods in Appendix F to simulate recovered phasors. Briefly, this was done simulating a heterogeneous set of Blood-Volume (BV) oscillations in a superficial layer, which has been observed [40], and a homogeneous Blood-Flow (BF) dominated oscillation in a deep layer. The motivation for these phasor relationships is explained in Chapter 6. Sensitivity to absorption change (\mathcal{S}) for every data-type in the DS probe was used to simulate the recovered apparent phasors given these simulated heterogeneous oscillations. The overall physiological meaning of this is discussed in Part II. The parameters used to setup these simulations are shown in Table 4.1.

This work culminated in presenting *in vivo* temporal DS traces for the first time. For this, the baseline calibrated slopes of linearized Intensity ($\ln(\rho^2 I)$) and phase (ϕ) versus ρ were measured using the Self-Calibrating (SC) method applied to DS measurements. Then, absolute absorption coefficient (μ_a) and reduced scattering coefficient (μ'_s) using the linear slopes

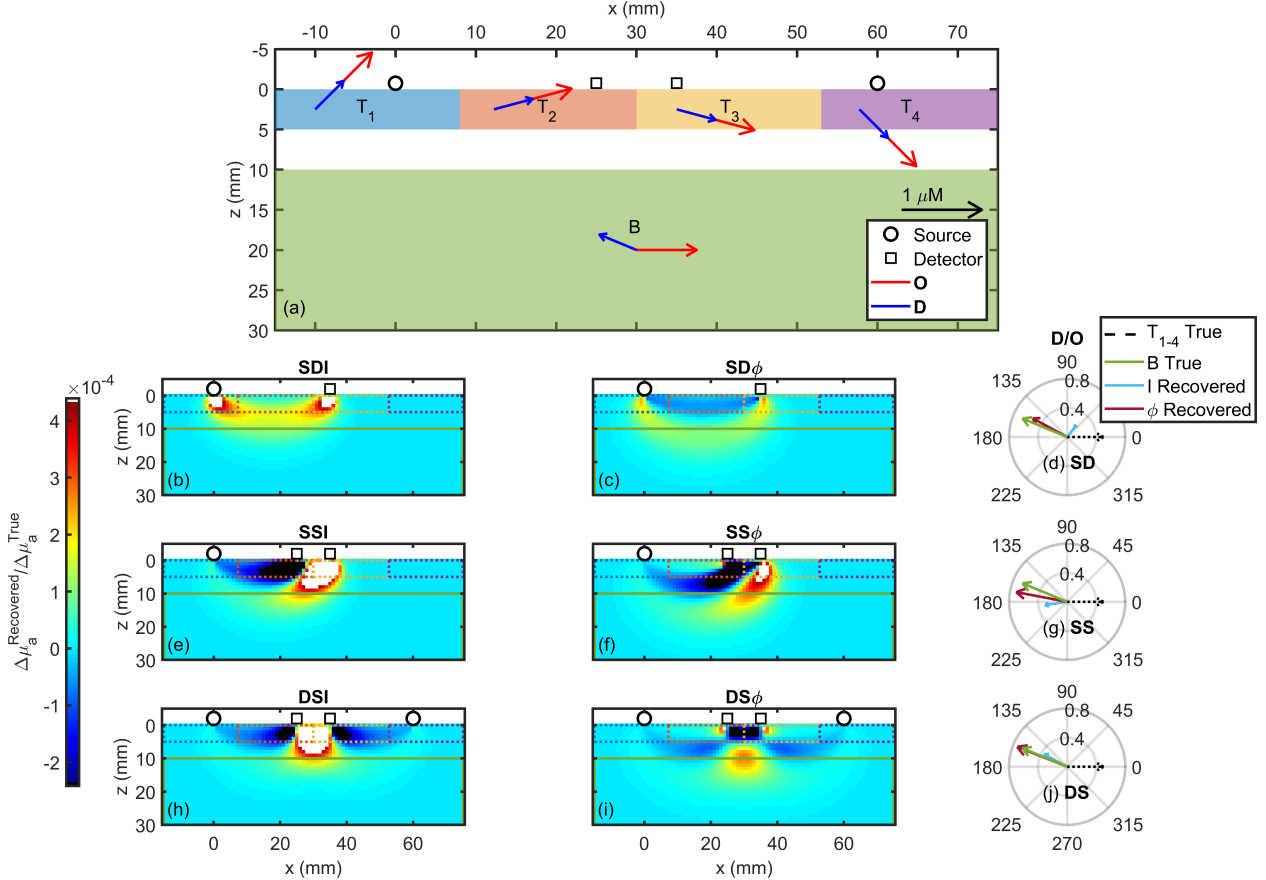


Figure 4.2: Example simulated phase and amplitude relationships between the Deoxy-hemoglobin phasor (\tilde{D}) and the Oxy-hemoglobin phasor (\tilde{O}) that would be measured (recovered) from a volume with 5 regions containing different actual (true) phasors. (a) Schematic of regions within the volume and true phasors. Two optical detectors (Squares) and optical sources shown. True Deoxy-hemoglobin phasor (\tilde{D}) (Blue) and Oxy-hemoglobin phasor (\tilde{O}) (Red) are shown in their regions Top 1 (T_1 , Blue), Top 2 (T_2 , Orange), Top 3 (T_3 , Mustard), Top 4 (T_4 , Purple), and Bottom (B, Green). (b)-(c)-(e)-(f)-(h)-(i) Sensitivity to absorption change (S) maps for: (b) Single-Distance (SD) Intensity (I), (c) SD phase (ϕ), (e) Single-Slope (SS) I , (f) SS ϕ , (h) Dual-Slope (DS) I , and (i) DS ϕ measurements. (d)-(g)-(j) Comparison of true phasor ratio vector between Deoxy-hemoglobin and Oxy-hemoglobin (\tilde{D}/\tilde{O}) for each of the 5 regions to the \tilde{D}/\tilde{O} that would be measured using I [Cyan] or ϕ [Maroon] data with the: (d) SD, (g) SS, or (j) DS method.

Note 1: These results can be found as Figure 3 in Blaney *et alia* Journal of Biophotonics (2020) [3].

Note 2: Extents of the five regions, their true phasor values, and other parameters can be found in Table 4.1.

Note 3: Methods for this simulation are shown in Appendix F.

method in Appendix B were calculated. These absolute properties were used with the methods in Appendix C to retrieve temporal traces of absorption coefficient change ($\Delta\mu_a$) which were converted to Oxy-hemoglobin concentration change (ΔO) and Deoxy-hemoglobin concentration change (ΔD) using the methods in

Appendix D. For the purpose of this chapter, only these temporal traces of ΔO and ΔD are shown. However, further Coherent Hemodynamics Spectroscopy (CHS) phasor analysis (Appendices H&G) was also done, whose results are shown in Chapter 8.

Table 4.1: Parameters used in the phasor simulation in Figure 4.2

Category	Parameter	Value		
Geometry	Full volume size	$x \in [-15, 75]$ mm	$y \in [-15, 15]$ mm	$z \in [0, 30]$ mm
	Voxel size	$\Delta x = 1$ mm	$\Delta y = 1$ mm	$\Delta z = 1$ mm
Baseline Optical Properties	Index of refraction	$n = 1.4$		
	Reduced scattering coefficient	$\mu'_s = 1.2 \text{ mm}^{-1}$		
	Absorption coefficient	$\mu_a = 0.01 \text{ mm}^{-1}$		
	Top 1 (T_1) block size	$x \in [-15, 7.25]$ mm	$y \in [-15, 15]$ mm	$z \in [0, 5]$ mm
	T_1 Oxy-hemoglobin phasor	$\tilde{O} = 1\angle 45^\circ \mu\text{M}$		
	T_1 Deoxy-hemoglobin phasor	$\tilde{D} = 0.5\angle 45^\circ \mu\text{M}$		
	Top 2 (T_2) block size	$x \in (7.25, 30]$ mm	$y \in [-15, 15]$ mm	$z \in [0, 5]$ mm
	T_2 Oxy-hemoglobin phasor	$\tilde{O} = 1\angle 15^\circ \mu\text{M}$		
	T_2 Deoxy-hemoglobin phasor	$\tilde{D} = 0.5\angle 15^\circ \mu\text{M}$		
	Top 3 (T_2) block size	$x \in (30, 52.75]$ mm	$y \in [-15, 15]$ mm	$z \in [0, 5]$ mm
	T_3 Oxy-hemoglobin phasor	$\tilde{O} = 1\angle -15^\circ \mu\text{M}$		
	T_3 Deoxy-hemoglobin phasor	$\tilde{D} = 0.5\angle -15^\circ \mu\text{M}$		
Region Properties	Top 4 (T_2) block size	$x \in (52.75, 75]$ mm	$y \in [-15, 15]$ mm	$z \in [0, 5]$ mm
	T_4 Oxy-hemoglobin phasor	$\tilde{O} = 1\angle -45^\circ \mu\text{M}$		
	T_4 Deoxy-hemoglobin phasor	$\tilde{D} = 0.5\angle -45^\circ \mu\text{M}$		
	$T_1, T_2, T_3, \& T_4$ phasor ratio	$\tilde{D}/\tilde{O} = 0.5\angle 0^\circ$		
	Bottom (B) block size	$x \in [-15, 75]$ mm	$y \in [-15, 15]$ mm	$z \in [10, 30]$ mm
Other	B Oxy-hemoglobin phasor	$\tilde{O} = 0.75\angle 0^\circ \mu\text{M}$		
	B Deoxy-hemoglobin phasor	$\tilde{D} = 0.5\angle -202.5^\circ \mu\text{M}$		
	B phasor ratio	$\tilde{D}/\tilde{O} = 0.67\angle -202.5^\circ$		
Other	Modulation frequency	$f_{\text{mod}} = 140.625 \text{ MHz}$		
	Optical wavelength	$\lambda = 690 \text{ nm and } 830 \text{ nm}$		

Note 1 These parameters can be found as Table A4 in Appendix III of Blaney *et alia* Journal of Biophotonics (2020) [3].

Note 2 These values are inputs to the methods in Appendix F.

4.2 Summary of Point Dual-Slope Results

4.2.1 Dual-Slope Phasor Simulations

Figure 4.2(b)(c)(e)(f)(h)(i) shows the Sensitivity to absorption change (\mathcal{S}) regions of Single-Distance (SD) Intensity (I), SD phase (ϕ), Single-Slope (SS) I , SS ϕ , Dual-Slope (DS) I , and DS ϕ which were previously shown in detail in Figures 3.4,3.5,&3.6. Using these \mathcal{S} maps, we simulated 5 regions of actual (so-called true) hemodynamic oscillations of Oxy-hemoglobin phasor (\tilde{O}) and Deoxy-hemoglobin phasor (\tilde{D}), and we computed the apparent measured (so-called recovered) phasor for each method. The goal of these simulations was to provide an example of how the \mathcal{S} of the different data-types result in different measurements when

the dynamics are heterogeneous. Figure 4.2(a) shows the different regions featuring hemodynamic oscillations, with 4 superficial regions and 1 deep region. This configuration models a heterogeneous superficial layer (which may be considered scalp), an intermediate non-oscillating layer, and a homogeneous bottom layer (which may be considered brain). Figure 4.2(d)(g)(j) shows the recovered and true phasor ratio vector between Deoxy-hemoglobin and Oxy-hemoglobin (\tilde{D}/\tilde{O}). Note that all superficial regions have the same \tilde{D}/\tilde{O} (despite having different absolute \tilde{O} and \tilde{D}). In general, SD I dose not accurately recover the oscillations in the deep region, while all ϕ measurements are relatively successful in doing that. All I measurements underestimate the amplitude of \tilde{D}/\tilde{O} . SS measurements are affected by the superficial heterogeneity and do not reconstruct the phase of \tilde{D}/\tilde{O} well. Overall, DS ϕ

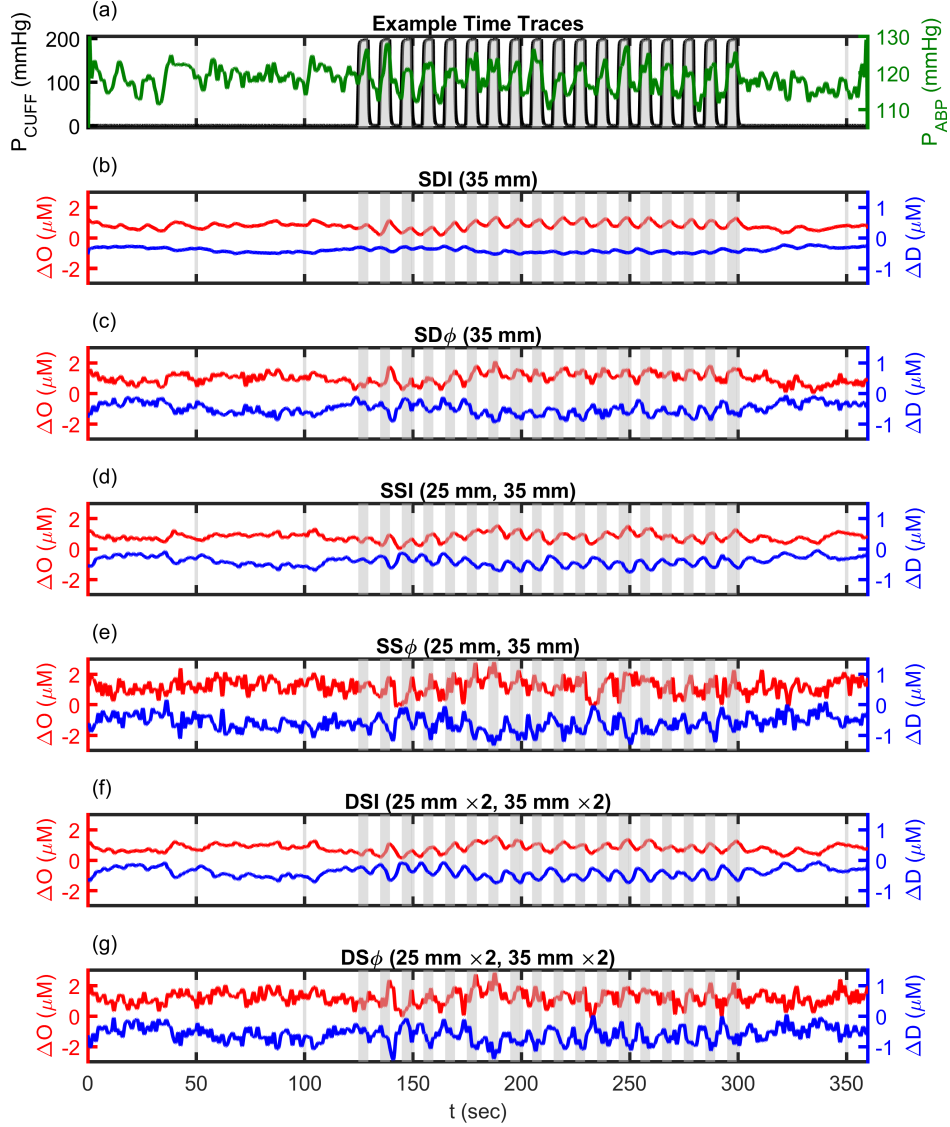


Figure 4.3: Example *in vivo* Dual-Slope (DS) time traces (Subject 4 from Blaney *et alia* Journal of Biophotonics (2020) [3]) for 0.1 Hz cuff oscillation experimental protocol and resulting Oxy-hemoglobin concentration change (ΔO) and Deoxy-hemoglobin concentration change (ΔD) from six different data analysis methods. (a) Pneumatic thigh cuff pressure (P_{CUFF}) [Black and Gray] and Arterial Blood Pressure (ABP) [Green]. (b) ΔO [Red, mean at $0.8 \mu\text{M}$] and ΔD [Blue, mean at $-0.4 \mu\text{M}$] resulting from Single-Distance (SD) Intensity (I) analysis. (c) ΔO [Red, mean at $1 \mu\text{M}$] and ΔD [Blue, mean at $-0.5 \mu\text{M}$] resulting from SD phase (ϕ) analysis. (d) ΔO [Red, mean at $0.8 \mu\text{M}$] and ΔD [Blue, mean at $-0.4 \mu\text{M}$] resulting from Single-Slope (SS) I analysis. (e) ΔO [Red, mean at $1.2 \mu\text{M}$] and ΔD [Blue, mean at $-0.6 \mu\text{M}$] resulting from SS ϕ analysis. (f) ΔO [Red, mean at $0.8 \mu\text{M}$] and ΔD [Blue, mean at $-0.4 \mu\text{M}$] resulting from Dual-Slope (DS) I analysis. (g) ΔO [Red, mean at $1.2 \mu\text{M}$] and ΔD [Blue, mean at $-0.6 \mu\text{M}$] resulting from DS ϕ analysis.

Note 1: These results can be found as Figure 2 in Blaney *et alia* Journal of Biophotonics (2020) [3].

Note 2: All signals lowpass filtered to 0.2 Hz, linearly detrended, and shifted by an arbitrary offset for visualization.

is the most successful, closely reconstructing the amplitude and phase of $\bar{D}/\bar{\phi}$ in the deeper region.

These simulation results (Figure 4.2) show a deeper sensitivity for ϕ over I regardless of the method (SD, SS, DS). Furthermore, they also show that DS has less superficial S than SD and SS. This is consistent with the development of the theory of DS [58]. As previously discussed in Chapters 2&3, slope methods (when compared to SD) in general have been shown to be less sensitive to homogeneous superficial layers using the phase in Frequency-Domain (FD) Near-InfraRed Spectroscopy (NIRS) [50, 55–57]. Experimental results also back up this conclusion. In Time-Domain (TD) NIRS, higher moments of the time-of-flight distribution (mean time-of-flight ($\langle t \rangle$) or the 1st moment, and variance or the 2nd moment) show deeper S and less S to superficial layers compared to the 0th moment (*id est* the average I) [42, 54]. Furthermore, in functional studies, the $\langle t \rangle$ has been shown to have better correlation with functional Magnetic Resonance Imaging (fMRI) activation signals [53]. In FD NIRS, ϕ has been used to measure functional brain activation at shorter source-detector distance (ρ) and to show less S to superficial hemodynamics [51]. We observe that at the modulation frequency (f_{mod}) typically used in FD NIRS (100 MHz to 150 MHz) ϕ is proportional to the 1st moment of the photon time-of-flight distribution ($\phi \approx 2\pi f_{mod} \langle t \rangle$). Therefore, the intuition from the TD studies may be applied to our FD studies with ϕ . Overall, these simulations further reinforce the previous literature regarding SS and $\langle t \rangle$, and also the previous discussions in Chapters 2&3.

4.2.2 First *in Vivo* Dual-Slope Results

Figure 4.3 represents the first *in vivo* time traces acquired using the DS method. The experiment was a standard Coherent Hemodynamics Spectroscopy (CHS) experiment with 0.1 Hz cuff oscillations. The oscillations at the pneumatic thigh cuff frequency are visible during the oscillation period of all the Oxy-hemoglobin concentration change (ΔO) traces. However, this is not true for

Deoxy-hemoglobin concentration change (ΔD) which does not have clear oscillations for SD I . Other data-types however do show visible oscillations in ΔD with DS ϕ having large oscillations is both ΔO and ΔD . This is even more evince that DS and ϕ data-types have advantages over SD and I which are common in NIRS measurements [18]. As stated in previous sections, full physiological interpretation and phasor analysis of the CHS results will be discussed in Part II.

Chapter 5

Dual-Slope Imaging

5.1 Design of a Dual-Slope Imaging Array

5.1.1 Discovering Dual-Slope Sets

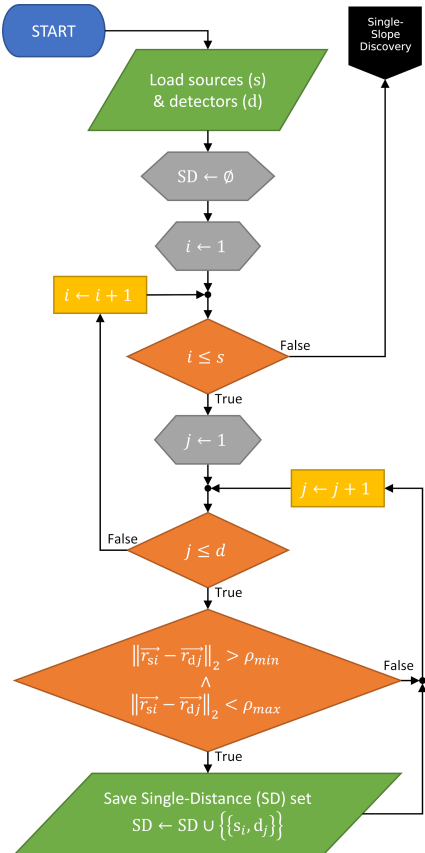


Figure 5.1: Flowchart showing the Single-Distance (SD) discovery part of the Dual-Slope (DS) discovery algorithm.

Note 1: Can be found as Figure 1 in Blaney *et alia* Review of Scientific Instruments (2020) [5].

Note 2: Implemented in Listing 5.1.

To design a Dual-Slope (DS) imaging arrangement we required a succinct set of methods that enforced the *requirements* and *constraints* stated in Section 3.1. We start with a pen and paper design of a configuration that is suitable to create many DS sets as in Blaney *et alia* Review of Scientific Instruments (2020) [5]. Then, we use a DS set discovery algorithm which takes the source and detector position vectors (\vec{r} s) as inputs. This algorithm finds all the possible DS sets that meet the *requirements* and *constraints*.

The algorithm starts by finding all the possible Single-Distance (SD) sets within a source-detector arrangement (Figure 5.1). This is trivial given that s sources and d detectors result in $s \times d$ possible SD sets. However, the algorithm then eliminates sets according to 1 check:

- Sets are eliminated that do not meet the minimum and maximum source-detector distance (ρ) constraints (20 mm and 40 mm, respectively; *Constraint 1* in Section 3.1).

This results in all SD sets that meet the ρ constraints within the arrangement (and their number m_{SD}). This portion of the algorithm is implemented with MathWorks MATrix LABoratory [Natick, MA USA] (MATLAB) code in Listing 5.1.

Then the algorithm moves on to find all the possible Single-Slope (SS) sets (Figure 5.2). This is done by looping through every combination of two different SD sets ($m_{\text{SD}} \times (m_{\text{SD}} - 1) \times 2$ combinations). For each possible combination of SD sets 2 checks are done to ensure the combination forms a valid new SS set:

- An exclusive or (*id est xor*) that the sources

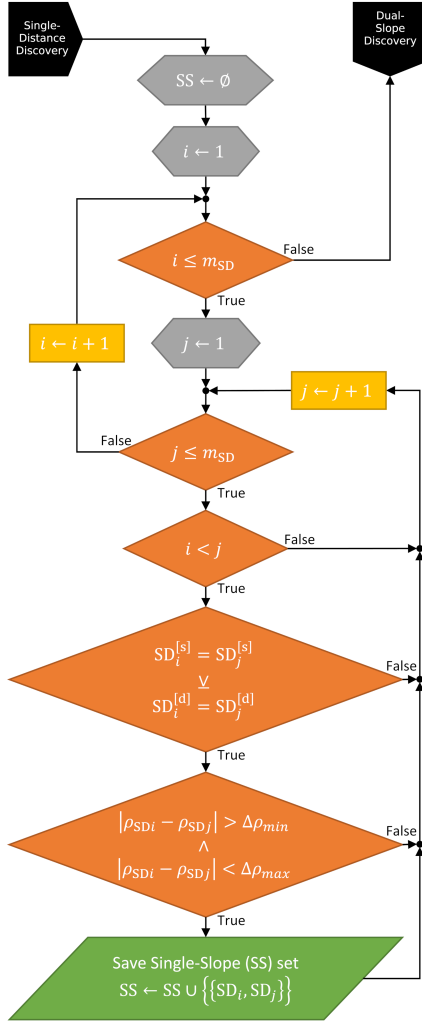


Figure 5.2: Flowchart showing the Single-Slope (SS) discovery part of the Dual-Slope (DS) discovery algorithm.

Note 1: Can be found as Figure 2 in Blaney *et alia* Review of Scientific Instruments (2020) [5].

Note 2: Implemented in Listing 5.2.

xor the detectors are the same for the two SD sets (*i.e.* est the SD sets share a source or a detector but not both; *Requirement 1* in Section 3.1).

- The difference in ρ s ($\Delta\rho$) between the two SD sets meets the minimum and maximum consideration (10 mm and 20 mm, respectively; *Constraint 2* in Section 3.1).

This step results in all the possible SS measurements in the arrangement (and their number

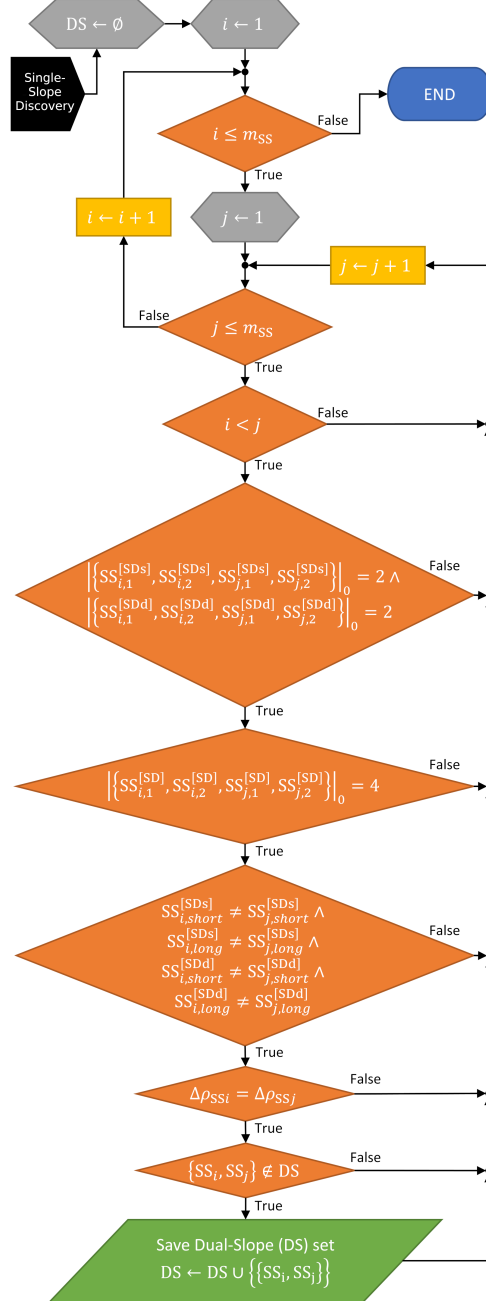


Figure 5.3: Flowchart showing the last part of the DS discovery algorithm where the DS sets themselves are found.

Note 1: Can be found as Figure 3 in Blaney *et alia* Review of Scientific Instruments (2020) [5].

Note 2: Implemented in Listing 5.3.

m_{SS}). This second part of the algorithm is implemented using MATLAB code in Listing 5.2.

Finally, the algorithm finds all the possible DS

sets within the arrangement (Figure 5.3). Again, a loop is entered that loops through all combinations, this time of **SS** sets which are not the same ($m_{\text{SS}} \times (m_{\text{SS}} - 1) \times 2$ combinations). For each **SS** combination 5 checks are done to ensure that the two **SS** sets form a new valid **DS** set:

- That between the 2 **SS** sets there are exactly 2 unique sources and 2 unique detectors (related to *Requirements 1&3* in Section 3.1).
- That between the 2 **SS** sets (4 **SD** sets) there are no repeated source-detectors pairs (*id est* there are four unique **SD** sets; related to *Requirements 1&3* in Section 3.1).
- Between the two **SS** sets the sources/detectors that make up the shorter/longer **SD** measurement are not the same (*id est* no source or detector is used for the long or the short measurement more than once; *Requirement 3* in Section 3.1).
- The difference between the **SD** ρ_{s} ($\Delta\rho$) for each **SS** set that comprise the **DS** set are the same (*Requirement 2* in Section 3.1).
- The **DS** set found at each iteration is new and has not already been found in a previous iteration.

The result of the algorithm is to identify all possible **DS** sets in the arrangement (and their number m_{DS}). Finally, this last part of the algorithm is implemented with MATLAB code in Listing 5.3.

The realization of this algorithm allows for the automatic discovery of **DS** sets from any list of source and detector \vec{r} . The various checks ensure the **DS requirements** are met, however there are also tunable parameters that allow the *constraints* to be changed (minimum ρ from *Constraint 1* in Section 3.1 *et cetera*). The algorithm has a run time of approximately 200 ms (for 10 detectors and 16 sources) on a Central Processing Unit (CPU) with clock speed of 2.6 GHz and 8 GB of Random Access Memory (RAM). Furthermore it can be used to iteratively refine the position of the sources and detectors by rearranging them (using different starting points) or applying position refinement (discussed in the

following sections) and finding the new possible **DS** sets over the multiple iterations.

5.1.2 Refining a Dual-Slope Array

Once all the **DS** sets for an arrangement have been identified, the exact positions of the sources and detectors are refined. This is done by introducing simulated forces between elements acting such that desired parameters of the **DS** sets are met. The dynamical system is then allowed to reach equilibrium through Euler's method for solving a system of ordinary differential equations, and the new coordinates of the sources and detectors are saved (Figure 5.4). Such a system can also be used to find valid source-detector arrangements that meet the **DS** requirements from random starting positions of the sources and detectors which is seen in Figure 5.4.

4 parameters control the final positions in the system:^a

- The nominal ρ for the short leg of a **SS** set ($\rho_{0,s}$).
- The nominal ρ for the long leg ($\rho_{0,l}$).
- The nominal difference between ρ_{s} in a **SS** set ($\Delta\rho_0$).
- The minimum source-detector separation (ρ_{min}).

The final arrangement will have **DS** sets with ρ_{s} as close to their nominal values as possible given the overall connections between the elements of the arrangement, and the minimum separation ensures no detector will be saturated by a close source. Other than the 4 parameters above, another 5 parameters control the dynamics of the simulation and how the equilibrium is reached:^b

- The element mass (\mathfrak{M} ; [mass]).
- The spring constant (\mathfrak{K} ; [mass · time⁻² or force · length⁻¹]).

^aThese source-detector distance (ρ) parameters are primarily related to the Dual-Slope (DS) constraints in Section 3.1.

^bThese dynamical parameters are not critical in their exact value, but are chosen to ensure system stability.

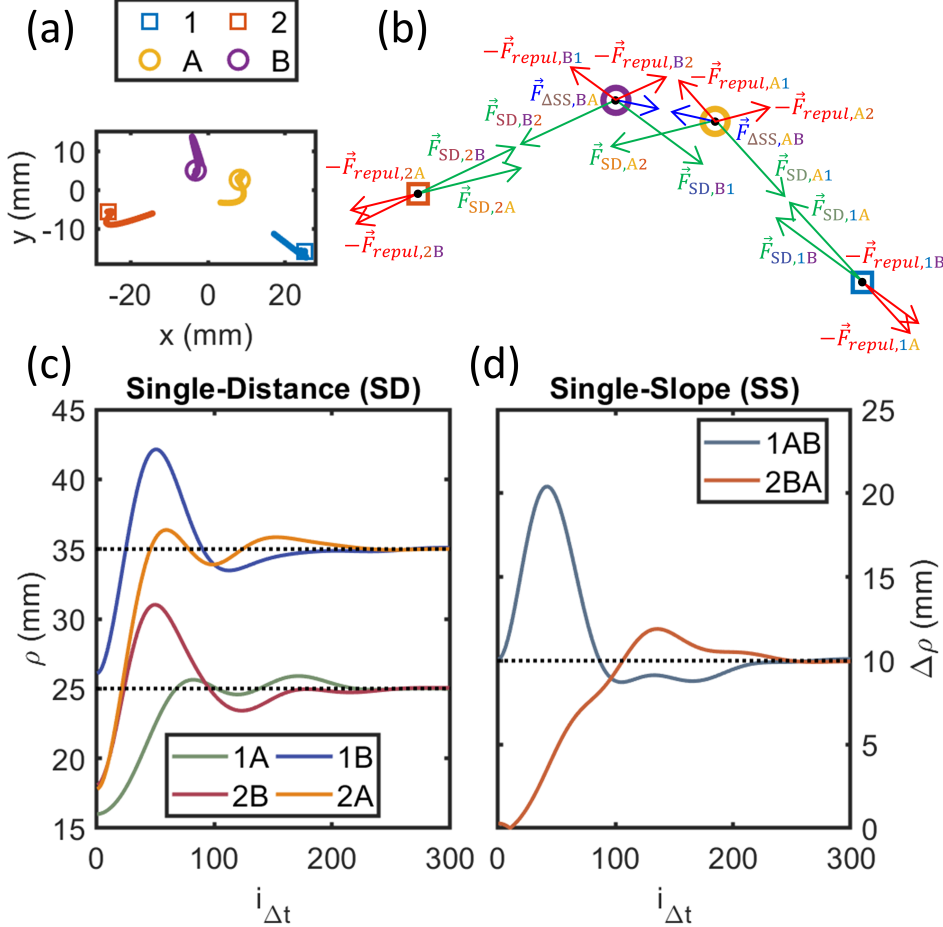


Figure 5.4: Example position refinement for 1 Dual-Slope (DS) set. (a) Evolution of the positions of sources (1 and 2) and detectors (A and B) after random start positions, showing their trajectories as lines and final positions as symbols. (b) Free body diagram of all forces acting on sources and detectors. (c) Evolution of the 4 SD source-detector distances (ρ s). (d) Evolution of the two SS ρ differences ($\Delta\rho$ s).

Note 1: This chart can be found as Figure 4 in Blaney *et alia* Review of Scientific Instruments (2020) [5].

- The damping ratio (ζ ; [-]).
- The repulsion coefficient [$\text{mass} \cdot \text{length}^2 \cdot \text{time}^{-2}$ or energy]).
- The time step (Δt ; [time]).

ζ controls the damping coefficient ($\mathfrak{D} = 2\zeta\sqrt{\kappa\mathfrak{M}}$ [mass · time $^{-1}$]) which is set to slightly below 1 to cause a slight under-damping, thus allowing the system to converge.

The above parameters are used to control 4 forces that act upon each source and detector which are combined using Newton's second law

of motion (Figure 5.4(b)):

$$\ddot{\mathfrak{M}\vec{r}} = \Sigma \vec{F}_{SD} + \Sigma \vec{F}_{\Delta SS} + \Sigma \vec{F}_{repul} + \vec{F}_{damp} \quad (5.1)$$

where, $\ddot{\vec{r}}$ is the acceleration vector for a given element, \vec{F}_{SD} is the SD force, $\vec{F}_{\Delta SS}$ is the SS difference in ρ force, \vec{F}_{repul} is the repulsion force, and \vec{F}_{damp} is the damping force. We note that the key force in this method encouraging the creation of DS sets is $\vec{F}_{\Delta SS}$, which, when applied to symmetric SSs, causes the arrangement to converge to a valid DS arrangement. The use of this force in this way makes this method novel and specific to DS.

The **SD** force causes sources and detectors to be attracted to positions that will create ρ close to the nominal values ($\rho_{0,s}$ or $\rho_{0,l}$):

$$\vec{F}_{\text{SD}} = \kappa(\|\vec{r}_{\text{SD}}\| - \rho_0)\hat{r}_{\text{SD}} \quad (5.2)$$

where, $\|\vec{r}_{\text{SD}}\|$ is the Euclidean distance between the element considered and its pair, \hat{r}_{SD} is the unit vector pointing from the element to its pair, and ρ_0 is the nominal distance between the elements ($\rho_{0,s}$ or $\rho_{0,l}$, depending on whether the **SD** pair is the short or long distance pair in a **SS** set).

The **SS** difference force causes **SS** sets to be attracted to configurations that have a difference in the ρ s close to the nominal value ($\Delta\rho_0$):

$$\vec{F}_{\Delta\text{SS}} = \kappa(\|\vec{r}_{\text{SD}2}\| - \|\vec{r}_{\text{SD}1}\|) - \Delta\rho_0)\hat{r}_{\Delta\text{SS}} \quad (5.3)$$

where, $\vec{r}_{\text{SD}1}$ and $\vec{r}_{\text{SD}2}$ are the Euclidean norms of source-detector displacement vectors for the two **SD** pairs, and $\hat{r}_{\Delta\text{SS}}$ is the unit vector pointing from the element considered to the element of the **SS** set of the same type. For example, for a common source **SS** set that contains one source and two detectors (A and B), there will be a $\hat{r}_{\Delta\text{SS}}$ pointing from A to B which controls the force that acts upon A, and vice versa for B. Thus, each **SS** set creates 2 $\vec{F}_{\Delta\text{SS}}$ forces which act on the non-common element types in the set. Additionally, if 2 **SS** sets form a **DS** set, the symmetric nature of the *requirements* creates resulting **SS** differences forces that encourage the **DS requirements** to be met.

The repulsive force pushes sources and detectors apart such that detectors will not become saturated by near sources. The force only activates if sources and detectors get closer than the minimum distance (ρ_{\min}):

$$\begin{aligned} \vec{F}_{\text{repul}} &= \xi \left(\frac{1}{\rho_{\min}} - \frac{1}{\|\vec{r}_{\text{repul}}\|} \right) \\ &\times H(\rho_{\min} - \|\vec{r}_{\text{repul}}\|) \hat{r}_{\text{repul}} \end{aligned} \quad (5.4)$$

where, $\|\vec{r}_{\text{repul}}\|$ is the Euclidean distance between the element and its repulsor, H is the Heaviside step function, and \hat{r}_{repul} is the unit vector pointing from the element its repulsor.

Finally, the damping force creates non-conservation friction within the system allowing for convergence:

$$\vec{F}_{\text{damp}} = -\mathcal{D}\dot{\vec{r}} \quad (5.5)$$

where $\dot{\vec{r}}$ is the velocity vector. Euler's method with a step of Δt is used to iteratively solve Equation 5.1 finding the \vec{r} of each source and detector at each time step. When the system converges to equilibrium, the new positions of the arrangement elements are saved, and the arrangement is optimized for the desired nominal distances. Furthermore, the **DS** set discovery algorithm may be run again in the case of iterative design.

Aside from the automated refinement, manual refinement may also be conducted. This manual refinement would be informed by the evaluation results of the array that will be discussed in the following sections. Essentially, any **DS** will go through many design iterations using all of the aforementioned and to be mentioned methods before it is actually constructed.

5.2 Image Reconstruction

5.2.1 The Sensitivity Matrix

The first step for image reconstruction is to determine the **Sensitivity to absorption change** (\mathcal{S}) maps for each measurement in a given array. This is done using the methods in Appendix E. Remember \mathcal{S} can be interpreted using Equation 2.1 which shows each \mathcal{S} value being related on two things. First, is the particular measurement (i in Equation 2.1), second, is the perturbation position vector (\vec{r}) within the diffuse medium (\vec{r}_j in Equation 2.1). Therefore, we can define a $m \times v$ matrix of sensitivity to absorption change (\mathcal{S}) for a given imaging array with m measurements and v voxels in the im-

aged medium:

$$\mathbf{S} = \begin{bmatrix} \mathcal{S}_1(\vec{r}_1) & \cdots & \mathcal{S}_1(\vec{r}_j) & \cdots & \mathcal{S}_1(\vec{r}_v) \\ \vdots & \ddots & \ddots & \ddots & \vdots \\ \mathcal{S}_i(\vec{r}_1) & \cdots & \mathcal{S}_i(\vec{r}_j) & \cdots & \mathcal{S}_i(\vec{r}_v) \\ \vdots & \ddots & \ddots & \ddots & \vdots \\ \mathcal{S}_m(\vec{r}_1) & \cdots & \mathcal{S}_m(\vec{r}_j) & \cdots & \mathcal{S}_m(\vec{r}_v) \end{bmatrix} \quad (5.6)$$

Now considering a so-called apparent $m \times 1$ vector of absorption coefficient changes ($\Delta\vec{\mu}_a$) that is measured by the array and a $v \times 1$ $\Delta\vec{\mu}_a$ of so-called actual voxel values, we can write following forward model based off Equation 2.1:

$$\Delta\vec{\mu}_{a,apparent} = \mathbf{S}\Delta\vec{\mu}_{a,actual} \quad (5.7)$$

Image reconstruction will focus on inverting Equation 5.7. Given that $\Delta\vec{\mu}_{a,apparent}$ is what we have and we can calculate \mathbf{S} (Appendix E), the inversion will be finding an inverse for \mathbf{S} which multiplied by $\Delta\vec{\mu}_{a,apparent}$ gives us $\Delta\vec{\mu}_{a,actual}$ (Equation 5.8). It is worth noting that since $m \ll v$ in these imaging problems, there will be many $\Delta\vec{\mu}_{a,actual}$ which satisfies Equation 5.7. Whatever inverse is chosen will find the $\Delta\vec{\mu}_{a,actual}$ which meets some properties according to the inverse. Since this so-called recovered $\Delta\vec{\mu}_a$ will not be unique, we will not call the particular one retrieved $\Delta\vec{\mu}_{a,actual}$ since it is almost certainly not the *actual* $\Delta\vec{\mu}_a$. Therefore, we will called the particular reconstructed v $\Delta\vec{\mu}_a$ from the inverse, the *recovered* (*id est* $\Delta\vec{\mu}_{a,recovered}$).

5.2.2 The Moore-Penrose Inverse

To invert Equation 5.7 we have chosen the Moore-Penrose inverse (MP) [63]. This retrieves the $\Delta\vec{\mu}_{a,recovered}$ with the lowest Euclidean norm of all $\Delta\vec{\mu}_a$ that would satisfy the forward model (Equation 5.7). As is convention, we use a superscript + to represent this inverse as follows:

$$\Delta\vec{\mu}_{a,recovered} = \mathbf{S}^+\Delta\vec{\mu}_{a,apparent} \quad (5.8)$$

The MP can be formulated in various ways, and may or may not include Tikhonov regularization, which aids in smoothing noise in the

measurement. The typical matrix formulation of the Moore-Penrose pseudoinverse with Tikhonov regularization is as follows [63, 64]:

$$\mathbf{S}^+ = \mathbf{S}^T (\mathbf{S}\mathbf{S}^T + \alpha\mathbf{I})^{-1} \quad (5.9)$$

where the T superscript is transpose, the -1 superscript is the matrix inverse, \mathbf{I} is the identity matrix, and:

$$\alpha = a_{tik} \times \max(\text{diag}(\mathbf{S}\mathbf{S}^T)) \quad (5.10)$$

where α is the Tikhonov regularization parameter which scales with the maximum singular value of \mathbf{S} , and a_{tik} is a tunable parameter which should be chosen based on the noise in the measurement to optimize signal-to-noise against smoothing in the reconstructed image.

The MP can also be formulated in terms of the Singular Value Decomposition (SVD) of \mathbf{S} :

$$\mathbf{S} = \mathbf{U}\Sigma\mathbf{V}^T \quad (5.11)$$

$$\Sigma = \begin{bmatrix} \sigma_1 & 0 & 0 & 0 & 0 & \cdots & 0 \\ 0 & \ddots & 0 & 0 & 0 & \cdots & 0 \\ 0 & 0 & \sigma_k & 0 & 0 & \cdots & 0 \\ 0 & 0 & 0 & \ddots & 0 & \cdots & 0 \\ 0 & 0 & 0 & 0 & \sigma_m & \cdots & 0 \end{bmatrix} \quad (5.12)$$

where \mathbf{U} is the $m \times m$ matrix of left singular vectors of \mathbf{S} , \mathbf{V} is the $v \times v$ matrix of right singular vectors of \mathbf{S} , and Σ is the diagonal $m \times v$ matrix of m singular values (σ_k) of \mathbf{S} . Using the SVD of \mathbf{S} , the MP without Tikhonov regularization is formulated as follows [63, 65]:

$$\mathbf{S}^+ = \mathbf{V}\Sigma^{-1}\mathbf{U}^T \quad (5.13)$$

the inverse of the non-square Σ has the trivial expression:

$$\Sigma^{-1} = \begin{bmatrix} \frac{1}{\sigma_1} & 0 & 0 & 0 & 0 \\ 0 & \ddots & 0 & 0 & 0 \\ 0 & 0 & \frac{1}{\sigma_k} & 0 & 0 \\ 0 & 0 & 0 & \ddots & 0 \\ 0 & 0 & 0 & 0 & \frac{1}{\sigma_m} \\ \vdots & \vdots & \vdots & \vdots & \vdots \\ 0 & 0 & 0 & 0 & 0 \end{bmatrix} \quad (5.14)$$

Here we note possible instability in the calculation of the MP if there are singular values that are close to zero. This is related to the condition number (κ) discussed in further sections.

Depending on the application and need, either formulation of the MP may be helpful. In the scope of this chapter we use both to examine and understand characteristics of the \mathcal{S} for a given Dual-Slope (DS) optical array and understand how the image reconstruction will behave. This understanding is used to inform the imaging array design process.

5.2.3 Evaluation of a Imaging System Using the Moore-Penrose Inverse

Given various DS arrays we need a way to specify the performance of different arrangements to choose the most effective for imaging. This is done by examining the imaging system in terms of the MP for image reconstruction. The following discussions assume no regularization. Substituting Equation 5.7 into Equation 5.8 yields:

$$\Delta\vec{\mu}_a,_{\text{recovered}} = \mathcal{S}^+ \mathcal{S} \Delta\vec{\mu}_{a,\text{actual}} \quad (5.15)$$

where the $v \times v$ inverse sensitivity matrix multiplied by the original sensitivity matrix ($\mathcal{S}^+ \mathcal{S}$) is the key operator that transforms the actual absorption perturbation vector into the recovered one. In the ideal case where the matrix $\mathcal{S}^+ \mathcal{S}$ is the identity matrix, the image reconstruction would be perfect. This requires the MP to be equal to the true inverse which implies that \mathcal{S} is a square matrix (*id est* $m = v$, same number of voxels as measurements). This can be achieved by choosing a medium voxelization with only m voxels and reconstructing equivalent absorption changes for those large voxels. However, this would require uniform absorption properties across such large voxels, and the use of a \mathcal{S} that reflects the size of such large voxels. Furthermore, the goal of imaging is to reconstruct maps of absorption perturbations with a fine voxel grade to represent arbitrary shapes of optical perturbations. Thus, we will focus on

cases where $v \gg m$ and we examine ways to specify how close $\mathcal{S}^+ \mathcal{S}$ is to the identity matrix.

5.2.3.A Maps Evaluating Array Performance

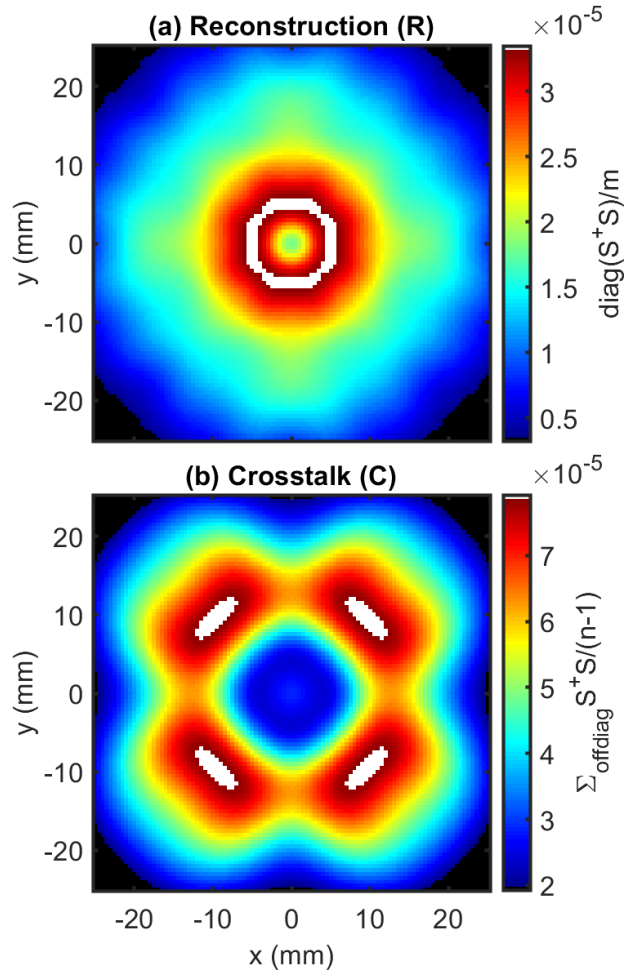


Figure 5.5: Inverse sensitivity matrix multiplied by the original sensitivity matrix ($\mathcal{S}^+ \mathcal{S}$) results: (a) reconstruction of voxels vector ($\vec{\mathcal{R}}$) and (b) cross-talk between voxels vector ($\vec{\mathcal{C}}$) for the circular arrangement.

Note 1: This figure can be found as Figure 8 in Blaney *et alia* Review of Scientific Instruments (2020) [5].

5.2.3.A.a Reconstruction and Cross-Talk Maps

The first method we use to examine $\mathcal{S}^+ \mathcal{S}$ is by producing the reconstruction of voxels vector ($\vec{\mathcal{R}}$) which can be visualized in a voxelated

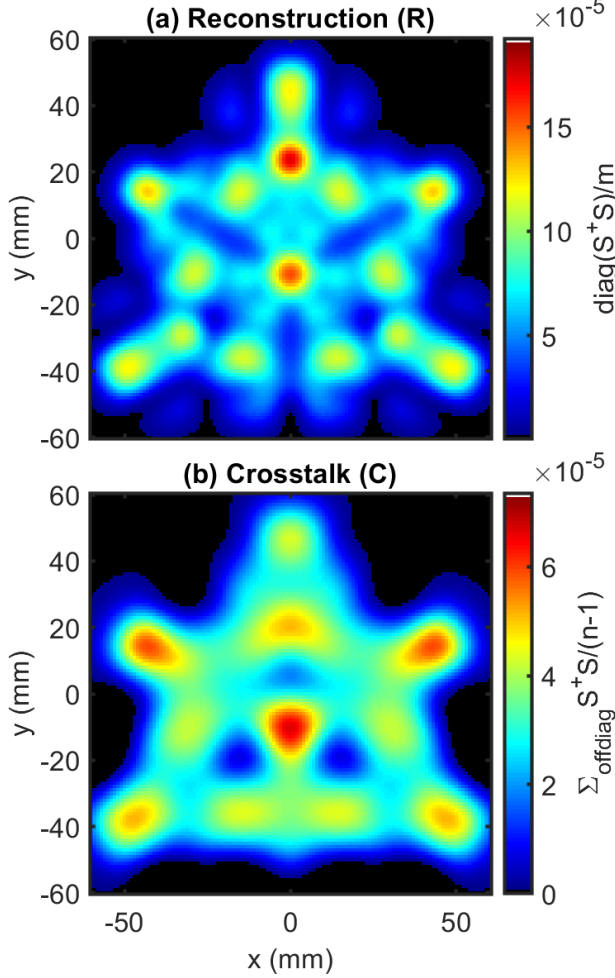


Figure 5.6: Inverse sensitivity matrix multiplied by the original sensitivity matrix ($\mathbf{S}^+\mathbf{S}$) results: (a) reconstruction of voxels vector ($\vec{\mathcal{R}}$) and (b) cross-talk between voxels vector ($\vec{\mathcal{C}}$) for the hexagonal arrangement.

Note 1: This figure can be found as Figure 9 in Blaney *et alia* Review of Scientific Instruments (2020) [5].

map. This vector is defined as:

$$\vec{\mathcal{R}} = \frac{\text{diag}(\mathbf{S}^+\mathbf{S})}{m} \quad (5.16)$$

where, the diagonal elements of $\mathbf{S}^+\mathbf{S}$ are normalized by m since the trace of $\mathbf{S}^+\mathbf{S}$ is equal to m [63]. This normalizes $\vec{\mathcal{R}}$ such that the sum of its elements is equal to 1. The $\vec{\mathcal{R}}$ map (made of the v values of the reconstruction vector elements for the v voxels) shows the weight with which the imaging system reconstructs an actual

perturbation into its true voxel (higher values are better). In the ideal case, the vector's elements would be all ones. Visualizing the $\vec{\mathcal{R}}$ map shows which parts of the medium will reconstruct perturbations well.

Examples of these $\vec{\mathcal{R}}$ and cross-talk between voxels vector ($\vec{\mathcal{C}}$) maps can be seen in Figures 5.5&5.6. These show the maps for two different array designs (Figures 5.12&5.11) which will be discussed in further sections.

The second map which is used to visualize $\mathbf{S}^+\mathbf{S}$ compared to the identity is the $\vec{\mathcal{C}}$. This vector is defined as:

$$\vec{\mathcal{C}} = \frac{\mathbf{S}^+\mathbf{S}\vec{1} - \text{diag}(\mathbf{S}^+\mathbf{S})}{v-1} \quad (5.17)$$

where, $\vec{1}$ is the $v \times 1$ vector of ones. Conceptually the elements of the cross-talk vector are the average of the off-diagonal elements of $\mathbf{S}^+\mathbf{S}$ for each row. The v values of the cross-talk vector elements indicate the average weight with which actual perturbations elsewhere in the medium are reconstructed to a given voxel (lower values are better). In the ideal case, $\vec{\mathcal{C}}$ would be a vector of zeros. When visualized as a map it shows where the imaging system will reconstruct actual perturbations in the incorrect voxel.

5.2.3.A.b Resolution and Localization Maps

Determining the resolution and offset (localization) of reconstructed perturbations can be done efficiently by considering $\mathbf{S}^+\mathbf{S}$ as a matrix of unit voxel impulse response vectors. This can be seen by examining Equation 5.15, and considering a $\Delta\vec{\mu}_{a,\text{actual}}$ that contains all zeros except a 1 in element j (a unit perturbation only in voxel j). Then $\Delta\vec{\mu}_{a,\text{recovered}}$ will be the j th column of $\mathbf{S}^+\mathbf{S}$. Thus, $\mathbf{S}^+\mathbf{S}$ contains the response vectors (in its rows and columns since it is symmetric) for a unit perturbation in each voxel. In this section, we discuss efficient ways to calculate resolution and localization maps in MathWorks MATrix LABoratory [Natick, MA USA] (MATLAB). However, the methods could be adapted to other programming languages.

For notation, we introduce the resolution matrix (\mathbf{T}) and the localization matrix (Δ) as fol-

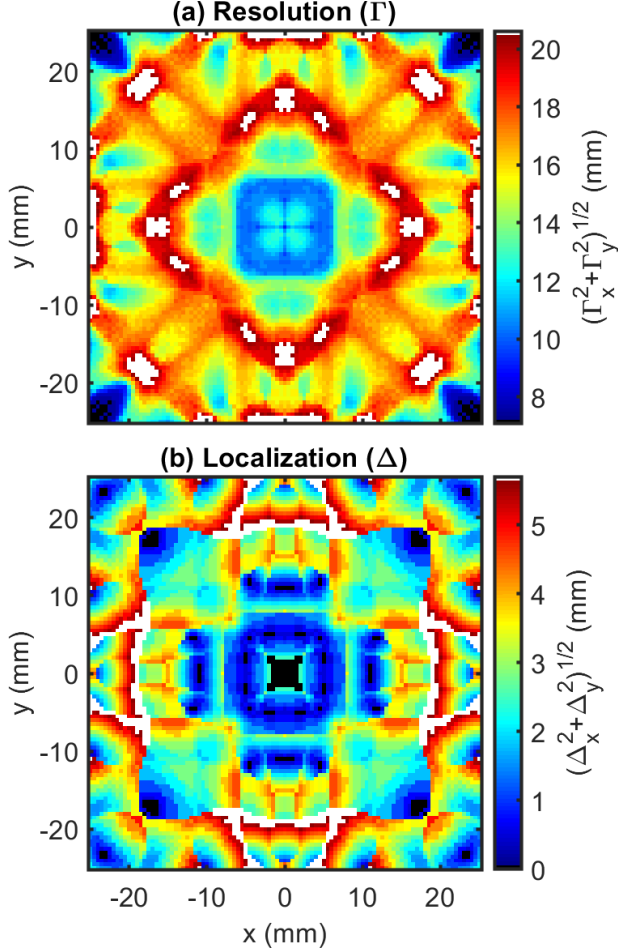


Figure 5.7: Inverse sensitivity matrix multiplied by the original sensitivity matrix ($\mathbf{S}^+\mathbf{S}$) impulse response results: (a) resolution matrix ($\boldsymbol{\Gamma}$) and (b) localization matrix ($\boldsymbol{\Delta}$) for the circular arrangement.

Note 1: This figure can be found as Figure 10 in Blaney *et alia* Review of Scientific Instruments (2020) [5].

lows:

$$\boldsymbol{\Gamma} = \left[\vec{\Gamma}_x, \vec{\Gamma}_y, \vec{\Gamma}_z \right] \quad (5.18)$$

$$\boldsymbol{\Delta} = \left[\vec{\Delta}_x, \vec{\Delta}_y, \vec{\Delta}_z \right] \quad (5.19)$$

where $\boldsymbol{\Gamma}$ and $\boldsymbol{\Delta}$ are both $v \times 3$ matrices containing the map of resolution or localization in each coordinate direction (3 columns for the coordinate directions x , y , and z). For example, the

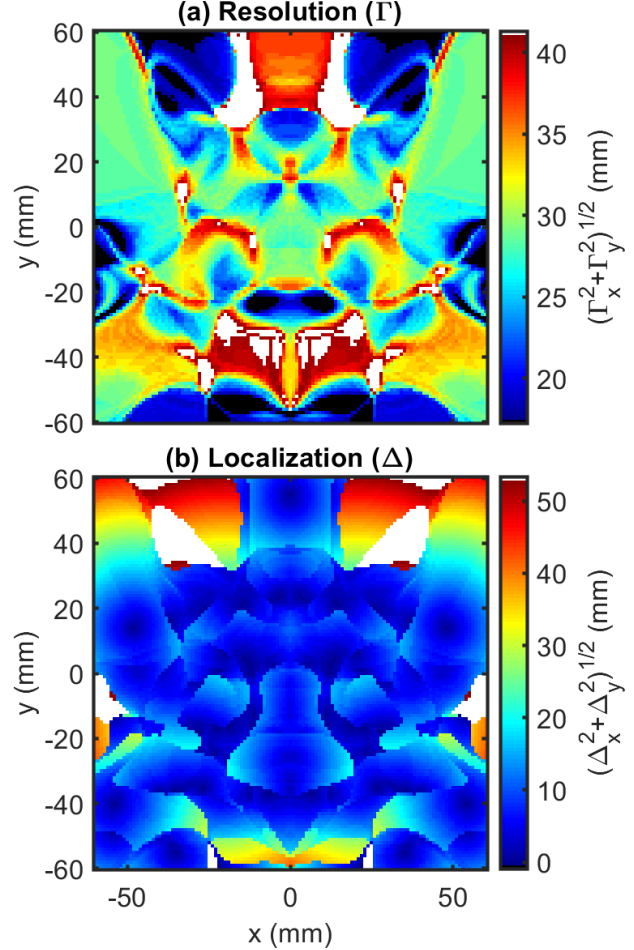


Figure 5.8: Inverse sensitivity matrix multiplied by the original sensitivity matrix ($\mathbf{S}^+\mathbf{S}$) impulse response results: (a) resolution matrix ($\boldsymbol{\Gamma}$) and (b) localization matrix ($\boldsymbol{\Delta}$) for the hexagonal arrangement.

Note 1: This figure can be found as Figure 11 in Blaney *et alia* Review of Scientific Instruments (2020) [5].

j^{th} element of $\vec{\Gamma}_x$ ($\vec{\Gamma}_{x,j}$) is the reconstructed Full-Width Half-Max (FWHM) resolution along x for a perturbation in voxel j . Additionally, the j^{th} element of $\vec{\Delta}_x$ ($\vec{\Delta}_{x,j}$) is the offset between the actual perturbation location and the reconstructed maximum location along x for a perturbation in voxel j .

For computation of these matrices in MATLAB, we must consider the data format. $\mathbf{S}^+\mathbf{S}$ (SpS) has size $v \times v$ ($[n,n]=\text{size}(\text{SpS})$ in MATLAB), but we want to consider the response

maps in a 3-dimensional (3D) coordinate system. Thus, \mathbf{SpS} is reshaped as follows:

```
1 SpS_grid2=reshape(SpS, ...
2 [ny,nx,nz,ny,nx,nz]);
```

where, nx , ny , and nz are the number of voxels in the x , y , and z directions, respectively. Now, $\mathbf{SpS_grid2}$ is a 6-dimensional (6D) array, where the first 3 dimensions can index a perturbation location and the remaining 3D array is the reconstructed map (note switching the indexing to the last three would produce the same result since \mathbf{SpS} is symmetric). For example:

```
1 reconMap=squeeze(...
2 SpS_grid2(iy,ix,iz,:,:,:));
```

where $\mathbf{reconMap}$ is the 3D array of the reconstructed map for a unit perturbation at voxel [$\mathbf{iy}, \mathbf{ix}, \mathbf{iz}$]. The resolution and localization are computed for each of the 3 dimensions. Thus, first we find the linear reconstruction along the axis of interest (x shown here):

```
1 Mrcn_gridx=sum(sum(...
2 SpS_grid2,4),6);
```

where $\mathbf{Mrcn_gridx}$ is the 4 non-singular dimension array containing the linear reconstruction (along the 5th dimension) for a perturbation in every voxel location (first 3 dimensions). This is obtained by summing the 3D reconstructed maps along the y and z directions (4th and 6th dimension). The same method can be used for the other 2 directions by summing over different indices. With $\mathbf{S}^+ \mathbf{S}$ in this form we can now quickly find the resolution and localization maps along each dimension.

We define the resolution in terms of the FWHM which can be computed in one line using the data structured in this way (x direction shown):

```
1 Gamma_x=sum(...
2 Mrcn_gridx>=...
3 (max(Mrcn_gridx,[],5)/2),...
4 5)*dx;
```

where $\mathbf{Gamma_x}$ is $\overline{\Gamma}_x$ reshaped to be a 3D map and \mathbf{dx} is the voxel pitch in the x direction. Similar reasoning follows for the other two directions.

For the localization map we must first create a 3D array of actual perturbation location indices in each dimension for every voxel location (x direction shown):

```
1 [~,XX,~]=meshgrid(1:ny,1:nx,1:nz);
```

where, \mathbf{XX} is the 3D array of the x indices of the actual perturbation location for a perturbation in every possible location in 3D. Next, the indices of the reconstructed maxima must be found (again for the x direction):

```
1 [~,maxInds_x]=max(Mrcn_gridx, ...
2 [], 5);
```

where, $\mathbf{maxInds_x}$ is the 3D array with the x index of the maximum of the reconstructed image for an actual perturbation in every voxel location. Finally, we can compare \mathbf{XX} to $\mathbf{maxInds_x}$ to find the localization map:

```
1 Delta_x=(maxInds_x-XX)*dx;
```

where, $\mathbf{Delta_x}$ is $\overline{\Delta}_x$ reshaped to be a 3D array for visualization. As before the same process can be used to find the y and z direction.

Examples of these $\overline{\mathcal{R}}$ and $\overline{\mathcal{C}}$ maps can be seen in Figures 5.7&5.8. These show the maps for two different array designs (Figures 5.12&5.11) which will be discussed in further sections.

The full MATLAB function that finds these maps for all three dimensions is shown in Listing 5.4. The simplicity of this method is quite impressive given that the typical approach for calculation of \mathbf{T} and $\mathbf{\Delta}$ is to simulate perturbations at various locations using loops over the whole medium. For this reason, this method has the advantage of speed, but the disadvantage of needing to store $\mathbf{S}^+ \mathbf{S}$ in Random Access Memory (RAM).

5.2.3.B Condition Number

There are also scalar values that can be used to evaluate the imaging effectiveness of \mathbf{S} . One value is the κ of \mathbf{S} , which represents the instability of the imaging system. The κ is defined as:

$$\kappa = \|\mathbf{S}\| \|\mathbf{S}^+\| \quad (5.20)$$

where smaller κ is better, meaning a more stable system [65]. In this work we use the ℓ_2 -norm for our discussion but the condition number can be defined with any norm that is desired. For comparison, in the best case of Gaussian random sampling, $\kappa = \mathcal{O}(1)$. But in the worst case of a singular \mathbf{S} , $\kappa = \infty$.

5.2.3.C Singular Value Decomposition and Singular Vectors

We can also think of the MP it in terms of SVD. Equation 5.13 shows this SVD based formulation, so we may now revisit $\mathbf{S}^+\mathbf{S}$ and κ from a different perspective. Combining Equations 5.11&5.13 yields:

$$\mathbf{S}^+\mathbf{S} = \mathbf{V}\Sigma^{-1}\mathbf{U}^T\mathbf{U}\Sigma\mathbf{V}^T \quad (5.21)$$

which can be simplified to:

$$\mathbf{S}^+\mathbf{S} = [\vec{V}_1, \dots, \vec{V}_m, \vec{0}, \dots, \vec{0}] \mathbf{V}^T \quad (5.22)$$

by the orthogonality of \mathbf{U} (*id est* $\mathbf{U}^{-1} = \mathbf{U}^T$) and the multiplication of Σ^{-1} and Σ which yields a $n \times n$ matrix with 1 in the first m diagonal elements and 0 elsewhere. In the above equation, $\vec{0}$ is an $m \times 1$ vector of zeros of which there are $v - m$ in the matrix within the brackets on the right-hand side. From this formulation, we can see that the imaging system matrix (*id est* $\mathbf{S}^+\mathbf{S}$) is completely formulated using the right singular vectors.

The importance of the right singular vectors of \mathbf{S} can be seen by applying Equation 5.15:

$$\Delta\vec{\mu}_{a,recovered} = [\vec{V}_1, \dots, \vec{V}_m, \vec{0}, \dots, \vec{0}] \mathbf{V}^T \Delta\vec{\mu}_{a,actual} \quad (5.23)$$

where, it can be seen by the orthogonality of \mathbf{V} , that if $\Delta\vec{\mu}_{a,actual}$ is any of the first m right singular vectors of \mathbf{S} (or any linear combination of them), then a perfect reconstruction will be achieved (*id est* $\Delta\vec{\mu}_{a,recovered} = \mathbf{V}^T \Delta\vec{\mu}_{a,actual}$). Conversely, if $\Delta\vec{\mu}_{a,actual}$ is any of the last $v - m$ right singular vectors, then a null reconstruction will be achieved (*id est* $\Delta\vec{\mu}_{a,recovered} = \vec{0}$). This means that $\Delta\vec{\mu}_{a,recovered}$ is spanned by the vectors $(\vec{V}_1, \dots, \vec{V}_m)$. In other words, any reconstructed image must be some linear combination

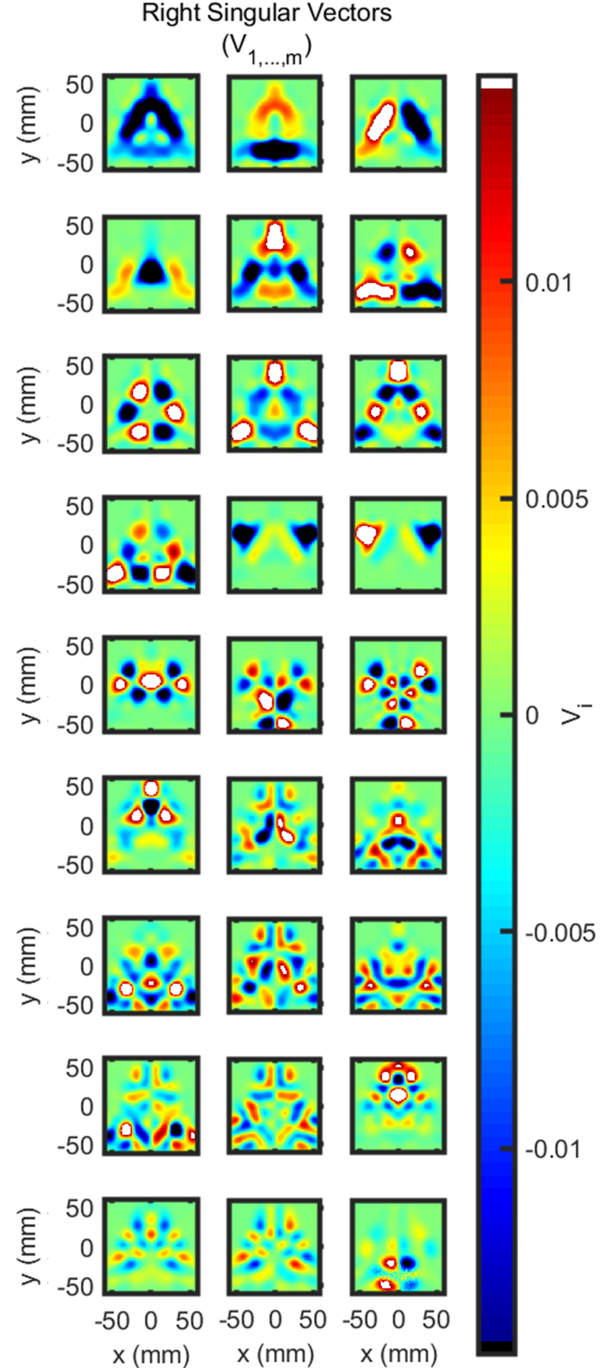


Figure 5.9: First $m = 27$ right singular vectors $(\vec{V}_1, \dots, \vec{V}_m)$ for the hexagonal arrangement.
Note 1: This figure can be found as Figure 12 in Blaney *et alia* Review of Scientific Instruments (2020) [5].

of the first m right singular vectors of \mathbf{S} . This fact can be used to further evaluate the imaging

system by visualizing these m vectors as maps in 3D space, keeping in mind that any image reconstructed by the system must be a linear combination of these maps. An example of a map of these singular vectors is shown in Figure 5.9 which corresponds to the array shown in Figure 5.11 which is discussed in the following sections.

We may also revisit the κ in terms of SVD. Σ contains the m singular values of \mathbf{S} ($\sigma_1, \dots, \sigma_m$). We consider the singular values ordered such that σ_1 is the maximum singular value and σ_m is the minimum singular value. Therefore κ can also be expressed as [65]:

$$\kappa = \frac{\sigma_1}{\sigma_m} \quad (5.24)$$

showing that the κ (meaning the system stability) can be thought of as the ratio of biggest and smallest singular values. This suggests that a better conditioned system will have a set of singular values within a relatively small range, while an ill-conditioned system will have a large difference between the largest and smallest singular values. Therefore, yet another method for looking at the stability/condition of the imaging system is to examine the m singular values and noting how much they differ. For example, if the first $m-1$ singular values have approximately the same order of magnitude but σ_m is near zero, the condition number of the system may be improved by ignoring a redundant measurement.

For better understanding of the use of singular values we may consider two simple examples with $m = 2$ and $v = 3$. First, we consider the case where one measurement is very weekly sensitive to the medium:

$$\mathbf{S} = \begin{bmatrix} 1/3 & 1/3 & 1/3 \\ 0 & 0 & 10^{-6} \end{bmatrix} \quad (5.25)$$

Then $\sigma_1 = 0.6$, $\sigma_2 = 8 \times 10^{-7}$, and $\kappa = 7 \times 10^5$, showing that one measurement is problematic. Second, consider the case where the two measurements have close to the same sensitivity:

$$\mathbf{S} = \begin{bmatrix} 1/3 & 1/3 & 1/3 \\ 1/3 & 1/3 + 10^{-6} & 1/3 - 10^{-6} \end{bmatrix} \quad (5.26)$$

Then $\sigma_1 = 0.8$, $\sigma_2 = 10^{-6}$ and $\kappa = 8 \times 10^5$, showing again there is a problematic measurement (because one measurement is redundant).

We note that examining these values cannot be done blindly since their magnitudes are dependent on the specific reconstruction parameters being considered, and different issues may cause similar effects. However, examining singular values can provide guidance when combined with other evaluation methods or when comparing two similar array designs.

5.3 Constructing a Dual-Slope Array

Once a geometrical arrangement of source and detector locations has been determined, a design must be created that physically realizes it. Depending on the specifics of the Near-InfraRed Spectroscopy (NIRS) instrument, the array may contain physical sources (laser diodes, light emitting diodes, *et cetera*) and detectors (photodiodes, avalanche photodiodes, *et cetera*), or it may contain optical fibers that deliver light to and from the investigated sample. In this work, we have used an ISS Imagent V2 [Champaign, IL USA] (Imagent) NIRS instrument, which uses laser diodes and PhotoMultiplier Tube (PMT) detectors that are coupled to optical fibers. Specifically, the light sources are coupled to SubMiniature version A (SMA) terminated multi-mode optical fibers, whereas the optical detectors are coupled to ferrule terminated fiber bundles connected via a collet. For the detector fibers we use 2 m, $\phi 3$ mm fiber bundles with $\phi 4.75$ mm Outer Diameter (OD) ferrules. 2 separate optical fibers, 1 for each of 2 optical wavelengths (λ s) 690 nm and 830 nm, deliver light at each source location. To accomplish this, we use custom-built, 2 m long 1×2 fan-out fiber bundles with 1 m ends. The optical fiber used was a $\phi 600$ μm multi-mode fiber with furcation tubing jacket. The split ends are terminated in SMA connectors, and the common end is terminated in a custom drilled and polished $\phi 2.5$ mm OD ferrule. Given these optical fiber terminations, the optical array was designed to arrange the $\phi 4.75$ mm OD detector fibers and the $\phi 2.5$ mm OD source fibers in the desired arrangement.

5.3.1 Fiber Array Design

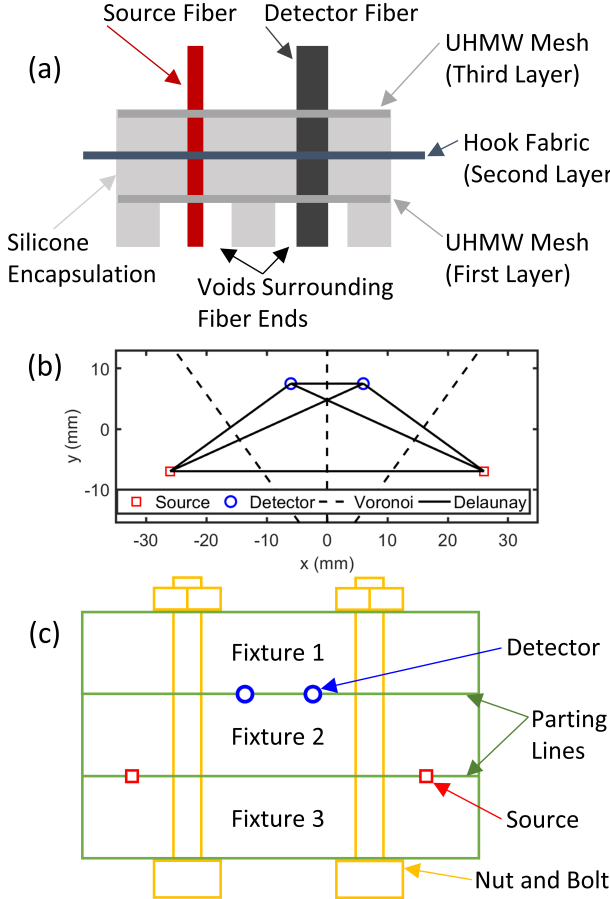


Figure 5.10: Example array design methodology. (a) Basic schematic of layered array geometry. (b) Example Delaunay triangulation used for mesh design, and Voronoi partition used for fiber void design for a single Dual-Slope (DS) set. (c) Basic schematic of parting line locations and fixture clamping methodology used to design the array mold.

Note 1: This chart can be found as Figure 5 in Blaney *et alia* Review of Scientific Instruments (2020) [5]. Acronyms: Ultra High Molecular Weight polyethylene (UHMW).

The overarching design of the array was a three-layer mesh structure encapsulated in Poly-DiMethylSiloxane (PDMS) (*id est* silicone; Figure 5.10(a)). The first and third layers of the array are constructed from Ultra High Molecular Weight polyethylene (UHMW) film and the middle (second) layer is built from polypropylene

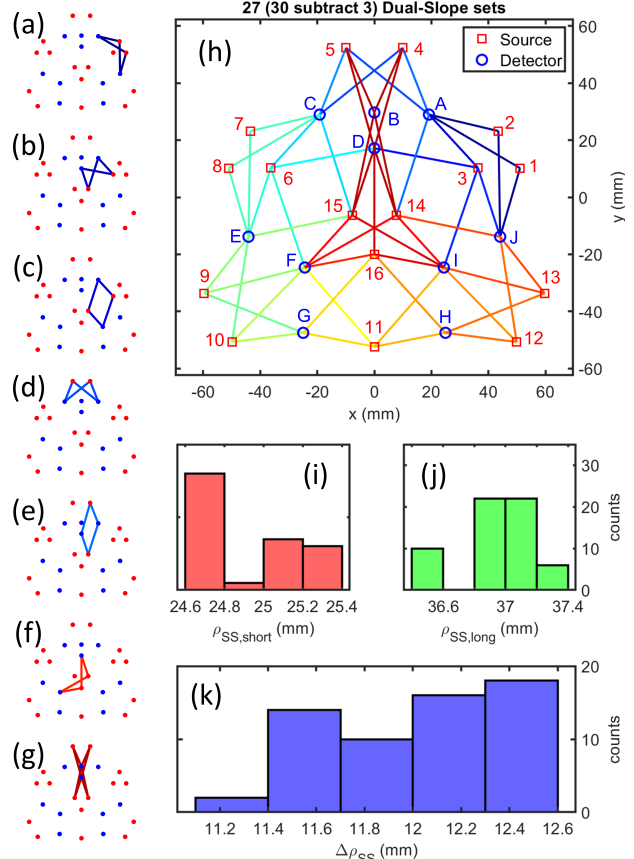


Figure 5.11: Final hexagonal design of the Dual-Slope (DS) imaging arrangement. (a)-(g) Examples of each of types of DS sets within the source-detector arrangement. (g) Four redundant DS sets combined into one. (h) Full array showing all sources (1-16), detectors (A-J), and Single-Distance (SD) measurement pairs (lines). (i) Histogram of all SD which make up the short distance of a Single-Slope (SS) set. (j) Histogram of all SD distances which make up the long distance of a SS set. (k) Histogram of all distance differences for SS sets.

Note 1: This figure can be found as Figure 7 in Blaney *et alia* Review of Scientific Instruments (2020) [5].

hook and loop fabric. The PDMS used to encapsulate the array mixed with Daler-Rowney Calli India-Ink [Bracknell, England] (cII) to pigment the array black.

The first and third UHMW mesh layers hold the fiber terminations in their place within the arrangement. The design methodology for the UHMW mesh is as follows:

1. Determine the locations of the source and detector ferrules.
2. At each ferrule location create a hole to accommodate the ferrule with a doughnut of UHMW surroundings it with a $\phi 14.5$ mm OD (*id est* we now have toroidal islands of UHMW at each ferrule location).
3. Connect the centers of the doughnuts with a Delaunay triangulation (Figure 5.10(b)), where each triangulation edge defines the center-line of a 5 mm wide UHMW connector.

The resulting mesh features circles of UHMW surrounding each ferrule with 5 mm wide connections between them. This design strategy creates an interconnected mesh which will hold the fibers in the arrangement locations. The fiber ferrules were epoxied to the UHMW mesh.

The middle layer of hook fabric is cut to remove as much material as possible, allowing the fibers to pass through the layer and PDMS to fully surround all the parts. Enough hook fabric remains to provide tension to the array when pulled, since this is the method with which the array will be attached to other components (such as a head cap). As such, the size of the hook fabric will overhang the array by 25 mm once it has been encapsulated with PDMS. Both the UHMW mesh and hook fabric are cut using a paper cutter.

Finally, after designing and constructing the various array layers, the assembly is encapsulated with PDMS. The first mesh layer is placed 5 mm from the ferrule ends, the second layer of hook fabric (hooks facing away from ferrule ends) is placed 5 mm from the first mesh, and the third layer of mesh is placed 5 mm above the hook fabric. Finally, the top of the PDMS is poured such that it is flush with the top of the third layer. This procedure results in a total array thickness of 15 mm. The outer perimeter of the array is such that it fully encapsulates the mesh layers and leaves a 25 mm hook fabric overhang. On the bottom of the optical array, there are voids in the PDMS surrounding each fiber ferrule to allow for the ferrules to push through hair (in the

case of non-invasive applications on the human head). These negative spaces are 5 mm in height and their shape is defined using a Voronoi partition (Figure 5.10(b)) between the fiber locations. The edges of the partition are of a non-zero width such that each ferrule is 7.5 mm to the edge of its void, or the partition width is 5 mm, whichever creates a larger partition wall width. This creates a design with walls of PDMS separating all fiber locations ensuring that light diffuses through the medium being probed and does not leak across the surface.

5.3.2 Fiber Array Construction Methods

To realize the array design, the structure of the array is built using a mold that holds all components in place while the PDMS is poured over the array. The general design of the array mold consists of a series of fixtures that bolt together such that the fiber ferrules are placed along the parting lines of the fixtures that are assembled to create the mold (Figure 5.10(c)). In other words, the assembly fixtures bolt together to sandwich the ferrules in place; once all the fixtures are bolted together their negative space creates the mold for the PDMS. Once this assembly is in place, a collar is bolted around the array such that the hook fabric is sandwiched to guarantee that when the PDMS is poured, the fabric will not be encapsulated and will overhang the array.

The order of assembly of the array is:

1. Pull the fibers through the 3 layers of mesh and hook fabric.
2. Place the ferrules sandwiched between the fixtures to create a mold.
3. Lower the layers into the mold negative space, epoxy the ferrules to the mesh, and affix the collar as to sandwich the middle layer.
4. Pour the PDMS and allow the array to set.

After which everything is disassembled and the flash removed.

The primary material used for the mold was PolyLactic Acid (PLA) fabricated using a Fused Filament Fabrication (FFF) 3-dimensional (3D) printer. The 3D printed material was sprayed with methyl methacrylate lacquer to ensure there was no cure inhibition of the PDMS. The mold is bolted together using M5×0.8 mm socket head cap screws of various lengths and matching nuts which were captured within the printed PLA mold.

5.3.3 Head-Cap Design

Here, we consider functional Near-Infrared Spectroscopy (fNIRS) applied to the human brain as the array's primary use. As such, it is designed to be placed on a human head to image optical property changes within brain tissue. To achieve this, a polychloroprene wet suit cap was modified to accept the array and connect to the overhanging hook fabric. Each cap can be designed to target a specific region on the subject's head and different sized caps can be made for different subjects. Additionally, caps can be washed between uses.

To construct a cap, a hole is cut to accommodate the profile of the array. Then, loop polypropylene hook and loop fabric are sewn into the inside of the cap with loops facing toward the head. The optical array can be placed within the cap hole and fixed to the cap via the hook and loop. Each cap is custom designed for size and head location. If necessary, hook and loop tie straps are sewn to the outside of the cap to provide extra tension to the array. This may be necessary to conform the array to the subject's head. Cap construction is done using a sewing machine and components are attached using black #69 polyester thread.

5.3.4 Example Dual-Slope Imaging Arrays

The evaluation methods and results in the following example arrays rely on the creation of sensitivity maps for each Dual-Slope (DS) set per Appendix E. For our simulations, we used the same medium parameters stated in Section 2.1.

These optical properties are consistent with previous work concerning sensitivity maps [58] and typical values for the human brain [66].

The goal of DS imaging is not to create 3D images but instead 2-dimensional (2D) images representative of deep perturbations. Thus, simulation geometry featured 2 layers of voxels ranging from 0 mm to 20 mm in depth, with each voxel 10 mm in height (z direction) and the second layer of voxels we focused on. Such layered geometry has been described for use with DS before this design work [5] in Blaney *et alia* Optics Letters (2020) [4].

The geometry was chosen to align with the goals of using DS phase (ϕ) to achieve preferential deep sensitivity. The second layer depth was chosen both because the brain is typically at a depth >10 mm [67, 68], and because the typical depth of maximal sensitivity for DS ϕ is greater than 10 mm. In accordance with these goals, we show the maps only for the second layer of voxels (10 mm to 20 mm) and only for DS ϕ .

5.3.4.A The Circular Array

We designed a circular source-detector arrangement with the purpose of using DS ϕ to preferentially image deep regions in a liquid phantom experiment in Blaney *et alia* Review of Scientific Instruments (2020) [5], Blaney *et alia* (2020) [11], and Blaney *et alia* Optics Letters (2020) [4]. Our goal was to design an arrangement with many overlapping measurements in a small area for high Signal-to-Noise Ratio (SNR) and resolution (Figure 5.12). This was to demonstrate the presented methods and validate DS imaging on a phantom.

This arrangement was designed for a total of 16 sources and 9 detectors. We started the design process by manually placing the sources and detectors in concentric circles. The arrangements with the largest number of overlapping sets was chosen. This resulting circular arrangement (Figure 5.12(p)) consists of $m = 116$ DS sets. There are 15 different DS set shapes either linear, trapezoidal, or rhombic (Figure 5.12(a)-(o)) [59]. However, for the phantom experiments only $m = 16$ of these DS sets were chosen of the asymmetric

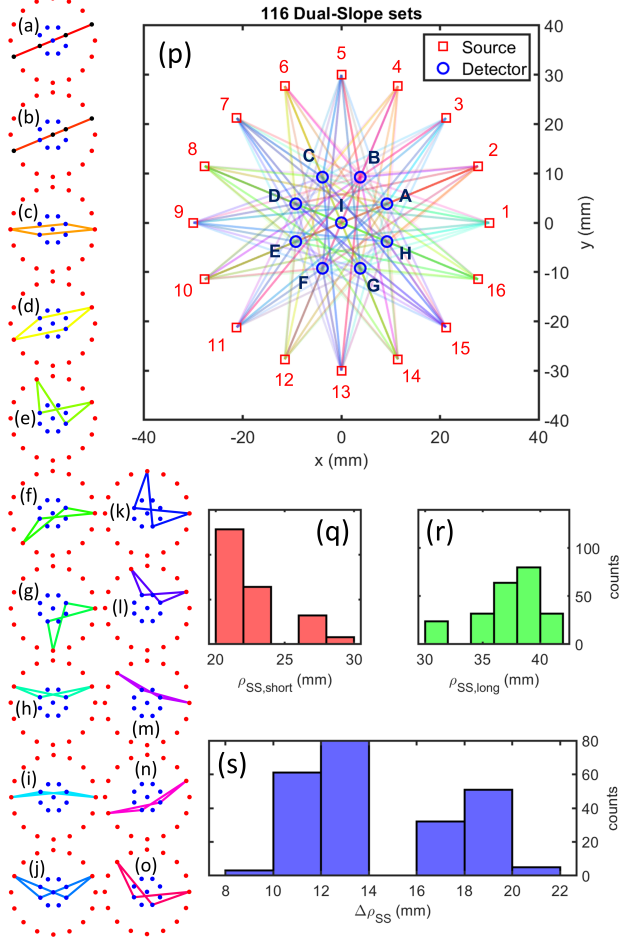


Figure 5.12: Circular design of the Dual-Slope (DS) imaging arrangement. (a)-(o) Examples of each of types of DS sets within the source-detector arrangement. (p) Full array showing all sources (1-16), detectors (A-I), and Single-Distance (SD) measurement pairs (lines). (q) Histogram of all SD which make up the short distance of a Single-Slope (SS) set. (r) Histogram of all SD distances which make up the long distance of a SS set. (s) Histogram of all distance differences for SS sets.

Note 1: This figure can be found as Figure 6 in Blaney *et alia* Review of Scientific Instruments (2020) [5].

linear or trapezoidal types (Figure 5.13). Laterally, for the circular array simulation, the full volume was $50.5 \text{ mm} \times 50.5 \text{ mm} \times 20 \text{ mm}$ with voxels of $0.5 \text{ mm} \times 0.5 \text{ mm} \times 10 \text{ mm}$, resulting in $v = 20,402$.

Examining the reconstruction of voxels vector ($\vec{\mathcal{R}}$) and cross-talk between voxels vector ($\vec{\mathcal{C}}$)

maps for the circular array, we notice the reconstruction is focused on a small central region (Figure 5.5(a)) and the crosstalk map suggests preferential reconstruction in a four-lobed ring around the center (Figure 5.5(b)). This is consistent with the design goals for this array which sought to confine the sensitivity to a small region. As a result, Figure 5.5 suggests the circular array has a coverage region with a radius of approximately 10 mm (approximately 300 mm^2) for which 116 DS which were considered here sets overlap.

Second, we examine the resolution matrix (\mathbf{T}) and localization matrix (Δ) maps. A typical (average in usable array region) lateral Full-Width Half-Max (FWHM) resolution of approximately 10 mm is achieved (Figure 5.7(a)) with a localization error of about 1 mm (Figure 5.7(b)). This suggests that the array could roughly resolve two point like perturbations in its small imaging area and reinforcing the goals for this design are met given that it is capable of fine precise imaging in a small area.

5.3.4.A.a Physical Realization of Circular Array

The circular array was used for a phantom imaging experiment in Blaney *et alia* Optics Letters (2020) [4] as seen in Figure 5.13. For this reason the array was not built into a PDMS probe but instead held by a 3D printed PLA fixture (Figure 5.14). This fixture suspended the sources and detectors on the surface of a liquid phantom made of 2% reduced fat milk, Higgins India-Ink [Leeds, MA USA] (II), and Water (W).

During the experiment PDMS solid phantoms were placed in the liquid and their perturbation measured by the array (Figure 5.13(b)). For these experiments only $m = 16$ DS sets were used since the investigation was prior to the invention of the DS discovery algorithm. The two types of DSs which were manually found and used for this study [4] are shown in Figure 5.13(a). The results from this experiment are discussed in subsequent sections.

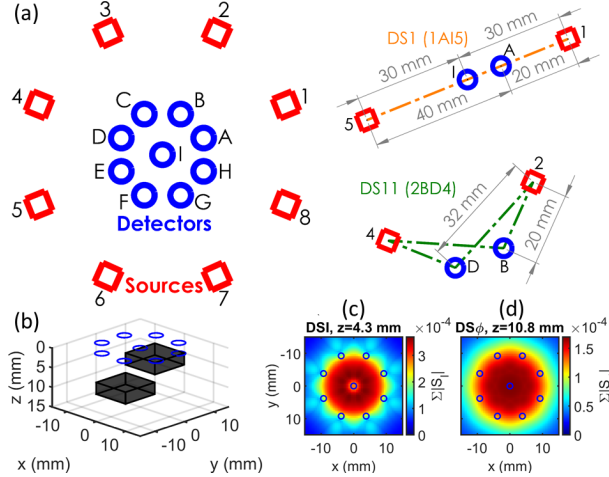


Figure 5.13: (a) Schematic of 8-source/9-detector imaging array that features 16 Dual-Slope (DS) sets [DS1, orange; DS11, green]. (b) Schematic of imaging configuration showing the superficial [at $(5\hat{x}+11.5\hat{z})$ mm] and deep [at $(-5\hat{x}+11.5\hat{z})$ mm] $10\text{ mm} \times 10\text{ mm} \times 3\text{ mm}$ perturbations. Region of sensitivity for Intensity (I) (c) and phase (ϕ) (d) at plane of maximal Sensitivity to absorption change (S).

Note 1: This figure can be found as Figure 1 in Blaney *et alia* Optics Letters (2020) [4].



Figure 5.14: Image of circular array used for liquid phantom imaging experiments in Blaney *et alia* Optics Letters (2020) [4].

5.3.4.B The Hexagonal Array

We designed a hexagonal arrangement with the purpose of using $\text{DS } \phi$ in fNIRS experiments. This with large lateral coverage and prioritization of localization of optical perturbations (Figure 5.11). This goal differs from a goal of spa-

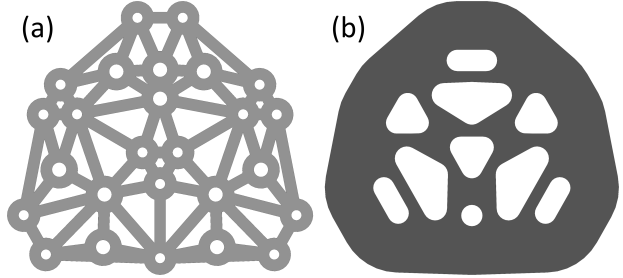


Figure 5.15: Layer profiles for the physical array construction. (a) First and third layer mesh. (b) Middle layer hook fabric.

Note 1: This figure can be found as Figure 13 in Blaney *et alia* Review of Scientific Instruments (2020) [5].

tial resolution (as with the circular array), which would imply the discrimination of two close perturbations, which is not the goal of the hexagonal array.

This arrangement was designed for a total of 16 sources and 10 detectors. We started the design process by manually placing the sources and detectors in various tessellations, and using the DS discovery algorithm to find all the possible DS sets (Listings 5.1, 5.2, & 5.3). The arrangements with the largest number of overlapping sets and best evaluation (focusing on the goal for each array) results was chosen. The final arrangement was based on a hexagonal tessellation (Figure 5.11). Within this hexagonal arrangement, there are 7 different shapes of DS sets [59] (Figure 5.11(a)-(g)) all of which are either rhomboids or trapezoids. The 4 redundant sets of the hexagonal arrangement (Figure 5.11(g)) should be averaged together since their regions of sensitivity are very close to each other, and considering them separately would increase condition number (κ) of the system. After considering this the hexagonal array contained $m = 27$ DS sets. The whole hexagonal array contains a small range of short and long distances (Figure 5.11(i)-(k)), showing that the position refinement successfully homogenized the array. Laterally, the array simulation full volume was $121\text{ mm} \times 121\text{ mm} \times 20\text{ mm}$ with $1\text{ mm} \times 1\text{ mm} \times 10\text{ mm}$ voxels, thus $v = 29,282$.

Now let's consider the $\vec{\mathcal{R}}$ and $\vec{\mathcal{C}}$ for the hexagonal array. Focusing on the reconstruction map (Figure 5.11(a)), we notice that the array does not feature homogeneous reconstruction. Noticeably, the array has high reconstruction values at the center and below the top 4 detectors (A-D). Additionally, there are low reconstruction values in various regions surrounding the center, suggesting compromised sensitivity and poor reconstruction quality in these regions. Looking at the crosstalk map (Figure 5.11(b)), we notice high values in the center and below sources 2 and 7, indicating that some perturbations will be incorrectly reconstructed there. Low values in the crosstalk map are seen below detectors I and F, which align with low values in the reconstruction map; this suggests that the array has blind spots in these locations. Overall, given our goal of large lateral coverage, the array performs reasonably well by covering a rough triangle of approximately 7200 mm^2 with the largest weakness being two poor sensitivity locations below detectors I and F. Keeping this imaging performance in mind, in a given experiment the array should be placed such that the best sensitivity area (underneath detectors A-D) is aligned with the region of interest.

Second, we examine the Γ and Δ maps. The resolution map (Figure 5.8(a)) shows that the expected lateral FWHM of the arrangement ranges from 20 mm to 30 mm in most regions. This value is quite large and shows that the arrangement will not be able to distinguish between two closely spaced perturbations. However, according to our goal, we prioritize localization over resolution. Thus, we look at the localization map (Figure 5.8(b)) for metrics of success. Over almost the entire array, the lateral localization is approximately 5 mm. Therefore, the arrangement achieves both a good localization and a large lateral coverage, along the lines of the design goals.

Finally, we consider the imaging system in terms of Singular Value Decomposition (SVD). The first m right singular vectors ($\vec{V}_1, \dots, \vec{V}_m$) show the span of all possible reconstructed images for the hexagonal array (Figure 5.9). For

this system, $m = 27$ and thus the reconstruction must fit into 27 degrees of freedom that are shown in these singular vectors. Through careful examination of these maps, we can see where it is possible for the system to reconstruct images and where it is not. Notably, the upper right and left corners of the map cannot be reconstructed well, which is expected since the array cannot have sensitivity there. Aside from the right singular vectors, κ of the system was also evaluated. This can be calculated using the matrix norm or SVD, with SVD having the advantage of giving the option to examine the other singular values as well. For this system, the condition number is on the order of 1×10^{14} , suggesting that the system is ill-conditioned. However, this is expected and known for a diffuse optical imaging system. What should be noted is the improvement that was achieved by averaging the redundant DS sets (Figure 5.11(g)). When the system considers these separately (in which case $m = 30$), the condition number is on the order of 1×10^{15} and the last three singular values approach zero. Therefore, removing the redundant measurements via averaging improved the condition of the system by an order of magnitude.

5.3.4.B.a Physical Realization of Hexagonal Array

The physical hexagonal array was designed around the arrangement in Figure 5.11 since large coverage was desired. This is because the intended use of the array was for fNIRS experiments involving brain activation or Coherent Hemodynamics Spectroscopy (CHS) oscillations. The array's design was described in Blaney *et alia* Review of Scientific Instruments (2020) [5] and Blaney *et alia* (2020) [11] and its use in Blaney *et alia* (2021) [12] and Blaney *et alia* (2022) [13].

To realize the array first, the mesh and hook fabric layers were designed and cut (Figure 5.15). All other components of the array were pre-fabricated (source and detector fibers). Then, the array was assembled using a mold built from clamped fixtures as described with Figure 5.10. The mold was constructed from 7 fixtures clamped together by 13 bolts such that

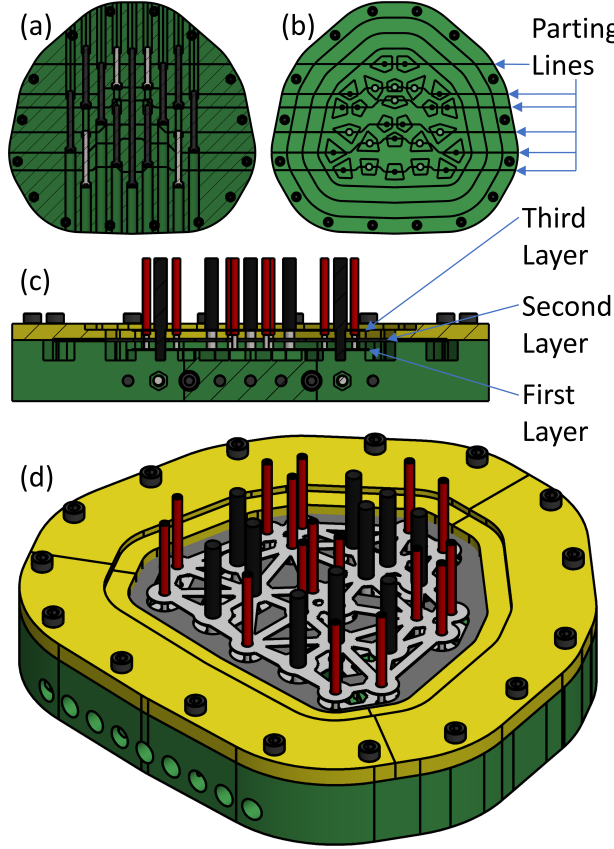


Figure 5.16: Mold design used to construct the final array. (a) Bottom view showing bolts attaching seven fixtures to create the mold. (b) Top view showing parting line locations sandwiching the fiber ends. (c) Cross section showing three layers captured within the mold. (d) Isometric view of the full mold assembly before encapsulating PolyDiMethylSiloxane (PDMS) is poured. Note 1: This figure can be found as Figure 14 in Blaney *et alia* Review of Scientific Instruments (2020) [5].

all 26 fibers were captured by being clamped at the parting lines (Figure 5.15(a)-(b)). The 3 layers were placed within the mold, with the middle layer of hook fabric clamped by a collar which encompassed the whole mold and was attached with 16 bolts (Figure 5.15(c)). The mesh layers (first and third layers) were fixed to the fibers with epoxy. Finally, with all parts held in place and the mold assembled, black PDMS was poured to encapsulate the array (Figure 5.16(d)). Once the PDMS cured, the mold was disassem-

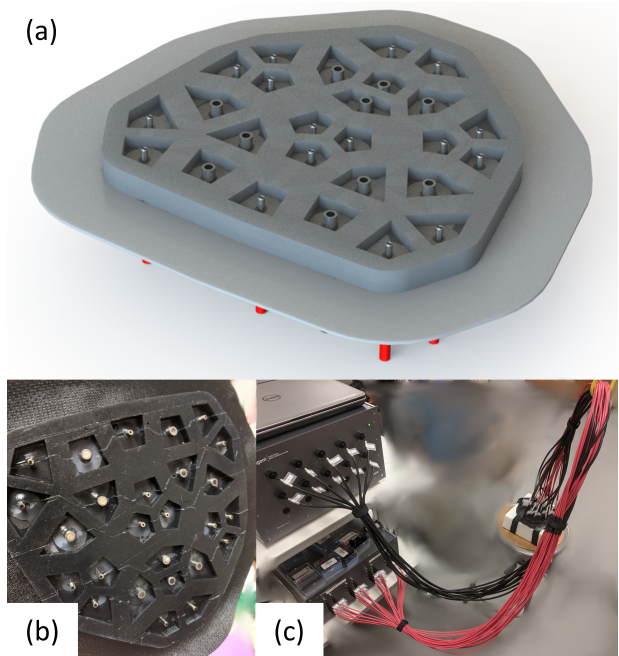


Figure 5.17: Final array design and construction. (a) Rendering of the bottom side of our final array design. (b) Picture of the final array after construction. (c) Picture of the final array attached to the Imagent V2 instrument with the array applied onto an optical phantom.

Note 1: This figure can be found as Figure 15 in Blaney *et alia* Review of Scientific Instruments (2020) [5].

bled, and the array cleaned to finish the build. Given the design, the array can flex to conform to various surfaces including the human head, and the fibers can push through hair given the voids surrounding them. The final array model and assembly is shown in Figure 5.17.

This hexagonal optical array was designed with the specific purpose of applications in fNIRS imaging. This is the first optical array specifically designed for DS ϕ imaging with Frequency-Domain (FD) NIRS on human subjects. Of course, this array also collects Single-Distance (SD) data, as well as optical Intensity (I) measured with Continuous-Wave (CW) NIRS. Therefore, the array may be used in experiments where the DS data (I or ϕ) is compared to SD data (I or ϕ) to investigate optimal conditions for imaging with selective Sensi-

tivity to absorption change (\mathcal{S}) to deeper versus superficial tissue. Additionally, the large size of the array and the emphasis on localization would allow for identification of brain activation location in fNIRS protocols. The large array size has the further advantage of broader coverage, which is important for experiments in which multiple neighboring brain areas are activated. Finally, this DS array design features the Self-Calibrating (SC) advantages of insensitivity to instrumental drifts and changes in optical coupling with tissue, and calibration-free absolute measurements [61]. This allows for robust measurements weakly impacted by motion or instrumental artifacts as discussed in Chapter 3.

Aside from fNIRS experiments, the array could also be used for non-invasive optical measurements of tissue where preferentially deep sensitivity is desired. Possible applications include breast and skeletal muscle imaging, where the tissue of interest is below a superficial layer of skin and adipose tissue. All the aforementioned applications would take advantage of the array's DS imaging capability; however, the array could also be implemented in SC mode by combining DS I and ϕ data. In such a mode, the goal would not be to achieve preferentially deep sensitivity like for phase DS, but rather to measure absolute optical properties. In SC mode, the array could image absolute optical properties of tissue without the need for calibration and with insensitivity to instrumental drifts. The applications of an array designed for DS data collection are numerous.

5.4 Dual-Slope Imaging Results

5.4.1 Dual-Slope Imaging on Phantoms

In Blaney *et alia* Optics Letters (2020) [4] we presented theoretical and experimental demonstrations of a novel Diffuse Optical Imaging (DOI) method that is based on the concept of Dual-Slopes (DSs) in Frequency-Domain (FD) Near-InfraRed Spectroscopy (NIRS). We considered the circular array of sources and detectors that collects Intensity (I) and phase (ϕ) data with

multiple DS sets. We had recently shown that DS ϕ data featured a deeper sensitivity with respect to DS I data in Blaney *et alia* Journal of Biophotonics (2020) [3] when we pursued this work. Therefore, in Blaney *et alia* Optics Letters (2020) [4] for the first time, we described a DS imaging approach based on the Moore-Penrose inverse (MP) of the matrix of sensitivity to absorption change (\mathcal{S}) for multiple DS data sets. We showed that DS I images are more sensitive to superficial (<5 mm) perturbations, whereas DS ϕ images are more sensitive to deeper (>10 mm) perturbations in highly scattering media.

To investigate the effectiveness of the novel imaging method based on DSs, we performed experiments on highly scattering liquid phantoms containing solid optical heterogeneous. Liquid phantoms were made from water, 2% reduced fat milk, and Higgins India-Ink [Leeds, MA USA] (II). For optical inclusions, solid phantoms were constructed from PolyDiMethylSiloxane (PDMS) using Rubber Glass Smooth-On [Macungie, PA USA] (silicone), Daler-Rowney Calli India-Ink [Bracknell, England] (cII), and AEE Titanium diOxide powder [Upper Saddle River, NJ USA] (TiO₂). The absorption coefficient (μ_a) and the reduced scattering coefficient (μ'_s) of the liquid and solid phantoms were measured using scanned Multi-Distance (MD) FD NIRS. We used the ISS Imagent V2 [Champaign, IL USA] (Imagent) FD NIRS instrument whose operational parameters are stated in Section 2.2.1.A. The optical probe consisted of $\phi 400\text{ }\mu\text{m}$ multi-mode fibers to deliver light, and $\phi 3\text{ mm}$ fiber bundles to collect light.

The circular array discussed above was used with $m = 16$ DS sets (Figure 5.13(a)). 8 DS sets are asymmetric linear sets that use source-detector distance (ρ) of 20 mm and 30 mm and 30 mm and 40 mm for the 2 paired Single-Slopes (SSs). The other 8 DS sets are trapezoidal sets that use ρ of 20 mm and 32 mm for both paired SSs. The individual sensitivity maps for these DS sets can be found in [59]. Figure 5.13(c)-(d) shows the overall region of Sensitivity to absorption change (\mathcal{S}) associated with all $m = 16$ sets for I (Figure 5.13(c)) and ϕ (Figure 5.13(d)) at the depth of respective maximum sensitivity

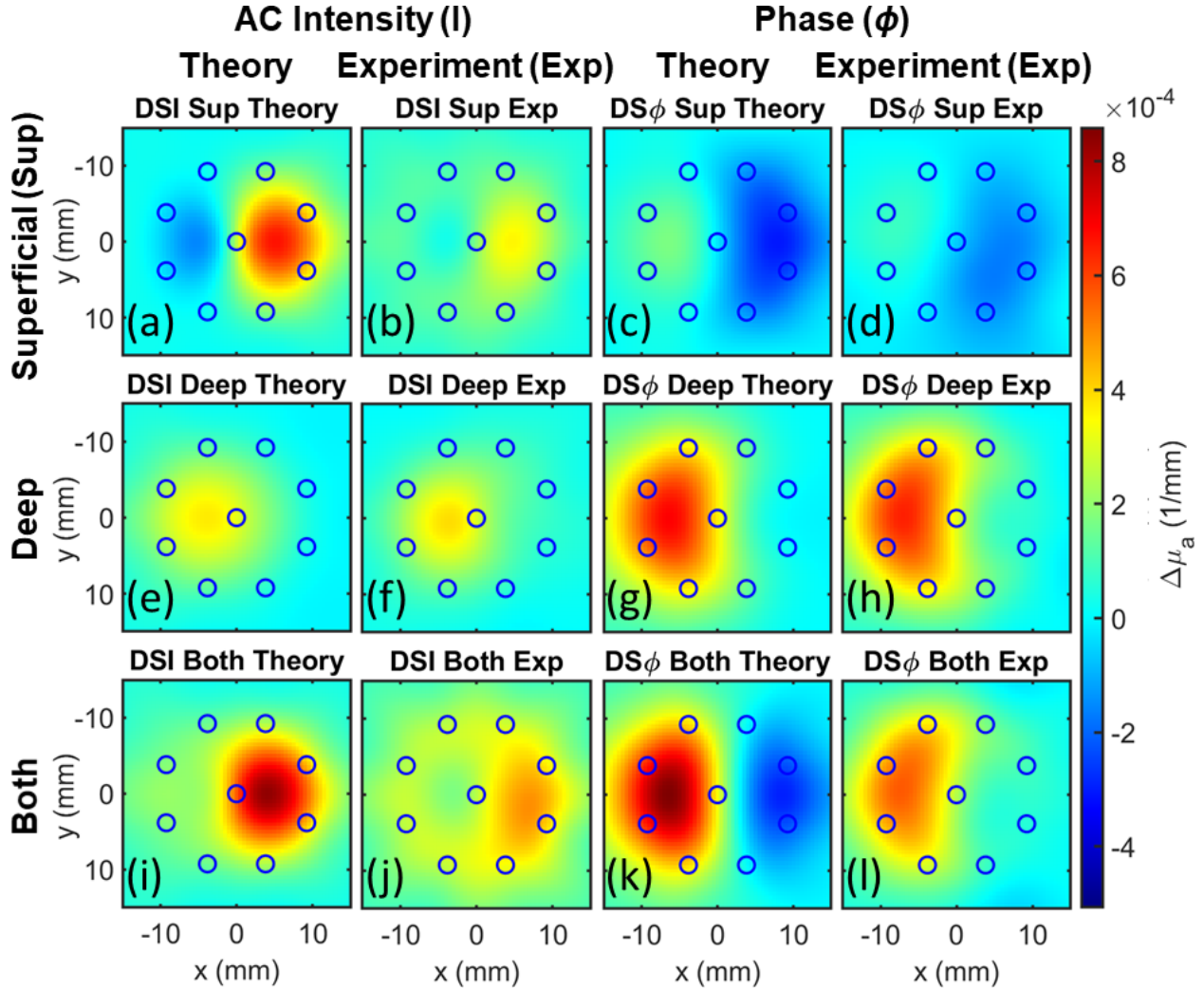


Figure 5.18: Dual-Slope (DS) Intensity (I) and DS phase (ϕ) images, as labeled with only the superficial perturbation [(a)(c): theory; (b)(d): experiment], only the deep perturbation [(e)(g): theory; (f)(h): experiment], and with both the superficial and the deep perturbation [(i)(k): theory; (j)(l): experiment].

Note 1: This figure can be found as Figure 2 in Blaney *et alia* Optics Letters (2020) [4].

Note 2: Superficial perturbation at $(5\hat{x} + 1.5\hat{z})$ mm and deep perturbation at $(-5\hat{x} + 11.5\hat{z})$ mm.

$(z = 4.3 \text{ mm for } I, z = 10.8 \text{ mm for } \phi)$. The \mathcal{S} was summed over all the DS measurements to obtain the overall sensitivity for DS I and DS ϕ at each voxel j in these insets.

We considered two perturbations (size: $10 \text{ mm} \times 10 \text{ mm} \times 3 \text{ mm}$); a superficial one centered at $(5\hat{x} + 1.5\hat{z})$ mm, and a deep one centered at $(-5\hat{x} + 11.5\hat{z})$ mm (see Figure 5.13(b)). In this experiment, we used an optical wavelength of 690 nm, for which

the optical properties of the liquid phantom were $\mu_a = (0.0093 \pm 0.0003) \text{ mm}^{-1}$ and $\mu'_s = (0.85 \pm 0.05) \text{ mm}^{-1}$, and those of the solid phantom were $\mu_a = (0.0130 \pm 0.0001) \text{ mm}^{-1}$ and $\mu'_s = (0.818 \pm 0.004) \text{ mm}^{-1}$. The optical properties of the liquid phantom resulted in Differential Slope Factor (DSF) values for I and ϕ of 7.4 and 1.4, respectively (Appendix C) [3]. Three cases were considered:

- The presence of only the superficial pertur-

bation (Superficial or Sup).

- The presence of only the deep perturbation (Deep).
- The presence of both superficial and deep perturbations (Both).

For each of these cases the solid phantom perturbation was immersed in the liquid phantom and held on the tip of a glass pipette which was filled with liquid phantom. To achieve the measurement, the perturbation was first placed far from the array during baseline then brought into the desired location by a 3-dimensional (3D) Computer Numerical Control (CNC) system.

Here, the goal is not to achieve a quantitative reconstruction of absolute changes in optical properties, but rather to identify and localize (in the lateral $x - y$ plane) deeper perturbations with minimal interference from shallower perturbations. This goal is consistent with the objective of brain measurements with non-invasive cerebral NIRS. In addition to collecting experimental data, we also present theoretical calculations assuming no scattering perturbations or refractive index mismatch at the perturbation boundary according to the methods in Appendix F. Additionally, we have investigated the effect of modeling a scattering perturbation so that we may comment on its effect.

For analysis, absorption coefficient change ($\Delta\mu_a$) from each DS set in the circular array was calculated using the methods in Appendix C for the various perturbation configurations. From these the \mathcal{S} was created using the methods in Appendix E and images of $\Delta\mu_a$ were recovered using Equation 5.8 with the MP. The image reconstruction utilized Tikhonov regularization with $a_{tik} = 0.01$ [64]. We sought to reconstruct 2-dimensional (2D) images in the $x - y$ plane that are mostly sensitive to deeper perturbations, while using the same voxel size in the analysis of I and ϕ data for a fair comparison of DS I and DS ϕ images. With this goal in mind, we chose voxels of size $0.5 \text{ mm} \times 0.5 \text{ mm} \times 5 \text{ mm}$ (superficial layer) and $0.5 \text{ mm} \times 0.5 \text{ mm} \times 10 \text{ mm}$ (deeper layer) in (x, y, z) , and we only show the $x - y$ image corresponding to the deeper layer of vox-

els ($z = 5 \text{ mm}$ to 15 mm). This layer of voxels includes a portion of the medium that is sensed by both data-types and that does not include the most superficial layer ($z = 0 \text{ mm}$ to 5 mm). This is in line with the overall goal of DS, which is to suppress signal contributions from superficial layers. Therefore, we do not wish to create images at different depths, we focus on 2D images representative of deep perturbations.

The results of the imaging experiments are shown in Figure 5.18(a)-(l) for I (column 1: theory; column 2: experiment) and ϕ (column 3: theory; column 4: experiment). In the images of Figure 5.18(a)-(l), the superficial perturbation is on the right, *id est* positive x (row 1), the deep perturbation is on the left, *id est* negative x (row 2), and both are present in row 3. Overall, there is a good agreement between theory and experiment. The images based on DS I (columns 1-2) show a stronger sensitivity to the superficial perturbation, whereas the images based on DS ϕ show a stronger sensitivity to the deeper perturbation.

In the presence of only the superficial perturbation, the theoretical DS I map (Figure 5.18(a)) features a greater $\Delta\mu_a$ than the experimental DS I maps (Figure 5.18(b)) (likely because of different boundary effects in the theoretical and experimental cases), whereas both theoretical and experimental DS ϕ maps (Figure 5.18(c)(d)) show a small absorption decrease at the perturbation location, due to the negative superficial sensitivity of DS ϕ [58]. In the presence of only the deep perturbation, the theoretical and experimental maps are in excellent agreement and show a smaller contrast with DS I (Figure 5.18(e)(f)) than with DS ϕ (Figure 5.18(g)(h)). In this case, the experimental localization error in the lateral plane ($x - y$) is 2 mm for both DS I and DS ϕ (reconstructed maximum and deep true location).

The most significant case is the one where both superficial and deep perturbations are present. This is the case that emulates the presence of superficial confounds (for example, scalp hemodynamics) in the non-invasive study of deeper optical dynamics (for example, cerebral hemodynamics). The absorption maps based on DS I (Figure 5.18(i)(j)) show that they are

mostly representative of the superficial perturbation (lateral localization error of the deep object: 12 mm), whereas the maps based on **DS** ϕ (Figure 5.18(k)(l)) are mostly representative of the deeper perturbation (lateral localization error of the deep object: 2 mm).

While there is general agreement between theory and experiment in the results of Figure 5.18, we have observed some discrepancy between the absolute values of the reconstructed absorption changes in theoretical and experimental results. We assign these discrepancies to experimental conditions that deviate from the assumptions made in theoretical calculations. These assumptions include:

- Lack of scattering contrast for the optical inclusion (in our experiments, the scattering contrast was in the range -9% to 2%).
- Index of refraction (n) matching at the inclusion/background interface (in our experiments, the absorbing inclusion had $n \approx 1.4$, while the liquid phantom had $n \approx 1.35$ [69]).
- Extrapolated boundary conditions at the flat phantom/air interface (in the experiment, the presence of illumination and collection optical fibers, surface tension effects, and the proximity of the perturbation to the phantom/air boundary resulted in modified boundary effects).

To investigate the most likely source of the discrepancy between theory and experiment, we performed theoretical calculations that included scattering perturbations consistent with the experimental conditions. We found that the scattering mismatch alone cannot explain the difference between theory and experiment. Therefore, we expect that the discrepancy is likely due to the second and third points above, which refer to the unknown n mismatch and to the inevitable variability of geometric conditions that cannot be fully controlled within the scope of this experiment. We have also opted to present theoretical results without modeling a scattering perturbation to emphasize our focus on measurements of absorption perturbations. However, we stress

that our goal here is not to achieve reconstruction of absolute optical properties but instead to:

- Correctly localize perturbations in the $x - y$ plane.
- Achieve a stronger relative sensitivity to deeper versus shallower perturbations.
- Correctly identify the direction of the absorption change caused by the perturbation (increase or decrease).

The key message is that **DS** ϕ features a deeper sensitivity and is less impacted by superficial perturbations than **DS** I . This feature is exploited for imaging in Figure 5.18, which shows that **DS** ϕ images selectively reproduce deeper perturbations (see Figure 5.18(k)(l)), whereas **DS** I images are more strongly affected by superficial perturbations (see Figure 5.18(i)-(j)). Of course, one can take advantage of the complementary information of **DS** I and **DS** ϕ images to extract information on both superficial and deep perturbations.

5.4.2 *In Vivo* Dual-Slope Imaging

5.4.2.A Dual-Slope Imaging of Muscle

In Blaney *et alia* (2021) [12] we utilized the hexagonal array (Figure 5.17) to measure maps of absolute optical properties in human skeletal muscle, and muscle hemodynamics during a **VO**. In each case, spatial maps were created. The maps of baseline absolute optical properties showed higher μ'_s in connective tissue and higher μ_a in muscle tissue. The analysis of hemodynamics found a greater blood accumulation during **VO** in muscle. Overall, muscle hemodynamics were shown to be spatially variable over a large area, suggesting the importance of imaging (as opposed to single-location) measurements. The preliminary data on human subjects with this new **DS** imaging array pave the way for applications in **functional Near-InfraRed Spectroscopy (fNIRS)** for mapping brain activation.

To test this array on hemodynamic measurements, a simple muscle experiment was carried out on one human subject. The subject gave their informed consent according to

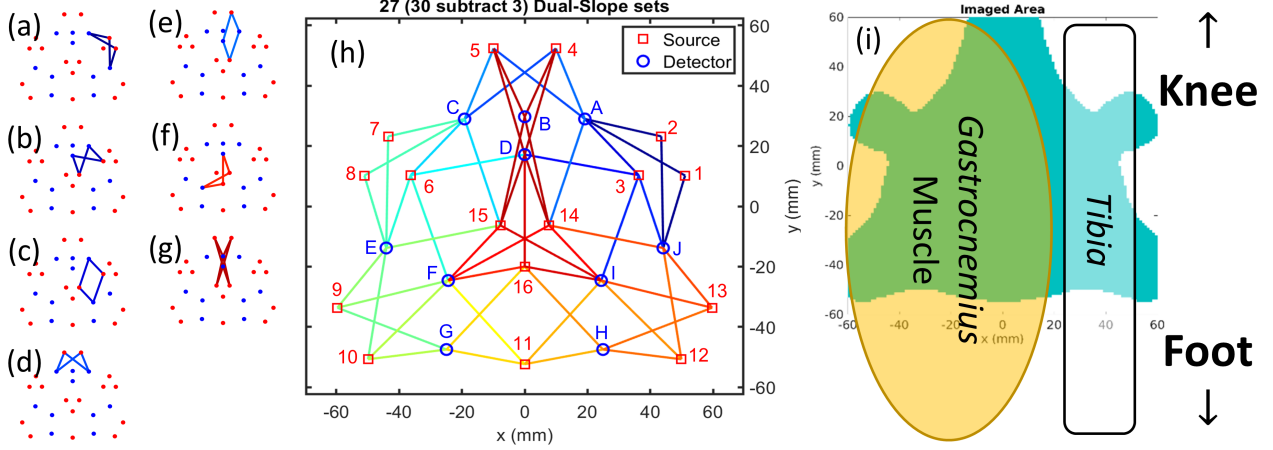


Figure 5.19: Schematic of Dual-Slope (DS) imaging array and array placement during muscle experiment. (a)-(g) Examples of the 7 DS set types in the array. (h) Diagram of all measurement pairs in the array resulting in 27 effective DS sets. (i) Placement of DS array over the subject's *gastrocnemius* muscle and *tibia*.

Note 1: This figure can be found as Figure 1 in Blaney *et alia* (2021) [12].

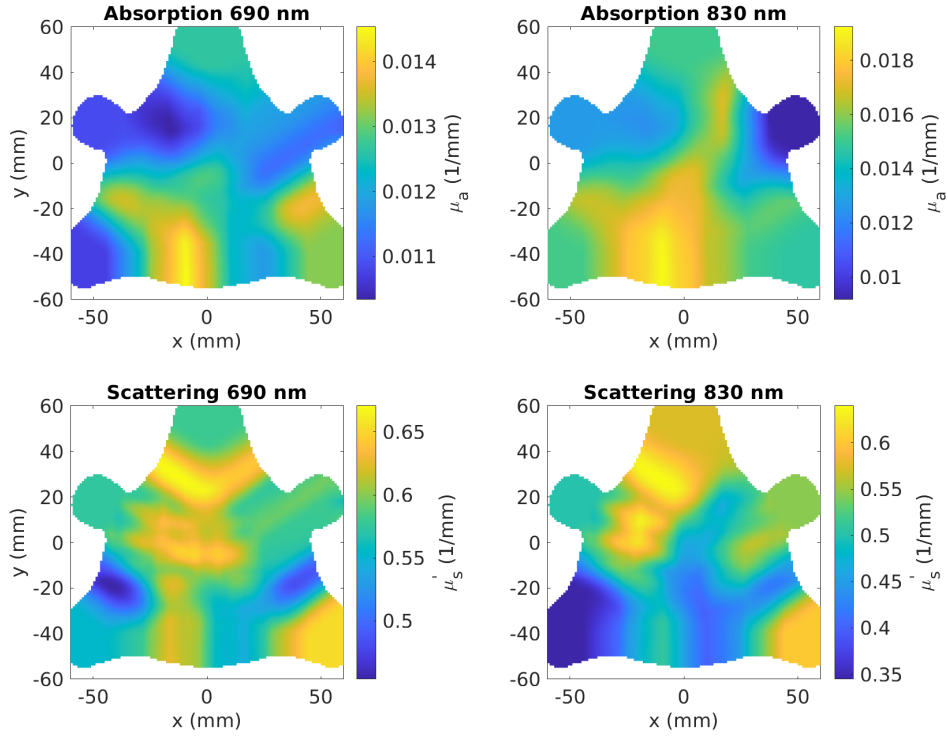


Figure 5.20: Maps of absolute absorption coefficient (μ_a) and absolute reduced scattering coefficient (μ'_s) on a subject's *gastrocnemius* muscle placed as seen in Figure 5.19(i).

Note 1: This figure can be found as Figure 2 in Blaney *et alia* (2021) [12].

the Tufts University Institutional Review Board (IRB) prior to the experiment. The array was

placed over the subject's left *gastrocnemius* muscle and *tibia* (Figure 5.19(i)). Then the following

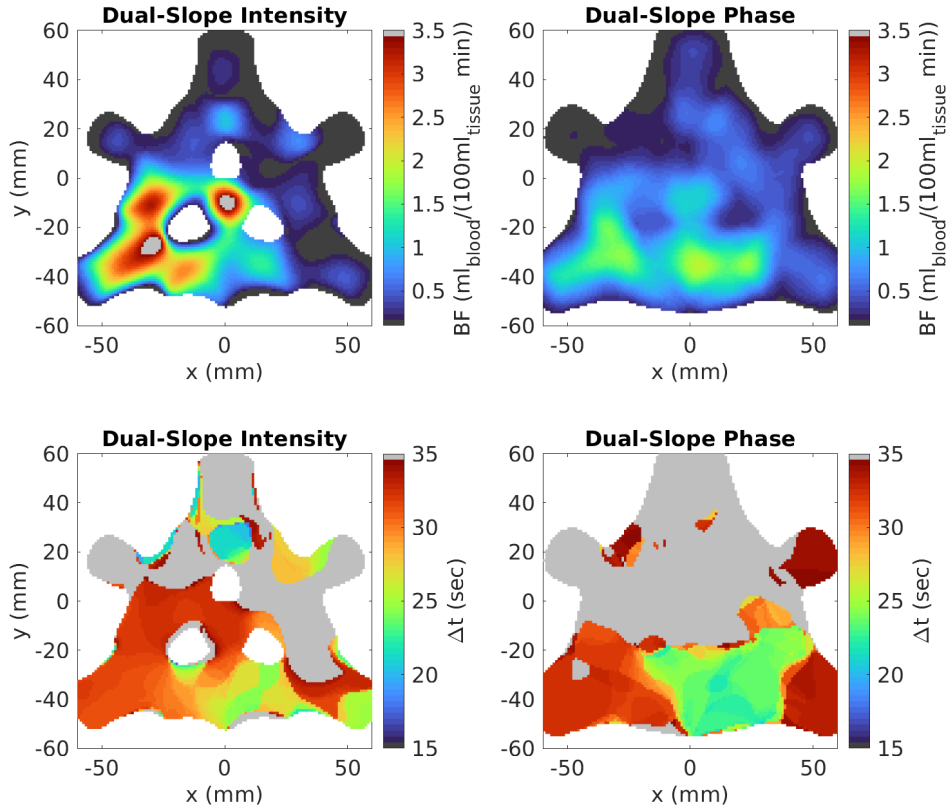


Figure 5.21: Maps of blood accumulation during a Venous Occlusion (VO) in Blood-Flow (BF) units and the delay until the accumulation maximum from the VO onset (Δt). Probe placement shown in Figure 5.19(i). Values are the average of three VOs.

Note 1: This figure can be found as Figure 3 in Blaney *et alia* (2021) [12].

protocol was conducted: 5 min baseline, 2 min VO, 2 min rest, 2 min VO, 2 min rest, 2 min VO, and 2 min baseline. We performed a total of 3 2 min long VOs, each achieved with a pneumatic thigh cuff wrapped around the subject's left thigh (same side as the array) and inflated to a pressure of 60 mmHg.

The array may be used in two modes:

- Self-Calibrating (SC) [61] for measurement of absolute optical properties.
- DS for measurement of $\Delta\mu_a$ with only DS I or DS ϕ .

To create a spatial map of the absolute μ_a and μ'_s the array was analysed in SC mode on the baseline data (averaged over time) with the iterative recovery methods in Appendix B. This resulted in a measurement of μ_a and μ'_s for each

of the $m = 27$ sets in the hexagonal array. To create a visual representation, the values were assigned to the spatial coordinate corresponding to the centroid of the optode sets they were derived from. Then a spatial map was created by interpolating the values between the points in two-dimensions. This resulted in an image of absolute μ_a and μ'_s beneath the array.

To use the array in DS mode, the DS derived $\Delta\mu_a$ was found for each time-point during the experiment using the methods in Appendix C. Then, a map of $\Delta\mu_a$ was reconstructed using methods previously described above via the MP and Equation 5.8 [4, 64]. The S of the array was calculated for two layers of voxels (one from $z = 0$ mm to 5 mm and the other for $z > 5$ mm). Then S was inverted on the vector of absorption coefficient changes ($\Delta\vec{\mu}_a$) DS data and the reconstructed image for the second layer presented.

From this method, an image of $\Delta\mu_a$ for 2 optical wavelengths (λs) was calculated for each time-point during the experiment. This was then converted to an image stack of Deoxy-hemoglobin concentration change (ΔD) and Oxy-hemoglobin concentration change (ΔO) using Appendix D.

During the VO, the maximum rate of blood accumulation (from a linear fit of Total-hemoglobin concentration change (ΔT)) was calculated for each voxel, as well as the time of this maximum rate (defined by the center of the linear fit where the rate is the slope of the fit). This was achieved by implementing a linear Savitzky–Golay filter with a support length equal to 10 s to each temporal vector in the image stack. Then the maximal slope (and its central time) of ΔT (from the Savitzky–Golay filter) for each VO was found and averaged across the three VOs. Finally, the maximal slope of ΔT was converted into the Blood-Flow (BF) units of $\text{mL}_{\text{blood}}/100 \text{ mL}_{\text{tissue}}/\text{min}$. This resulted in spatial maps of blood accumulation maximum (in units of BF) and delay time of the maximum (Δt from the VO onset) for both DS *I* and DS ϕ .

Figure 5.20 shows the results from the DS array in SC mode, which retrieved maps of absolute optical properties without the need for calibration. Then, Figure 5.21 presents the hemodynamic data derived from the array in DS mode. Dynamic data is the mean of all three VOs.

Examining the spatial maps (Figure 5.20) of absolute optical properties and comparing them to the placement of the array (Figure 5.19(i)), one can see some correspondence between values and anatomy. Specifically, the parts of the array measuring the *tibia* and tendons connecting to the knee ($y > 20 \text{ mm}$) exhibit higher values of scattering. Also, the portion of the array probing the largest part of the muscle ($y < -20 \text{ mm}$ and $x < 0 \text{ mm}$) shows higher values of absorption. This is consistent with the hypothesis that connective tissues exhibit higher scattering while muscle exhibits higher absorption. These results suggest the viability of this array in measuring spatial maps of absolute optical properties.

Next, the hemodynamic data (Figure 5.21) collected with the array can be evaluated. Note that the highest rate of blood accumulation occurred

in the part of the array where the largest part of the muscle was probed (Figure 5.19(i)). Additionally, the accumulation showed spatial variation in delay time. Both of these suggest that the hemodynamics during a VO may have high spatial variability. Interestingly, this spatial variation was consistent between the 3 repeated VOs (average shown). Aside from the spatial variation of hemodynamics, differences between DS *I* and DS ϕ may also provide information about the depth of these changes. Understanding these differences is still an area of active research. Regardless, this experiment showed the possibility of using this novel DS imaging array for hemodynamic measurements.

5.4.2.B Dual-Slope Imaging of Brain

In Blaney *et alia* (2022) [13] we demonstrated the ability of the DS method to measure brain activation during a visual stimulation protocol. The measured hemodynamic traces associated with visual stimulation exhibited a larger amplitude when they are derived from DS versus Single-Distance (SD) data, and from ϕ versus *I* data. In particular, the functional hemodynamics obtained from DS ϕ data feature the largest amplitude. These results indicate the greater sensitivity to brain tissue achieved by DS versus SD data, and by ϕ versus *I* data. The conclusion of this work is that DS *I* (in Continuous-Wave (CW) fNIRS) and DS or SD ϕ (in FD fNIRS) appear to be most effective for functional brain measurements, with the significant practical advantage offered by the minimal sensitivity of DS measurements to a variety of artifacts and preferential \mathcal{S} to deep tissue.

In this work the hexagonal DS array from the above sections was utilized. It realized $m = 30$ DS sets in this work, each made up of 4 SD sets,^c two short (approximately 25 mm) and two long (approximately 37 mm), see Figure 5.22[Left]. The Imagent was again utilized with the same operating parameters stated in Section 2.2.1.A, and a sampling frequency of 5 Hz. The array

^cDual-Slope (DS) sets may share Single-Distance (SD) sets so the number of SD sets is less than or equal to the number of DS sets times four, in general.

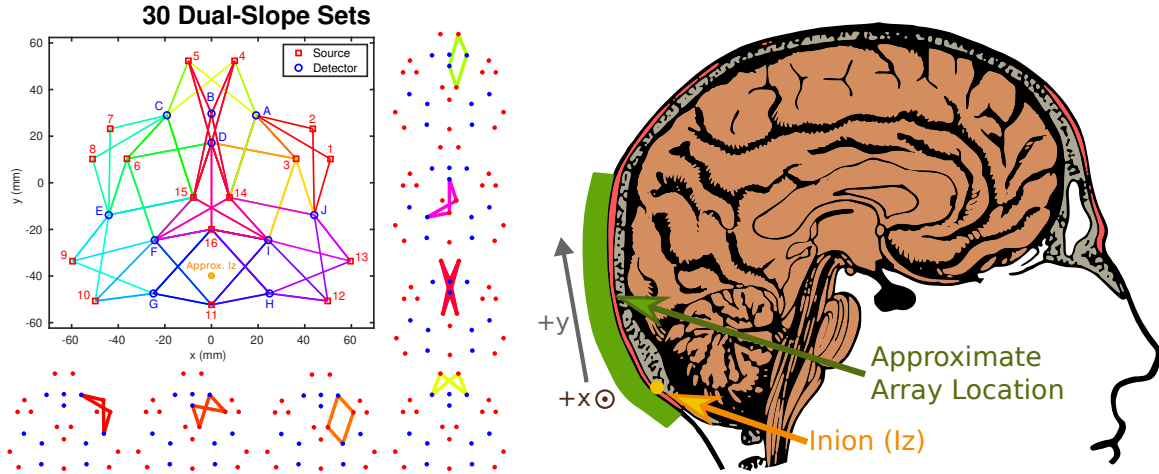


Figure 5.22: [Left] Schematic of Dual-Slope (DS) array, lines of different colors represent different DS sets. Seven examples of different types DS sets are shown around the right and bottom edge. Overall the array used short distances of approximately 25 mm and long distances of approximately 37 mm. [Right] Approximate array placement. The *inion* was placed between sources 11 and 16 such that the upper array was over the visual cortex.

Note 1: This figure can be found as Figure 1 in Blaney *et alia* (2022) [13].

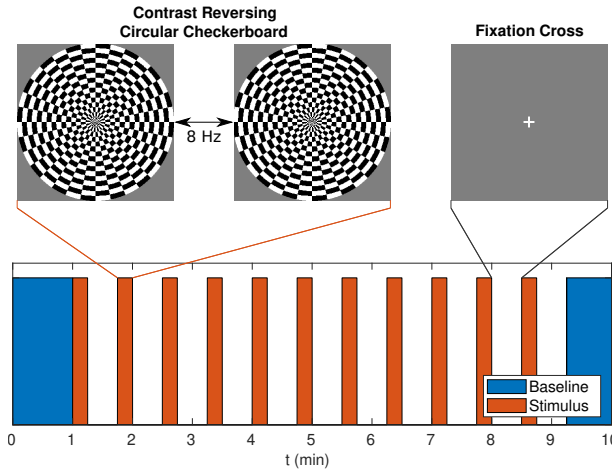


Figure 5.23: Organization of visual stimulation protocol and examples of contrast reversing circular checkerboards plus fixation cross.

Note 1: This figure can be found as Figure 2 in Blaney *et alia* (2022) [13].

was placed over on the back of the subject's head such that the top of the array was over the visual cortex (Figure 5.22[Right]).

The visual stimulation was conducted in accordance with the Tufts University IRB. It con-

sisted of a 1 min of baseline, followed by the experimental period. Then the experimental period contained 11 stimulus periods each consisting of 15 s of a 8 Hz contrast reversing circular checkerboard and 30 s of rest. The experiment ended with a 45 s baseline for a total time of 10 min. Figure 5.23 shows the organization of the protocol as well as the visual stimuli presented to the subject. Data from one such experiment session and one subject is presented was presented in Blaney *et alia* (2022) [13].

For an absolute measurement, the array was again used in SC mode on the averaged baseline data using the iterative recovery method in Appendix B. Absolute optical properties were found and the complex effective path-lengths calculated [58], which were required to calculate the Differential Path-length Factors (DPFs) and DSFs for the relative measurement [3] as described in Appendix C. For image reconstruction \mathcal{S} was calculated using Appendix E and inverted with the MP and Equation 5.8.

For a relative measurement, ΔO and ΔD traces were calculated for each SD and DS set from $\Delta \mu_a$ per the methods in Appendix D. The signals were low-pass filtered to 0.5 Hz and fold-

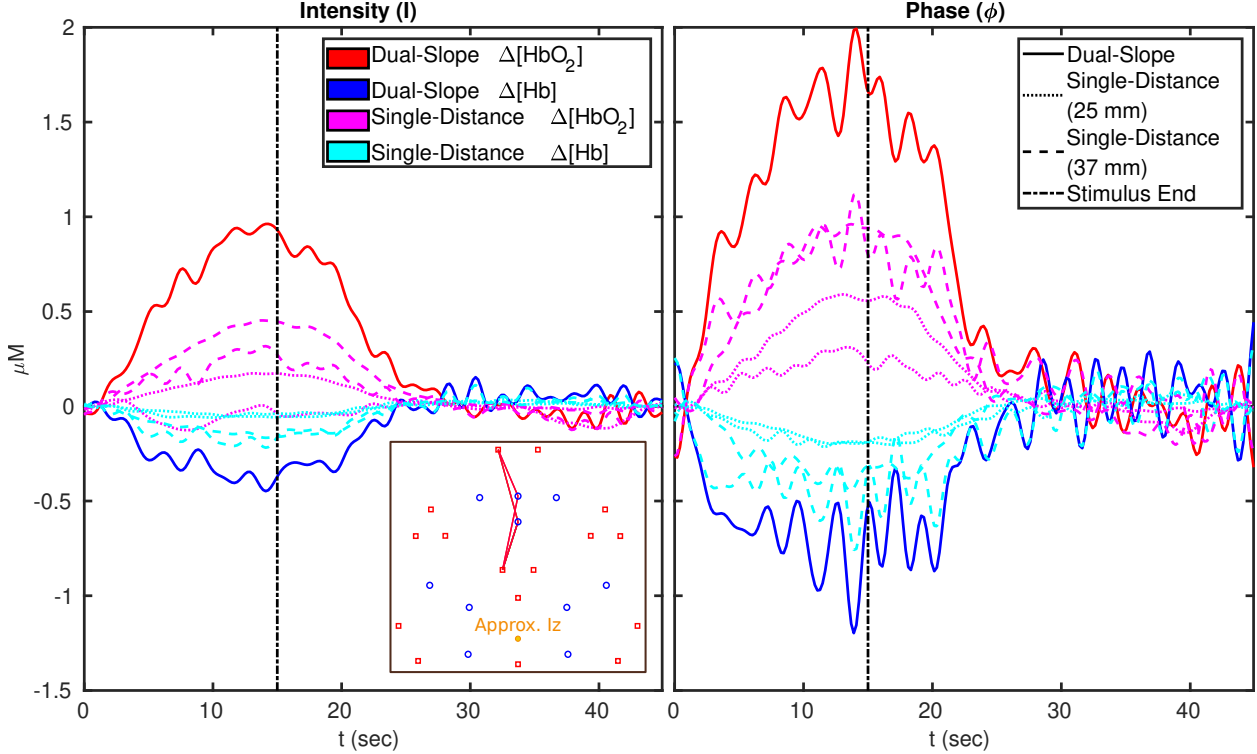


Figure 5.24: Temporal traces of hemodynamics during the visual stimulation protocol. The Intensity (I) data is in the left subplot while the phase (ϕ) is in the right. Dual-Slope (DS) data is shown in solid red or blue lines for Oxy-hemoglobin concentration change (ΔO) and Deoxy-hemoglobin concentration change (ΔD), respectively. Short Single-Distance (SD) traces are dotted while long SD are dashed with colors of magenta and cyan for ΔO and ΔD , respectively. These traces were low-pass filtered to 0.5 Hz and folding averaged over the 11 stimulus periods. The baseline optical properties for this set were measured as 0.011 & 0.010 mm⁻¹ for the absorption coefficient (μ_a) and 0.98 & 0.83 mm⁻¹ for the reduced scattering coefficient (μ'_s) at 690 & 830 nm, respectively.

Note 1: This figure can be found as Figure 4 in Blaney *et alia* (2022) [13].

ing averaged across the 11 activation periods.^d An example DS set for these data was chosen and is presented to compare SD and DS during visual stimulation.

Figure 5.24 shows the filtered and folding averaged DS & SD hemodynamic data for the visual stimulation protocol. The presented set was above the left *occipital* lobe (Figure 5.22). The figure shows both I and ϕ data on the left and right, respectively, with the plots being on the same scale. DS traces are presented in solid red or blue for ΔO and ΔD , respectively. Mean-

while, short SD traces are dotted while long SDs are dashed with colors of magenta and cyan for ΔO and ΔD , respectively.

The characteristic brain activation signal is an increase in ΔO and a decrease in ΔD which is indicative of a increase in BF [32]. In all measurement types, including SD short, ϕ data exhibited this characteristic brain activation behavior while the same is not true for I . Additionally, DS data-types always showed a larger amplitude response compared to SD. Furthermore, comparing each ϕ trace to its corresponding I trace it can be seen that amplitude of the change in ΔO or ΔD was always larger for ϕ . This is most striking when examining the short SDs. For I one of the short SD ΔOs does not increase while

^dDuring the folding average the data were de-trended so that the first and last 2s of data have averaged of zero to remove slow drifts expected to be present in Single-Distance (SD).

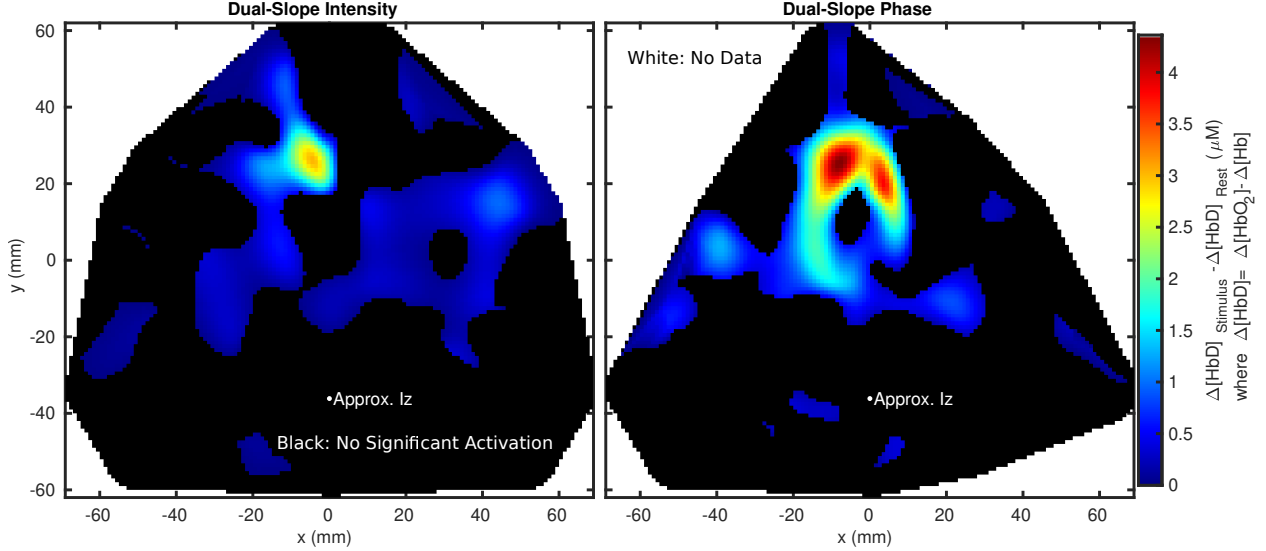


Figure 5.25: Map of hemoglobin difference increase during stimulation, masked by activation significance. Higher values show larger activation amplitude, black shows not significant activation, and white shows no data.

Note 1: This figure was presented in Blaney *et alia* (2022) [13] as part of the talk.

corresponding trace for ϕ does increase, where it is worth pointing out that the physical optodes are the same in this situation and the difference is just from the different data-type. The same is true for ΔD , where the short SDs do not change significantly for I but do have a noticeable decrease for ϕ .

Finally, Figure 5.25 shows the first example of DS imaging on the human brain during a fNIRS protocol. For this activation protocol it is expected that the visual cortex will show a BF increase and thus activation in the image. Given the placement of the array the visual cortex was under the upper port of the array. Therefore the DS activation image in Figure 5.25 is consistent with the expectation since it shows large activation amplitude in the upper center portion of the array. Furthermore, DS ϕ has a larger activation contrast compared to DS I which is consistent with the hypothesis that ϕ data is more brain specific. These results are bolstered by the fact that no significant change in heart rate was observed, thus the change due to visual stimulation should really have been brain specific and not systemic.

Overall, the results herein suggest that DS or ϕ

data exhibit higher amplitude activation than SD or I , respectively, for both ΔO and ΔD . Further, these preliminary traces suggest that if these DS array data were applied to imaging DS and ϕ data derived images would exhibit higher contrast compared to SD and I , respectively. This is consistent with DS's expected preferentially deep sensitivity shown in Chapter 3, which has been observed during systemic blood pressure oscillations [3] and while imaging perturbations within a phantom [4].

Listings

Listing 5.1: MATLAB code for Single-Distance (SD) set discovery (Figure 5.1)

```

1 function armt=findSDsets(armt, arry)
2 %armt=findSDsets(armt, arry)
3 % Giles Blaney
4 % Inputs:
5 %   armt – Struct with the following fields:
6 %     – rSrc: n_src X 3 array of source coordinates:
7 %       [x, y, z;...]
8 %     – rDet: n_det X 3 array of detector coordinates:
9 %       [x, y, z;...]
10 %   arry – Struct with the following fields:
11 %     – rRng: 1 X 2 array defining single-distance distance range:
12 %       [rho_min, rho_max]
13 % Outputs:
14 %   armt – Same as input armt struct with the following added fields:
15 %     – SDprs: n_SDprs X 2 array of single distance pairs:
16 %       [sInd1, dInd1;...
17 %        sInd2, dInd2; ...
18 %        ... ;sIndn, dIndn]
19
20 armt.SDprs=[];
21 r_all=NaN(size(armt.rSrc, 1), size(armt.rDet, 1));
22
23 for sInd=1:size(armt.rSrc, 1)
24     for dInd=1:size(armt.rDet, 1)
25         % Check distance range
26         % requirement (arry.rRng)
27         r=norm(armt.rSrc(sInd, :)-armt.rDet(dInd, :));
28         r_all(sInd, dInd)=r;
29
30         if r<arry.rRng(1) || r>arry.rRng(2)
31             continue;
32         end
33
34         armt.SDprs(end+1, :)=[sInd, dInd];
35     end
36 end
37 end

```

Acronyms: MathWorks MATrix LABoratory [Natick, MA USA] (MATLAB).

Available at:

<https://github.com/DOIT-Lab/DOIT-Public/tree/master/Dissertations/GilesBlaney2022/code>

Listing 5.2: MATLAB code for Single-Slope (SS) set discovery (Figure 5.2)

```

1 function armt=findSSsets(armt, arry)
2 %armt=findSSsets(armt, arry)
3 % Giles Blaney
4 % Inputs:
5 %   armt – Struct with the following fields:
6 %     – rSrc: n_src X 3 array of source coordinates:
7 %       [x, y, z;...]

```

```

8      %           — rDet: n_det X 3 array of detector coordinates:
9      %           [x, y, z;...]
10     %           — SDprs: n_SDprs X 2 array of single distance pairs:
11     %           [sInd1, dInd1;...
12     %           sInd2, dInd2; ...
13     %           ... ;sIndn, dIndn]
14     % arry — Struct with the following fields:
15     %           — lRng: 1 X 2 array defining SS distance difference range:
16     %           [DELTArho_min, DELTArho_max]
17     % Outputs:
18     % armt — Same as input armt struct with the following added fields:
19     %           — SSprs: 2 X 2 X n_SSprs array of single slope pairs:
20     %           SSprs(:, :, n_SSprs)=...
21     %           [sInd1, dInd1;...
22     %           sInd2, dInd2]
23
24     armt.SSprs=[];
25     n=0;
26     for sd1Ind=1:size(armt.SDprs, 1)
27         for sd2Ind=1:size(armt.SDprs, 1)
28             if sd1Ind>=sd2Ind
29                 continue;
30             end
31
32             s1Ind=armt.SDprs(sd1Ind, 1);
33             d1Ind=armt.SDprs(sd1Ind, 2);
34             s2Ind=armt.SDprs(sd2Ind, 1);
35             d2Ind=armt.SDprs(sd2Ind, 2);
36
37             if xor(s1Ind==s2Ind, d1Ind==d2Ind)
38                 r1=norm(armt.rSrc(s1Ind, :) - armt.rDet(d1Ind, :));
39                 r2=norm(armt.rSrc(s2Ind, :) - armt.rDet(d2Ind, :));
40
41                 % Check lever arm
42                 % requirement (arry.lRng)
43                 if r1~ =r2 && and(abs(r1-r2)>=arry.lRng(1),...
44                     abs(r1-r2)<=arry.lRng(2))
45
46                     n=n+1;
47
48                     if r1<r2
49                         armt.SSprs(:, :, n)=[s1Ind, d1Ind; s2Ind, d2Ind];
50                     elseif r2<r1
51                         armt.SSprs(:, :, n)=[s2Ind, d2Ind; s1Ind, d1Ind];
52                     end
53                 end
54             end
55         end
56     end
57 end

```

Acronyms: MathWorks MATrix LABoratory [Natick, MA USA] (MATLAB).

Available at:

<https://github.com/DOIT-Lab/DOIT-Public/tree/master/Dissertations/GilesBlaney2022/code>

Listing 5.3: MATLAB code for Dual-Slope (DS) set discovery (Figure 5.3)

```

1  function armt=findDSsets(armt, arry)
2  %armt=findSSsets(armt, arry)
3  % Giles Blaney
4  % Inputs:
5  %   armt – Struct with the following fields:
6  %       – rSrc: n_src X 3 array of source coordinates:
7  %           [x, y, z;...]
8  %       – rDet: n_det X 3 array of detector coordinates:
9  %           [x, y, z;...]
10 %       – SSprs: 2 X 2 X n_SSprs array of single slope pairs:
11 %           SSprs(:, :, n_SSprs)=...
12 %               [sInd1, dInd1;...
13 %                   sInd2, dInd2]
14 %   arry – Struct with the following fields:
15 %       – lTol: Double defining differnece between single-slopes
16 %           distance difference tolerance
17 % Outputs:
18 %   armt – Same as input armt struct with the following added fields:
19 %       – DSprs: 2 X 2 X 2 X n_DSprs array of dual slope pairs:
20 %           SSprs(:, :, 1, n)=...
21 %               [sInd11, dInd11;...
22 %                   sInd12, dInd12]
23 %           SSprs(:, :, 2, n)=...
24 %               [sInd21, dInd21;...
25 %                   sInd22, dInd22]
26
27 armt.DSprs=[];
28 sdAllHist={};
29 n=0;
30
31 for ss1Ind=1:size(armt.SSprs, 3)
32     for ss2Ind=1:size(armt.SSprs, 3)
33         if ss1Ind>=ss2Ind
34             continue;
35         end
36
37         s11Ind=armt.SSprs(1, 1, ss1Ind);
38         d11Ind=armt.SSprs(1, 2, ss1Ind);
39         s21Ind=armt.SSprs(1, 1, ss2Ind);
40         d21Ind=armt.SSprs(1, 2, ss2Ind);
41         s12Ind=armt.SSprs(2, 1, ss1Ind);
42         d12Ind=armt.SSprs(2, 2, ss1Ind);
43         s22Ind=armt.SSprs(2, 1, ss2Ind);
44         d22Ind=armt.SSprs(2, 2, ss2Ind);
45
46         if length(unique([s11Ind, s21Ind, s12Ind, s22Ind]))==2 &&...
47             length(unique([d11Ind, d21Ind, d12Ind, d22Ind]))==2
48
49             sd11=[s11Ind, d11Ind];
50             sd21=[s21Ind, d21Ind];
51             sd12=[s12Ind, d12Ind];
52             sd22=[s22Ind, d22Ind];
53

```

```

54     sdAll=[sd11; sd21; sd12; sd22];
55
56     if sum(size(sdAll)==size(unique(sdAll, 'rows')))==2
57
58         r11=norm(armt.rSrc(s11Ind, :)-armt.rDet(d11Ind, :));
59         r21=norm(armt.rSrc(s21Ind, :)-armt.rDet(d21Ind, :));
60         r12=norm(armt.rSrc(s12Ind, :)-armt.rDet(d12Ind, :));
61         r22=norm(armt.rSrc(s22Ind, :)-armt.rDet(d22Ind, :));
62
63         %Order of slope 1
64         [~, ord1]=sort([r11, r12]);
65         %Order of slope 2
66         [~, ord2]=sort([r21, r22]);
67
68         s1Inds=[s11Ind, s12Ind];
69         %Ordered slope 1 sources
70         s1Inds=s1Inds(ord1);
71         s2Inds=[s21Ind, s22Ind];
72         %Ordered slope 2 sources
73         s2Inds=s2Inds(ord2);
74
75         d1Inds=[d11Ind, d12Ind];
76         %Ordered slope 1 detectors
77         d1Inds=d1Inds(ord1);
78         d2Inds=[d21Ind, d22Ind];
79         %Ordered slope 2 detectors
80         d2Inds=d2Inds(ord2);
81
82         if sum([s1Inds==s2Inds, d1Inds==d2Inds])>0
83             continue;
84         end
85
86         if abs(abs(r12-r11)-abs(r22-r21))<=arry.lTol
87
88             newSet=true;
89             for i=1:length(sdAllHist)
90                 if size(unique(...
91                     [sdAllHist{i}; sdAll], 'rows'))<=4
92
93                     newSet=false;
94                     break;
95                 end
96             end
97
98             if newSet
99                 n=n+1;
100                sdAllHist{n}=sdAll;
101
102                armt.DSprs(:, :, 1, n)=...
103                    armt.SSprs(:, :, ss1Ind);
104                armt.DSprs(:, :, 2, n)=...
105                    armt.SSprs(:, :, ss2Ind);
106            end
107        end

```

```

108      end
109    end
110  end
111 end
112 end

```

Acronyms: MathWorks MATrix LABoratory [Natick, MA USA] (MATLAB).

Available at:

<https://github.com/DOIT-Lab/DOIT-Public/tree/master/Dissertations/GilesBlaney2022/code>

Listing 5.4: MATLAB code for calculating resolution matrix (Γ) and localization matrix (Δ)

```

1 function [Gamma_grid, Delta_grid]=
2   GammaDelta(SpS, sz_grid, dr)
3 %armt=findSSsets(armt, arry)
4 % Giles Blaney
5 % Inputs:
6 % SpS      - n X n array of pinv(S)*S
7 % sz_grid - 1 X 3 array with size of grid coordinate system:
8 %           [n_y, n_x, n_z]
9 % dr       - 1 X 3 array with gird spacing:
10 %           [dy, dx, dz]
11 % Outputs:
12 % Gamma_grid - sz_grid X 3 array of full-width half-max resolutions in
13 %               all axis directions
14 % Delta_grid - sz_grid X 3 array of localization errors in all axis
15 %               directions
16
17 initVar=NaN([sz_grid, 3]);
18 Gamma_grid=initVar;
19 Delta_grid=initVar;
20 clear initVar;
21
22 for i=1:3
23   yesInd=i+3;
24   noInds=4:6;
25   noInds(noInds==yesInd)=[];
26
27   switch i
28     case 1
29       [~, R, ~]=...
30         meshgrid(1:sz_grid(1), 1:sz_grid(2), 1:sz_grid(3));
31     case 2
32       [R, ~, ~]=...
33         meshgrid(1:sz_grid(1), 1:sz_grid(2), 1:sz_grid(3));
34     case 3
35       [~, ~, R]=...
36         meshgrid(1:sz_grid(1), 1:sz_grid(2), 1:sz_grid(3));
37     otherwise
38       R=[];
39   end
40
41 Xm_grid=sum(sum(reshape(SpS, [sz_grid, sz_grid]), ...
42   noInds(1)), noInds(2));
43

```

```
44     Gamma_grid(:, :, :, i)=...
45         sum(Xm_grid>=(max(Xm_grid, [], yesInd)/2), yesInd)*dr(i);
46
47     [~, maxInds]=max(Xm_grid, [], yesInd);
48     Delta_grid(:, :, :, i)=(maxInds-R)*dr(i);
49
50 end
51 end
```

Acronyms: MathWorks MATrix LABoratory [Natick, MA USA] (MATLAB).

Available at:

<https://github.com/DOIT-Lab/DOIT-Public/tree/master/Dissertations/GilesBlaney2022/code>

Part II

Cerebral Hemodynamics

Chapter 6

Introduction to Wavelet Coherent Hemodynamics Spectroscopy

6.1 Hemodynamic Oscillations

Measurements of hemodynamic oscillations using Near-InfraRed Spectroscopy (NIRS) have been relevant for studying both diseased and healthy human brain. The oscillations in Oxy-hemoglobin (O) and Deoxy-hemoglobin (D) concentrations and their corresponding phase and amplitude relationships, either between themselves or with respect to oscillatory physiological quantities such as Arterial Blood Pressure (ABP), have been investigated for both spontaneous and induced oscillations[43].

Spontaneous cerebral hemodynamic oscillations (in the broad frequency range 0.01 Hz to 1 Hz) occur naturally within the human body and can have a wide range of sources, both from systemic contributions of cardiovascular dynamics (*exempli gratia*, from heart rate, ABP) and from local effects of metabolic and flow regulations (*exempli gratia*, local vascular reactivity, focal metabolism)[70]. NIRS studies of spontaneous oscillations of Oxy-hemoglobin concentration change (ΔO) and Deoxy-hemoglobin concentration change (ΔD) have been conducted in infants[71, 72] and adult[73, 74] human subjects. Besides spontaneous oscillations, cerebral hemodynamics can be induced by several protocols based on systemic perturbations in the ABP. These protocols include paced breathing[45][75], cyclic inflation and deflation of pneumatic thigh cuffs[76], periodic head-up-tilting[46], and repeated squat-stand[77] or sit-stand maneuvers[78]. Even without a physiolog-

ical model that provides a quantitative description of oscillations of ΔO and ΔD or their associated Oxy-hemoglobin phasor (\tilde{O}) and Deoxy-hemoglobin phasor (\tilde{D}), their relative amplitude and phase have already been correlated to healthy or diseased conditions of cerebral tissue and brain perfusion. For example, a study conducted on patients with unilateral carotid obstruction in a paced breathing protocol at 0.1 Hz found that the phase difference between \tilde{O} and \tilde{D} is larger in the *contralateral* hemisphere (the healthy one) compared to the *ipsilateral* hemisphere (the affected one) and to healthy controls. The authors associated this result with impaired cerebral Auto-Regulation (AR) in the affected side of the brain[74]. Spontaneous hemodynamic oscillations are more appealing for diagnostic purposes because they are readily available in all subjects, do not require subjective cooperation (*exempli gratia* paced breathing) or forcing maneuvers (*exempli gratia* cyclic thigh cuff occlusion and release) which may not be appropriate for some diseased individuals. However, in order to draw meaningful conclusions from any hemodynamic oscillations study, stable phase and amplitude relationships between the measured oscillating quantities are required. A preliminary study that investigated both spontaneous and induced hemodynamic oscillations in the frontal area of human subjects concluded that induced oscillations are coherent with higher incidence and are characterized by more stable phase relationship between \tilde{O} and \tilde{D} as compared to spontaneous oscillations[79].

One method that we have introduced for studying hemodynamic oscillations is **Coherent Hemodynamics Spectroscopy (CHS)**. It differs from other methods of using hemodynamic oscillations for medical diagnostic in two aspects:

- A spectrum of hemodynamic oscillations at different frequencies are investigated in order to measure the frequency-resolved phase and amplitude relationship between \tilde{O} and \tilde{D} by considering phasor ratio vector between Deoxy-hemoglobin and Oxy-hemoglobin (\tilde{D}/\tilde{O}).
- A dedicated mathematical model is used to translate these phase and amplitude relationships into physiological parameters useful for monitoring micro-vascular integrity, such as capillary and venous transit times and a parameter related to the effectiveness of cerebral AR.

We have demonstrated the potential of CHS in several studies, both in healthy controls[80] and a diseased population[81]. We have also used CHS for estimating the transfer function between ABP and Total-hemoglobin (T) to assess cerebral AR[82].

One well known issue that needs to be addressed in non-invasive cerebral NIRS is the high sensitivity of optical signals to hemodynamics occurring in the superficial, extracerebral tissue layers (mainly scalp and skull) as discussed in Part I. In the case of CHS, we need to consider the problem of extracerebral contamination. However, this problem is somewhat different than in the case of brain activation, since the driving force of hemodynamic oscillations is not a brain stimulus, but rather a systemic perturbation in ABP. Therefore, a high level of correlation between NIRS measurements at different source-detector distances (ρ_s) is expected. In functional Near-Infrared Spectroscopy (fNIRS) studies of brain activation, it is possible to observe task-related hemodynamic oscillations in the superficial tissue layers, which may be highly correlated with brain hemodynamics[83]. However, the source of extracerebral contamination is likely to be different than in CHS. For exam-

ple, in an fNIRS study[84], the authors found that the extracerebral contamination was mainly observed in ΔO , as a result of task-evoked sympathetic arterial vasoconstriction followed by a decrease in venous volume in the scalp. Since CHS is reliant on more systemic changes in hemodynamics, methods that localize the entire recovered signal or the Sensitivity to absorption change (S) are desirable. For this reason the preferentially deep methods based on optics itself such as Multi-Distance (MD) and Dual-Slope (DS) in Part I are well tailored to CHS.

6.2 Determination of Hemodynamic Phasors with Wavelet

A key aspect of Coherent Hemodynamics Spectroscopy (CHS) is the measurement of Oxy-hemoglobin phasor (\tilde{O}), Deoxy-hemoglobin phasor (\tilde{D}), and Arterial blood pressure phasor (\tilde{A}). Simply these phasor measurements are not sufficient, as the measurements must also be representative of true hemodynamics and exhibit stable amplitudes and phase. This leads us to the etymology of CHS, where *coherent* is referring to the reliability and stability of the phasors, and hemodynamics spectroscopy refers to the measurement of these phasors of *hemodynamic* qualities at various oscillation frequencies to make a *spectrum*.

CHS can be done with various measures of coherence and signal analysis[85]. After considering various methods we have settled on a wavelet based approach. This approach uses wavelet Coherence (C) as the measure of coherence and wavelet coefficients as the measure of phasors which are time and frequency resolved. The specifics of wavelet phasor analysis is in Appendix G and of coherence is in Appendix H. To determine if the C is significantly high we generate thresholds from random surrogate data[6, 85]. The generation of these thresholds is discussed in detail in Blaney *et alia* Biomedical Signal Processing and Control (2020) [6] and Chapter 7.

The phasors themselves are not easily interpreted, thus we focus on phasor ratio vec-

tors (Appendix G). Additionally, \mathfrak{C} requires a statement comparing two signals (Appendix H). Therefore, for every pair of phasors there is an associated vector representing their transfer function and a \mathfrak{C} value. In CHS the individual signals considered are of Oxy-hemoglobin concentration change (ΔO), Deoxy-hemoglobin concentration change (ΔD), Total-hemoglobin concentration change (ΔT), and Arterial blood pressure change (ΔA). The phasor ratio vector between Deoxy-hemoglobin and Oxy-hemoglobin ($\overrightarrow{D/O}$) and phasor ratio vector between Total-hemoglobin and Arterial blood pressure phasor ($\overrightarrow{T/A}$), as well as the Coherence between Oxy-hemoglobin and Arterial blood pressure phasor ($\mathfrak{c}(\overrightarrow{O}, \overrightarrow{A})$), Coherence between Deoxy-hemoglobin and Arterial blood pressure phasor ($\mathfrak{c}(\overrightarrow{D}, \overrightarrow{A})$), and Coherence between Total-hemoglobin and Arterial blood pressure phasor ($\mathfrak{c}(\overrightarrow{T}, \overrightarrow{A})$) also find particular relevance. For $\overrightarrow{T/A}$ to be considered coherent, $\mathfrak{c}(\overrightarrow{T}, \overrightarrow{A})$ must be above the significance threshold; and for $\overrightarrow{D/O}$ to be significant both $\mathfrak{c}(\overrightarrow{O}, \overrightarrow{A})$ and $\mathfrak{c}(\overrightarrow{D}, \overrightarrow{A})$ must be above threshold (Chapter 7). This comes from the assumption that Arterial Blood Pressure (ABP) is the chief driver in these hemodynamic oscillations.

6.3 Meanings of Select Phasors and Vectors

In the previous section, the phasor ratio vector between Deoxy-hemoglobin and Oxy-hemoglobin ($\overrightarrow{D/O}$) and phasor ratio vector between Total-hemoglobin and Arterial blood pressure phasor ($\overrightarrow{T/A}$) are introduced as relevant vectors for analysis. To understand why this is we shall look at their physiological meaning. First, we should introduce the concepts of Blood-Volume (BV) and Blood-Flow (BF) oscillations with corresponding blood Volume unit phasor (\hat{V}) and blood Flow unit phasor (\hat{F}). Total-hemoglobin concentration change (ΔT) is considered a surrogate for BV change and Oxy-hemoglobin minus Deoxy-hemoglobin concentration change (ΔD) and surrogate for BF change. Therefore, Total-hemoglobin phasor (\tilde{T}) is modeled as along the \hat{V} direction and Oxy-hemoglobin phasor (\tilde{O}) and

Deoxy-hemoglobin phasor (\tilde{D}) components associated with BF (which is designated with the V subscript) are along the same direction and add to \tilde{T} . Additionally, the \tilde{O} and \tilde{D} components associated with BF (which is designated with the F subscript) as modeled with a 180° phase difference. Finally, the \hat{F} is expected to have a parameter dependent phase difference between it and \tilde{O}_F . This phase correction for \hat{F} is in-fact one of the chief differences between Coherent Hemodynamics Spectroscopy (CHS) and previous work which considered ΔD as BF, as CHS temporally corrects ΔD to more directly measure BF[43, 86].

Figure 6.1(a) shows all of the aforementioned phasor relationships and connects them to the measured phasors \tilde{O} , \tilde{D} , \tilde{T} , and Arterial blood pressure phasor (\tilde{A}) for an example at 0.1 Hz[80]. Key phasor relationships follow:

$$\tilde{T} = \tilde{O} + \tilde{D} = \tilde{O}_V + \tilde{D}_V \quad (6.1)$$

$$\tilde{O} = \tilde{O}_V + \tilde{O}_F \quad (6.2)$$

$$\tilde{D} = \tilde{D}_V + \tilde{D}_F \quad (6.3)$$

$$\tilde{O}_F = -\tilde{D}_F \quad (6.4)$$

The CHS hemodynamic model[79] allows us to find physiological interpretations for all of these relations. The measurable \tilde{O} and \tilde{D} are decomposed into contributions from blood volume and BF and BV (here, we neglect oscillations in the metabolic rate of oxygen). \tilde{O}_V and \tilde{D}_V are in phase with each other and with \tilde{T} and \hat{V} as mentioned above. The relative amplitude of \tilde{O}_V and \tilde{D}_V is determined by the oxygen saturation of the volume-oscillating vascular compartment which is assumed to be 75 %[87]. As described, \tilde{O}_F and \tilde{D}_F are in opposition of phase and have the same magnitude. \tilde{O}_F lags \hat{F} as a result of the blood transit time in the microvasculature[43], here this was assumed to be 40° as computed with our model using typical values for the blood transit times and other model parameters. Finally, BF

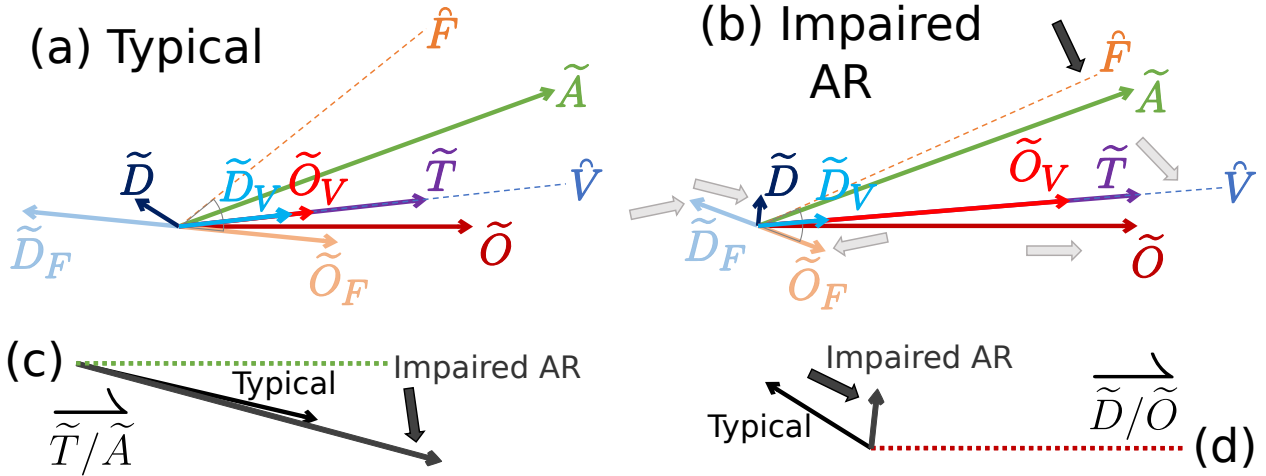


Figure 6.1: Example Coherent Hemodynamics Spectroscopy (CHS) phasor relationships at 0.1 Hz. (a) A typical case. (b) Result from taking the typical case and impairing Auto-Regulation (AR) by reducing phase between Blood-Flow (BF) and Arterial Blood Pressure (ABP) (dark gray arrow) with all knock on effects (light gray arrows). (c) Resulting phasor ratio vector between Total-hemoglobin and Arterial blood pressure phasor (\tilde{T}/\tilde{A}) that would be measured in both cases, impairing AR created a slightly more negative phase difference. (d) Resulting phasor ratio vector between Deoxy-hemoglobin and Oxy-hemoglobin (\tilde{D}/\tilde{O}) that would be measured in both cases, impairing AR created a strongly more negative phase difference.

Note 1: A version of this diagram was presented in Blaney *et alia* (2019) [10] and Khaksari *et alia* Journal of Biomedical Optics (2018) [1].

Acronyms and Symbols: Auto-Regulation (AR); blood Flow (F subscript); blood Volume (V subscript); blood Flow unit phasor (\hat{F}); blood Volume unit phasor (\hat{V}); Arterial blood pressure phasor (\tilde{A}); Total-hemoglobin phasor (\tilde{T}); Oxy-hemoglobin phasor (\tilde{O}); Deoxy-hemoglobin phasor (\tilde{D}); phasor ratio vector between Total-hemoglobin and Arterial blood pressure phasor (\tilde{T}/\tilde{A}); and phasor ratio vector between Deoxy-hemoglobin and Oxy-hemoglobin (\tilde{D}/\tilde{O}).

oscillations lead the \tilde{A} in the presence of Auto-Regulation (AR), with a greater lead phase for more effective AR, and they are in phase with the \tilde{A} in the absence of AR. This is key to interpreting these phasor relations, since simply by changing the phase difference between \hat{F} and \tilde{A} all of the measured phasors also change. This model allows for interpretation of such a change in AR.

Figure 6.1(b) simulates a impaired AR compared to Figure 6.1(a) by moving \hat{F} closer to \tilde{A} . We have kept the amplitude of \tilde{O} , the phase of \tilde{T} (*id est* the phase of \hat{V}), and the phase angle between \hat{F} and \tilde{O}_F (which reflects the blood transit time in the microvasculature) constant.

Figure 6.1(c)(d) also shows the \tilde{D}/\tilde{O} and \tilde{T}/\tilde{A} (at 0.1 Hz in this case) which is the actual output of Coherence (\mathcal{C}) threshold a wavelet CHS

analysis. The key is how these vectors change with impaired AR, which can be used as an interpretation of measured CHS results. First, focusing on \tilde{D}/\tilde{O} , when AR was impaired the phase became strongly more negative and the amplitude ratio decreased. For \tilde{T}/\tilde{A} the impaired AR caused a weakly more negative phase and an increase in amplitude. This tells us that if we see these effects in measured data they can be interpreted as AR impairment. Additionally, this indicates that the strongest measure of AR is the phase of \tilde{D}/\tilde{O} . Further chapters present such data *in vivo* and provide physiological interpretation motivated by these models.

Chapter 7

Test for Significant Coherence

7.1 Applications for a Significant Coherence Test

In Blaney *et alia* Biomedical Signal Processing and Control (2020) [6] we developed a method to determine whether or not a given pair of signals exhibits significant **Coherence (\mathfrak{C})**. A quantitative assessment of the level of \mathfrak{C} between two signals is important in many applications. Two biomedically relevant cases are Transfer-Function Analysis (TFA) [77] of cerebral Auto-Regulation (AR) and Coherent Hemodynamics Spectroscopy (CHS) [43] (Chapter 6), where the first signal is Arterial Blood Pressure (ABP) and the second signal is either cerebral Blood-Flow (BF) velocity in the middle cerebral artery (with trans-cranial Doppler ultrasound) or Oxy-hemoglobin concentration change (ΔO) and Deoxy-hemoglobin concentration change (ΔD), in the cases of TFA and CHS, respectively. To determine the time intervals and frequency bands in which the signals are significantly coherent, a \mathfrak{C} threshold is required.

In **TFA** of **AR**, one describes **AR** in terms of a high-pass transfer function between **ABP** and **BF** velocity [88]. In **CHS**, one measures cerebral hemodynamics (typically the cerebral ΔO and ΔD with Near-InfraRed Spectroscopy (NIRS)) that are coherent with a specific physiological signal, most commonly **Arterial blood pressure change (ΔA)** [44, 85]. The goal of **CHS** is to translate cerebral **NIRS** measurements into physiologically relevant information on cerebral perfusion, including **AR** [1, 80] and cerebral **BF** [86].

Methods based on **TFA** rely on a high level of \mathfrak{C} between signals considered as input and output of a linear system. A high \mathfrak{C} between in-

put and output signals supports the assumption of a linear, uni-variate relationship between input and output signals. However, the question of how can one efficiently determine a threshold value of significant \mathfrak{C} for the specific signals and experimental conditions of a given measurement protocol is still open.

This key requirement of determining of time intervals and frequency bands that feature significant \mathfrak{C} between the measured signals is just as important for **CHS** as for **TFA**. In **CHS** the key signals are ΔO , ΔD , Total-hemoglobin concentration change (ΔT), and ΔA [85]. A difficulty arises in considering multiple coherence functions when additional physiological effects beyond **ABP** must be taken into account [89]. An additional difficulty of **CHS**, and of any time-varying process, are non-stationary conditions, for which the identification of short-lived the coherent periods require a time resolved signal processing technique. Therefore, accounting for this non-stationary nature and to determine time periods and frequency bands of significant \mathfrak{C} , a \mathfrak{C} threshold must be found for each time-frequency point.

7.2 The Coherence Threshold Time-Frequency Map

The work in Blaney *et alia* Biomedical Signal Processing and Control (2020) [6] focused on an algorithm for the determination of this **Coherence (\mathfrak{C})** threshold for use in non-stationary Transfer-Function Analysis (TFA), Coherent Hemodynamics Spectroscopy (CHS), and similar

techniques. This threshold of significant \mathfrak{C} can be found using multiple samples of surrogate data to generate a distribution of \mathfrak{C} . Then the percentile of the distribution can be used as the threshold corresponding to a significance level. However, storing the entire \mathfrak{C} distribution uses a large amount of Random Access Memory (RAM). To address this problem, we have developed an algorithm to determine the \mathfrak{C} threshold with little RAM. In-fact, a sub-field of data streaming algorithms is devoted to finding quantiles using little RAM.

In non-stationary TFA and CHS, we are interested in identifying time intervals and frequency bands that feature significant \mathfrak{C} and then analyzing the phase and gain relationships of these \mathfrak{C} signals. While various signal processing methods can be used, this work will focus on wavelet analysis. Using the analytic Morlet mother wavelet, the wavelet \mathfrak{C} scalogram and wavelet transfer function scalogram are found for pairs of signals. The wavelet \mathfrak{C} calculated from experimental data (Appendix H) is compared against a threshold of \mathfrak{C} (obtained from surrogate data) to determine times and frequencies of significant \mathfrak{C} , and then only those regions in the time-frequency space are analyzed (Appendix G). This workflow relies on the predetermination of a \mathfrak{C} threshold map in time-frequency space. Such \mathfrak{C} thresholds are obtained by generating multiple 100 to 10 000 surrogate data signals with Gaussian Random Number (GRN) to create a distribution of \mathfrak{C} [85, 90–94]. The 95th percentile corresponding to a significance level $\alpha = 0.05$ of these distributions is then taken as the \mathfrak{C} threshold. However, some studies in the literature used a higher number of iterations to find a single \mathfrak{C} threshold that was then applied to the entire time-frequency space or as a function of frequency but not time [85, 90, 91, 94]. Additionally, cases with large amount of surrogate data (approximately 10 000) limited their sample length to 512 [91]. In principle, each time-frequency point should have its own \mathfrak{C} threshold since the \mathfrak{C} distribution changes with frequency and proximity to the temporal edges of the time-frequency map. This process of finding \mathfrak{C} thresholds for each pixel can be very expensive in terms of RAM usage due to the requirement

to store the entire distribution of \mathfrak{C} values.

7.3 Methods for Creating the Coherence Threshold Map

The problem of determining the desired percentile of a large distribution of data with limited Random Access Memory (RAM) can be classified as a streaming problem, for which a variety of techniques has been proposed [95–98]. The goal of this work is not to devise a conceptually novel streaming algorithm, but rather to develop an efficient method suited for the specific needs of Transfer-Function Analysis (TFA) and Coherent Hemodynamics Spectroscopy (CHS) to determine a wavelet coherence threshold from Gaussian Random Number (GRN) surrogate data. We describe an approach to determine wavelet Coherence (\mathfrak{C}) thresholds with little RAM usage. The algorithm is tailored to the Math-Works MATrix LABoratory [Natick, MA USA] (MATLAB) and takes advantage of the native matrix operations since the desired result is a map (2-dimensional (2D) array) of thresholds in the time-frequency space.

One method for estimating thresholds of significant coherence in signal analysis is the random surrogate data method [90], which has been applied to TFA of Auto-Regulation (AR) [91] and CHS [85]. In this method, GRNs are used to populate two signals in time. These random time signals are then analyzed with whatever coherence analysis is desired, and the \mathfrak{C} of the GRN signals found. GRN signals are generated over many iterations (typically 100) to create a distribution of \mathfrak{C} values for these surrogate data [85, 90]. There have been cases where large numbers of iterations have been reported of 15 000, but this was done for a single threshold value and not a map [91]. Other methods exist such as scrambling a real signal either in Time-Domain (TD) or Frequency-Domain (FD) [90]; however, all surrogate data methods result in distributions of \mathfrak{C} . Although 100 iterations have been used in the past, 1000 to 10 000 or greater iterations are desirable for more accurate threshold estimates since threshold maps show heterogeneity when

too few iterations are performed. An example of this heterogeneity will be shown in the subsequent sections. A threshold of significance is defined as a given percentile of the coherence distribution for surrogate data, with the 95th percentile being a typical choice ($\alpha = 0.05$).

7.3.0.A Simple Threshold Determination

The simplest method for determination of the desired threshold corresponding to a given percentile involves storing the entire \mathfrak{C} distribution in **RAM** over the multiple iterations of **GRN** signals. Once all \mathfrak{C} values in the distribution have been populated, the values are sorted and the one corresponding to the desired percentile accessed. The main disadvantage of this method is the need for large amounts of **RAM**. Since many signal processing techniques create time-frequency maps of coherence, each iteration will create a **2D** array (rows and columns representing time and frequency, respectively) of \mathfrak{C} values. This means that the distribution of \mathfrak{C} values will be stored in a **3-dimensional (3D)** array (rows by columns by pages) with the samples indexed along the page dimension. In an example where we have a time signal made of 10 000 points and the signal analysis method will produce 200 frequencies (reasonable for wavelet analysis), we will have a $10\,000 \times 200$ array of type double (8 B) where n_{samp} is the number of surrogate data samples. For typical values of n_{samp} , one requires 1.6 GB of **RAM** for this one variable. However, if we consider more desirable values for n_{samp} of 1000 to 10 000 we find the need for 16 GB to 160 GB of **RAM**, matching or exceeding the full capacity of memory of most desktop computers at the time of this work. This large **RAM** requirement likely has led to either few iterations being chosen [85, 90] or a single threshold (instead of a map) being estimated [91]. Therefore, this simple method of threshold determination is not practical when a threshold map is desired.

7.3.0.B Memory Efficient Algorithm for Coherence Threshold Determination

7.3.0.B.a Summary of Memory Efficient Algorithm Here we present a method to estimate the $((1 - \alpha) \times 100)^{\text{th}}$ percentile and associated coherence threshold without having to store the entire coherence distribution in **RAM** (Listing 7.1) as in Blaney *et alia* Biomedical Signal Processing and Control (2020) [6]. The algorithm is summarized below and will be described in detail in the following sections. Additionally, whenever a \mathfrak{C} value is retrieved that methods in Appendix H are used. To estimate the desired percentile with less **RAM**, we start with an initial step that requires building the \mathfrak{C} distribution for several surrogate data samples ($2m_{kp} \approx 100$) that is much smaller than the desired value of n_{samp} 1000 to 10 000 or greater) but similar to the lesser number of sample iterations used in the past [85, 90]. Throughout each iterative step of the proposed algorithm, which processes a new sample of the \mathfrak{C} distribution, the approach is to retain only \mathfrak{C} values that are close to the current threshold estimate (Figure 7.1). For this purpose, a **3D** array **ABN** (time by frequency by surrogate sample index; **AB** in Listing 7.1) is built. The notations **ABN** follows from the fact that this **3D** array is made of three sub-arrays **A**, **B**, and **N**; however, these sub-arrays are never separated in **RAM** and always stored as the combination **ABN**. **ABN** consists of a total $2m_{kp} + 1$ ($2m_{kp}$ is **Nkp** in Listing 7.1) pages, where each page is a **2D** time-frequency array: the first m_{kp} pages contain coherence values below the desired percentile (**3D** subarray **A**); the next m_{kp} pages contain \mathfrak{C} values above the desired percentile (**3D** sub-array **B**; the last page is used in the algorithm to accept a new \mathfrak{C} sample in each iteration (**2D** array **N**). The first page of **B** is named **T** (**cohThresh** in Listing 7.1), which is a **2D** array containing the \mathfrak{C} threshold estimates for each time and frequency. First, the algorithm initializes the first $2m_{kp}$ pages **AB** by populating them with the first $n_f \times n_t \times 2m_{kp}$ coherence samples and, after ordering the samples along the page dimension at each time-frequency

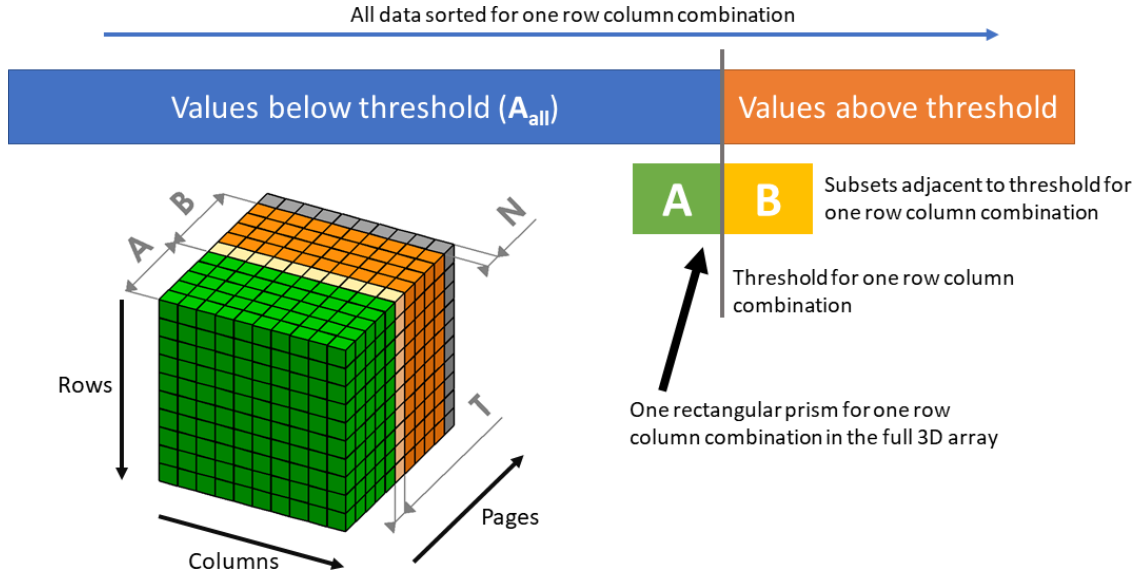


Figure 7.1: Structure of the 3-dimensional (3D) array **ABN** used in the efficient threshold algorithm. Each voxel contains a Coherence (\mathfrak{C}) value and the values are increasing in the direction of increasing page number. All \mathfrak{C} values below the threshold make up the conceptual array \mathbf{A}_{all} , this array is never stored in its entirety, but only its subset **A**. The 2-dimensional (2D) array $\mathbf{n}_{\mathbf{A}_{all}}$ is stored and contains the length of the conceptual \mathbf{A}_{all} for each row and column combination. **A** and **B** contain the \mathfrak{C} sample subsets adjacent to the desired percentile. The threshold 2D array (**T**) is the first element in the sorted **B** set. The cube shows the implementation of the **A**, **B**, and **N** sets in a 3D array. The rows and columns are the time and frequency dimensions while the page dimension is \mathfrak{C} value samples. The last page of **ABN** is a null page (**N**) that contains a new \mathfrak{C} sample at each iterative step of the algorithm.

Note 1: This chart can be found as Figure 1 in Blaney *et alia* Biomedical Signal Processing and Control (2020) [6].

pixel, estimates the threshold (Figure 7.2(a-c)) and Listings 7.1(101-123)). Here, n_f and n_t are the number of frequency samples and the number of time samples (**N1** and **N2** in Listing 7.1), respectively. Next, a loop is entered, where a new \mathfrak{C} sample is taken at each iteration. In the loop, the new 2D array of coherence samples is first added to **ABN** (in the last page, **N** and then the elements of **ABN** are properly shifted in the page dimension to keep the \mathfrak{C} threshold array **T** at the same page index. Note that during this rearrangement some \mathfrak{C} values that were present in the **ABN** array will be discarded and will be substituted by some elements of the new coherent sample. The method to shift the elements of **ABN** is controlled by a 2D array, $\mathbf{n}_{\mathbf{A}_{all}}$ (An in Listing 7.1), which contains the total number of samples (updated at each iterative step)

that are below threshold at each time-frequency pixel. $\mathbf{n}_{\mathbf{A}_{all}}$ is named such since it represents the length of the conceptual set \mathbf{A}_{all} which contains all the samples below the threshold estimate ever extracted until that step of the loop (including samples that were extracted and are no more in the array **ABN**). In the example where a $10\,000 \times 200$ time-frequency array of thresholds is desired; each page would take 16 MB of RAM. For $m = 50$ (*id est* if **A** and **B** are each 50 pages deep), the 3D array **ABN** would consist of 101 pages. This is 1.6 GB of RAM, reasonable for most desktop computers at the time of this work, but allowing for an arbitrary n_{samp} of 1000 to 10 000 or greater. Notice that if we compare this amount of memory to the examples where all coherence samples were saved, the memory usage is equivalent to $n_{samp} = 100$ for all sam-

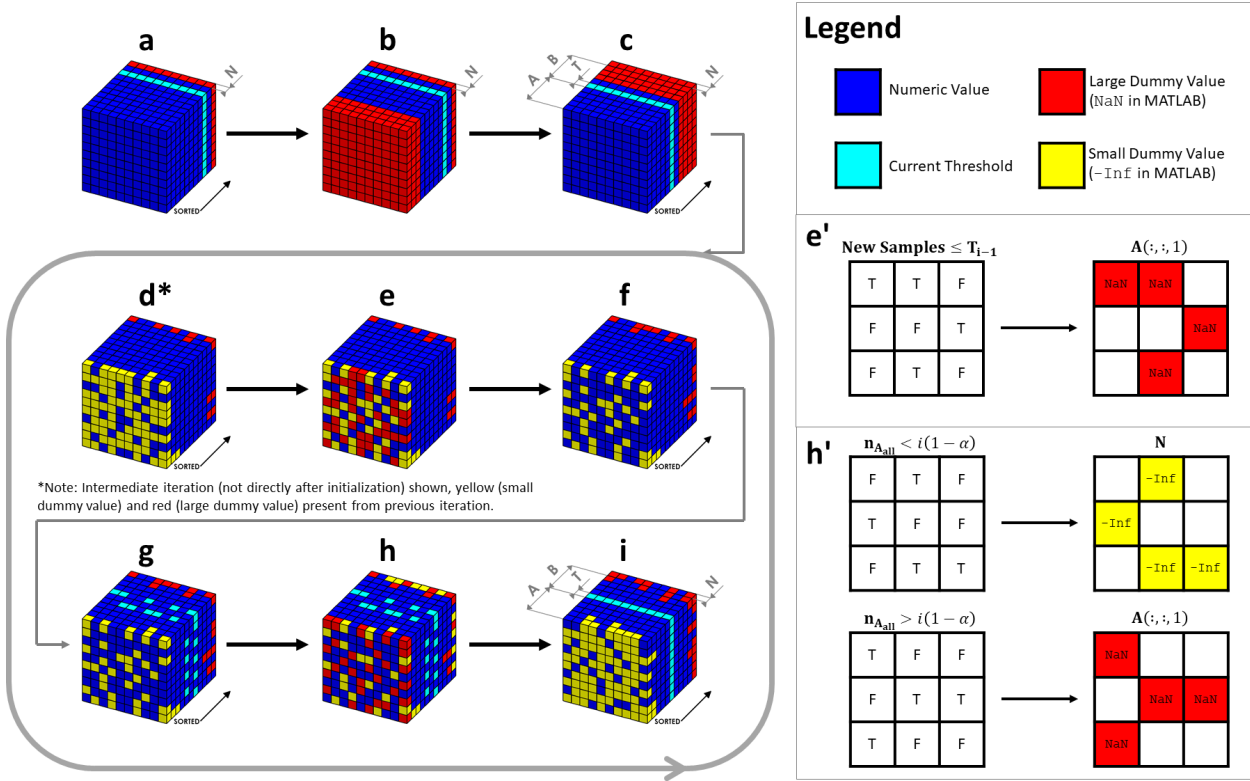


Figure 7.2: [(a-c) Initialization] a) **ABN** Array is initialized with $2m_{kp}$ samples and sorted. At the end of this phase the thresholds will be at page at index $[m_{kp}(1 - 2\alpha)]$. b) In order to shift the threshold page (**T**) to the first page of (**B**), elements too small to be in **A** (which belong to its first $[m_{kp}(1 - 2\alpha)]$ pages) are set to the large dummy value (NaN in MathWorks MATrix LABoratory [Natick, MA USA] (MATLAB)). c) **ABN** is sorted, and the thresholds are set in the correct page, **T**. [(d-f) Adding Samples] d) 2-dimensional (2D) array of new coherence samples is placed in **N** replacing what was there. Then the **ABN** is sorted. Note that the figure does not show an example of first iteration, thus various dummy values are already present. e) For row and columns combinations where the new element was less than or equal to the last threshold estimate, the first page of the array is set to the large dummy value. f) Array is sorted. [(g-i) Shifting Elements] g) Based on the value of the new samples it is calculated whether they belonged to the **A** set or the **B** set and whether the sets are the right size for the desired threshold to be at their boundary. Now it can be seen that the current threshold estimate is scattered in the page dimension and the pages must be shifted for each row and column combination. h) For row and column combinations for which set **A** is now too large, a large dummy value is placed in the first page of the array. For cases where the **A** set is now too small, a small dummy value (-Inf in MATLAB) is placed in the last page of the array. i) Again, **ABN** is sorted setting the thresholds to be in the correct page, **T**.

Note 1: This is found as Figure 2 in Blaney *et alia* Biomedical Signal Processing and Control (2020) [6].

Note 2: The full algorithm is shown in Listing 7.1.

Note 3: **A**: Set below threshold; **B**: Set above threshold; **T**: Page corresponding to threshold estimate; **N**: Extra null page. Blue: Number; Light Blue: Number belonging to threshold estimate; Yellow: Lower dummy value (-Inf in MATLAB); Red: Upper dummy value (NaN in MATLAB).

ples saved. This is the key advantage of the algorithm, namely the ability to consider an arbitrarily large number of samples with RAM usage as

if $n_{\text{samp}} = 2m_{kp} + 1$ and all samples were saved. Below, we describe in detail the three steps of the algorithm: initialization (Listings 7.1(101-

123)), adding samples (Listings 7.1(125-145)), and shifting elements (Listings 7.1(147-168)).

7.3.0.B.b Initialization First, the initial $2m_{kp}$ values of \mathbf{C} obtained from analyzing GRN data with Appendix H. These \mathbf{C} values are used to populate the first $2m_{kp}$ pages of the **ABN** (Listings 7.1(101-123)). Those values are sorted in the page dimension (Figure 7.2(a) and Listing 7.1(116)) so that **T** is easily identified. For example, in the case of **A** and **B** having 50 pages each $m_{kp} = 50$ and $\alpha = 0.05$, the coherence thresholds will be at page 96 of **ABN**. Second, we shift the coherence thresholds to the first element of the **B** sub-array (or page $m_{kp}+1$, page 51 in this example, of the **ABN** array); to do this, the pages with the smallest $[m_{kp}(1 - 2\alpha)]$ values in the **A** sub-array (*id est* in the first 45 pages in this example with $m_{kp} = 50$ and $\alpha = 0.05$) are re-defined to the large dummy value (in the case of MATLAB implementation, **NaN**) (Figure 7.2(b) and Listing 7.1(117)). Third, the **ABN** array is again sorted in the page dimension, thus placing the page **T** at the first page of the **B** sub-array (Figure 7.2(c) and Listing 7.1(118)), or at page 51 of the **ABN** array. At this stage, the 3D array **ABN** has the first $m_{kp} = 50$ pages with \mathbf{C} values under threshold (**A** array), the 5 following pages (the first 5 pages of **B**) with \mathbf{C} value equal or above threshold (first page of **B**), and all the remaining pages of the **B** and **N** sub-arrays are filled with the large dummy value (**NaN** in MATLAB). **T** is accessed to obtain the current coherence threshold estimates (Listing 7.1(122)). A 2D array is created ($\mathbf{n}_{\mathbf{A}_{all}}$; nA in Listing 7.1(118)) where each element contains the number of samples below the threshold estimate for each time-frequency pixel. Per the $((1 - \alpha) \times 100)^{\text{th}}$ percentile, all elements of this array are initialized to the same value $((1 - \alpha) \times 100) = 95$ in this example). Because of this initialization, most of the **B** array is set to the large dummy value and the values in the **ABN** array are sorted in the page dimension.

7.3.0.B.c Adding Samples The first step taken during each iteration of the threshold up-

dating loop is to obtain a new 2D array of coherence value samples from GRN's input into the Appendix H methods. This 2D array fills the last page, **N**, of the **ABN** array (Figure 7.1), replacing its current values (Listing 7.1(128)). For each row and column combination, if the new \mathbf{C} sample is below the current threshold estimate, $\mathbf{n}_{\mathbf{A}_{all}}$ is incremented by one; otherwise $\mathbf{n}_{\mathbf{A}_{all}}$ is unchanged (Listing 7.1(135-136)). Then the **ABN** array is sorted in the page dimension (Figure 7.2(d) and Listing 7.1(137)), moving the new \mathbf{C} samples into **A** if they are below the threshold estimate, or into **B** if they are above the threshold estimate. As a result, one may end up with some \mathbf{C} values below the current threshold estimate that are in **B** (this happens if there is at least one element in **N** below threshold). To shift these elements into **A** (where they belong), we set the corresponding elements of the first page of **ABN** to the large dummy value (**NaN** in MATLAB; Figure 7.2(e) and Listing 7.1(142-145)). After re-sorting the array **ABN**, all the elements of **ABN** below the threshold estimate will be in **A**.

7.3.0.B.d Shifting Elements The second step taken during each iteration loop is to determine the new threshold estimate. This step is based on a comparison between the current values in each row and column combination of $\mathbf{n}_{\mathbf{A}_{all}}$ and the expected value of $i(1 - \alpha)$ ($(1 - \alpha)*n$ in Listing 7.1(152-153)) where i is the iteration number (n in Listing 7.1) including the $2m_{kp}$ initialization samplings. This is because the initialization of the algorithm is considered to take $2m_{kp}$ iterations so that the iteration number i is representative of the total number of samples taken thus far. We describe the performed comparisons following MATLAB notation where arrays can be compared to scalars resulting in Boolean arrays: if $\mathbf{n}_{\mathbf{A}_{all}} < i(1 - \alpha)$ ($\mathbf{An} < ((1 - \alpha)*n)$ in Listing 7.1(152)), elements must be taken from **B** and added to **A** (at those time-frequency pixels of the Boolean array where there is a **true**); if $\mathbf{n}_{\mathbf{A}_{all}} > i(1 - \alpha)$ ($\mathbf{An} > ((1 - \alpha)*n)$ in Listing 7.1(153)), (this statement generates an almost complementary

Boolean array to the previous one) an element must be taken from **A** and added to **B**; no action is needed if $\mathbf{n}_{\mathbf{A}_{\text{all}}} = i(1 - \alpha)$. Thus, the row and column combinations that require their elements shifted are found (Figure 7.2(g)). In cases where pixels must be shifted to lower-index pages (from **B** to **A**), a large dummy value replaces the first page of **ABN** (Listing 7.1(162)). In cases where pixels must be shifted to larger-index pages (from **A** to **B**), a small dummy value (in the case of MATLAB implementation, $-\text{Inf}$) replaces the last page of **ABN** (Figure 7.2(h) and Listing 7.1(164)). $\mathbf{n}_{\mathbf{A}_{\text{all}}}$ values are incremented by one if a sample was moved from **B** to **A**, and decremented by one in the opposite case. Finally, the **ABN** array is sorted for the last time placing the updated threshold estimates at the **T** page, the first page of the **B** array (Listing 7.1(168)). The **T** page is accessed to extract the new threshold estimate (Listing 7.1(172)). Because of this step, the **ABN** array is sorted, $\mathbf{n}_{\mathbf{A}_{\text{all}}}$ and **T** are updated, and the **ABN** array is ready for the new loop iteration.

7.3.1 Testing the Memory Efficient Algorithm

7.3.1.A Testing with Constructed Distributions

To validate the results of the algorithm, its output was compared to the true percentile given by a data set consisting of 20 000 samples. The test set was not a \mathfrak{C} distribution, but rather a constructed distribution. In addition, this test was carried out for one threshold value, equivalent to one pixel in a real \mathfrak{C} map. In this example, we take $m_{kp} = 50$ to be consistent with the previous sections. The test data resulted from two random Gaussian distributions, one with mean 0 and standard deviation 0.2, and the other with mean 0.5 and standard deviation 0.5. Each of the 20 000 samples had an equal likelihood of coming from either of the Gaussian distributions. The test values of these distributions were limited to the range 0 to 1 inclusive. The purpose of creating this test data set was to create a bag of numbers to test the algorithm against, any bag of

numbers constructed in various ways could have been used.

The algorithm was run pulling samples from this test data set to construct its estimate of the 95th percentile. All the samples from the distribution were saved, and the true 95th percentile for all the data samples pulled thus far was calculated for each iteration of the loop. The algorithm was run for all $n_{\text{samp}} = 20000$ samples and did not show a difference from the true 95th percentile within the third significant digit (Figure 7.3). The true final percentile value was determined by finding the 95th percentile from the whole sample distribution.

7.3.1.B Application of Wavelet Coherence Analysis

One intended application of this algorithm is to find thresholds for significant \mathfrak{C} in wavelet signal analysis (Appendices G&H). Using a map of \mathfrak{C} thresholds, one can determine which points in frequency and time are significantly coherent for a given pair of signals. The computation of \mathfrak{C} threshold as a function of time and frequency can be a computationally demanding task for more data samples (longer time acquisitions assuming a fixed sampling frequency). To evaluate the capabilities of the algorithm presented here, we used it to generate \mathfrak{C} thresholds for the \mathfrak{C} calculated by the MATLAB `wcoherence` function, which was modified to remove smoothing in frequency (Figure 7.4) which is discussed in Appendix H. The threshold map presented in the right panel of Figure 7.4 was given a limit of 24 h to run the algorithm on a typical desktop computer at the time of this work. The algorithm completed 22 601 iterations in that time on a 9375×145 map of \mathfrak{C} 1 359 375 individual \mathfrak{C} thresholds). This map represented thresholds for a 20 min long signal acquired at a sample rate of 7.8125 Hz with analyzed frequencies from 0.001 Hz to 3.730 Hz. The left panel of Figure 7.4 shows the initialization of the algorithm (thresholds from 100 iterations). Comparing the 100 iteration map to the 22 601 iteration map, 100 iterations yield a much greater heterogeneity compared to 22 601 iterations. This is representative

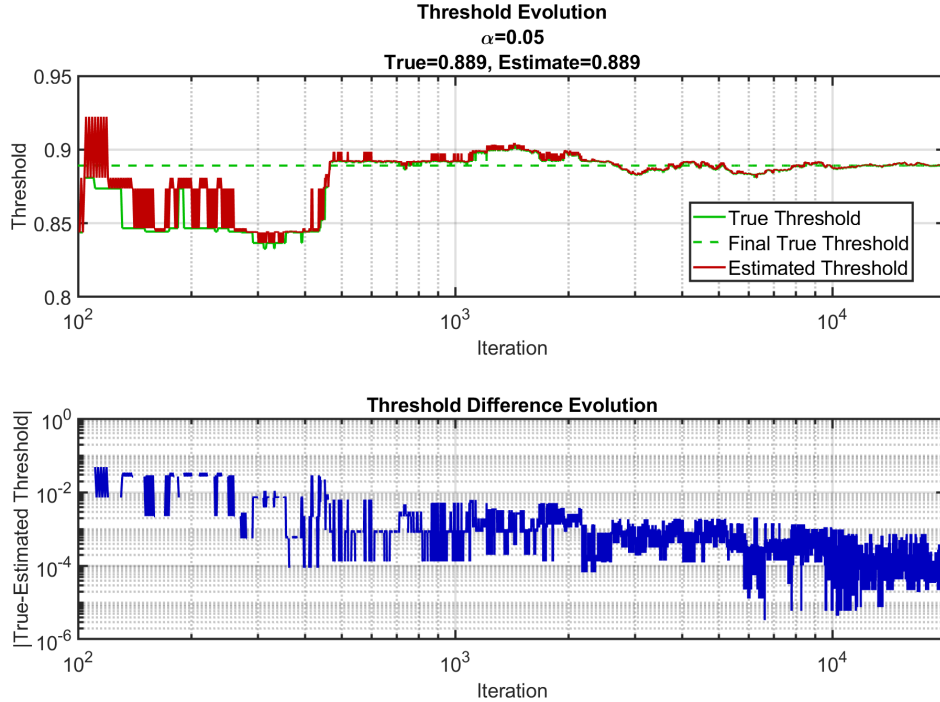


Figure 7.3: Comparison of true 95th percentile and estimated 95th percentile of a test distribution. Top) True threshold over all iterations compared to estimated threshold. Bottom) Absolute value of the difference between the estimated threshold and the true threshold over all iterations. Note that the iteration axis starts at 100, since 100 samples were taken during initialization of the algorithm. Note 1: This chart can be found as Figure 3 in Blaney *et alia* Biomedical Signal Processing and Control (2020) [6].

of thresholds generated for a real experimental protocol on actual distributions of \mathfrak{C} (instead of a single constructed distribution as in the previous section). It is worth noting that if this map was generated by storing the entire \mathfrak{C} distributions 246 GB of memory would have been required, compared to the 1 GB used by the **ABN** array in the algorithm.

7.3.2 Discussion of the Memory Efficient Algorithm

We presented an algorithm designed to calculate threshold values of significant \mathfrak{C} . The algorithm was designed with the specific objective of calculating time-frequency maps of \mathfrak{C} thresholds for wavelet analysis, but it could be used for any application that requires the estimation of a desired percentile of a sampled distribution. The algorithm allows the calculation of thresh-

olds from large number of samples without requiring large amounts of computer **RAM**. This is because the proposed method employs only the distribution values that fall within a region around an iteratively updated threshold. With this method, the limitation in the number of samples is determined by available computing time, since the **RAM** that the algorithm requires does not increase as more and more samples are acquired. The algorithm will allow for the accurate estimation of \mathfrak{C} thresholds when analyzing pairs of signals. Physiologically relevant signals include Arterial Blood Pressure (ABP) and either Blood-Flow (BF) or Oxy-hemoglobin concentration change (ΔO), and Deoxy-hemoglobin concentration change (ΔD) which are relevant for TFA of AR and CHS.

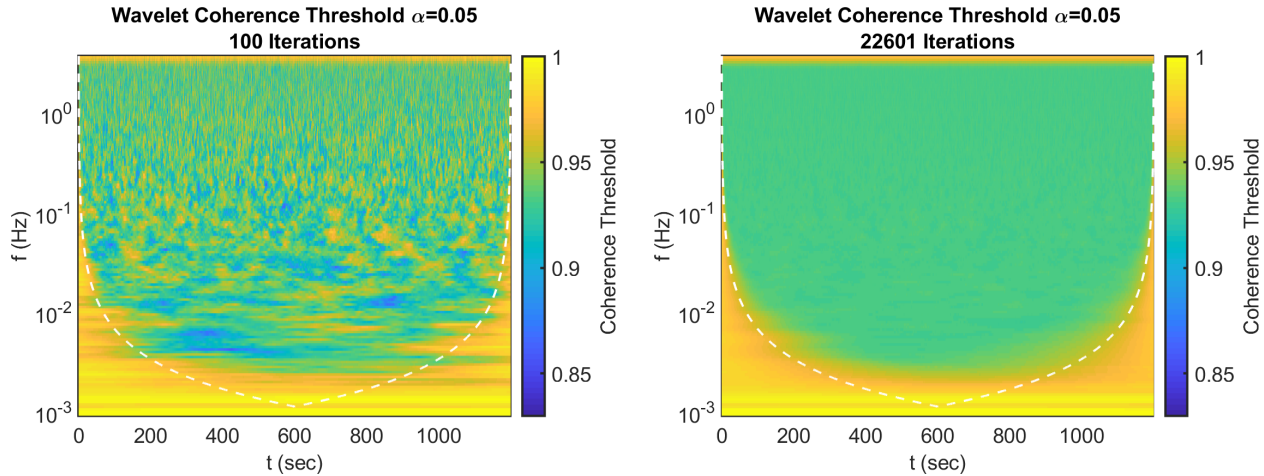


Figure 7.4: Example map of Coherence (\mathfrak{C}) thresholds generated by the algorithm with size 9375×145 (1 359 375 pixels). Map shows 95 % \mathfrak{C} threshold for a 20 min long signal sampled at 7.8125 Hz with a frequency range from 0.001 Hz to 3.730 Hz. \mathfrak{C} was found using a version the MathWorks MATrix LABoratory [Natick, MA USA] (MATLAB) `wcoherence` function, modified to remove smoothing in frequency (see Appendix H). Left) Thresholds generated form 100 iterations using the entire \mathfrak{C} distribution (initialization of the algorithm). Right) Thresholds generated using the algorithm in 24 h with 22 601 iterations on a typical desktop computer at the time of this work. Note 1: This chart can be found as Figure 4 in Blaney *et alia* Biomedical Signal Processing and Control (2020) [6].

7.3.2.A Values of the Number of Coherence Samples Taken and Kept

The main aim of the algorithm is to estimate threshold maps with large n_{samp} (iterations id *est* the number of samples taken) without large **RAM** usage. Previous works have either used small n_{samp} or not generated full threshold maps (but rather just one threshold value) [85, 90, 91]. From Figures 7.3&7.4 it can be seen that 100 samples are not enough to get a good estimate of the threshold [85, 90]. The threshold map shown in the left panel of Figure 7.4 shows a visible heterogeneity in the time-frequency map of the threshold. This example, generated from 100 samples, shows that some regions may feature significant coherence when a more accurate threshold estimate would not. Thus, more \mathfrak{C} samples are required (1000 to 10 000 or greater) but, as discussed in, a simple threshold determination would require too much **RAM** to generate a threshold map. Thus, a single threshold estimate (not a map) with a large n_{samp} has been used [91]. But from the right panel of Figure 7.4

the threshold map does not contain a constant value as the threshold depends on frequency and temporal proximity to the edge. Therefore, we need a method to estimate entire threshold maps using large n_{samp} but little **RAM**, the algorithm presented here achieves this goal.

The value chosen for m_{kp} (size of **A** and **B** along the page dimension id *est* the number of samples kept) has some effect on the algorithm. In principle, it should be set as large as possible without using too much **RAM** or reducing computation time. Here, $m_{kp} = 50$ was chosen since it was found to be large enough without using unreasonable amounts of **RAM**. m_{kp} can also be chosen to be too small. If this is the case, there is a risk of the dummy values appearing in the threshold estimate array.

7.3.2.B Applicability of the Algorithm

A method that can easily and accurately generate threshold maps is important because a different map may be needed for different experimental protocols. Different experimental protocols

may last different durations in time. The data could be collected at different sampling rates. In addition, different experiments may require different coherent analysis parameters (smoothing in wavelet for example). These differences across experimental protocols require \mathbf{C} maps to be generated frequently without the need for a specialized computer. The algorithm presented here is capable of this, since it does not have large memory requirements, and most desktop computers at the time of this work can be used to generate thresholds. This leads to the possibility of generating thresholds for an experiment overnight on one's computer and then being able to complete the turnaround on coherence analysis within one day of a new experiment.

The algorithm was developed for and inspired by the need for significant \mathbf{C} in TFA and CHS. However, its use is not limited to these modalities. In principle it could be applied to any application that needs percentile estimates of many samples with little RAM usage. This is the sub-field of quantile estimation in the field of streaming algorithms. This work does not aim to develop a new streaming algorithm but rather to create a specific implementation that has been optimized for MATLAB and importantly for estimation of 2D arrays of percentiles. Note that this algorithm is implemented without for loops to index the arrays, but uses instead native array operations in MATLAB, an important consideration when optimizing for MATLAB. This suggests that the algorithm may be applicable to modalities outside TFA and CHS.

Finally, there is a possibility for this algorithm to be implemented in other languages. Despite it being optimized for MATLAB by using the native array operations, MATLAB has disadvantages. First, development in MATLAB requires expensive licenses making it inaccessible to some. Second, MATLAB is inherently not as fast as other languages since it is designed for data analysis and visualization, not writing and compiling standalone programs. Due to these disadvantages it may be desirable to implement the algorithm in another language. There is nothing about the algorithm that would prevent this. Array operations could be implemented in nested

for loops and large positive and negative numbers could be used for the dummy values, thus lending to the possible applicability of the algorithm outside MATLAB.

7.3.2.C Considerations and Limitations of the Algorithm

The primary problem that can arise running this algorithm is dummy values showing up in the \mathbf{T} page and ruining the estimation of the threshold. It is recommended that a check for dummy values be implemented at every iteration of the threshold estimates, and to disregard them. For these cases, either the previous iteration estimate, or the max sample value (at a time-frequency pixel where a dummy value is present in \mathbf{T}) may be used as the updated estimate. The latter is more conservative, possibly overestimating the \mathbf{C} threshold. Such conservative estimates are sometimes desirable in determining thresholds. In this conservative spirit, we used the first page of \mathbf{B} as the threshold instead of the average of the last page of \mathbf{A} and the first page of \mathbf{B} .

It is also worth noting that three sorting operations are required for each iteration of this algorithm. Sorting operations are one of the more computationally expensive operations in terms of processing time. Considering the sort operations, the cost of the algorithm is $\mathcal{O}(6n_{\text{samp}}n_f n_t m_{kp} \log_2(2m_{kp}))$ since MATLAB uses quick sort on the $2m_{kp} + 1$ values in \mathbf{ABN} . This sort must be repeated three times for every iteration n_{samp} , frequency row n_f , and time column n_t . Thus, it may be said that this algorithm reduces memory cost at the expense of an increased processing cost. Parallelism may be a way to alleviate the cost of sorting; because the sort is done for row-column n_f and n_t . Of course, there may be further opportunities to improve the algorithm through parallelism. However, the time-frequency analysis of the GRN signals that must be done at every iteration dominates the processing time in each step and may overshadow the cost of sorting.

The efficacy of the algorithm maybe further improved to reduce computation cost or better take advantage of parallelization. One such im-

provement may involve changing the way new data is added. Instead of adding one sample at a time, new data may be added in blocks of multiple surrogate data samples (like repeating the initialization step in the iterations). This may require fewer sorting operations but would be more costly in terms of RAM.

Listings

Listing 7.1: MATLAB code for memory efficient algorithm for coherence threshold determination

```

1  function [cohThresh, t, f, n, eltime, alpha, coi]=genWAVthresh(...
2      rtime, tTot, fs, alpha, svBool)
3  % [cohThresh, t, f, n, eltime, alpha, coi]=genWAVthresh(...
4  %     rtime, tTot, fs, alpha, svBool)
5  % Giles Blaney
6  % Inputs:
7  %     rtime      — Approximate time to run in seconds
8  %     tTot       — Total length of protocol in seconds
9  %     fs         — Sampling frequency in Hz
10 %    alpha       — Significance level
11 %    svBool     — Boolean to save threshold map
12 % Outputs:
13 %    cohThresh — Wavelet coherence threshold map
14 %    t          — Time vector seconds
15 %    f          — Frequency vector in Hz
16 %    n          — Number of samples run
17 %    eltime     — Time to run in seconds
18 %    alpha      — Significance level
19
20 %% Set Defaults
21 if nargin<=0
22     rtime=60; %sec
23 end
24 if nargin<=1
25     tTot=10*60; %sec
26 end
27 if nargin<=2
28     fs=9.9306; %Hz
29 end
30 if nargin<=3
31     alpha=0.05;
32 end
33 if nargin<=4
34     svBool=true;
35 end
36
37 %% Make time-axis
38 % Number of samples in time
39 nsamp=floor(tTot*fs);
40 % Create time vector (sec)
41 t=(0:(1/fs):((nsamp-1)/fs))';
42
43 %% Run coherence on signals of correct
44 %% length to get frequency vector, cone
45 %% of influence vector, and example
46 %% coherence array
47 sig1=ones(nsamp, 1);
48 sig2=ones(nsamp, 1);
49 [Xtemp, ~, ~, ~, f, coi]=wcoherence(sig1, sig2, fs);
50

```

```

51 %% Set size of A set and B set
52 % Number of samples to keep each
53 % iteration
54 Nkp=100;
55 % A set is half of all kept samples
56 AN=floor(Nkp*0.5);
57 % B set is other half of all kept
58 % samples
59 BN=ceil(Nkp*0.5);
60 % Size of A in initialization step
61 Ainit=round(Nkp*(1-alpha));
62 % Size of B in initialization step
63 Binit=Nkp-Ainit;
64
65 %% Get expected size of coherence array
66 %% and initialize AB array and threshold
67 %% array of NaN
68 N1=size(Xtemp, 1);
69 N2=size(Xtemp, 2);
70 AB=NaN*ones(N1, N2, Nkp+1);
71 cohThresh=NaN*ones(N1, N2);
72
73 %% Clear variables that will not be used
74 %% later
75 clear tTot Xtemp N1 N2;
76
77 %% Begin algorithm
78 tic; % Start timer
79 n=0; % Initialize iteration number
80 eltime=toc; % Initialize current time
81 % Run while current time is less than
82 % run time or iteration number is less
83 % then the amount of samples needed to
84 % initialize AB
85 while eltime<rtime || n<Nkp
86     n=n+1; % Increment iteration number
87     % Generate Gaussian random signals
88     sig1=randn(nsamp, 1);
89     sig2=randn(nsamp, 1);
90
91     % Calculate coherence of random
92     % signals
93     X_now=wcoherence(sig1, sig2, fs);
94
95     if n<=Nkp % If AB is not initialized
96         % Populate AB with current sample
97         AB(:,:, n)=X_now;
98
99         %% Initialization of AB
100        % If at last step of AB
101        % initialization
102        if n==Nkp
103            % Set number of samples in Aall
104            % set to the size of A at

```

```

105      % initialization
106      An=ones(size(X_now))*Ainit;
107
108      % Set all values too small to be
109      % in A to NaN and sort
110      AB=sort(AB, 3);
111      AB(:, :, 1:(BN-Binit))=NaN;
112      AB=sort(AB, 3);
113
114      % Initialize threshold array with
115      % the first page of B
116      cohThresh=AB(:, :, AN+1);
117  end
118 else % If AB is initialized
119     %% Add New Sample
120     % Place the current sample in the
121     % last page of AB
122     AB(:, :, end)=X_now;
123
124     % Find the number of new samples
125     % that belong in A, increment the
126     % number of samples in Aall if this
127     % is the case, and sort AB with the
128     % new sample
129     Aadd=AB(:, :, end)<=cohThresh;
130     An=An+double(Aadd);
131     AB=sort(AB, 3);
132
133     % If the current sample was placed
134     % in A set the first page of A to
135     % NaN and sort
136     Amin=AB(:, :, 1);
137     Amin(Aadd)=NaN;
138     AB(:, :, 1)=Amin;
139     AB=sort(AB, 3);
140
141     %% Shift Samples
142     % Find if the number of samples in
143     % Aall is too large or too small
144     % given the current divide between A
145     % and B
146     Asmall=An<((1-alpha)*n);
147     Abig=An>((1-alpha)*n);
148
149     % If Aall is too small set the first
150     % page of A to NaN and increment
151     % Aall, if Aall is too big set the
152     % last page of B to -Inf, then sort
153     % AB
154     Amin=AB(:, :, 1);
155     Bmax=AB(:, :, end);
156     Amin(Asmall)=NaN;
157     An(Asmall)=An(Asmall)+1;
158     Bmax(Abig)=-Inf;

```

```

159      An(Abig)=An(Abig)-1;
160      AB(:, :, 1)=Amin;
161      AB(:, :, end)=Bmax;
162      AB=sort(AB, 3);
163
164      % Set the threshold to the first
165      % element in B
166      cohThresh=AB(:, :, AN+1);
167
168      %% Check for Problem Elements
169      % Check if NaN or -Inf where placed
170      % in the threshold estimate, if so
171      % replace with the max sample value
172      thresh_bad=or(isinf(cohThresh), isnan(cohThresh));
173      ABmax=max(AB, [], 3, 'omitnan');
174      cohThresh(thresh_bad)=ABmax(thresh_bad);
175  end
176
177  eltime=toc; % Get current time
178
179  % If iteration number is multiple of
180  % 100 print status
181  if mod(n, 100)==0
182      fprintf('Sample %d\t%.1f sec / %.0f sec\n', n, eltime, rtime);
183  end
184 end
185 fprintf('Loop Done\n');
186
187 if svBool % If desired save output
188     % Create string of sampling frequency
189     % replacing . with o
190     fsString=num2str(fs);
191     fsString=replace(fsString, '.', 'o');
192
193     % Find file path for this function
194     funPathStr=which('genWAVthresh.m');
195     funDir=dir(funPathStr);
196
197     % Construct filename to be saved
198     svString=[funDir.folder '\WAVcohThresh_' fsString '_' ...
199             num2str(nsamp) '_' num2str(n) '.mat'];
200
201     % Save
202     save(svString, 'cohThresh', 't', 'f', 'n',...
203          'eltime', 'alpha', 'coi');
204
205     fprintf('Saving Done\n');
206 end
207 end

```

Acronyms: MathWorks MATrix LABoratory [Natick, MA USA] (MATLAB).

Available at:

<https://github.com/DOIT-Lab/DOIT-Public/tree/master/Dissertations/GilesBlaney2022/code>

Chapter 8

In-Vivo Cerebral Hemodynamics

8.1 Overview Coherent Hemodynamics Spectroscopy Results

In Khaksari *et alia* Journal of Biomedical Optics (2018) [1], Blaney *et alia* Photonics (2019) [2], and Blaney *et alia* Journal of Biophotonics (2020) [3] we conducted Coherent Hemodynamics Spectroscopy (CHS) measurements on the brain of healthy human subjects using the various Near-Infrared Spectroscopy (NIRS) techniques discussed in Part I. Those techniques sought to preferentially access the brain using either long source-detector distance (ρ) in Multi-Distance (MD) measurements [1, 2] or using Dual-Slope (DS) [3].

In these studies we reported CHS oscillations at 0.1 Hz. The physiological source of the coherent hemodynamic fluctuations are Arterial Blood Pressure (ABP) oscillations at a frequency of, induced by cyclic inflation (to a pressure of 200 mmHg) and deflation of two thigh cuffs wrapped around the subject's thighs [1–3] or paced breathing [2]. To interpret these results we utilized the CHS phasor model (Figure 6.1), by extracting from the NIRS data the Oxy-hemoglobin phasor (\tilde{O}), Deoxy-hemoglobin phasor (\tilde{D}), and Total-hemoglobin phasor (\tilde{T}), using the methods in Appendices H&G. We also extracted the Arterial blood pressure phasor (\tilde{A}) from ABP measurements using finger plethysmography.

In Khaksari *et alia* Journal of Biomedical Optics (2018) [1] and Blaney *et alia* Photonics (2019) [2] the measurements were done on hu-

man forehead at multiple ρ s (10 mm to 40 mm; Chapter 2). In Khaksari *et alia* Journal of Biomedical Optics (2018) [1] there was one location and in Blaney *et alia* Photonics (2019) [2] it was bilateral (two locations). Both of these studies utilized Single-Distance (SD) Intensity (I) while only Blaney *et alia* Photonics (2019) [2] utilized SD phase (ϕ) and Single-Slope (SS) I .^a

Then, in Blaney *et alia* Journal of Biophotonics (2020) [3] we presented a first *in vivo* application of DS ϕ , measured with Frequency-Domain (FD) NIRS to demonstrate its enhanced sensitivity to cerebral hemodynamics (Chapters 3&4). These data were analyzed for all possible data-types in the DS probe (Figure 3.1) which are SD, SS, and DS either I or ϕ .

In general the conclusions from all three of these works was that longer ρ s, DS data, and ϕ data show CHS measurements more indicative of what was expected in the brain. That being a stronger Blood-Flow (BF) versus Blood-Volume (BV) contribution and higher Auto-Regulation (AR) in the brain versus the superficial tissue. This was consistent with what we learned about the Sensitivity to absorption change (S) profiles and maps in Part I.

8.2 Multi-Distance Studies

The methods used in the Multi-Distance (MD) work are explained in Section 2.2.1 and in the

^aIn Blaney *et alia* Photonics (2019) [2] Single-Slope (SS) was measured between using source-detector distance (ρ) with a difference of approximately 10 mm.

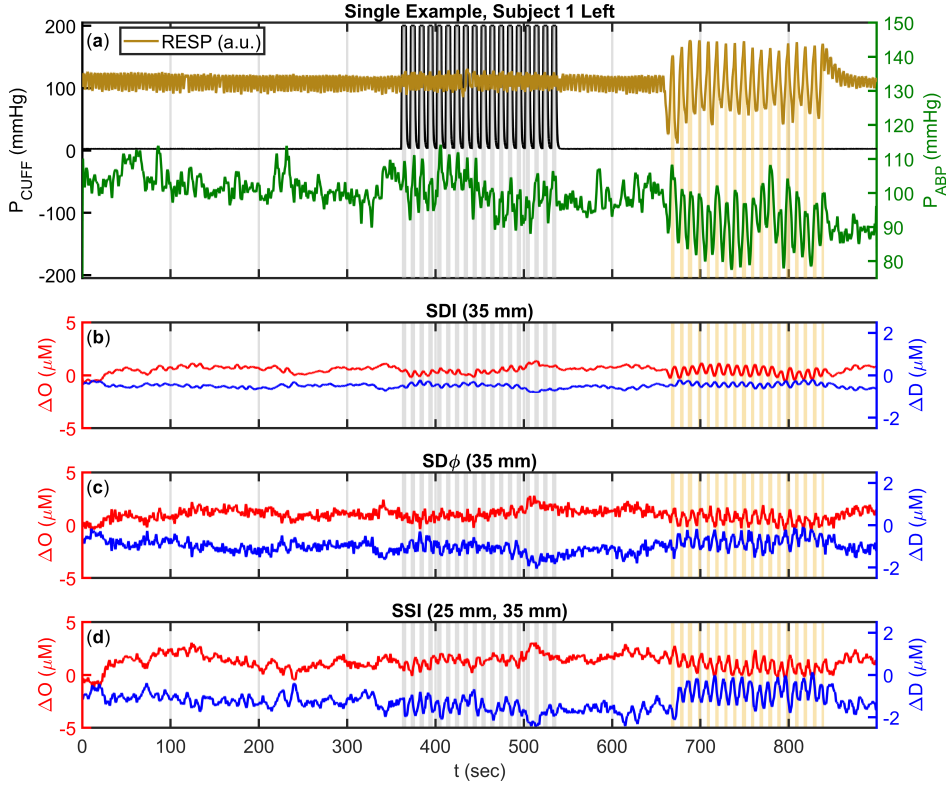


Figure 8.1: Example temporal traces for experimental protocol in Blaney *et alia* Photonics (2019) [2] using the Multi-Distance (MD) probe in Figure 2.3. (a) Pneumatic cuff pressure (Black), Arterial Blood Pressure (ABP) (Green), Respiration signal (Mustard). (b) Oxy-hemoglobin concentration change (ΔO) (Red; mean at $0.5 \mu\text{M}$) and Deoxy-hemoglobin concentration change (ΔD) (Blue, mean at $-0.5 \mu\text{M}$) measured using Single-Distance (SD) Intensity (I) with Source 6 (35 mm; Figure 2.3). (c) ΔO (Red; mean at $1 \mu\text{M}$) and ΔD (Blue, mean at $-1 \mu\text{M}$) measured using SD phase (ϕ) with Source 6 (35 mm; Figure 2.3). (d) ΔO (Red; mean at $1.25 \mu\text{M}$) and ΔD (Blue; mean at $-1.25 \mu\text{M}$) measured using Single-Slope (SS) I with Sources 4&6 (25 mm and 35 mm; Figure 2.3).

Note 1: This figure can be found as Figure 2 in Blaney *et alia* Photonics (2019) [2].

Note 2: All traces are low-pass filtered to 0.2 Hz, and shifted from zero baseline for visualization.

parent publications Khaksari *et alia* Journal of Biomedical Optics (2018) [1] and Blaney *et alia* Photonics (2019) [2]. In general, the probe in Figure 2.3 was used with the ISS Imagent V2 [Champaign, IL USA] (Imagent), and 0.1 Hz Arterial Blood Pressure (ABP) oscillations were induced either by cuff or paced breathing. Example temporal traces from such a Coherent Hemodynamics Spectroscopy (CHS) protocol are shown in Figure 8.1. phasor ratio vector between Deoxy-hemoglobin and Oxy-hemoglobin (\vec{D}/\vec{O}) and phasor ratio vector between Total-hemoglobin and Arterial blood pressure phasor (\vec{T}/\vec{A}) data was extracted from the Near-InfraRed

Spectroscopy (NIRS) data using the methods in Appendices C,D,H,&G.

8.2.1 Only Considering Cuff Oscillations and Single-Distance Intensities

8.2.1.A Summary of Single-Distance Multi-Distance Cuff Oscillation Results

An example trace of the data collected from cuff oscillations in Khaksari *et alia* Journal of Biomedical Optics (2018) [1] can be found in Figure 2.4. These temporal traces were further ana-

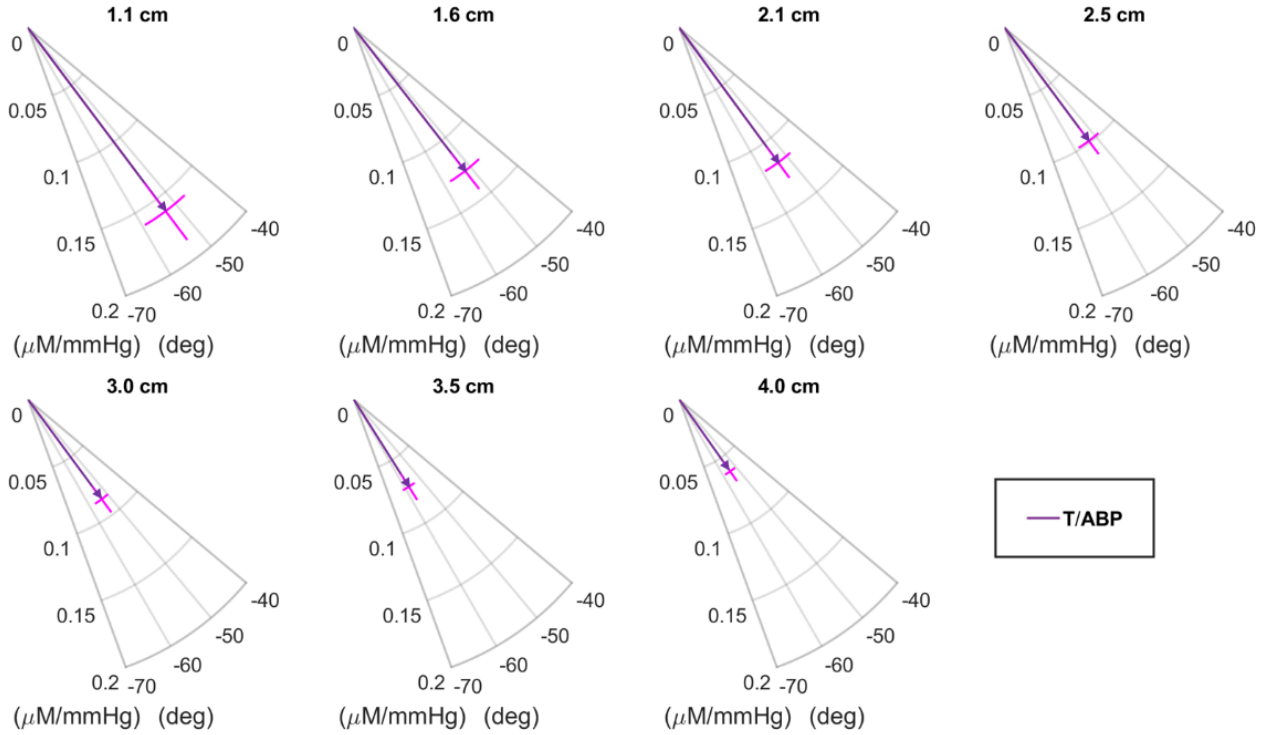


Figure 8.2: Example phasor ratio vector between Total-hemoglobin and Arterial blood pressure phasor ($\overrightarrow{T/A}$) at different source-detector distance (ρ). Data from subjects in Khaksari *et alia* Journal of Biomedical Optics (2018) [1].

Note 1: This figure can be found as Figure 4(a) in Khaksari *et alia* Journal of Biomedical Optics (2018) [1].

lyzed to extract $\overrightarrow{D/O}$ and $\overrightarrow{T/A}$ (Appendices G&H).

Figure 8.2 reports $\overrightarrow{T/A}$ and Figure 8.3 reports phasor ratio vector between Deoxy-hemoglobin and Arterial blood pressure phasor ($\overrightarrow{D/A}$) and phasor ratio vector between Oxy-hemoglobin and Arterial blood pressure phasor ($\overrightarrow{O/A}$) for the seven source-detector distances (ρ s) in a representative case (Subject 4 in Khaksari *et alia* Journal of Biomedical Optics (2018) [1]). The error bars of the ratio of amplitude and phase lags are also reported in Figures 8.2&8.3. This representative case exhibits the typical finding that the phase of Total-hemoglobin phasor (\tilde{T}) is relatively insensitive to ρ , and a phase angle between Deoxy-hemoglobin phasor (\tilde{D}) and Oxy-hemoglobin phasor (\tilde{O}) increases with ρ . This result is described in more detail in the next two sections.

8.2.1.A.a Total-Hemoglobin versus Arterial Blood Pressure Phasor Ratio Vector

\tilde{T} , which is reported here in relation to the Arterial blood pressure phasor (\tilde{A}), represents a Blood-Volume (BV) response to ABP oscillations. We have modeled the frequency dependence of $\overrightarrow{T/A}$ with the following expression [82]:

$$\overrightarrow{T/A} = K^{(a)} + \frac{K^{(v)}}{1 + i2\pi f_{\text{CHS}}\tau_{\text{AR}}} \quad (8.1)$$

where $K^{(a)}$ and $K^{(v)}$ are effective arterial and venous compliance factors, respectively, f_{CHS} is the frequency of the hemodynamics oscillations, and τ_{AR} is a time constant for cerebral Auto-Regulation (AR). According to Equation 8.1, the phase of \tilde{T} relative to \tilde{A} results from the sum of two complex terms, a first one representing an arterial contribution with a zero phase, and a second one representing a venous contribution with a negative phase:

$$\angle \overrightarrow{T/A} = -\arctan(2\pi f_{\text{CHS}}\tau_{\text{AR}}) \quad (8.2)$$

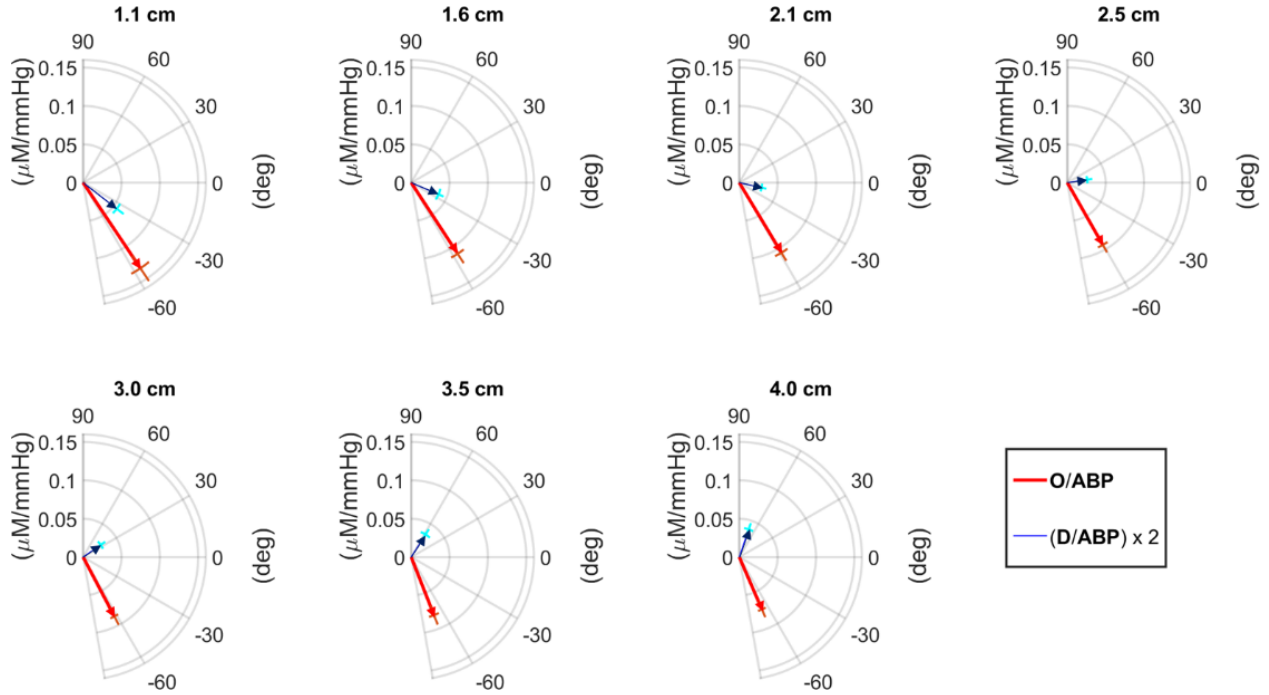


Figure 8.3: Example phasor ratio vector between Deoxy-hemoglobin and Arterial blood pressure phasor ($\overrightarrow{D/A}$) and phasor ratio vector between Oxy-hemoglobin and Arterial blood pressure phasor ($\overrightarrow{O/A}$) at different source-detector distance (ρ). Note that the phasor ratio $\overrightarrow{D/A}$ is multiplied by 2 for better visualization. Data from subjects in Khaksari *et alia* Journal of Biomedical Optics (2018) [1].

Note 1: This figure can be found as Figure 4(b) in Khaksari *et alia* Journal of Biomedical Optics (2018) [1].

According to this model, a more negative phase of $\overrightarrow{T/A}$ may result from a longer time constant τ_{AR} (*id est* a less effective AR) or a greater venous-to-arterial relative contribution to the measured hemodynamics.

Figure 8.4 shows the amplitude ratio (panel (a)) and the phase difference (panel (b)) for $\overrightarrow{T/A}$ for each subject in Khaksari *et alia* Journal of Biomedical Optics (2018) [1], with insets reporting the grand average over all subjects. The amplitude of $\overrightarrow{T/A}$ consistently decreases with ρ in all subjects (starting at a distance of 10 mm in Subjects 1,4,&6, at 15 mm in Subject 5, and at 25 mm in Subjects 2&3 all in Khaksari *et alia* Journal of Biomedical Optics (2018) [1]), indicating a greater BV oscillation in the superficial tissue layers (scalp, skull, *et cetera*) versus the deeper, intracranial cerebral tissue. This result reflects the mechanical constraint set by the skull, which limits the cerebral BV response to

changes in ABP.

The phase of $\overrightarrow{T/A}$ does not show a significant dependence on ρ , except for Subject 1 in Khaksari *et alia* Journal of Biomedical Optics (2018) [1]. In fact, a Watson-Williams test [99] for comparison of the combined three measurements at 10 mm to 20 mm distances with the combined three measurements at 30 mm to 40 mm finds a significant decrease at the $\alpha = 0.05$ level only in Subject 1 in Khaksari *et alia* Journal of Biomedical Optics (2018) [1] (p -value = 0.017). A phase of $\overrightarrow{T/A}$ that is constant with ρ indicates that the timing of the BV response to ABP changes is the same at different tissue depths. According to the model of Equation 8.1 there are two factors that affect the phase of $\overrightarrow{T/A}$:

- The relative contribution of arterial (zero phase) and venous (negative phase) vascular compartments, with less negative phase values associated with greater arterial-to-

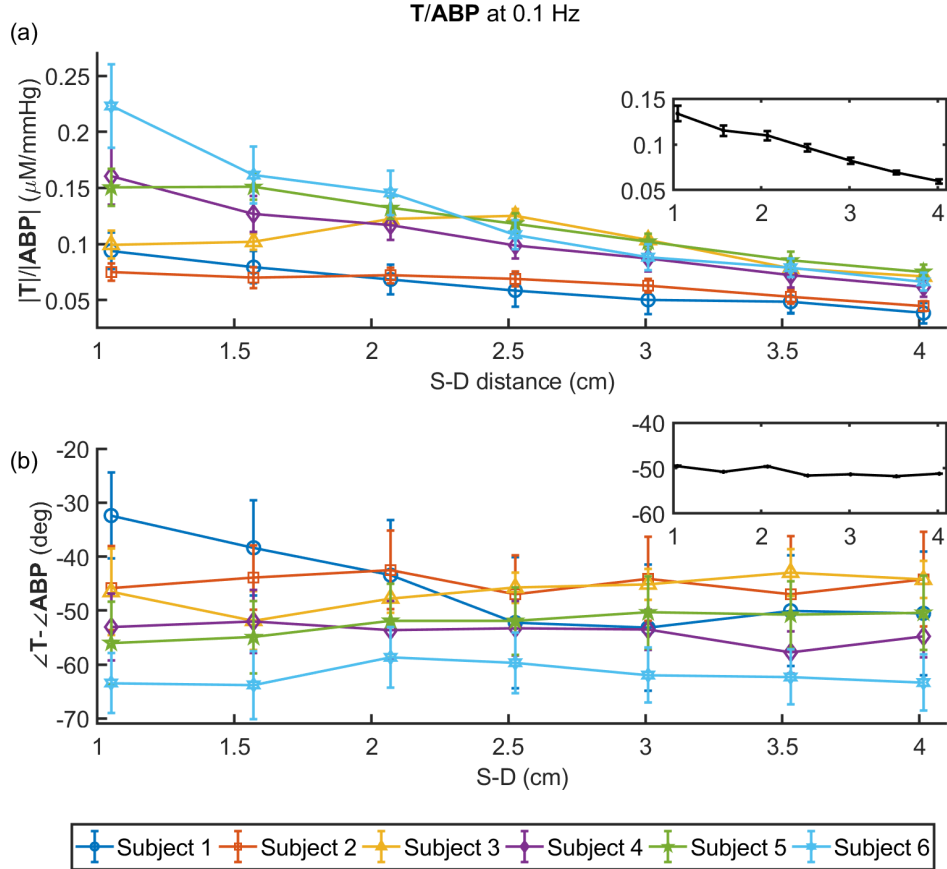


Figure 8.4: Amplitude (a) and phase (b) of phasor ratio vector between Total-hemoglobin and Arterial blood pressure phasor (\tilde{T}/\tilde{A}) versus source-detector distance (ρ) at 0.1 Hz for all subjects in Khaksari *et alia* Journal of Biomedical Optics (2018) [1]. The inset in each panel shows the grand average, over 6 subjects.

Note 1: This figure can be found as Figure 5 in Khaksari *et alia* Journal of Biomedical Optics (2018) [1].

venous relative contributions.

- The effectiveness of AR, with less negative phase values associated with a more effective AR (*id est* a smaller time constant τ_{AR}).

When both effects are present they may reinforce or compensate each other. The more negative phase (*id est* greater delay) of \tilde{T}/\tilde{A} at larger ρ observed in Subject 1 in Khaksari *et alia* Journal of Biomedical Optics (2018) [1] is consistent with a smaller arterial-to-venous contribution in deeper tissue versus superficial tissue which dominates the other effect due to improved AR that is likely to be detected at larger ρ . Because the arterial term is frequency independent, we can verify the trend of the arterial term by consid-

ering \tilde{T} and \tilde{A} oscillations at the heart rate frequency (where the arterial contribution term in Equation 8.1 dominates). We observed a significant decrease of the amplitude of \tilde{T}/\tilde{A} versus ρ , not just in Subject 1 but in all subjects in Khaksari *et alia* Journal of Biomedical Optics (2018) [1]. This result is shown in Figure 8.5, where the grand average of the amplitude of \tilde{T}/\tilde{A} at the heart rate is plotted as a function of ρ . The heart rate throughout the 11 min protocol was (1.41 ± 0.07) Hz, (1.29 ± 0.05) Hz, (1.4 ± 0.1) Hz, (1.34 ± 0.07) Hz, (0.98 ± 0.04) Hz and (0.89 ± 0.03) Hz, for Subjects 1-6 in Khaksari *et alia* Journal of Biomedical Optics (2018) [1], respectively. In Subjects 2,3,4&6 in Khaksari *et alia* Journal of Biomedical Optics (2018) [1] we

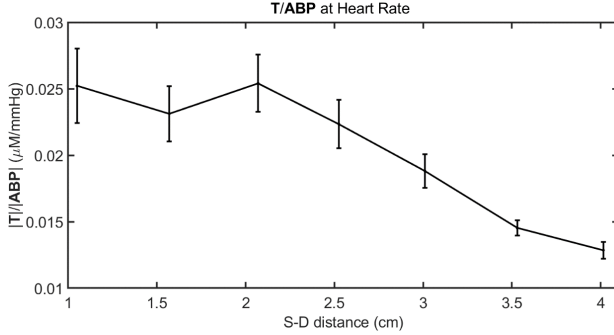


Figure 8.5: Grand average of the amplitude of phasor ratio vector between Total-hemoglobin and Arterial blood pressure phasor ($\overrightarrow{T}/\overrightarrow{A}$) versus source-detector distance (ρ) at the heart rate for all subjects in Khaksari *et alia* Journal of Biomedical Optics (2018) [1].

Note 1: This figure can be found as Figure 6 in Khaksari *et alia* Journal of Biomedical Optics (2018) [1].

observed a constant phase of $\overrightarrow{T}/\overrightarrow{A}$, suggesting that the reduced arterial-to-venous contributions may have been compensated by a more effective AR in deeper (cerebral) versus superficial (extracerebral) tissue.

8.2.1.A.b Deoxy-Hemoglobin versus Oxy-Hemoglobin Phasor Ratio Vector

Figure 8.6 shows the amplitude ratio (panel (a)) and the phase difference (panel (b)) for $\overrightarrow{D}/\overrightarrow{O}$ for each subject, with insets reporting the grand average over all subjects. In most subjects, the amplitude of $\overrightarrow{D}/\overrightarrow{O}$ as a function of ρ shows an initial decrease (up to a distance of 20 mm to 35 mm, depending on the subject) followed by an increase up to the maximum distance of 40 mm.

The phase of $\overrightarrow{D}/\overrightarrow{O}$ shows a consistent and significant increase with ρ in all subjects. Depending on whether one considers a positive or negative phase difference between Deoxy-hemoglobin (D) and Oxy-hemoglobin (O) oscillations, this means that D oscillations lead by a greater amount or lag by a lesser amount, respectively, oscillations in O. We have previously argued that one should consider the phase of $\overrightarrow{D}/\overrightarrow{O}$ to be negative, meaning that D oscillations lag O oscillations, and this is the reason for the negative phases reported in

Figure 8.6(b).

8.2.1.B Discussion of Single-Distance Multi-Distance Cuff Oscillations

In Khaksari *et alia* Journal of Biomedical Optics (2018) [1], we studied the amplitude and phase relationships of $\overrightarrow{T}/\overrightarrow{A}$, as well as $\overrightarrow{D}/\overrightarrow{O}$ as a function of ρ (10 mm to 40 mm) at one frequency (0.1 Hz) of cyclic inflation and deflation of pneumatic thigh cuffs. NIRS measurements at longer ρ feature a greater Sensitivity to absorption change (S) to deeper tissue (Figure 2.1), so that the measurements reported here provide information on the transition from a weak S to the brain (10 mm) to a stronger S to the brain (40 mm). We assume here that our hemodynamic models are applicable to NIRS data collected at different ρ s, by considering physiological parameters that depend on ρ . The dependence on d provides an indication of the different values of physiological parameters, *exempli gratia* the AR time constant, in superficial versus cerebral tissue.

It would be of practical use to extract information on the brain AR by using a MD source-detector arrangement and using only one frequency of the inducing oscillating mechanism. Our results for $\overrightarrow{T}/\overrightarrow{A}$ 0.1 Hz (Figure 8.4) show that their amplitude ratio decreases monotonically with ρ (Figure 8.4(a)), whereas their phase difference is approximately constant (Figure 8.4(b)). The trend of the amplitude $\overrightarrow{T}/\overrightarrow{A}$ as a function of ρ reflects the mechanical constraint set by the skull, which limits the cerebral BV response to changes in ABP. This effect is more relevant at larger values of ρ , where the optical channels are more sensitive to cerebral hemodynamic oscillations. About the phase trend of $\overrightarrow{T}/\overrightarrow{A}$, we have argued that two competing mechanisms occur:

- A reduced arterial versus venous contribution at larger values of ρ (which causes a more negative phase angle of $\overrightarrow{T}/\overrightarrow{A}$).
- A smaller value of τ_{AR} at increasing ρ (which causes a less negative phase angle of $\overrightarrow{T}/\overrightarrow{A}$).

The latter behavior reflects the increased sensitivity of optical measurement at larger ρ to the

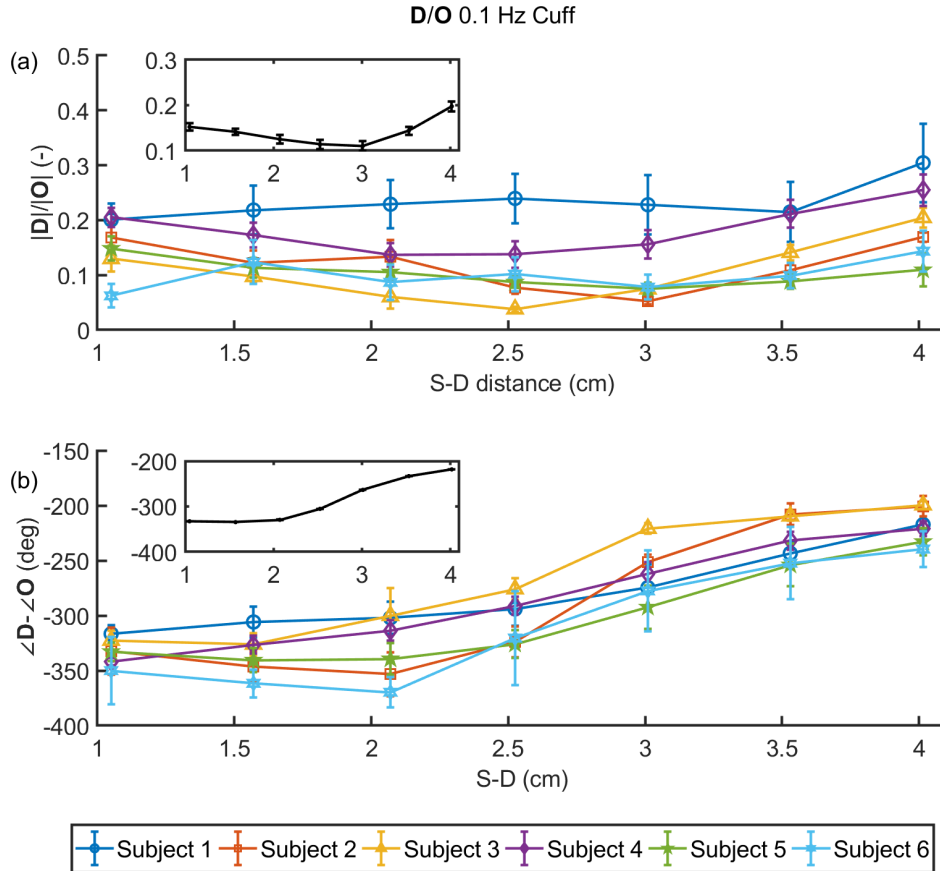


Figure 8.6: Amplitude (a) and phase (b) of phasor ratio vector between Deoxy-hemoglobin and Oxy-hemoglobin (\tilde{D}/\tilde{O}) as a function of source-detector distance (ρ) at 0.1 Hz for all subjects in Khaksari *et alia* Journal of Biomedical Optics (2018) [1]. The inset in each panel shows the grand average, over the 6 subjects.

Note 1: This figure can be found as Figure 7 in Khaksari *et alia* Journal of Biomedical Optics (2018) [1].

cerebral arterioles that regulate brain AR. More precisely, Figure 8.4(a)(b) are consistent with both arterial and venous contributions to Total-hemoglobin (T) that decrease with ρ , but with the arterial contribution decreasing faster than the venous one, and an AR time constant τ_{AR} that decreases with ρ (a smaller τ_{AR} corresponds to a more effective AR). Because of these two competing mechanisms it is possible that in some subjects (*exempli gratia* in Subject 1 in Khaksari *et alia* Journal of Biomedical Optics (2018) [1]) one mechanism prevails on the other, yielding a ρ dependence in the relative phase of \tilde{T}/\tilde{A} . Therefore, because the modeled transfer function between ABP and T depends on two competing contributions that feature different frequency de-

pendencies (the arterial one is frequency independent, at least in the frequency range of interest here), their discrimination may be achieved by collecting data at multiple frequencies, in the spirit of the CHS approach.

We have also shown how the measurements of \tilde{D} and \tilde{O} , especially the increase in their phase angle with ρ , is a direct signature of improved AR according to our CHS mathematical model1 which has been used in Figure 6.1. We have decomposed the measured phasors \tilde{O} and \tilde{D} into their BV (\tilde{O}_V , \tilde{D}_V) and Blood-Flow (BF) (\tilde{O}_F , \tilde{D}_F) components, by assuming a value of 75 % for the hemoglobin saturation of the volume oscillating compartment [81]. A larger phase of \tilde{D} (at larger ρ), impacts the amplitude of \tilde{T} (as shown

in the results) and impacts also the phase between the blood Flow unit phasor (\hat{F}) and \tilde{A} , which is an indicator of cerebral AR. Figure 6.1 also provides a visual interpretation of the result of Figure 8.6. In fact, given the weak sensitivity of the phase of \tilde{T} and \tilde{O} on the ρ , one would expect a minimum value of the magnitude of \tilde{D} when the phase angle of \tilde{D}/\tilde{O} is about 90° (or -270°), which is confirmed in Figure 8.6, especially in the insets that report the grand average over all subjects.

In summary, the results in Khaksari *et alia* Journal of Biomedical Optics (2018) [1] showed an increase in the phase angle between \tilde{O} and \tilde{D} at larger ρ . This was assigned to greater BF versus BV contributions and to a stronger BF AR in deeper tissue (brain cortex) with respect to superficial tissue (scalp, skull). The relatively constant phase lag of \tilde{T}/\tilde{A} at all ρ was assigned to competing effects from stronger AR and smaller arterial-to-venous contributions in deeper tissue with respect to superficial tissue. This work demonstrated the application of the CHS model to interpret hemodynamics measured with NIRS and to assess the different nature of shallow (extracerebral) versus deep (cerebral) tissue hemodynamics.

8.2.2 Considering Various Oscillations with Frequency-Domain Data Types

In Blaney *et alia* Photonics (2019) [2], we reported Frequency-Domain (FD) NIRS measurements on the forehead of healthy human subjects, during paced breathing and cuff oscillations at 0.1 Hz. This protocol is typical of CHS and very similar to that discussed for Khaksari *et alia* Journal of Biomedical Optics (2018) [1] but with the addition of more repeated measurements, measurement locations (bilateral), paced breathing, phase (ϕ) data, and Single-Slope (SS) data. As before the probe in Figure 2.3 was utilized to realize MD measurements. The rationale for this study is the sets of NIRS data, as discussed in Part I, which feature different levels of sensitivity to deeper versus superficial tissue may provide indications on cerebral versus

extracerebral tissue hemodynamics, thus helping to address the issue of extracerebral tissue contamination in NIRS signals.

8.2.2.A Summary of Frequency-Domain Multi-Distance Oscillation Results

An example trace of the data collected from cuff oscillations in Blaney *et alia* Photonics (2019) [2] can be found in Figure 8.1. These temporal traces were further analyzed to extract \tilde{D}/\tilde{O} for the various FD data-types of Single-Distance (SD) or SS with either Intensity (I) or ϕ .

8.2.2.A.a Absolute Optical Properties

Table 8.1 reports the baseline absolute optical properties from the calibrated linear slopes method in Appendix B, at the 2 optical wavelengths (λ s) of 690 nm and 830 nm, averaged over all days and locations for the five subjects in Blaney *et alia* Photonics (2019) [2]. From the absorption coefficient (μ_a) at two λ s, we have obtained absolute concentrations of O, D, and T, as well as tissue oxygen Saturation (S) assuming a 70 % Water (W) [66] using the methods in Appendix D. The measured values of optical properties and hemoglobin parameters are consistent with previously reported values using a similar FD, MD approach [66].

8.2.2.A.b Coherence Between Arterial Blood Pressure and One of Oxy-hemoglobin, Deoxy-hemoglobin, or Total-Hemoglobin

The temporal traces of wavelet Coherence (\mathfrak{C}) at a frequency of 0.1 Hz are reported in Figure 8.7 for Coherence between Oxy-hemoglobin and Arterial blood pressure phasor ($\mathfrak{c}(\tilde{O}, \tilde{A})$) (Figure 8.7(a)(b)), Coherence between Deoxy-hemoglobin and Arterial blood pressure phasor ($\mathfrak{c}(\tilde{D}, \tilde{A})$) (Figure 8.7(c)(d)), and Coherence between Total-hemoglobin and Arterial blood pressure phasor ($\mathfrak{c}(\tilde{T}, \tilde{A})$) (Figure 8.7(e)(f)), for Oxy-hemoglobin concentration change (ΔO), Deoxy-hemoglobin concentration change (ΔD), and Total-hemoglobin concentration change (ΔT) obtained with SD I , SS I , and SD ϕ data. Figure 8.7(a)(c)(e) are

Table 8.1: Average baseline optical properties, hemoglobin concentrations, and hemoglobin saturation for the 5 subjects from Blaney *et alia* Photonics (2019) [2].

Gender	Age (yr)	$\mu_a(690 \text{ nm})$ (mm $^{-1}$)	$\mu_a(830 \text{ nm})$ (mm $^{-1}$)	$\mu'_s(690 \text{ nm})$ (mm $^{-1}$)	$\mu'_s(830 \text{ nm})$ (mm $^{-1}$)	O (μM)	D (μM)	T (μM)	S (%)
Female	25	0.0098 ± 0.0006	0.0106 ± 0.0006	0.90 ± 0.05	0.75 ± 0.04	22 ± 3	18 ± 2	40 ± 3	55 ± 4
Female	29	0.010 ± 0.001	0.0104 ± 0.0005	1.05 ± 0.08	0.89 ± 0.03	19 ± 3	18 ± 2	37 ± 3	51 ± 5
Male	29	0.011 ± 0.001	0.0125 ± 0.0008	1.00 ± 0.04	0.80 ± 0.01	28 ± 3	18 ± 2	46 ± 4	60 ± 4
Female	34	0.0095 ± 0.0009	0.0092 ± 0.0003	0.89 ± 0.05	0.69 ± 0.03	18 ± 2	17 ± 1	35 ± 2	51 ± 3
Male	53	0.012 ± 0.001	0.013 ± 0.001	1.07 ± 0.06	0.86 ± 0.05	31 ± 4	20 ± 3	51 ± 6	61 ± 2

Note 1 These values can be found as Table 1 of Blaney *et alia* Photonics (2019) [2].

Note 2 Errors are the standard deviations.

Note 3 The absolute optical properties were calculated using the calibrated linear slopes method in Appendix B.

Note 4 The hemoglobin parameters are obtained assuming a 70 % water volume fraction and the methods in Appendix D.

Acronyms and Symbols Absorption coefficient (μ_a); reduced scattering coefficient (μ'_s); Oxy-hemoglobin (O); Deoxy-hemoglobin (D); Total-hemoglobin (T); and tissue oxygen Saturation (S).

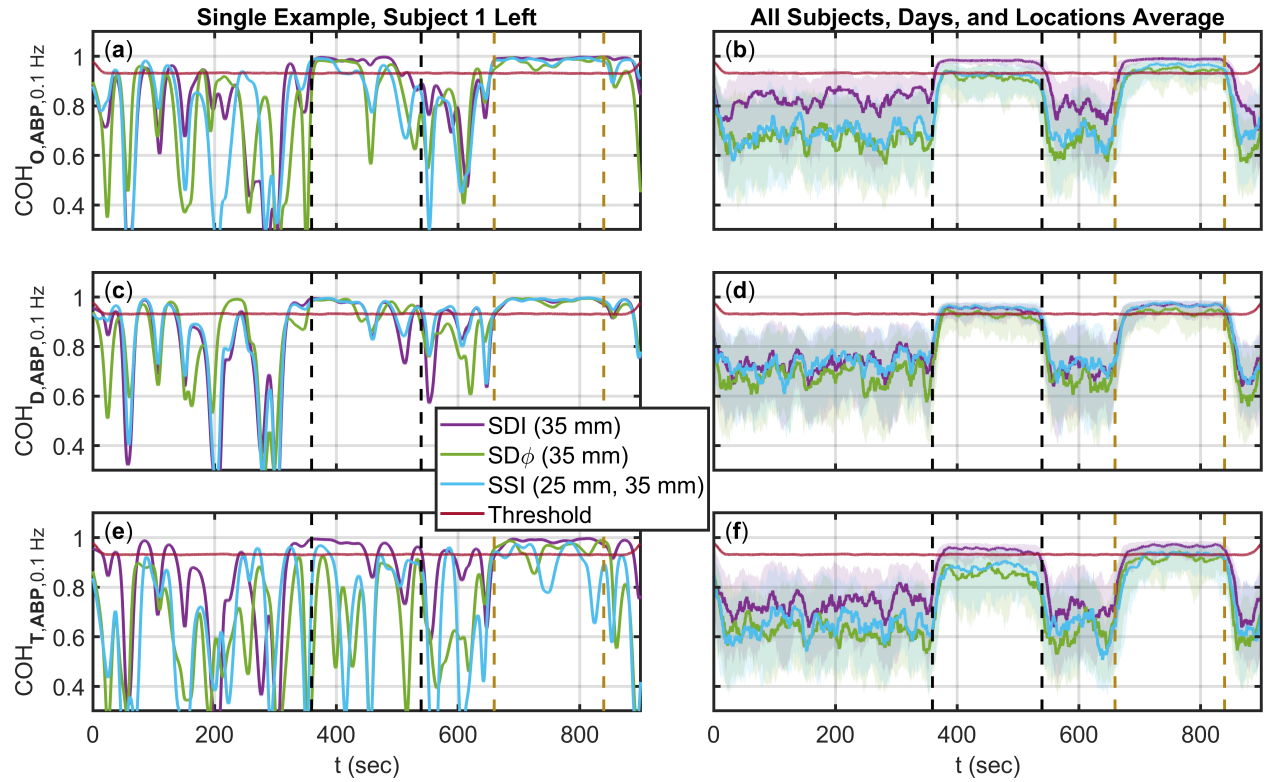


Figure 8.7: Temporal traces of Coherence (\mathcal{C}) at 0.1 Hz for 3 phasor pairs Coherence between Oxy-hemoglobin and Arterial blood pressure phasor ($\mathcal{C}(\tilde{O}, \tilde{A})$), Coherence between Deoxy-hemoglobin and Arterial blood pressure phasor ($\mathcal{C}(\tilde{D}, \tilde{A})$), and Coherence between Total-hemoglobin and Arterial blood pressure phasor ($\mathcal{C}(\tilde{T}, \tilde{A})$). Shown for 3 analysis methods Single-Distance (SD) Intensity (I) (Purple), SD phase (ϕ) (Green), and Single-Slope (SS) I (Cyan). Threshold of significant wavelet \mathcal{C} determined via Chapter 7 is also shown (Maroon). Time periods of induced cuff oscillations (Dashed Black) and induced paced breathing (Dashed Mustard) oscillations shown. (a)(b): $\mathcal{C}(\tilde{O}, \tilde{A})$ at 0.1 Hz. (c)(d): $\mathcal{C}(\tilde{D}, \tilde{A})$ at 0.1 Hz. (e)(f): $\mathcal{C}(\tilde{T}, \tilde{A})$ at 0.1 Hz. (a)(c)(e): Example subject, day, and location from Blaney *et alia* Photonics (2019) [2]. (b)(d)(f): Average across all subjects, days, and locations from Blaney *et alia* Photonics (2019) [2], with error regions shown as Inter-Quartile Range (IQR).

Note 1: This figure can be found as Figure 3 in Blaney *et alia* Photonics (2019) [2].

for a single measurement session on a single subject (Subject 1 in Blaney *et alia* Photonics (2019) [2]) and single location (left), whereas Figure 8.7(b)(d)(f) are the average over all subjects, all days, and both locations from Blaney *et alia* Photonics (2019) [2]. The time periods featuring cyclic cuff inflation and paced breathing at 0.1 Hz are indicated by black and mustard vertical dashed lines, respectively, and they feature induced hemodynamics at 0.1 Hz. During baseline, low-frequency spontaneous hemodynamic oscillations in the 0.1 Hz frequency region are present as a result of systemic physiological oscillations as well as local vasomotion [100]. Figure 8.7 also shows the threshold for significant \mathcal{C} from Chapter 7. Figure 8.7 shows that tissue hemodynamics at 0.1 Hz feature a much greater level of \mathcal{C} with ABP during cyclic cuff inflation and paced breathing than during baseline. For this reason, in the following we only consider coherent hemodynamics during cyclic cuff inflation and during paced breathing. Furthermore, the \mathcal{C} of SD I data is typically greater than the \mathcal{C} of SS I , and SD ϕ data. This latter result is certainly determined, at least in part, by the greater noise of SS I , and SD ϕ data with respect to SD I data, but it may also result from a greater \mathcal{C} between superficial hemodynamics (to which SD I data are strongly sensitive) and ABP, versus cerebral hemodynamics and ABP.

8.2.2.A.c Deoxy-Hemoglobin and Oxy-Hemoglobin Phasor Ratio as a Function of Source-Detector Distance for Different Measurement Methods Optical measurements exhibit increasing S to deeper tissue as the ρ (*id est*, the distance between the illumination and collection points) increases (Figure 2.1). This is true for both SD and SS methods (Figures 2.1&2.2). It is also important to consider that I and ϕ data feature different S to deeper versus superficial tissue. Figure 8.8 reports the SD I and SD ϕ measurements at ρ from 11 mm to 40 mm (Figure 2.3), as well as SS I obtained from data at two ρ separated by approximately 10 mm (in this case, the data points are assigned

to the mean ρ in Figure 8.8) for the amplitude and phase $\overrightarrow{D}/\overrightarrow{O}$. Data for both protocols, cyclic cuff inflation, and paced breathing are shown in Figure 8.8 for one representative subject (Subject 1 in Blaney *et alia* Photonics (2019) [2]) and both sides of the forehead (Figure 8.8(a)(c): left; Figure 8.8(b)(d): right). For both protocols, there is a trend of SD I data versus ρ :

- The amplitude of $\overrightarrow{D}/\overrightarrow{O}$ increases from a value <0.1 at short ρ , to a value that approaches 0.5 at long ρ .
- The phase of $\overrightarrow{D}/\overrightarrow{O}$ evolves from an in-phase behavior (-360°) at short ρ to an opposition-of-phase behavior (-180°) at long ρ .

The results obtained at short ρ are consistent with superficial tissue hemodynamics that mostly represent arterial BV oscillations (for which \tilde{D} and \tilde{O} would be in phase, and their amplitude ratio would reflect the oxygen saturation of the oscillating arterial compartment as in Figure 6.1 [43]). The results obtained at long ρ are consistent with deeper tissue hemodynamics that are characterized mostly by BF oscillations (for which \tilde{D} and \tilde{O} would be in opposition of phase, and would have the same amplitude as in Figure 6.1 [43]). In fact, SD ϕ and SS I data, which are more specifically sensitive to deeper tissue, yield relatively large values (>0.5) for the amplitude of $\overrightarrow{D}/\overrightarrow{O}$ and opposition-of-phase (-180°) conditions for the phase of $\overrightarrow{D}/\overrightarrow{O}$. This point is reinforced by the significantly greater amplitude of $\overrightarrow{D}/\overrightarrow{O}$ measured with SD ϕ (35 mm) versus SD I (35 mm) (p -value < 0.0001), and with SS I (30 mm and 40 mm) versus SD I (35 mm) (p -value < 0.0001). It is worth noting that SD I data (and, to a lesser extent, SD ϕ data) still show an increasing trend for the amplitude ratio versus ρ , whereas the phase of $\overrightarrow{D}/\overrightarrow{O}$ is relatively insensitive to the ρ used for SD I and SD ϕ measurements unless very short ρ are considered.

It is apparent from Figure 8.8 that SS I and SD ϕ measurements at ρ of approximately 20 mm yield values of $\overrightarrow{D}/\overrightarrow{O}$ that are only obtained at longer ρ (>35 mm) with SD I . Particularly for the amplitude of $\overrightarrow{D}/\overrightarrow{O}$, it appears that the val-

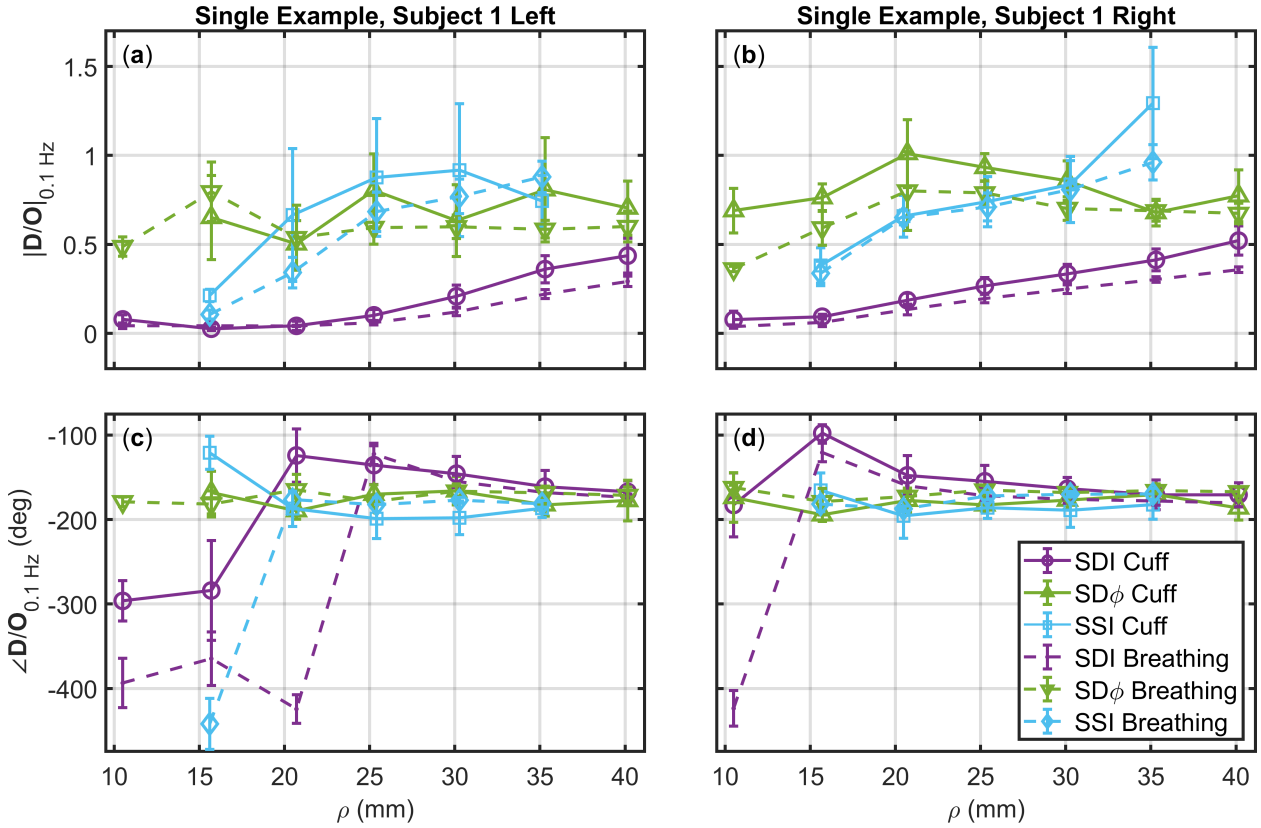


Figure 8.8: Amplitude ((a)(b)) and phase ((c)(d)) of phasor ratio vector between Deoxy-hemoglobin and Oxy-hemoglobin (\bar{D}/\bar{O}) at 0.1 Hz as a function of source-detector distance (ρ). Data were measured on Subject 1 in Blaney *et alia* Photonics (2019) [2] on the left side ((a)(c)) and on the right side ((b)(d)) of the subject’s forehead. Shown for the cyclic thigh cuff inflation (Solid Lines) and paced breathing (Dashed Lines) protocols, and three analysis methods: Single-Distance (SD) Intensity (I) (Purple), SD phase (ϕ) (Green), and Single-Slope (SS) I (Cyan).

Note 1: This figure can be found as Figure 4 in Blaney *et alia* Photonics (2019) [2].

Note 2: SS I measurements analyzed with two sources spaced by 10 mm, plotted such that ρ is the average of the source-detector distances of the two sources.

Note 3: Error bars represent the standard deviation of all analyzed pixels that show significant Coherence (C) in the wavelet transfer function scalogram (Appendix G).

ues obtained with SS I and SD ϕ at 25 mm represent asymptotic values for SD I (*id est*, values that are attained with SD I in the limit of large ρ) that are not reached even at the largest ρ considered (40 mm). These results reported for a single subject in Figure 8.8, are confirmed by the average over all subjects, shown in Figure 2.5(a)(c) and backed up by phasor simulations Figure 2.5(b)(d).

8.2.2.A.d Deoxy-Hemoglobin and Oxy-Hemoglobin Phasor Ratio Measured at

Long Source-Detector Distances with Different Methods Figure 8.9 shows \bar{D}/\bar{O} for each individual subject (left side, average over all measurement days) and for both protocols (cuff and paced breathing) from Blaney *et alia* Photonics (2019) [2] measured with SD I (35 mm), SD ϕ (35 mm), and SS I (25 mm and 35 mm). These long ρ measurements (approximately 25 mm to 35 mm) are typically used in cerebral NIRS as it is well established that they achieve a suitable penetration depth to probe the brain. We recall that the amplitude and the phase of \bar{D}/\bar{O}

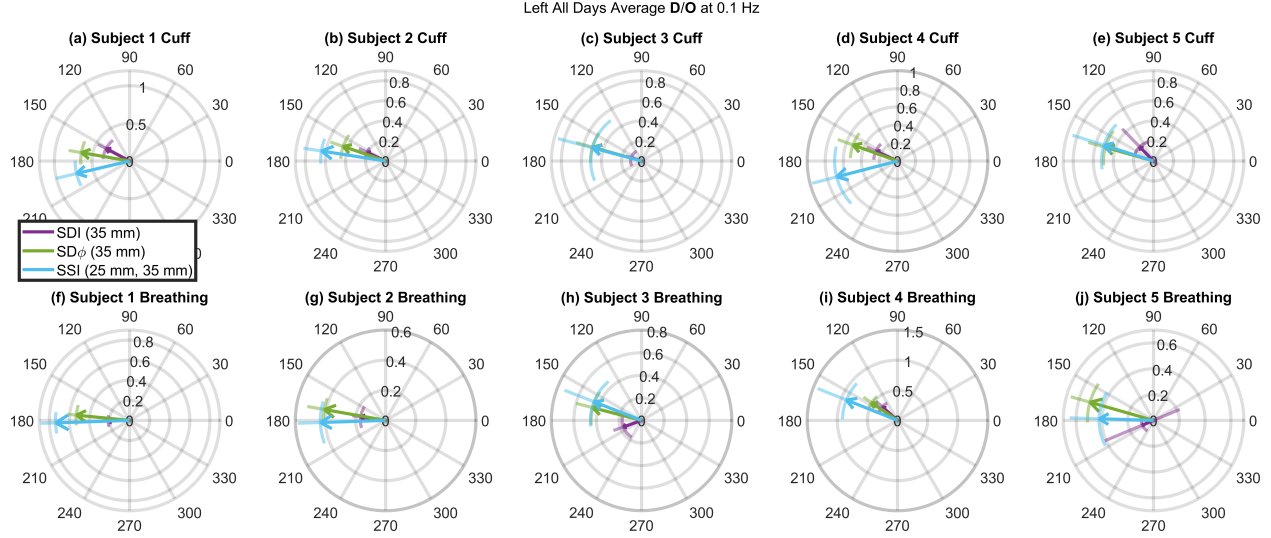


Figure 8.9: Phasor ratio vector between Deoxy-hemoglobin and Oxy-hemoglobin ($\overrightarrow{D}/\overrightarrow{O}$) whose magnitude and phase represent the amplitude ratio and the phase difference, respectively of the Deoxy-hemoglobin phasor (\tilde{D}) and Oxy-hemoglobin phasor (\tilde{O}) phasors at 0.1 Hz. The $\overrightarrow{D}/\overrightarrow{O}$ are averaged over all days for each subject in Blaney *et alia* Photonics (2019) [2] at 1 location (left side of the forehead). 3 measurement methods are shown: Single-Distance (SD) Intensity (I) (Purple), SD phase (ϕ) (Green) and Single-Slope (SS) I (Cyan). (a)(b)(c)(d)(e) refer to the cyclic cuff inflation protocol, whereas (f)(g)(h)(i)(j) refer to the paced breathing protocol. Each column (a)(f), (b)(g), (c)(h), (d)(i), and (e)(j) refers to 1 subject from Blaney *et alia* Photonics (2019) [2], as indicated in the title of each rose.

Note 1: This figure can be found as Figure 6 in Blaney *et alia* Photonics (2019) [2].

Note 2: Error bars are shown as arcs for the phase and line segments extending from the arrow point for the amplitude. These show standard deviation of all analyzed pixels over all days that show significant coherence in the wavelet transfer function scalogram (Appendix G).

(*id est*, the length and direction of the arrows in Figure 8.9) represent the amplitude ratio and the phase difference, respectively, of the \tilde{D} and \tilde{O} phasors.

A first result of Figure 8.9 is that the amplitude of $\overrightarrow{D}/\overrightarrow{O}$ is consistently and significantly greater when measured with SS I and SD ϕ (values of about 0.4 or more) than with SD I (values of about 0.2 or less) (p -value < 0.0001). This result suggests that brain tissue (which is most effectively probed with SS I and SD ϕ versus SD I) features amplitudes of ΔD oscillations that approach the amplitude of ΔO oscillations.

A second result of Figure 8.9 is that the phase of $\overrightarrow{D}/\overrightarrow{O}$ is significantly closer to -180° when measured with SS I or SD ϕ than with SD I (p -value < 0.0001 for both). By recalling that pure BF velocity oscillations (or oscillations in

metabolic rate of oxygen) result in \tilde{O} and \tilde{D} that are in opposition of phase, this result suggests that brain tissue features BF oscillations that dominate over BV oscillations.

8.2.2.B Discussion of Frequency-Domain Multi-Distance Oscillations

The dependence of measured hemodynamics in Blaney *et alia* Photonics (2019) [2] on p , the results obtained with the two protocols (cyclic cuff occlusion, paced breathing) are similar (Figures 2.5&8.8). A close inspection of the results obtained at large p separation (Figure 8.9) shows some differences between the SD I data collected in the two protocols. Typically, the phase of $\overrightarrow{D}/\overrightarrow{O}$ is more negative in the cuff protocol than in the paced breathing protocol. If this result

is assigned to the brain, a possible explanation is the better cerebral AR during paced breathing, if the subject hyperventilates and therefore creates hypocapnia [10]. However, this difference between protocols is not visible in the SS *I* data, for which the phase of \tilde{D}/\tilde{O} vectors are closer and do not show a consistent phase difference between protocols, and even less so in the SD ϕ data, for which the phase of \tilde{D}/\tilde{O} vectors is essentially the same for the two protocols. Therefore, we assign the differences between protocols observed in the SD *I* data to extracerebral tissue contributions, as a result of variable scalp hemodynamic changes in the 2 protocols. While the relatively small number of subjects (5) in Blaney *et alia* Photonics (2019) [2] does not allow for a statistically significant comparison of the results obtained with the two protocols, we contend that the subjective nature of the paced breathing protocol will introduce a level of variability that is intrinsically linked to the specific subject population. The value of the results reported in this work, which fall short of demonstrating the equivalence or the difference between the two protocols for CHS, lies in confirming the feasibility of both protocols for CHS and in demonstrating a qualitative similarity of the coherent hemodynamics elicited by the 2 protocols.

We did not observe consistent differences between the right and left sides of the forehead, and across measurement days in Blaney *et alia* Photonics (2019) [2], at least not within the experimental uncertainties of measured amplitude and phase of \tilde{O} and \tilde{D} . For this reason, we opted to resort to averages over all subjects, days, and locations in Figure 2.5(a)(c) and over all days in Figure 8.9. However, the temporal and spatial variability of oscillatory cerebral hemodynamics in response to controlled systemic perturbations, as studied in CHS, is worth of careful consideration as it may provide valuable functional and physiological information [43]. The spatial dependence of coherent cerebral hemodynamics is an important future direction for CHS imaging.

A key finding of this study is that measurements of the \tilde{D}/\tilde{O} vector that are more sensitive to brain tissue indicate amplitude of \tilde{D} and \tilde{O} that are comparable in amplitude and that ap-

proach opposition of phase. This result is consistent with the previous sections and Khaksari *et alia* Journal of Biomedical Optics (2018) [1] based on SD *I* measurements during a cyclic thigh cuff occlusion protocol. The CHS model shows that \tilde{D} and \tilde{O} are in phase in the case of pure BV oscillations (because both D and O change in the same direction as a result of BV changes), whereas they are in opposition of phase in the case of pure BF oscillations (because in the absence of BV changes any increase in O must be associated with a decrease in D and *vice versa*) [43]. This relationship is explained in Figure 6.1 and Chapter 6. Nevertheless, it is well established that cerebral BV changes during brain activation, with increases of the order of 30% as measured with functional Magnetic Resonance Imaging (fMRI) [101, 102]. Such BV changes appear to be inconsistent with the in-compressible nature of brain tissue and its enclosure within the in-extensible skull. A possible resolution to this apparent paradox has been proposed by hypothesizing water exchange between capillaries and brain tissue to maintain a constant total tissue volume while expanding the capillary bed [103]. The optical measurements of hemoglobin concentration changes obtained with SD ϕ and SS *I*, which are more specific to the brain, may help elucidate the actual cerebral BV changes associated with the brain activation, hypercapnia, *et cetera*.

In summary, in Blaney *et alia* Photonics (2019) [2] we found that, on average, the \tilde{D}/\tilde{O} obtained with SD *I* at 11 mm to 40 mm changes from $0.1\angle-330^\circ$ to $0.2\angle-200^\circ$, respectively. SD ϕ and the SS *I* featured a weaker dependence on p separation, and yielded \tilde{D}/\tilde{O} of about $0.5\angle-200^\circ$ at p greater than 20 mm. The key findings from these results were:

- SD ϕ and SS *I* are sensitive to deeper tissue compared to SD *I*.
- Deeper tissue hemodynamic oscillations, which more closely represent the brain, feature \tilde{D} and \tilde{O} that are consistent with a greater relative BF to BV contributions in brain tissue compared to extracerebral, superficial tissue.

These conclusions further reinforce the ones drawn in Khaksari *et alia* Journal of Biomedical Optics (2018) [1] and expands them to various FD data-types.

8.3 Dual-Slope Study

In the work presented in previous sections, namely Khaksari *et alia* Journal of Biomedical Optics (2018) [1], and Blaney *et alia* Photonics (2019) [2], we reported the hemodynamics measured at a range of source-detector distance (ρ) (11 mm to 40 mm) using Single-Distance (SD) Intensity (I), SD phase (ϕ), and Single-Slope (SS) I . In Blaney *et alia* Journal of Biophotonics (2020) [3], we reported human brain measurements conducted with Frequency-Domain (FD) Near-Infrared Spectroscopy (NIRS) during a typical Coherent Hemodynamics Spectroscopy (CHS) protocol, in which we compare all 6 methods of data analysis available in a Dual-Slope (DS) probe (Figure 3.1) in the point measurement mode (Chapter 4). The experimental schematic can be found in Figure 4.1. Specifically, the 6 methods considered are: SD, SS, and (for the first time in Blaney *et alia* Journal of Biophotonics (2020) [3]) DS for I and ϕ . The DS probe used for these experiments is shown in Figure 3.1 which contained ρ s of 25 mm and 35 mm. Example traces from this first DS CHS study are shown in Figure 4.3.

8.3.1 Summary of First Frequency-Domain Dual-Slope Oscillation Results

8.3.1.A Phase and Amplitude Relationships of Total-Hemoglobin and Arterial Blood Pressure During Systemic Oscillations for Different Measurement Methods

Figure 8.10 shows the phase and amplitude of phasor ratio vector between Total-hemoglobin and Arterial blood pressure phasor (\bar{T}/\bar{A}) at 0.1 Hz during the cyclic inflation and deflation of the thigh cuffs for all 4 subjects and all measurement methods in Blaney *et alia* Journal of Bio-

photronics (2020) [3]. Notice that SD I has a consistent \bar{T}/\bar{A} relationship across all 4 subjects with a mean phase difference of (40 ± 4) deg and mean amplitude ratio of (0.037 ± 0.002) $\mu\text{M mmHg}^{-1}$ (5 % error). This is within the range of values for \bar{T}/\bar{A} at 0.1 Hz reported [82]. However, the other analysis methods (SD ϕ , SS, and DS) do not show this consistent relationship and feature a large variance in some cases. For example, DS ϕ shows a mean phase difference and amplitude ratio of (0.018 ± 0.005) $\mu\text{M mmHg}^{-1}$ and (10 ± 10) deg (28 % error), respectively. Generally, most other analysis methods' vectors are in quadrant IV (same as SD I), but SD I is the only method that shows such a consistent relationship for \bar{T}/\bar{A} .^b

8.3.1.B Phase and Amplitude Relationships of Deoxy-Hemoglobin and Oxy-Hemoglobin During Systemic Arterial Blood Pressure Oscillations for Different Measurement Methods

Figure 8.11 shows the phase and amplitude of phasor ratio vector between Deoxy-hemoglobin and Oxy-hemoglobin (\bar{D}/\bar{O}) at 0.1 Hz during the cuff oscillation period for all four subjects and all measurement methods in Blaney *et alia* Journal of Biophotonics (2020) [3]. Notice that the amplitude of \bar{D}/\bar{O} for SD I is smaller than for all other methods in all subjects, and that it shows no consistent value across subjects (ranging from 0.6 in Subject 1 to 0.07 in Subject 2 in Blaney *et alia* Journal of Biophotonics (2020) [3]). Similarly, the phase of \bar{D}/\bar{O} for SD I also does not show a consistent value (ranging from -187° in Subject 3 to -268° in Subject 2 within Blaney *et alia* Journal of Biophotonics (2020) [3]). In some cases (Subject 2 in Blaney *et alia* Journal of Biophotonics (2020) [3]) the SS measurements show different relative phase values than DS, while DS, particularly, DS ϕ shows a consistent phase and amplitude of \bar{D}/\bar{O} across all subjects with a mean phase of (-196 ± 2) deg and a mean amplitude of 0.75 ± 0.08 (11 % error). This compared to

^b Errors stated in this section are Standard-Error of the Mean (SEM).

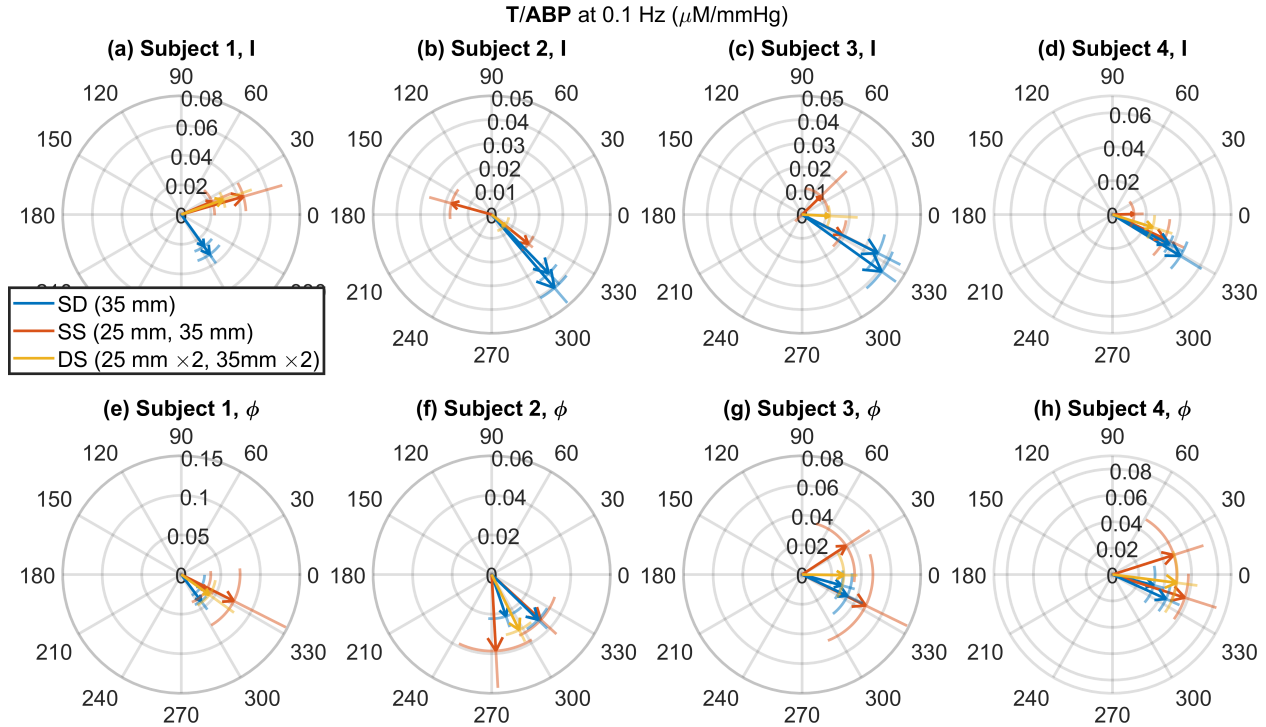


Figure 8.10: Phasor ratio vector between Total-hemoglobin and Arterial blood pressure phasor ($\overrightarrow{T/ABP}$) at 0.1 Hz. Shown for 3 analysis methods Single-Distance (SD) (Blue), Single-Slope (SS) (Orange), and Dual-Slope (DS) (Mustard); 2 data types Intensity (I) ((a) to (d)) and phase (ϕ) ((e) to (h)); and 4 subjects Subject 1 ((a) and (e)), Subject 2 ((b) and (f)), Subject 3 ((c) and (g)), and Subject 4 ((d) and (h)) from Blaney *et alia* Journal of Biophotonics (2020) [3].

Note 1: This figure can be found as Figure 5 in Blaney *et alia* Journal of Biophotonics (2020) [3].

SD I 's inconsistent phase difference and amplitude ratio with means of (-220 ± 10) deg and 0.20 ± 0.06 (30 % error), respectively.^b We were able to roughly recreate the measured vector relationships using phasor simulations in Figure 4.2.

8.3.2 Discussion Frequency-Domain Dual-Slope Oscillations

Examining Figure 8.11, and comparing ϕ results to I , the results for Deoxy-hemoglobin phasor (\overrightarrow{D}) and Oxy-hemoglobin phasor (\overrightarrow{O}) measured with ϕ show a closer opposition of phase (*id est* a phase closer to 180°) and a higher amplitude ratio (*id est* a ratio closer to 1) for $\overrightarrow{D}/\overrightarrow{O}$ suggesting a stronger contribution from Blood-Flow (BF) oscillations in the brain than in the scalp (Figure 6.1). This result is also consistent with previous results in previous sections which examined Multi-Distance (MD) data collected ρ in the

range 11 mm to 40 mm [1, 2], and also pointed to the deeper Sensitivity to absorption change (S) of ϕ compared to I .

The conclusions about the advantages of DS and ϕ in Part I are supported by comparing the simulations in Figure 4.2(g) to our experimental results for Subject 2 from Blaney *et alia* Journal of Biophotonics (2020) [3] in Figure 8.11(b), and by other work showing the possibility of heterogenous scalp hemodynamics [40]. Examining our experimental results for $\overrightarrow{D}/\overrightarrow{O}$ (Figure 8.11), we observe robust and consistent findings from DS data across subjects. This suggests that DS is the most robust measurement method, among those presented here, for non-invasive sensing of the human brain. This is likely due to the minimal S to the superficial layer and insensitivity to drifts (Chapter 3). Therefore, we conclude that DS coupled with ϕ (DS ϕ) features the deepest

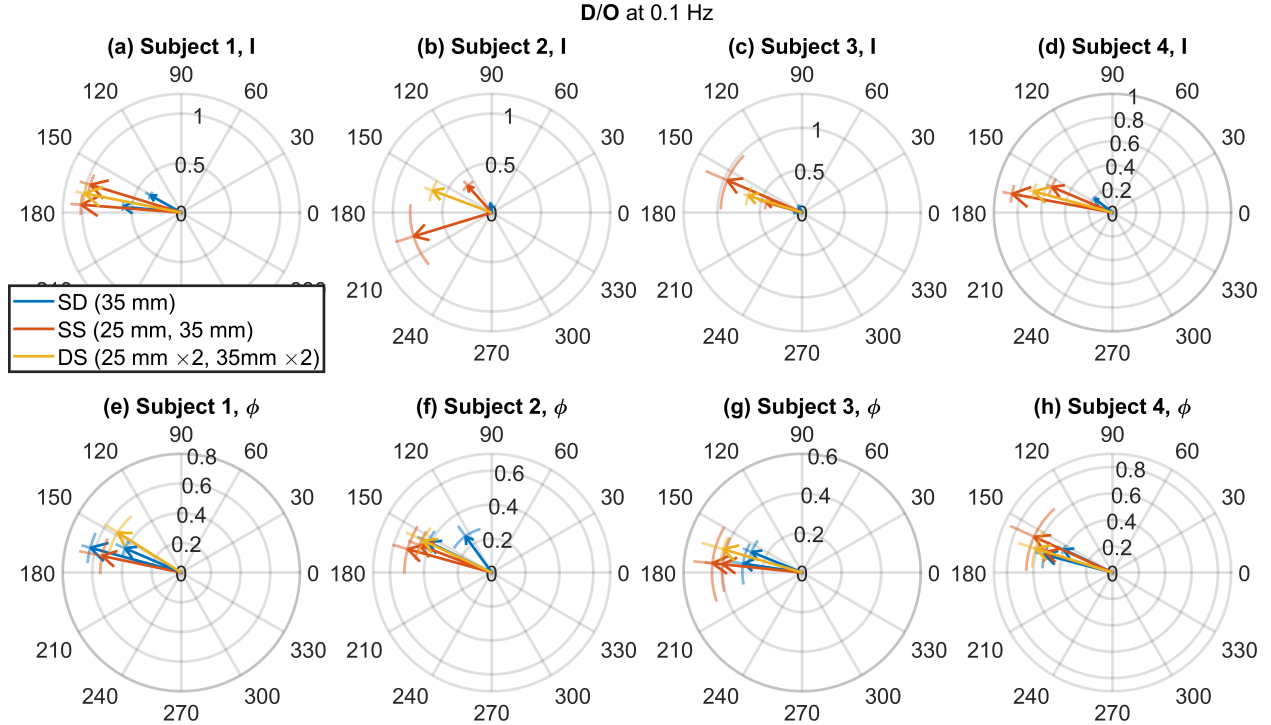


Figure 8.11: Phasor ratio vector between Deoxy-hemoglobin and Oxy-hemoglobin ($\overrightarrow{D/O}$) at 0.1 Hz. Shown for 3 analysis methods Single-Distance (SD) (Blue), Single-Slope (SS) (Orange), and Dual-Slope (DS) (Mustard); 2 data types Intensity (I) ((a) to (d)) and phase (ϕ) ((e) to (h)); and 4 subjects Subject 1 ((a) and (e)), Subject 2 ((b) and (f)), Subject 3 ((c) and (g)), and Subject 4 ((d) and (h)) from Blaney *et alia* Journal of Biophotonics (2020) [3].

Note 1: This figure can be found as Figure 6 in Blaney *et alia* Journal of Biophotonics (2020) [3].

maximal S , combined with the least superficial S , and is the most robust method among those considered here.

8.3.2.A A Greater Amplitude Ratio of Deoxy-Hemoglobin versus Oxy-Hemoglobin in the Brain Suggests a Smaller Blood Volume Change

Our experimental results for $\overrightarrow{D/O}$ (Figure 8.11) show a BF dominated oscillation in deeper layers when examined with the eyes of CHS (Figure 6.1) [43]. The closer the phase difference of $\overrightarrow{D/O}$ gets to -180° and its amplitude ratio to 1, the smaller the Total-hemoglobin phasor (\tilde{T}) amplitude. Total-hemoglobin (T) is considered a surrogate for Blood-Volume (BV). Thus, our results suggest less of a BV oscillation in the brain compared to the superficial layer, and more of a

BF oscillation in the brain. The effect of this is seen in our $\overrightarrow{T/A}$ results in Figure 8.10, where the most superficial methods (SD I) shows the most consistent relationship for $\overrightarrow{T/A}$. We presented model in Equation 8.1 based on these consistent $\overrightarrow{T/A}$ results measured with SD I [82]. However, the results presented here do not show the same consistent $\overrightarrow{T/A}$ for deeper tissue, suggesting that the previous data and model in Equation 8.1 may have been mostly representative of scalp hemodynamics.

It might be noted that the amplitude of $\overrightarrow{T/A}$ presented here is greater for all methods other than SD I . This result may be impacted by the coherence analysis (Chapter 7 and Appendix H), which preferentially selects higher amplitude \tilde{T} periods (due to their higher Coherence (C)). However, when we examine the relationship of $\overrightarrow{D/O}$ coupled with the less consistent results for

$\overline{T/\Delta}$, we can conclude that, in our results, the analysis methods sensitive to deeper tissue show either a smaller or less consistent **BV** oscillation.

This premise that the brain shows a small **BV** oscillation has been discussed in other works. Despite functional Magnetic Resonance Imaging (fMRI) having consistently measured **BV** changes [101, 102], the models involved require complicating fitting procedures and are not a direct measure of **BV** [101]. This, combined with the fact that the skull contains an incompressible fluid, has led to the suggestion that **BV** changes are in fact a redistribution of water from tissue to the vascular space [103]. NIRS methods, unlike fMRI, measure the **T** in units of effective tissue concentration. If there were a redistribution of water (leaving the amount of **T** the same) within the **S** volume of NIRS, little or no **BV** change would be measured with NIRS. Furthermore, work with fMRI has observed that changes resulting from brain activation are primarily caused by **BF** changes rather than by **BV** changes [104], in agreement with the results reported in Blaney *et alia* Journal of Biophotonics (2020) [3].

There has been evidence, from methods that preferentially measure the brain, in support of relatively small changes in **T**. Functional Near-Infrared Spectroscopy (fNIRS) studies have shown this result when analyzing the optical signals with Independent Component Analysis (ICA) [38] or a linear model [41], using a normalized time gating technique [52] or mean time-of-flight ($\langle t \rangle$) [53] in Time-Domain (TD). Additionally, the normalized time gating technique also showed little change in **T** during a systemic change [52]. Our results of a **BF** dominated hemodynamic oscillations in the brain may point to a smaller **BV** oscillation in the brain versus the scalp, a possibility that has been discussed and presented previously (primarily concerning the in-compressibility of fluid and rigidity of the skull). These are supported by what was reported using MD methods in the previous sections, Khaksari *et alia* Journal of Biomedical Optics (2018) [1], and Blaney *et alia* Photonics (2019) [2].

In summary, the *in vivo* results in Blaney *et*

alia Journal of Biophotonics (2020) [3] indicate a qualitative difference of ϕ data especially DS ϕ and **I** data especially SD **I**, which we assign to stronger contributions from scalp hemodynamics to SD **I** and from cortical hemodynamics to DS ϕ . Our findings suggest that scalp hemodynamic oscillations may be dominated by **BV** dynamics, whereas cortical hemodynamics may be dominated by **BF** dynamics. These conclusions are again consistent with the physiological conclusions from Khaksari *et alia* Journal of Biomedical Optics (2018) [1] and Blaney *et alia* Photonics (2019) [2].

Part III

Calibration-Free Spectroscopy

Chapter 9

Dual-Slope Based Absolute Broadband-Spectroscopy

9.1 Motivation for Dual-Slope Based Spectroscopy

Blaney *et alia* Applied Sciences (2021) [7] presented the design and validation of an instrument for Dual-Slope (DS) broadband Diffuse Reflectance Spectroscopy (bDRS). This instrument afforded calibration-free, Continuous-Wave (CW) measurements of broadband absorbance of optically diffusive media, which may be translated into absolute absorption coefficient (μ_a) spectra by adding Frequency-Domain (FD) measurements of reduced scattering coefficient (μ'_s) at two optical wavelengths (λ_s). μ_a and μ'_s are the chief quantities of interest in the field of diffuse optics and diffuse biomedical optics [17, 18, 105, 106], and they feature a λ dependence that is often of crucial importance. In the case of most biological tissues, the dominating scattering condition of diffuse optics is realized in the optical window used by Near-Infrared Spectroscopy (NIRS). Measurements of the λ dependent μ_a of tissue yields information about the concentration of chromophores with known extinction coefficient (ϵ) spectra, while measurements of μ'_s spectra yields structural information related to the size and density of scattering centers [17].

The primary difficulty in these measurements is the decoupling of μ_a and μ'_s contributions to the measured optical signal. Both FD and Time-Domain (TD) are capable of doing this [16, 107]. In FD both μ_a and μ'_s may be measured using the spatial dependence of linearized Inten-

sity ($\ln(\rho^2 I)$) and phase (ϕ) to retrieve complex effective attenuation coefficient ($\tilde{\mu}_{eff}$) as discussed in Appendix B. The chief complication of this technique is calibration, since each source-detector pair may have differing instrumental contributions (because of the individual source emission and detector sensitivity properties as seen in Chapter 3) and differing coupling factors between optodes and sample. A method which compensates for the differing instrumental contributions is the so-called Multi-Distance (MD) scanning, where either the source or the detector is moved across the surface of the optical medium [108]. In doing so, the instrumental factors remain the same for each source-detector distance (ρ) (same source and same detector used for each distance) and thus the measurement of slope is independent of these factors. However, differing coupling factors may still be present if during the scan the source (or detector) moves away or toward the tissue surface (in a non-contact case), or experiences a variable contact pressure (in a contact case). Aside from MD scanning, the Self-Calibrating (SC)/DS method is also capable of making absolute measurements [13, 61]. This is since calibration factors cancel in the averaging of slope as shown in Chapter 3. When the SC / DS optode geometry (Figure 3.1) is used for only measurement of one optical data-type it is named DS instead of Single-Distance (SD). When used in CW only Reflectance (R) is retrieved, so the method is referred to as DS. Using CW DS the calibration-free absolute effective attenuation coefficient (μ_{eff}) can be retrieved,

similar to how calibration-free absolute $\tilde{\mu}_{eff}$ can be retrieved from SC FD.^a

One of the limitations of time-resolved NIRS methods, such as FD NIRS, is the added instrumental complexity compared to CW. There has been work in broadband time-resolved spectroscopy [109], however, such instruments require complex instruments (super-continuum lasers, single photon counting, and instrument response calibration). Because of this, the norm in time-resolved NIRS methods is the use of two or a few λ s as opposed to a continuous broadband spectrum [16]. In contrast, CW methods may use broadband light sources, such as halogen lamps, and spectrometer detectors, since there is no need for measurements of fast temporal characteristics. These spectroscopic methods in CW lead to the name bDRS due to their collection geometry and use of a spectrometer as a detector (instead of Avalanche Photo-Diodes (APDs) or PhotoMultiplier Tubes (PMTs) typical in time-resolved methods). Therefore, CW bDRS has the advantage of collecting data over many λ s but the disadvantage that μ_a and μ'_s are coupled within μ_{eff} due to the use of CW illumination. A solution that has become more and more common is to combine a time-resolved NIRS instrument at few λ s with a CW bDRS system [110–115]. Such a technique allows extrapolation of scattering from few to many λ s, by assuming a power law decay of μ'_s with λ [17], and decoupling of μ_a from μ_{eff} retrieved from the CW bDRS data (Appendix B).

At this point, a small note on nomenclature is valuable. The acronym combination MD FD NIRS refers to a FD method capable of measuring absolute $\tilde{\mu}_{eff}$ (which can separate μ_a and μ'_s) at discrete λ s from measurements at multiple ρ s. The acronyms DS CW bDRS refers to a technique capable of measuring λ -resolved calibration-free μ_{eff} (which depends on μ_a and μ'_s) over a range of many λ s. It is noted that the distinction between SC and DS is the use of

^aEffective attenuation coefficient (μ_{eff}) can not be separated into absorption coefficient (μ_a) and reduced scattering coefficient (μ'_s) as complex effective attenuation coefficient ($\tilde{\mu}_{eff}$) can. To find μ_a from μ_{eff} , μ'_s must be known.

complex Reflectance (\tilde{R}) in SC FD versus R in DS DS (Appendix B).

9.2 Techniques, Experiments, and Absolute Absorption Retrieval

9.2.1 Techniques

9.2.1.A Frequency-Domain Multi-Distance Near-Infrared Spectroscopy

Frequency-Domain (FD) Near-Infrared Spectroscopy (NIRS) was implemented with the purpose of measuring absolute complex effective attenuation coefficient ($\tilde{\mu}_{eff}$) (to retrieve absorption coefficient (μ_a) and reduced scattering coefficient (μ'_s)) of highly scattering media. The ISS Imagent V2 [Champaign, IL USA] (Imagent) whose parameters were stated in Section 2.2.1.A was used for this purpose.

FD NIRS was implemented in a Multi-Distance (MD) scan. To achieve this, a single detector fiber bundle ($\phi 3\text{ mm}$) was held at a fixed location and two co-localized source fibers ($\phi 600\text{ }\mu\text{m}$; two optical wavelengths (λ s)) were scanned via a linear stage (Figure 9.1(a)). In doing so, the complex Reflectance (\tilde{R}) (amplitude and phase) was measured at 11 distances (from 15 mm to 25 mm spaced by 1 mm; Figure 9.1(b)). This MD scan allowed for measurements of \tilde{R} slopes versus source-detector distance (ρ) without the need for calibration.^b These measurements were used to calculate the absolute $\tilde{\mu}_{eff}$ and then the absolute μ_a and μ'_s of the diffuse medium as described in Appendix B.

9.2.1.B Continuous-Wave Dual-Slope Broadband Diffuse Reflectance Spectroscopy

Continuous-Wave (CW) broadband Diffuse Reflectance Spectroscopy (bDRS) was implemented

^bWithout calibration assuming unchanging coupling with the sample since the same fibers are used for each distance and the fiber/sample contact remains about the same during the linear scan.

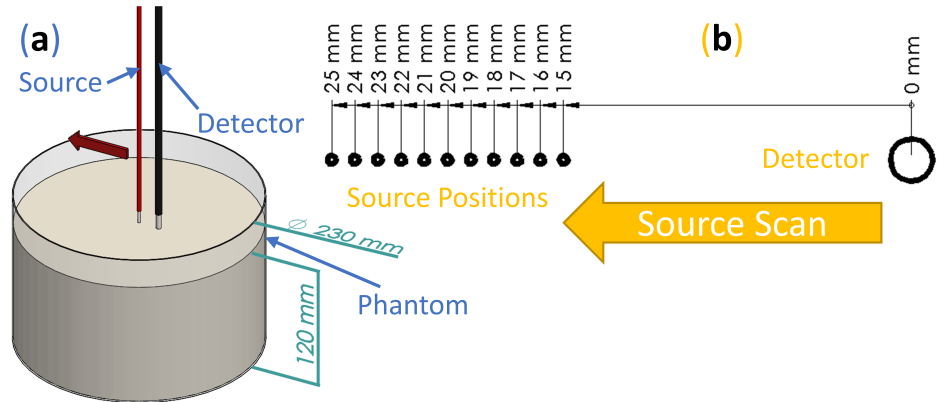


Figure 9.1: Frequency-Domain (FD) Near-Infrared Spectroscopy (NIRS) methods to achieve measurements of absolute complex effective attenuation coefficient ($\bar{\mu}_{eff}$). (a) Render of Multi-Distance (MD) scan done on diffuse optical phantoms. (b) Schematic of 11 different source-detector distance (ρ) realized during the MD scan.

Note 1: This figure can be found as Figure 1 in Blaney *et alia* Applied Sciences (2021) [7].

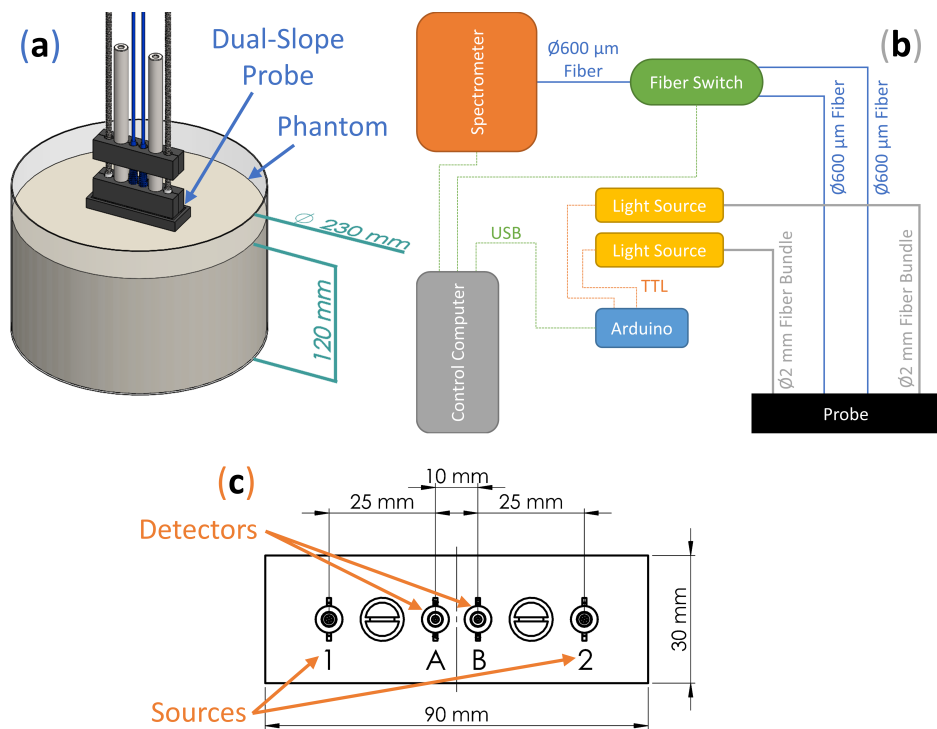


Figure 9.2: Broadband Diffuse Reflectance Spectroscopy (bDRS) methods to achieve measurements of absolute effective attenuation coefficient (μ_{eff}) spectra. (a) Render of bDRS probe on a diffuse optical phantom. (b) Schematic of Dual-Slope (DS) bDRS device. (c) Schematic of the source (1 and 2) and detector (A and B) positions on the DS bDRS probe.

Note 1: This figure can be found as Figure 2 in Blaney *et alia* Applied Sciences (2021) [7].

Acronyms: Universal Serial Bus (USB); and Transistor-Transistor Logic (TTL).

in with the purpose of measuring absolute effective attenuation coefficient (μ_{eff}) spectra of optically diffusive media (Figure 9.2(a)). This was realized using a Dual-Slope (DS) optode geometry which allowed for calibration-free measurements of the CW Reflectance (R) slope (versus ρ). The DS optode configuration (Figure 9.2(c)) used was the same as described in Blaney *et alia* Journal of Biophotonics (2020) [3] and Figure 3.1; it contained 2 source positions and 2 detector positions. The linearly symmetric arrangement resulted in a calibrated measurement from 25 mm to 35 mm.

This DS CW bDRS system was custom built to achieve the multiplexing needed for DS measurements. The measurement requires the R signal be acquired from all combinations of sources (named 1 and 2; Figures 9.2(c)&3.1) and detectors (named A and B; Figures 9.2(c)&3.1). To do so, both the sources and detectors must be multiplexed (Figure 9.2(b)). Sources were multiplexed by using 2 shuttered Avantes AvaLight-HAL-S-Mini [Louisville, CO USA] (HAL) light sources, each connected to 1 source position. Shutter state was controlled via a Transistor-Transistor Logic (TTL) signal from an Arduino Uno R3 [Ivrea, Italy] (Arduino) micro-controller which was connected to the control computer via Universal Serial Bus (USB). Light was delivered from the sources to the probe using $\phi 2$ mm fiber bundles. The light sources output an approximate black-body spectrum with a temperature of about 2650 K (peak at about 1000 nm). On the detector side, diffuse CW light was collected using a $\phi 600$ μ m fiber at each of the 2 detector positions. Multiplexing of the detector positions was done using a Photonwares 1×2 LBMB [Woburn, MA USA] (LBMB) fiber switch where the common end was connected to a Avantes AvaSpec-HERO [Louisville, CO USA] (HERO) spectrometer via a $\phi 600$ μ m fiber. The spectrometer was configured with a 500 μ m slit and collected 1024 λ s between about 498 nm to 1064 nm.

The bottleneck in the multiplexing sequence is the switching time of the LBMB fiber switch. Because of this, the cycle of source-detector position combinations was optimized to minimize LBMB actuation. Naming source-detector combinations

as source number (1 or 2) then detector letter (A or B; Figure 9.2(c)) an example measurement sequence could be:

$$\dots 1A \rightarrow [1A \diamond 2A \blacktriangleright 2B \diamond 1B] \rightarrow \\ [1B \diamond 2B \blacktriangleright 2A \diamond 1A] \rightarrow [1A \dots]$$

where, \diamond is a source switch, \blacktriangleright is a detector switch, and the square brackets show one full DS set acquisition. The R from each source-detector combination is linearly interpolated to the average absolute time for their corresponding DS set. Thus 4 R measurements that contribute to a DS measurement are effectively synchronous, thus preventing potential temporal artifacts when studying dynamic samples or biological tissue.

9.2.2 Validation Experiments

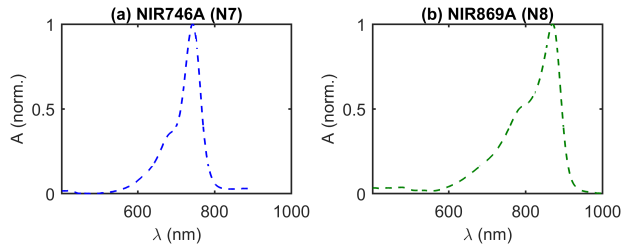


Figure 9.3: Expected spectral features of near-infrared dyes in water, provided by the manufacturer. (a) Normalized Absorbance (A) versus optical wavelength (λ) of QCR Solutions NIR746A [Palm City, FL USA] (N7) dye. (b) Normalized A of QCR Solutions NIR869A [Palm City, FL USA] (N8) dye.

Note 1: This figure can be found as Figure 3 in Blaney *et alia* Applied Sciences (2021) [7].

The purpose of the experiments in Blaney *et alia* Applied Sciences (2021) [7] was to validate the DS bDRS instrument. This was done using a liquid optical phantom which was measured at different dyes concentrations to confirm the DS CW bDRS's ability to distinguish spectral features and measure absolute μ_a . A total of 5 L of the phantom was made, and placed in a cylindrical tank (Figures 9.1(a)&9.2(a)). The base of the phantom was made of 2% reduced fat milk and Water (W) (43% milk and 57% W volume fraction) such that the scattering properties

were similar to those of biological tissue in the near-infrared range. The μ'_s was assumed to not change as dyes were added since the addition of the dyes is expected to have a negligible effect on scattering. Each time the phantom was measured, the measurement was done by both MD FD NIRS and DS CW bDRS.

Three dyes were added in the following order: Higgins India-Ink [Leeds, MA USA] (II), QCR Solutions NIR746A [Palm City, FL USA] (N7), and QCR Solutions NIR869A [Palm City, FL USA] (N8). II is expected to have a relatively flat or decreasing μ_a spectrum with λ in the near-infrared range [116, 117]. By contrast, N7 and N8 are expected to have μ_a peaks at around 746 nm and 869 nm, respectively (Figure 9.3). However, the actual peak λ may shift depending on the chemical properties of the solvent according to the dye documentation and previous experiments [118].

The measurements and dye additions proceeded as follows (measurements meaning both MD FD NIRS and DS CW bDRS). First, the milk and W base phantom was mixed, then measured. Then, II was mixed in and the phantom measured again. Next N7 was mixed and again the phantom measured. Finally, N8 was also mixed into the phantom and the measurement was done for a final time. The amount of each addition of dye was such that all μ_a spectra were expected to stay within typical μ_a values of biological tissue (approximately 0.005 mm^{-1} to 0.020 mm^{-1} [17]).

The temporal sampling parameters of the DS CW bDRS system were set to yield a relatively fast sampling rate while still measuring a relevant λ range. Along these lines, DS CW bDRS data were analyzed between 600 nm to 900 nm and the sampling rate was set to 2.5 Hz. For DS CW bDRS 5 min of data were averaged for analysis. The MD FD NIRS measurement took 30 s at each step for a total measurement time of 5.5 min (11 steps; Figure 9.1), and had a sampling rate of 2.8 Hz. These parameters were chosen such that the rate and time of DS CW bDRS and MD FD NIRS were approximately equal.

Therefore the phantom experiments in Blaney *et alia* Applied Sciences (2021) [7] resulted in

MD FD NIRS measurements of $\tilde{\mu}_{eff}$ at 2 λ s and DS CW bDRS measurements of μ_{eff} between 600 nm to 900 nm for four phantoms (milk and W, milk and W plus II, milk and W plus II plus N7, and milk and W plus II plus N7 plus N7). Appendix B describes the analysis of these data to result in these absolute $\tilde{\mu}_{eff}$ and μ_{eff} .

9.2.3 Retrieval of Absolute Absorption Spectra

Since the DS CW bDRS method yields a real μ_{eff} , μ'_s must be known to find μ_a using the following expression [7]:

$$\mu_a = \sqrt{\frac{\mu'^2_s}{4} + \frac{\mu_{eff}^2}{3}} - \frac{\mu'_s}{2} \quad (9.1)$$

To address the need to know μ'_s , the $\tilde{\mu}_{eff}$ data from the MD FD NIRS measurements were used. FD NIRS yielded a measurement of μ'_s at 2 λ s ($\mu'_{sFD}(\lambda_1)$ and $\mu'_{sFD}(\lambda_2)$; where λ is the 2 from FD) from $\tilde{\mu}_{eff}$ (Appendix B). These μ'_{sFD} measurements are then extrapolated using the following expression based on reduced scattering power coefficient (b) to find μ'_s at all the λ s used by bDRS:

$$\mu'_s(\lambda) = \mu'_{sFD}(\lambda_1) \times \left(\frac{\lambda}{\lambda_1} \right)^{-b} \quad (9.2)$$

$$b = \frac{\ln [\mu'_{sFD}(\lambda_2)/\mu'_{sFD}(\lambda_1)]}{\ln [\lambda_1/\lambda_2]} \quad (9.3)$$

Therefore, when analyzing DS CW bDRS data, μ_a is found for each λ using the assumed μ'_s expressed above for each λ .

9.3 Results from Validation Experiment

The phantom experiment described consisted of measuring 4 phantoms, each with both Multi-Distance (MD) Frequency-Domain (FD) Near-Infrared Spectroscopy (NIRS) (Figure 9.1(a)) and Dual-Slope (DS) Continuous-Wave (CW) broadband Diffuse Reflectance Spectroscopy (bDRS) (Figure 9.2(a)). The phantoms were

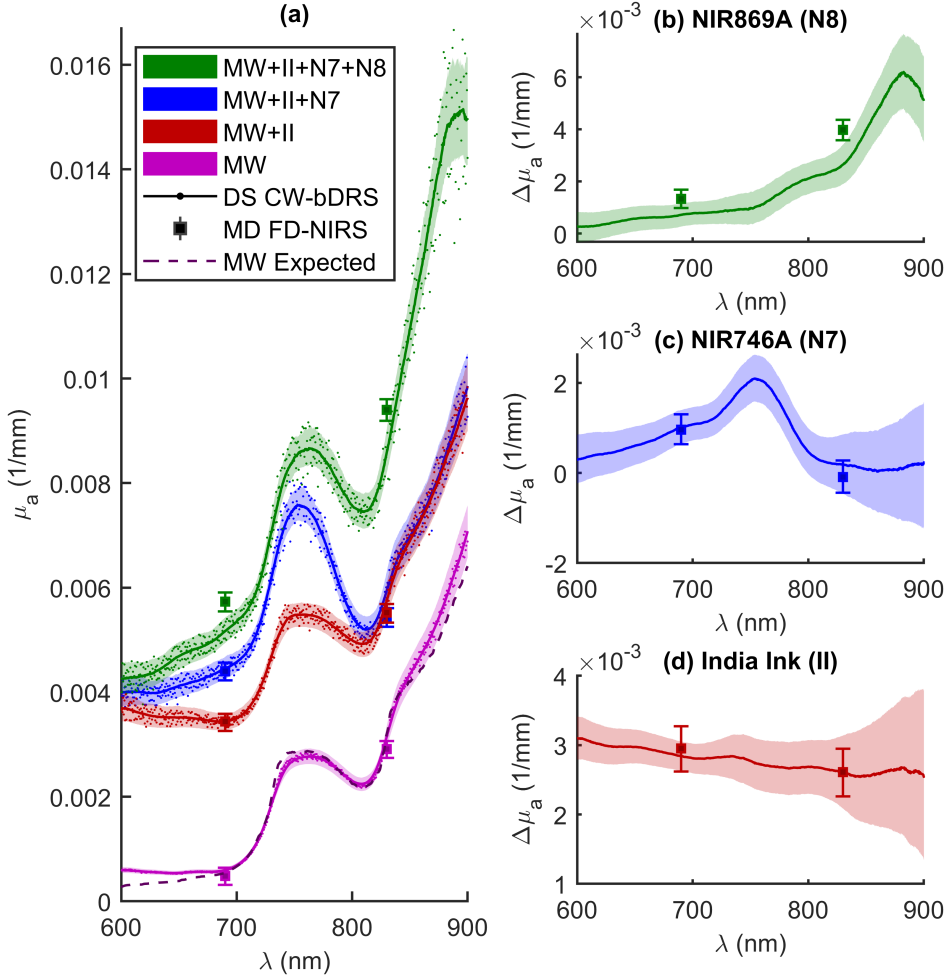


Figure 9.4: Results from phantom experiment in Blaney *et alia* Applied Sciences (2021) [7]. (a) Absolute absorption coefficient (μ_a) spectra as a function of optical wavelength (λ). Showing results from Dual-Slope (DS) Continuous-Wave (CW) broadband Diffuse Reflectance Spectroscopy (bDRS) and Multi-Distance (MD) Frequency-Domain (FD) Near-InfraRed Spectroscopy (NIRS) measurements. Spectra shown for the following phantoms: Milk and Water (MW), MW plus Higgins India-Ink [Leeds, MA USA] (II), MW plus II plus QCR Solutions NIR746A [Palm City, FL USA] (N7), and, finally, MW plus II plus N7 plus QCR Solutions NIR869A [Palm City, FL USA] (N8). DS CW bDRS points show individual λ measurements and lines show smoothed (moving average) spectra for visualization. Dashed line shows the expected μ_a spectrum for MW modeled as Water (W) and Lipid (L) extinction coefficient (ϵ). (b) Absorption coefficient change ($\Delta\mu_a$) from adding N8, (c) $\Delta\mu_a$ from adding N7, and (d) $\Delta\mu_a$ from adding II.

Note 1: This figure can be found as Figure 4 in Blaney *et alia* Applied Sciences (2021) [7].

milk and Water (W), that with Higgins India-Ink [Leeds, MA USA] (II) added, then that again with QCR Solutions NIR746A [Palm City, FL USA] (N7) added, and then that yet again with QCR Solutions NIR869A [Palm City, FL USA] (N8) added.

Figure 9.4 shows the results of this experiment.

The absolute absorption coefficient (μ_a) spectrum is shown across optical wavelengths (λ s) for all 4 phantoms and 2 measurement methods (Figure 9.4(a)). Additionally, Figure 9.4(a) shows a dashed line representing the modeled (as 99.1% W [119, 120] and 0.9% Lipid (L) [121] volume fractions) μ_a of the milk and W phantom. The

expected μ_a spectrum for this milk and W phantom was computed using the forward model for μ_a in Appendix A. The coefficient of determination (R^2) was calculated for the milk and W data and model, yielding a value of 0.98, implying that 98 % of the variance in the milk and W μ_a data is explained by the modeled milk and W extinction coefficient (ϵ) spectra. In Figure 9.4(b)-(d) the absorption coefficient change ($\Delta\mu_a$) as a result of adding the 3 different dyes (II, N7, and N8) is shown. The error regions in all plots are dominated by the systematic uncertainty in the source-detector distance (ρ) on the DS CW bDRS probe (estimated at ± 0.1 mm for chained dimensions) and within the MD FD NIRS measurement (estimated at ± 0.5 mm for initial position and ± 0.01 mm for scan pitch). Note the flat μ_a contribution from II and the spectral features from N7 and N8. Particularly, a peak between 700 nm to 800 nm for N7 and a peak between 800 nm to 900 nm for N8.

9.4 Discussion of Dual-Slope Broadband Spectroscopy Validation

9.4.1 The Milk and Water Absorption Spectrum

First, before any dyes were added in the validation experiment (just milk and Water (W)) the phantom was measured to yield an absorption coefficient (μ_a) spectrum dominated by W (Figure 9.4(a)). This milk and W spectra had the expected spectral features of water (hump at about 750 nm and sharp increase starting at about 800 nm) [120]. Further, the expected milk and W extinction coefficient (ϵ) spectrum agrees (within error) with the experimental data for the spectral range between 690 nm to 830 nm, where reduced scattering coefficient (μ'_s) is interpolated (not extrapolated) from the Multi-Distance (MD) Frequency-Domain (FD) Near-Infrared Spectroscopy (NIRS) measurement. Below 690 nm the agreement is lost likely due to the very low W μ_a , such that even low μ_a contributions from fat, proteins, or other milk

constituents in the milk and W medium may become detectable. Above 830 nm the agreement also degrades possibly because of incorrect μ'_s values (from extrapolation) or contributions from other absorbers in the milk other than W and Lipid (L). Overall the quantitative agreement between the expected and measured milk and W spectra (Appendix A) are quite good with a coefficient of determination (R^2) of 0.98, indicating an accurate measurement of absolute μ_a by Dual-Slope (DS) Continuous-Wave (CW) broadband Diffuse Reflectance Spectroscopy (bDRS).

9.4.2 Comparing Frequency-Domain and Continuous-Wave Retrieved Absorption

Further, the μ_a measured by MD FD NIRS agrees within error with DS CW bDRS at all points of comparison except for QCR Solutions NIR869A [Palm City, FL USA] (N8). For N8 the difference between the measurements is about 10 %, and the combined errors for the 2 measurements amount to about 8 % (dominated by uncertainty in source-detector distance (ρ)). Admittedly, μ'_s found by MD FD NIRS is used to find the μ_a for DS CW bDRS, and thus the measurements are related. However, the observed agreement demonstrates a reliable absolute measurement of the slope of Reflectance (R) with the DS CW bDRS instrument, given the accurate measurements with the scanning MD method used by MD FD NIRS in controlled laboratory conditions. In the case of N8, where the 2 instruments do not agree, the most likely explanation is instrumental error (ρ uncertainty and boundary conditions). The ρ uncertainty accounts for most of the difference between the measurements, and the remaining unaccounted disagreement may be explained by uncertainties in boundary conditions (true depth of fibers in phantom, existence of meniscus, *et cetera*). These ρ uncertainties and boundary effects may have changed for each measurement, since after the addition of each dye the instruments needed to be re-setup and placed on the phantom. This may explain why instrumental errors impacted differently the measurements of different dyes. Additionally, there is ev-

idence that the QCR Solutions NIR746A [Palm City, FL USA] (N7) and N8 dyes are not stable over time (discussed below) and the 2 measurements are not simultaneous (5 min to 10 min between measurements). Any of these considerations may have lead to the lack of agreement for N8. However, given the existence of these considerations and the close agreement in 6 out of 8 cases, we find that the results serves to validate the absolute absorbance measured by DS CW bDRS.

9.4.3 The Additions of Dye to the Phantom

Focusing on the individual dye additions allows for validation of the measurement of spectral features. The first dye added was Higgins India-Ink [Leeds, MA USA] (II), which is expected to have a flat or decreasing spectral dependence with optical wavelength (λ) [116]. The change in the μ_a spectrum observed confirmed this λ dependence and, again, agreed with the measurements at 2 λ_s with MD FD NIRS (Figure 9.4(d)). Further evaluation was carried out to estimate the recovered concentration of II given the measured absorption coefficient change ($\Delta\mu_a$). The true concentration (in volume fraction) of II in the phantom was 5.7×10^{-6} given the phantom volume and the amount of II added. The same II was measured in transmission in non-diffuse solutions of known concentrations to yield spectra of the total attenuation coefficient (μ_t) (assuming only un-scattered light is detected). To yield the spectrum of μ_a (needed to recover concentration in the diffuse experiment) for II, the single scattering albedo (a) must be assumed:

$$\mu_a = \mu_t(1 - a) \quad (9.4)$$

This must be considered for II since it is not in solution in water but instead a suspension of carbon particles. λ independent values of $a = 0$ to 0.15 were assumed which yielded recovered concentrations of 5.2×10^{-6} to 6.1×10^{-6} , respectively. This range of low a values of pure II indicates that its scattering coefficient (μ_s) is much smaller than the μ_a coefficient, which is consistent with the literature [116, 117]. The range re-

sulted in measurement errors of -8.8% to 7.0% (given true value of 5.7×10^{-6}). Therefore, it is expected that DS CW bDRS is capable of recovering accurate chromophore concentrations given that the ϵ spectra is known (not the case here since the a for II was not measured). For N7 and N8 the concentration recovery was not carried out due to temporal and spectral instability of the dyes (discussed below).

Moving on from II, the next 2 dyes were expected to feature a more interesting spectrum (Figure 9.3). N7 was added after II and the $\Delta\mu_a$ presented in Figure 9.4(c). The expected peak between 700 nm to 800 nm was present. However, upon closer examination, the exact peak location is shifted about 12 nm higher for the DS CW bDRS measurement compared to the expected spectrum (Figure 9.5(a)). When the next and final dye, N8, was added, yet again there was a peak present in approximately the expected location (Figure 9.4(b)). But, as with N7 there was an about 12 nm shift to longer λ_s in the DS CW bDRS measurement. This is consistent with a bathochromic shift, which is possible for these dyes given the manufacturer information and previous studies [118]. The hypothesis is that when in milk the dyes exhibit a bathochromic shift due to the different bulk polar nature of milk versus W. To test this possibility, 2 further measurements were done on N8. N8 was measured in transmission (in a semi-micro cuvette) both in water and in the milk and W mixture (Figure 9.5(b)). The results show that the transmission spectral absorbance for N8 in milk matches the DS CW bDRS peak location, whereas the transmission spectral absorbance of N8 in water matches the manufacturer provided spectra. Thus, this transmission experiment supports the hypothesis that these dyes exhibit a bathochromic shift of about 12 nm when in the milk and W mixture. However, it is unknown if the amplitude of the μ_a peak is also effected (hyperchromic or hypochromic shift) for these dyes. The dyes were also found to be temporally unstable, as extended time in solution caused N7 to lose its near-infrared μ_a peak, and N8's peak shifted roughly 200 nm to the blue. These spectral and temporal instabilities stopped the anal-

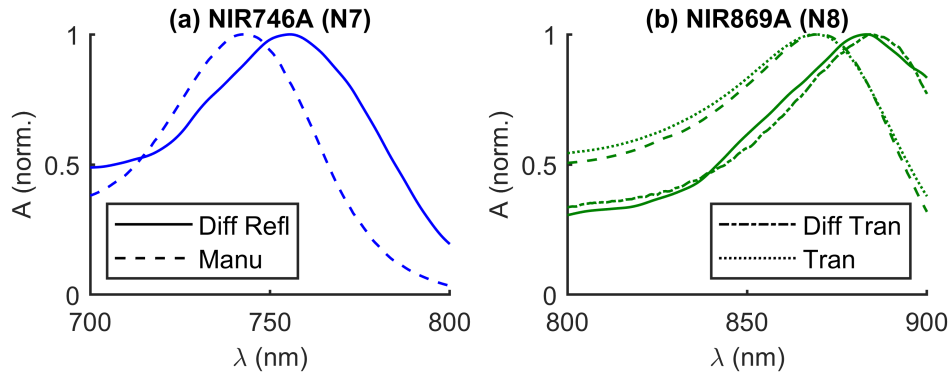


Figure 9.5: Comparison of optical wavelength (λ) normalized Absorbance (A) peak locations for 2 dyes. 4 types of spectra shown: Diffuse Reflectance (Diff Refl, *id est*, in milk from validation experiment), provided by the Manufacturer (Manu; *id est* in water), Diffuse Transmittance (Diff Tran; *id est*, in milk), and Transmission (Tran; *id est*, in water). (a) QCR Solutions NIR746A [Palm City, FL USA] (N7) dye. (b) QCR Solutions NIR869A [Palm City, FL USA] (N8) dye.

Note 1: This figure can be found as Figure 5 in Blaney *et alia* Applied Sciences (2021) [7].

ysis of the concentrations of these dyes in the diffuse phantom. But, despite this, DS CW bDRS was still capable of distinguishing the dye's spectral features.

9.5 Summary of Dual-Slope Broadband Diffuse Reflectance Spectroscopy Validation

Summarizing the discussion above, the results in Blaney *et alia* Applied Sciences (2021) [7] on the liquid phantom serve to validate the Dual-Slope (DS) Continuous-Wave (CW) broadband Diffuse Reflectance Spectroscopy (bDRS) instrument's ability to measure spectral features and absolute values of absorption coefficient (μ_a) in a diffuse medium. In 6 of 8 cases (all except 690 nm and 830 nm for QCR Solutions NIR869A [Palm City, FL USA] (N8)), the absolute μ_a measured with DS CW bDRS agreed within error with Multi-Distance (MD) Frequency-Domain (FD) Near-InfraRed Spectroscopy (NIRS). DS CW bDRS also accurately measured the expected μ_a spectrum of milk and Water (W) mixed ($R^2 = 0.98$). Additionally, the DS CW bDRS instrument correctly measured the flat spectra of Higgins India-Ink [Leeds, MA USA] (II) and the peaks of QCR

Solutions NIR746A [Palm City, FL USA] (N7) and N8. The concentration of II was estimated suggesting the ability to recover chromophore concentrations given the extinction. Finally, it was confirmed that the recovered peak locations of the N7 and N8 dyes are what is expected for these dyes in milk. The follow chapter shows the application of this technique on biological tissue.

Chapter 10

Absolute Absorption Spectroscopy of Tissue

10.1 *In-Vivo* Absolute Absorption Measurements of Muscle

In Blaney *et alia* Applied Optics (2021) [8] absolute absorption coefficient (μ_a) spectra (optical wavelength (λ) approximately 600 nm to 1024 nm) of 6 tissues in 3 healthy subjects were measured using the Dual-Slope (DS) Continuous-Wave (CW) broadband Diffuse Reflectance Spectroscopy (bDRS) plus Self-Calibrating (SC) Frequency-Domain (FD) Near-InfraRed Spectroscopy (NIRS) method described in the previous chapter and Blaney *et alia* Applied Sciences (2021) [7]. The spectral fit of a linear combination of Oxy-hemoglobin (O), Deoxy-hemoglobin (D), Water (W), and Lipid (L) extinction coefficients (ϵ s) was carried out to find absolute concentrations of said chromophores. The goodness of these fits and possible artifact origins are discussed in the following sections.

10.1.1 *In-Vivo* Muscle Measurement Procedure

Various tissues were measured using the combined DS CW-bDRS/SC FD-NIRS approach from Chapter 9. In Blaney *et alia* Applied Optics (2021) [8] 3 human subjects were labeled A, B, & C and were measured at 6 locations (Table 10.1). Informed consent was obtained per the Tufts University's Institutional Review Board (IRB). The 6 tissue locations were:

- The upper arm (*biceps brachii* muscle).

- The forearm (*brachioradialis* muscle).
- The chest (*pectoralis major* muscle in male, breast in female).
- The abdomen (*abdominal* muscles).
- The inner thigh (*gracilis* muscle).
- The calf (*gastrocnemius* muscles).

These tissues were chosen to feature a large range of adipose layer thickness, and to exhibit various chromophore concentrations. For Subject A, the measurements were repeated seven times on each tissue, while for Subjects B & C they were repeated 3 times. In each case the repeated measurements were taken over multiple days.

The instrumentation and methods for DS CW-bDRS/SC FD-NIRS measurements were the same as the Chapter 9 and Blaney *et alia* Applied Sciences (2021) [7] with the replacement of Multi-Distance (MD) SC for the FD measurements. 2 separate optical probes were used, 1 for SC FD NIRS and 1 for DS CW bDRS, that realized a linear symmetric DS arrangement in Figure 3.1 with source-detector distance (ρ) of 25 mm and 35 mm. CW and FD measurements were taken within a few minutes and millimeters of each other (since the goal was absolute baseline measurements, which are not expected to quickly vary spatially nor temporally). In the DS CW bDRS measurements, the λ range was 600 nm to 1064 nm (sampled about every 0.5 nm). The lower λ was chosen based on the

Table 10.1: Subject Demographics and Top Layer Thicknesses for Blaney *et alia* Applied Optics (2021) [8]

Sub	Age (yr)	Sex	Height (m)	Mass (kg)	Tissue	z_{top} (mm)
A	27	Male	1.96	99.8	Forearm	5.8 \pm 0.2
					Arm	7.2 \pm 0.4
					Chest	11.1 \pm 0.5
					Abdomen	32.9 \pm 0.4
					Thigh	21.5 \pm 0.7
					Calf	6.4 \pm 0.2
B	30	Male	1.78	77.5	Forearm	2.6 \pm 0.2
					Arm	5.5 \pm 0.6
					Chest	6.7 \pm 0.5
					Abdomen	29.7 \pm 0.9
					Thigh	16.2 \pm 0.5
					Calf	2.63 \pm 0.08
C	24	Female	1.47	57.4	Forearm	4.8 \pm 0.2
					Arm	4.7 \pm 0.2
					Chest	17.4 \pm 0.6
					Abdomen	15.8 \pm 0.3
					Thigh	14.2 \pm 0.3
					Calf	9.4 \pm 0.5

Note ¹ This table can be found as Table 1 in Blaney *et alia* Applied Optics (2021) [8].

Note ² Errors are Standard-Error of the Mean (SEM).

Acronyms and Symbols Subject (Sub); top layer thickness (z_{top}).

Signal-to-Noise Ratio (SNR) of the measured Intensity (I). The DS CW-bDRS measurements were averaged over approximately 5 min since only static spectra were sought, though the current instrument is capable of dynamic measurements at about 0.25 Hz. In the case of SC FD NIRS, approximately 1 min of data were averaged and the discrete λ s were 690 nm and 830 nm.

In addition to the optical measurements, skin-fold calipers were used to measure the top-layer thickness (z_{top} ; caliper reading was divided by 2) for each tissue. These measurements are representative of adipose tissue thickness [122]. The z_{top} measurement was repeated 3 times at each of 3 places beneath where the optical probe was placed. These 9 (3 repeats at 3 places) measurements were averaged for each subject and tissue (Table 10.1).

10.1.2 From Absolute Absorption to Absolute Chromophore Concentrations

2 dominant chromophores in NIRS are O [123] and D [123]. Additionally, at longer λ s (about 900 nm to 1100 nm) W [120] and L [121] show significant μ_a , and collagen provides a minor contribution [124]. Cytochrome-C-Oxidase (CCO) is another relevant NIRS absorber, providing information about cellular metabolism and whose measurement benefits from broadband measurements [125]. These chromophores may be fit for using a linear combination of their ϵ spectra to explain the measured μ_a (Appendices A&D). Broadband μ_a spectroscopy increases the accuracy of chromophore concentration measurements and reduces cross-talk among chromophores compared to measurements at discrete λ [109, 115, 126].

Another approach that takes advantage of

broadband data is derivative spectroscopy. For example, the spectral second derivative of absorbance at 930 nm to 970 nm [127] or 825 nm to 850 nm [128] was proposed to quantify the **W** concentration. First-derivative absorbance spectroscopy may then be used to obtain other chromophore concentrations and reduced scattering coefficient (μ'_s) spectra [128, 129]. Advantages of derivative spectroscopy include auto-calibrating features, reduced sensitivity to unknown coupling factors, and investigation of hard-to-distinguish chromophores [130]. These are balanced by the disadvantage of a greater degree of noise in the derivative spectra compared to the original spectra.

Regardless of the type of spectral fit, these concentration measurements often report effective values, considering tissue as homogeneous. Attempts to address this assumption have involved two-layer models, which leverage the added information of broadband spectra or multiple ρ s [131–134]. However, the question of how the measured effective concentrations relate to the actual, spatially distributed concentrations in tissue is still open and depends on the methods used for the measurement.

10.1.2.A Effective Homogeneous Chromophore Fits

In Blaney *et alia* Applied Optics (2021) [8] absolute μ_a was retrieved using DS CW bDRS plus SC FD NIRS and the methods in Appendix B and Blaney *et alia* Applied Sciences (2021) [7]. These μ_a spectra were fit to O, D, W, and L_{es} using the methods in Appendix D. Additionally, the fits were done a second time allowing an spectrally constant artifact ϵ in the fit to retrieve μ_{aBck} as a fifth parameter [8, 109]. This allowed us to examine the goodness of the fits with and without the μ_{aBck} parameter, and how the recovered O, D, W, and L changed between the 2 fits. The need to use μ_{aBck} to achieve a good fit was considered a measure of fit artifact. These 2 fits are referred to as No Bck and Yes Bck depending on the presence of μ_{aBck} .

In each case, the recovered chromophore concentrations were used to calculate the fitted μ_a

spectrum, which is compared with the one obtained from the data. The goodness of these fits was evaluated using the adjusted coefficient of determination (\bar{R}^2) which characterizes fits in a similar way to the coefficient of determination (R^2), but accounting for the degrees-of-freedom. In these fits, the number of explanatory variables was taken as the n_C and the number of measurements as n_{CW}/n_{FWHM} where, n_{FWHM} is the Full-Width Half-Max (FWHM) of the DS CW-bDRS system's spectral point-spread function in λ samples. For the system employed here, $n_{FWHM} = 20$ samples or about 10 nm, as measured using a helium-neon laser. Thus, the number of independent measurements, and further the fit goodness accounted for the spectral width of the system.

10.1.2.B Effective Two-Layer Chromophore Fits

A third inverse method aside from the No Bck and Yes Bck homogeneous recoveries was performed in Blaney *et alia* Applied Optics (2021) [8]. This was a pseudo-recovery of effective two-layer chromophore concentrations and scattering parameters. This method is so-called *pseudo* since the result may not be the global minimum of the optimization problem (only local) and thus, may not be unique. The two-layer fit was implemented using the MathWorks MATrix LABoratory [Natick, MA USA] (MATLAB) optimization toolbox and the fmincon function fitting for 12 parameters (4 chromophores plus 2 reduced scattering values for each layer). The start point was set as the values for Model I in Table 10.2 for every tissue and subject, these values were also used to scale the problem (*id est* normalize parameters). The layer thickness was fixed to the value measured and presented in the main paper. Both bound and inequality constraints were used for both layers as follows:

- $0 \mu\text{M} \leq \text{O} \leq 200 \mu\text{M}$
- $0 \mu\text{M} \leq \text{D} \leq 100 \mu\text{M}$
- $0 \leq \text{W} \leq 1$
- $0 \leq \text{L} \leq 1$

Table 10.2: Input and start point for two-layer model and pseudo-recovery

Model	Layer	O (μM)	D (μM)	W (%)	L (%)	μ'_s (mm ⁻¹)		T (μM)	S (%)	b
						690 nm	830 nm			
I	1	10	2	5	70	0.61	0.60	12	83	0.10
	2	80	40	90	20	0.53	0.40			
II	1	10	2	5	70	0.41	0.40	12	83	0.10
	2	80	40	90	20	0.79	0.60			

Note¹ This table can be found as Table S2 of the supplementary material in Blaney *et alia* Applied Optics (2021) [8].

Acronyms and Symbols Oxy-hemoglobin (O); Deoxy-hemoglobin (D); Water (W); Lipid (L); reduced scattering coefficient (μ'_s); Total-hemoglobin (T); tissue oxygen Saturation (S); reduced scattering power coefficient (b) from Equations 9.2&9.3 and Appendix A.

- $0 \text{ mm}^{-1} \leq \mu'_s(690 \text{ nm}) \leq 10 \text{ mm}^{-1}$
- $0 \text{ mm}^{-1} \leq \mu'_s(830 \text{ nm}) \leq 10 \text{ mm}^{-1}$
- $D \leq O$ (*id est* $S \geq 0.5$)
- $W + L \leq 1$
- $\mu'_s(830 \text{ nm}) \leq \mu'_s(690 \text{ nm})$ (*id est* $b \geq 0$)
- $\mu'_s(690 \text{ nm}) \leq \mu'_s(830 \text{ nm}) \times \left(\frac{690 \text{ nm}}{830 \text{ nm}}\right)^{-4}$ (*id est* $b \leq 4$)

where, O is Oxy-hemoglobin concentration, D is Deoxy-hemoglobin concentration, W is Water volume fraction, L is Lipid volume fraction, μ'_s is reduced scattering coefficient, S is tissue oxygen Saturation, b is the reduced scattering power coefficient (b) (Equations 9.2&9.3 and Appendix A). Optimization was carried out with the `interior-point` algorithm of `fmincon`. For each fit it was unsure that a local minimum was either found or possibly found by the optimization algorithm.

The cost function was the square of the Euclidean norm of the difference between the measured and simulated recovered optical properties (*id est* the sum of the squared residuals). The simulated recovered optical properties utilized Appendix A to simulate Reflectance (R) and complex Reflectance (\tilde{R}) then Appendix B on said R and \tilde{R} to retrieve simulated recovered μ_a and μ'_s at the various experimental λ s (Appendix F and Blaney *et alia* Applied Optics (2021) [8]). For optimization, z_{top} was fixed

using the values in Table 10.1 and the remaining 12 parameters varied and fit for. These parameters were: O, D, W, L, $\mu'_s(690 \text{ nm})$, and $\mu'_s(830 \text{ nm})$ for both layer 1 and 2. These fits goodnesses were also evaluated using \bar{R}^2 just as the previous section considering the number of explanatory variables as 12 and the number of measurements as $n_{CW}/n_{FWHM} + 2$ to account for the two FD measurements as well as the CW measurements.

10.1.3 *In-Vivo* Spectral Results

10.1.3.A Absolute Effective Absorption Spectra Recovered *In-Vivo*

Figure 10.1 shows the average absolute μ_a spectra for all 3 subjects and 6 tissues in Blaney *et alia* Applied Optics (2021) [8]. The μ'_s measurements can be found in Table 10.3. The errors represent the Standard-Error of the Mean (SEM) over the repeated measurements, thus, the μ_a spectra were found to be highly reproducible, with intra-subject variability for each tissue much smaller than the inter-subject variability in most cases. Some general observations about the spectra include:

- The dominant lipid peak at about 925 nm for tissues with larger z_{top} (Table 10.1).
- Conversely, the dominant water peak at about 975 nm and overall higher μ_a for tissues with smaller z_{top} , consistent with expectations on adipose versus muscle tissue

Table 10.3: Scattering measured by frequency-domain near-infrared spectroscopy in Blaney *et alia* Applied Optics (2021) [8]

Tissue	Sub	μ'_s (mm ⁻¹)		
		690 nm	830 nm	b
Forearm	A	0.59 ± 0.02	0.49 ± 0.01	1.0 ± 0.2
	B	0.36 ± 0.01	0.290 ± 0.007	1.2 ± 0.2
	C	0.477 ± 0.009	0.43 ± 0.01	0.6 ± 0.2
Arm	A	0.56 ± 0.05	0.53 ± 0.05	0.3 ± 0.7
	B	0.4316 ± 0.0009	0.367 ± 0.002	0.87 ± 0.03
	C	0.465 ± 0.002	0.430 ± 0.002	0.43 ± 0.04
Chest	A	0.40 ± 0.02	0.40 ± 0.02	0.0 ± 0.4
	B	0.479 ± 0.002	0.459 ± 0.002	0.24 ± 0.04
	C	0.4 ± 0.1	0.52 ± 0.03	0 ± 1
Abdomen	A	0.53 ± 0.02	0.52 ± 0.02	0.1 ± 0.3
	B	0.521 ± 0.008	0.540 ± 0.008	0.0 ± 0.2
	C	0.50 ± 0.03	0.52 ± 0.03	0.0 ± 0.5
Thigh	A	0.53 ± 0.02	0.52 ± 0.02	0.1 ± 0.3
	B	0.56 ± 0.02	0.56 ± 0.02	0.0 ± 0.3
	C	0.53 ± 0.04	0.55 ± 0.03	0.0 ± 0.5
Calf	A	0.56 ± 0.01	0.53 ± 0.01	0.3 ± 0.2
	B	0.549 ± 0.009	0.49 ± 0.01	0.6 ± 0.1
	C	0.56 ± 0.03	0.54 ± 0.03	0.2 ± 0.4

Note 1 This table can be found as Table S1 of the supplementary material in Blaney *et alia* Applied Optics (2021) [8].

Acronyms and Symbols Subject (Sub); reduced scattering coefficient (μ'_s); reduced scattering power coefficient (b) from Equations 9.2&9.3 and Appendix A.

[135].

- Typically higher μ_a values for Subject B.

10.1.3.B Recovered Effective Homogeneous Chromophores

Using data in Figure 10.1, the effective homogeneous chromophore fit was carried out both for No Bck and Yes Bck. These results are found in Table 10.4. One striking observation is that the fit improves (even accounting for the change in the degrees-of-freedom) by adding a spectrally independent background for 15 of 18 cases (fit goodness is unaffected in the remaining three cases). Furthermore, this fit improvement is achieved solely by a spectrally constant μ_{aBck} since higher order backgrounds (linear, quadratic, *et cetera*) do not significantly improve

the fits, as can be seen in Figure 10.2.

Examining the effect of the inclusion of μ_{aBck} in the fits, it can be seen that this background typically decreases the recovered O and D concentration, and thus the recovered Total-hemoglobin (T) concentration (in cases where Yes Bck exhibited fit improvement over No Bck). This is not the case for W and L concentrations, which show little to no difference. Additionally, tissue oxygen Saturation (S) is also negligibly impacted by the inclusion of μ_{aBck} .

Further, the effect of this μ_a background on the spectral fit shape can also be seen in Figure 10.3, which shows 2 cases, one where there is significant improvement for Yes Bck versus No Bck, and one where there is no improvement. It can be seen that for the data from Subject A's calf (a case with a relatively thin $z_{top} = 6.4$ mm; Ta-

Table 10.4: Recovered chromophores from Blaney *et alia* Applied Optics (2021) [8] for homogeneous recovery with and without a constant background absorption

Tissue	Sub	Bck	O (μM)	D (μM)	W (%)	L (%)	$\mu_a Bck$ (m ⁻¹)	\bar{R}^2	T (μM)	S (%)
Forearm	A	No	44.1 ± 0.8	12.4 ± 0.3	34.0 ± 0.6	50 ± 2	-	0.849	56.5 ± 0.8	78 ± 2
		Yes	16 ± 1	6.5 ± 0.4	33.1 ± 0.6	50 ± 2	7.5 ± 0.3	0.988	22 ± 1	71 ± 7
	B	No	87.7 ± 1.0	47.7 ± 0.8	62.4 ± 0.9	40 ± 4	-	0.889	135 ± 1	64.8 ± 1.0
		Yes	46 ± 2	28 ± 1	57.7 ± 1.0	35 ± 4	13.2 ± 0.6	0.985	75 ± 2	62 ± 3
	C	No	59.0 ± 0.9	11.4 ± 0.4	36.2 ± 0.9	59 ± 3	-	0.748	70 ± 1	84 ± 2
		Yes	23 ± 2	6.5 ± 0.5	35.3 ± 0.9	57 ± 3	9.3 ± 0.4	0.978	30 ± 2	78 ± 8
Arm	A	No	29.6 ± 0.8	8.3 ± 0.3	15.0 ± 0.8	55 ± 3	-	0.881	37.9 ± 0.9	78 ± 3
		Yes	14 ± 2	4.4 ± 0.5	14.4 ± 0.8	55 ± 3	4.3 ± 0.3	0.990	18 ± 2	80 ± 10
	B	No	73 ± 2	24.8 ± 0.5	41 ± 2	39 ± 8	-	0.831	98 ± 2	75 ± 3
		Yes	35 ± 4	13.9 ± 1.0	39 ± 2	39 ± 8	10.8 ± 0.8	0.989	48 ± 4	71 ± 9
	C	No	50 ± 1	11.1 ± 0.4	30 ± 1	52 ± 5	-	0.762	61 ± 1	82 ± 2
		Yes	21 ± 2	7.2 ± 0.6	29 ± 1	50 ± 5	7.5 ± 0.4	0.977	28 ± 2	74 ± 9
Chest	A	No	31 ± 2	5.2 ± 0.5	15 ± 2	74 ± 7	-	0.795	36 ± 2	86 ± 6
		Yes	13 ± 3	3.7 ± 0.5	14 ± 2	72 ± 7	4.5 ± 0.5	0.989	17 ± 3	80 ± 20
	B	No	36.2 ± 0.3	17.1 ± 0.2	27.5 ± 0.4	33 ± 2	-	0.880	53.3 ± 0.4	67.9 ± 0.8
		Yes	16.8 ± 0.8	12.3 ± 0.3	26.7 ± 0.4	33 ± 2	5.3 ± 0.2	0.982	29.1 ± 0.8	58 ± 3
	C	No	14 ± 1	2.0 ± 0.3	13 ± 1	74 ± 6	-	0.996	16 ± 1	88 ± 9
		Yes	14 ± 2	1.9 ± 0.4	13 ± 1	74 ± 6	0.1 ± 0.3	0.996	15 ± 2	90 ± 20
Abdomen	A	No	10.7 ± 0.7	2.2 ± 0.2	7.1 ± 0.8	65 ± 4	-	0.992	12.9 ± 0.8	83 ± 8
		Yes	11 ± 1	2.1 ± 0.3	7.1 ± 0.8	65 ± 4	0.1 ± 0.2	0.992	13 ± 1	80 ± 10
	B	No	9.25 ± 0.06	1.55 ± 0.03	4.69 ± 0.08	60.5 ± 0.4	-	0.992	10.79 ± 0.07	85.7 ± 0.8
		Yes	9.7 ± 0.1	1.58 ± 0.04	4.70 ± 0.08	60.6 ± 0.4	-0.11 ± 0.04	0.992	11.2 ± 0.2	86 ± 2
	C	No	12.2 ± 0.5	2.0 ± 0.2	6.7 ± 0.5	71 ± 2	-	0.987	14.2 ± 0.5	86 ± 5
		Yes	10.0 ± 0.8	1.8 ± 0.2	6.6 ± 0.5	71 ± 2	0.6 ± 0.2	0.992	11.8 ± 0.8	85 ± 9
Thigh	A	No	10.1 ± 0.5	2.7 ± 0.2	5.6 ± 0.5	70 ± 2	-	0.976	12.8 ± 0.6	79 ± 5
		Yes	7.4 ± 0.9	2.4 ± 0.2	5.5 ± 0.5	69 ± 2	0.7 ± 0.2	0.986	9.8 ± 0.9	80 ± 10
	B	No	19.1 ± 0.6	3.5 ± 0.1	6.8 ± 0.5	59 ± 2	-	0.909	22.5 ± 0.6	85 ± 3
		Yes	11.2 ± 0.7	2.8 ± 0.1	6.6 ± 0.5	58 ± 2	2.0 ± 0.1	0.988	14.0 ± 0.7	80 ± 7
	C	No	11.35 ± 0.06	2.07 ± 0.04	5.05 ± 0.05	65.4 ± 0.6	-	0.986	13.42 ± 0.07	84.6 ± 0.6
		Yes	9.7 ± 0.2	1.93 ± 0.06	5.01 ± 0.05	65.3 ± 0.6	0.43 ± 0.05	0.989	11.6 ± 0.2	83 ± 2
Calf	A	No	29.8 ± 0.4	7.1 ± 0.2	18.1 ± 0.4	64 ± 2	-	0.715	36.9 ± 0.4	81 ± 1
		Yes	7.9 ± 0.8	4.1 ± 0.2	17.5 ± 0.4	63 ± 2	5.7 ± 0.2	0.987	12.0 ± 0.8	66 ± 8
	B	No	63 ± 3	23 ± 1	32 ± 2	60 ± 10	-	0.767	86 ± 3	73 ± 5
		Yes	25 ± 6	11 ± 2	30 ± 2	60 ± 10	11 ± 1	0.988	36 ± 6	70 ± 20
	C	No	32.1 ± 0.8	5.0 ± 0.2	13.1 ± 0.7	68 ± 3	-	0.765	37.0 ± 0.8	87 ± 3
		Yes	13 ± 1	2.3 ± 0.2	12.6 ± 0.7	67 ± 3	5.1 ± 0.2	0.989	15 ± 1	80 ± 10

Note 1 This table can be found as Table 2 in Blaney *et alia* Applied Optics (2021) [8].

Note 2 1 m⁻¹ = 0.001 mm⁻¹.

Note 3 Colors applied only to Bck Yes row.

Note 3.1 Text colors: Blue: $X_{No\ Bck} > X_{Yes\ Bck}$, Black: $X_{No\ Bck} \approx X_{Yes\ Bck}$, Red: $X_{No\ Bck} < X_{Yes\ Bck}$.

Note 3.2 Cell colors: Red: $\bar{R}_{No\ Bck}^2 > \bar{R}_{Yes\ Bck}^2$, Yellow: $\bar{R}_{No\ Bck}^2 \approx \bar{R}_{Yes\ Bck}^2$, Green: $\bar{R}_{No\ Bck}^2 < \bar{R}_{Yes\ Bck}^2$.

Note 4 Nominal values are the fit estimate and errors are the standard error of the estimate.

Acronyms and Symbols Subject (Sub); Background absorption (Bck); Oxy-hemoglobin (O); Deoxy-hemoglobin (D); Water (W); Lipid (L); absorption coefficient (μ_a); adjusted coefficient of determination (\bar{R}^2); Total-hemoglobin (T); and tissue oxygen Saturation (S).

ble 10.1) the background significantly improves the agreement between the fit and the measurement. This is particularly true at lower λ s, where hemoglobin dominates the μ_a spectrum. In the case of data from Subject C's chest (a tissue expected to be relatively homogeneous based on $z_{top} = 17.4$ mm and tissue type; Table 10.1) the inclusion of background has almost no effect on the fit, which is reflected by the small recovered μ_{aBck} and the unimproved \bar{R}^2 (Table 10.4). The

detailed fits and residual spectra can be found in the supplementary material of Blaney *et alia* Applied Optics (2021) [8] for every subject and tissue.

Table 10.5: Results from Blaney *et alia* Applied Optics (2021) [8] for two-layer pseudo-recovery

Tissue	Sub	Layer	O (μM)	D (μM)	W (%)	L (%)	μ'_s (mm ⁻¹) 690 nm	μ'_s (mm ⁻¹) 830 nm	\bar{R}^2	T (μM)	S (%)	b
Forearm	A	1	0	0	16	67	0.59	0.51	0.996	0	87	0.72
		2	45	21	73	27	0.98	0.71		67	68	1.79
	B	1	56	0	52	0	0.49	0.30	0.984	56	100	2.63
		2	100	57	37	27	0.38	0.36		157	64	0.28
	C	1	0	0	8	82	0.47	0.45	0.995	0	86	0.17
		2	63	24	81	19	0.67	0.55		87	73	1.13
Arm	A	1	4	0	0	55	0.56	0.56	0.994	4	98	0.01
		2	31	12	41	58	0.98	0.76		43	71	1.42
	B	1	13	0	24	70	0.48	0.41	0.995	13	100	0.80
		2	84	49	96	4	0.61	0.47		133	63	1.37
	C	1	0	0	2	56	0.45	0.45	0.995	0	90	0.00
		2	50	21	62	38	0.62	0.53		71	71	0.87
Chest	A	1	4	4	9	83	0.46	0.46	0.994	8	50	0.00
		2	63	19	45	1	2.72	1.30		82	76	3.98
	B	1	4	4	17	75	0.51	0.49	0.994	8	55	0.17
		2	38	28	50	0	0.69	0.59		66	58	0.91
	C	1	24	1	19	79	0.45	0.45	0.988	26	94	0.00
		2	3	3	0	39	1.43	0.68		5	50	4.00
Abdomen	A	1	11	2	7	67	0.54	0.52	0.991	13	84	0.13
		2	5	5	2	98	0.66	0.66		10	50	0.00
	B	1	9	1	5	61	0.54	0.54	0.986	11	88	0.00
		2	33	33	0	0	2.92	2.92		66	50	0.00
	C	1	13	0	4	70	0.54	0.53	0.993	14	96	0.09
		2	7	6	16	84	0.43	0.43		13	56	0.00
Thigh	A	1	8	2	6	74	0.58	0.54	0.987	10	84	0.32
		2	10	10	13	87	0.46	0.46		19	50	0.00
	B	1	12	1	5	61	0.67	0.64	0.993	13	91	0.26
		2	24	15	30	69	0.35	0.31		40	61	0.68
	C	1	15	0	2	65	0.57	0.54	0.991	15	100	0.27
		2	6	5	14	86	0.48	0.48		11	53	0.00
Calf	A	1	0	0	5	66	0.53	0.52	0.995	0	58	0.12
		2	26	14	42	58	1.00	0.86		39	66	0.80
	B	1	0	0	10	80	0.41	0.39	0.992	0	53	0.29
		2	51	23	62	38	1.04	0.84		74	68	1.12
	C	1	3	3	6	69	0.63	0.61	0.994	5	50	0.15
		2	52	13	48	52	3.48	1.66		65	80	4.00

Note 1 This table can be found as Table S3 in the supplementary material of Blaney *et alia* Applied Optics (2021) [8].

Note 2 Text colors applied to Layer 2 row, cell colors correspond to the two-layer fit as a whole.

Note 2.1 Text colors: Blue: $X_{Layer 1} > X_{Layer 2}$, Black: $X_{Layer 1} \approx X_{Layer 2}$, Red: $X_{Layer 1} < X_{Layer 2}$.

Note 2.2 Cell colors: Blue: $[\bar{R}_{Two-Layer}^2 < \bar{R}_{No\ Bck}^2] \wedge [\bar{R}_{Two-Layer}^2 > \bar{R}_{Yes\ Bck}^2]$, Red: $[\bar{R}_{Two-Layer}^2 < \bar{R}_{No\ Bck}^2] \wedge [\bar{R}_{Two-Layer}^2 < \bar{R}_{Yes\ Bck}^2]$,

Yellow: $[\bar{R}_{Two-Layer}^2 > \bar{R}_{No\ Bck}^2] \wedge [\bar{R}_{Two-Layer}^2 < \bar{R}_{Yes\ Bck}^2]$, Green: $[\bar{R}_{Two-Layer}^2 > \bar{R}_{No\ Bck}^2] \wedge [\bar{R}_{Two-Layer}^2 > \bar{R}_{Yes\ Bck}^2]$.

Acronyms and Symbols Subject (Sub); Oxy-hemoglobin (O); Deoxy-hemoglobin (D); Water (W); Lipid (L); reduced scattering coefficient (μ'_s); adjusted coefficient of determination (\bar{R}^2); Total-hemoglobin (T); tissue oxygen Saturation (S); reduced scattering power coefficient (b) from Equations 9.2&9.3 and Appendix A.

10.1.3.C Pseudo-Recovered Effective Two-Layered Chromophores and Two-Layer Modeling

Figure 10.3 additionally presents the fit and residuals for the two-layer pseudo-recovery. One

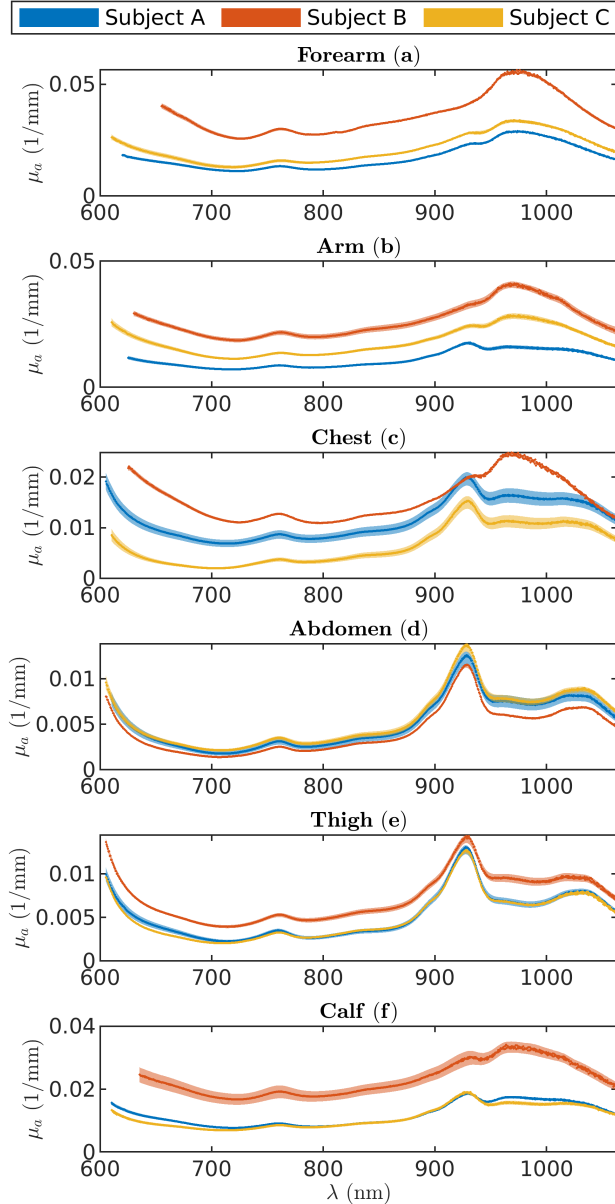


Figure 10.1: Mean absorption coefficient (μ_a) spectra over optical wavelength (λ) for 3 subjects and 6 tissues in Blaney *et alia* Applied Optics (2021) [8]: (a) Forearm, (b) Arm, (c) Chest, (d) Abdomen, (e) Thigh, (f) Calf. Shaded error region (too small to see in some cases) shows Standard-Error of the Mean (SEM) over repeated measurements.

Note 1: This figure can be found as Figure 1 in Blaney *et alia* Applied Optics (2021) [8].

can see that when the Yes Bck improves upon the homogeneous fit, the two-layer fit also results in

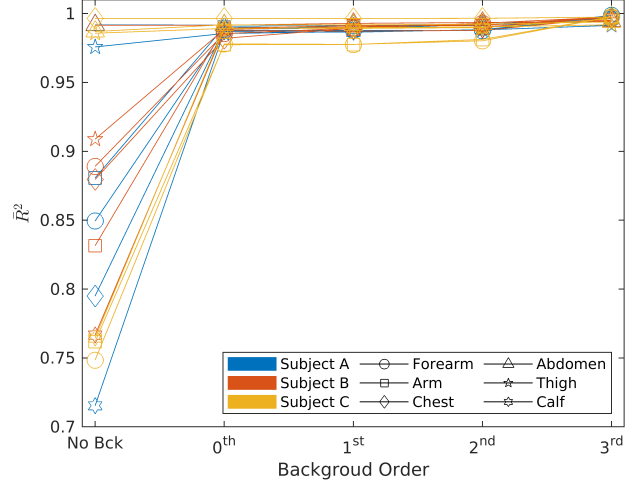


Figure 10.2: Adjusted coefficient of determination (\bar{R}^2) for homogeneous chromophore fits adding additional degrees of freedom (higher order background absorptions).

Note 1: This figure can be found as Figure S7 in the supplementary material of Blaney *et alia* Applied Optics (2021) [8].

Note 2: No Bck is a fit without an absorption background.

an improvement upon the homogeneous fit (Figure 10.3, Subject A calf, for example). These and all other two-layer pseudo-recovery results can be found in Table 10.5, which shows that the two-layer pseudo-recovery is better than the homogeneous recovery with Yes Bck in 14 of 18 cases. It is emphasized that the two-layer pseudo-recovery is named pseudo since its goal is not to recover the true two-layer chromophores, but instead a set of two-layer properties that recreates the measured effective homogeneous μ_a . Additionally, it is not expected that the second-layer properties for thick top-layers are valid (as the deep layer has little effect on the measurement).

An inspection of Table 10.5, in conjunction with the top layer thicknesses (z_{top}) reported in Table 10.1, results in 3 observations for the cases when $z_{top} < 12$ mm (namely, in the forearm, arm, chest for Subjects A and B, and calf):

- The first observation being that the two-layer fits yielded higher **T** and **W** concentrations in the second (bottom) layer, and higher **L** concentrations in the first (top)

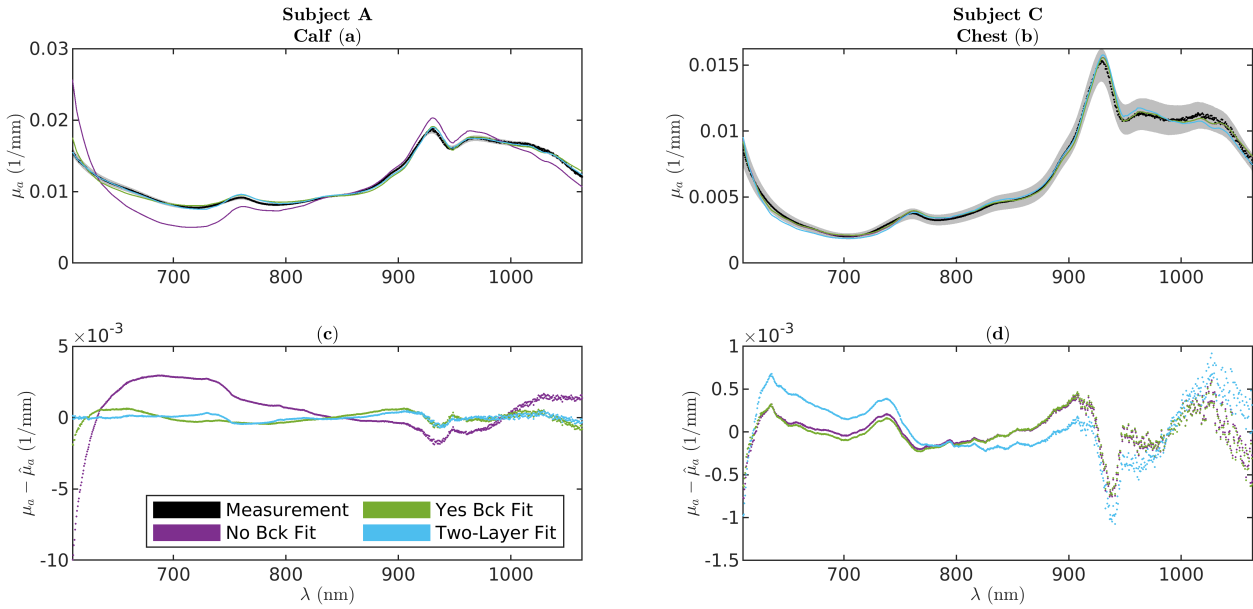


Figure 10.3: Example fits ($\hat{\mu}_a$) of mean absorption coefficient (μ_a) spectra over optical wavelength (λ) for two data sets from Blaney *et alia* Applied Optics (2021) [8]. (a)-(b) μ_a spectra, error region shows Standard-Error of the Mean (SEM). (c)-(d) Fit residual spectra. (a)&(c) Subject A calf. (b)&(d) Subject C chest.

Note 1: This figure can be found as Figure 2 in Blaney *et alia* Applied Optics (2021) [8].

layer.

- The second observation is that μ'_s was found to be greater and to feature a stronger λ dependence (*id est* a larger b) in the second (bottom) layer. These results are consistent with an adipose top layer and muscle bottom layer [135], particularly in terms of the lower μ_a and weaker λ dependence of scattering in the top layer.
- A third observation, by further consideration of the results in Table 10.4, is that when $z_{top} < 12$ mm the homogeneous O and D concentrations obtained without μ_a background (No Bck) are consistently closer to the corresponding concentrations in the second layer (Table 10.5) than to those in the first layer.

Additionally, in the same case ($z_{top} < 12$ mm), the homogeneous O and D concentrations obtained with μ_a background (Yes Bck) are intermediate between those in the first and second layers (Table 10.5), and usually closer to the

first layer concentrations. When $z_{top} < 12$ mm (namely in the chest for Subject C, abdomen, and thigh), the introduction of the μ_a background has a minimal effect on the homogeneous concentrations of O, D, W, and L, which are all close to the corresponding concentrations in the first layer (Table 10.5). A final observation is that the μ'_s measured with SC FD NIRS (Table 10.3) are always closer to the first layer μ'_s , a result that is somewhat surprising, especially in the cases of small z_{top} , and indicates that scattering sensitivity is mostly confined to the top-layer. This observation is consistent with studies we have conducted regarding the two-layer sensitivity to scattering perturbations. However, these results pertain to absolute sensitivity, whose calculation is non-obvious.

To further understand the background artifact's relation to heterogeneity, the value of the μ_{aBck} (Table 10.4) is plotted in Figure 10.4 versus the chief heterogeneity parameter (*id est* z_{top} ; Table 10.1). Additionally, Figure 10.5 displays the recovered chromophore concentrations (Ta-

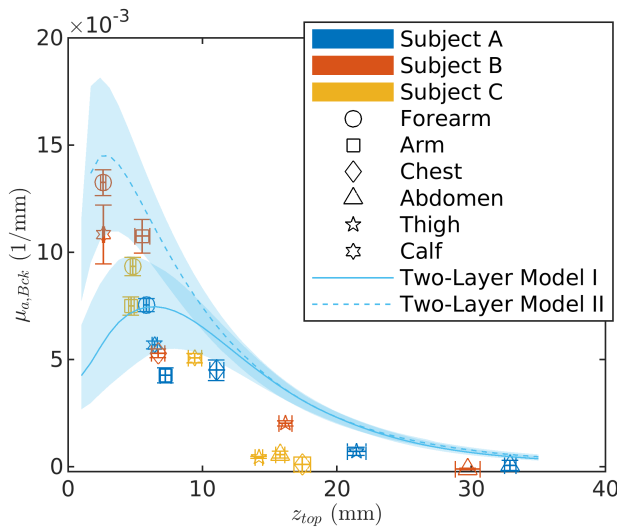


Figure 10.4: Measured (points) and modeled (lines) recovered constant absorption background ($\mu_{a,Bck}$) values versus top layer thickness (z_{top}). Measured data found in Tables 10.1&10.4. Model parameters for two-layer model found in Table 10.2 (based on naïve interpretation of data in Figure 10.5). Models I&II have the same absorption coefficient (μ_a) and reduced scattering power coefficient (b) parameters, with the only difference being in reduced scattering coefficient (μ'_s): Model I $\mu'_{s,Layer\ 1}(830\text{ nm}) > \mu'_{s,Layer\ 2}(830\text{ nm})$; Model II $\mu'_{s,Layer\ 1}(830\text{ nm}) < \mu'_{s,Layer\ 2}(830\text{ nm})$. Shaded region represents varying each parameter by $\pm 25\%$ without co-variation.

Note 1: This figure can be found as Figure 3 in Blaney *et alia* Applied Optics (2021) [8].

ble 10.4; both No Bck and Yes Bck) and μ'_s parameters (Table 10.3) versus z_{top} .

In addition to the *in vivo* data, Figures 10.4&10.5 show lines obtained from theory using the two-layer forward model with the modeled chromophore concentrations and scattering parameters reported in Table 10.2. 2 cases of scattering properties were considered:

- (Model I) The top layer is higher μ'_s than the bottom layer.
- (Model II) The top layer is lower μ'_s than the bottom layer (the value at only 830 nm was switched between models, and the b_s remained the same).

For these theoretical simulations, methods in Appendices A,B,F,&D were used to obtain effective homogeneous recovered chromophore concentrations, which are plotted. These curves are not fits to the data, but rather models based on the naïvely chosen properties reported in Table 10.2; the top and bottom layer parameters were chosen as representative values of the *in vivo* data for large and small z_{top} values, respectively. In general these curves appear to follow the general shape of the measured data, despite the parameters being naïvely chosen.

10.1.4 Discussion of *In-Vivo* Spectral Results

10.1.4.A Heterogeneity as the Origin of the Absorption Background

An analysis of various aspects of the data presented in Blaney *et alia* Applied Optics (2021) [8], and consideration of a number of possible reasons for the improvement of the fits by the addition of an μ_a background (discussed in the next section), suggested that the origin of the background was tissue heterogeneity. A comparison of the *in vivo* data points with the two-layer model curves in Figures 10.4&10.5 shows that the *in vivo* data are consistent with a two-layered distribution of the chromophores in tissue. While these model curves are not fits to the data, as they are based on naïvely chosen optical properties (Table 10.2), the curves follow the general shape of the measured data quite well. Additionally, the different curves of Model I versus Model II show the strong dependence on the optical properties of the 2 layers, and the *in vivo* data were collected on different tissues and different subjects with varying optical properties (which are also not strictly distributed over two layers). Thus, it should not be expected that the data closely match a two-layer model or the even same model for each data point, and one should instead look at the qualitative shape of the experimental data and theoretical curves. Furthermore, the quantitative agreement between the data and the models may be affected by the assigned top-layer thickness of tissues. It is possible

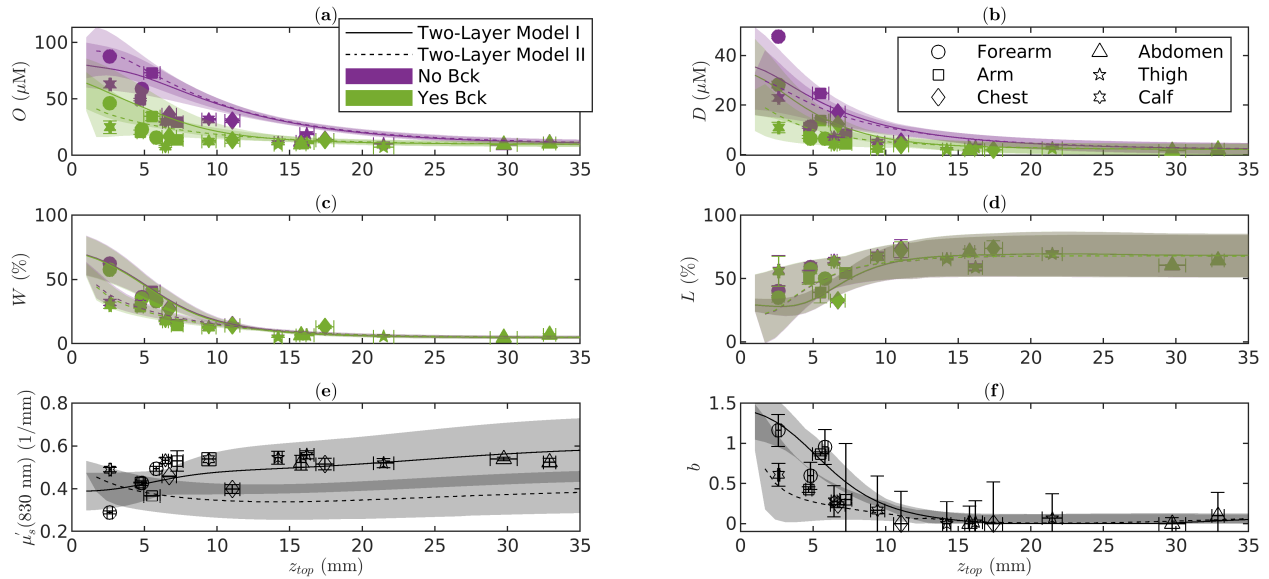


Figure 10.5: Measured (points) and modeled (lines) recovered chromophore concentrations ((a) Oxy-hemoglobin (O); (b) Deoxy-hemoglobin (D); (c) Water (W); (d) Lipid (L)) and reduced scattering parameters ((e) reduced scattering coefficient at 830 nm, $\mu'_s(830 \text{ nm})$; (f) reduced scattering power coefficient (b)) versus top layer thickness (z_{top}). Recovery conducted both without a constant absorption background (No Bck) and with it (Yes Bck). Measured data found in Tables 10.1, 10.4, & 10.3. Parameters for two-layer models found in Table 10.2 (based on naïve of interpretation of data lower and upper limits) same as Figure 10.4. Models I&II have the same absorption coefficient (μ_a) and b parameters with the only difference being in reduced scattering coefficient (μ'_s): Model I $\mu'_{s\text{Layer 1}}(830 \text{ nm}) > \mu'_{s\text{Layer 2}}(830 \text{ nm})$; Model II $\mu'_{s\text{Layer 1}}(830 \text{ nm}) < \mu'_{s\text{Layer 2}}(830 \text{ nm})$. Shaded region represents varying each parameter by $\pm 25\%$ without co-variation.

Note 1: This figure can be found as Figure 4 in Blaney *et alia* Applied Optics (2021) [8].

Note 2: Yes Bck and No Bck have no difference in scattering parameters.

that the skin-fold measurement of the top layer thickness in tissues does not correspond to the optical equivalent thicknesses of the first layer in the models [122, 136]. Thus, some or all of the *in vivo* data may need to be shifted along the horizontal (thickness) axis (*id est* there may be an offset between modeled and measured thickness), possibly resulting in a better agreement between data and models.

It is also noteworthy that the μ_a background falls off at larger top layer thicknesses (Figure 10.4), which correspond to more effectively homogeneous tissues, considering the limited depth of sensitivity of the optical measurements. Furthermore, the goodness of the fit is improved beyond the homogeneous Yes Bck case by the two-layer pseudo-recovery in 14 of 18 cases (Table 10.5). Cases where the two-layer pseudo-

recovery does not do well are those with large top layer thickness, such as abdomen and female chest, and with the thinnest top layer thickness, Subject B's forearm (Table 10.1). In these cases, the tissue may be effectively homogeneous (the top layer either extends over most of the optical region of sensitivity, or it is too thin to affect the DS optical measurements), so that a two-layer model may not properly describe the data.

In summary, two aspects of these data, namely their dependence as a function of top layer thickness (Figures 10.4&10.5) and the goodness of the fits with two-layer pseudo-recovery (Table 10.5), point to the μ_a background being consistent with a heterogeneous distribution of the chromophores.

10.1.4.B Other Possible Origins of the Absorption Background

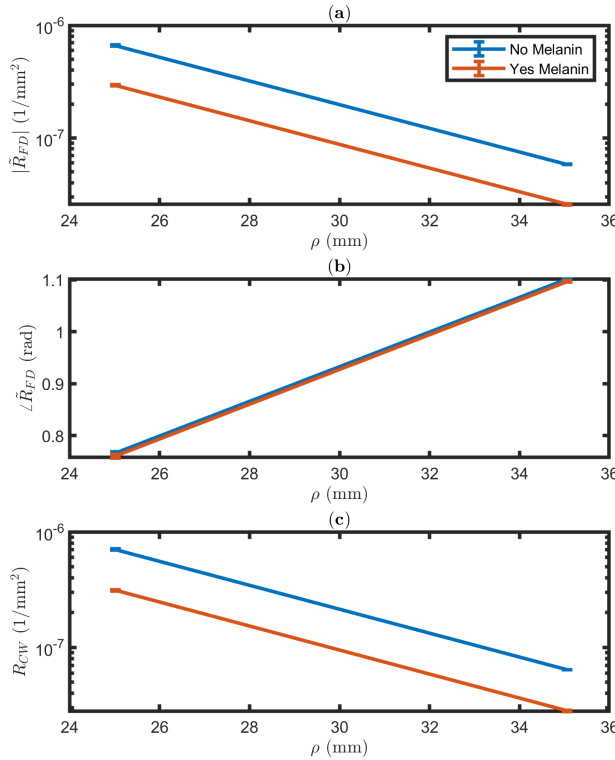


Figure 10.6: Monte Carlo simulation of measurement with (Yes Melanin) and without melanin (No Melanin). Showing mean and standard deviation from four simulations. (a) Amplitude of Frequency-Domain (FD) complex Reflectance (\tilde{R}) as a function of source-detector distance (ρ). (b) Phase of FD \tilde{R} versus ρ . (c) Continuous Wave (CW) Reflectance (R) versus ρ .

Note 1: This figure can be found as Figure S8 in the supplementary material of Blaney *et alia* Applied Optics (2021) [8].

For a complete investigation, other possible reasons for the fit improvement achieved by adding a spectrally constant μ_a background were considered. First, this background μ_a may represent an additional chromophore besides O, D, W, and L. Possible additional tissue chromophores include collagen [124], melanin [137, 138], and CCO [125]. Previous work including collagen in the spectral fits also found the need to introduce a constant background to improve the quality of the fits [109]. In fact, the collagen μ_a spectrum

has strong spectral features (a decreasing μ_a in the 600 nm to 850 nm range, a peak at about 910 nm, *et cetera*) [124] that are inconsistent with a spectrally flat (or linear) μ_a . The data presented here were also fit including collagen (not shown), but the fits did not improve to the level achieved by including the flat μ_a background.

Considering that melanin has no prominent spectral features as its μ_a monotonically decreases between 600 nm to 1000 nm [137, 138], it seems likely a good candidate to replace a spectrally flat (or linear) μ_a . In fact, a test including melanin in the fits (not shown) did show fit improvements comparable to those obtained with a flat μ_a background. However, previous work indicates that slope-based measurements (such as DS) at ρ greater than 20 mm should be insensitive to chromophores in a thin (less than a couple of mm) superficial layer [3, 50], and melanin is confined to within the superficial epidermis layer that has a thickness of about 50 μm to 300 μm [139]. To confirm this a three-layer Monte Carlo (epidermis, dermis, and subcutaneous tissue; Table 10.6) was used to simulate how the measurement would be effected by melanin in the epidermis. Figure 10.6 shows the results from the Monte Carlo simulations. Since the slopes (not the absolute values) of the optical signals are used in the analysis, the presence of melanin has an un-measurable effect. When analyzed the no melanin case resulted in a recovered absorption of 0.009 885 mm^{-1} and the yes melanin case resulted in a value of 0.009 886 mm^{-1} . Thus, the inclusion of melanin had an effect on the order of 10^{-6} mm^{-1} on the recovered absorption in this simulation, 3 to 4 orders of magnitude less than the observed background. Thus it is unlikely that melanin contributes to the tissue spectra measured in this work, while it can significantly contribute to optical spectra measured at much shorter ρ , such as 1 mm [140].

Moving to CCO, the lack of its inclusion in the spectral analysis is also not likely to be the reason for poor spectral fits. In fact, the λ dependence of CCO μ_a would not result in a fit improvement comparable with the one obtained with the spectrally flat background μ_a due to its spectral features. It is also important to

Table 10.6: Three-layer Monte Carlo model of melanin rich epidermis

Model	Layer	Δz (mm)	μ_a (mm^{-1})	μ'_s (mm^{-1})
No Melanin	1	0.1	0.03	1.5
	2	2.0	0.03	1.5
	3	-	0.01	1
Yes Melanin	1	0.1	1.40	1.5
	2	2.0	0.03	1.5
	3	-	0.01	1

Note ¹ This table can be found as Table S4 in the supplementary material of Blaney *et alia* Applied Optics (2021) [8].

Acronyms and Symbols Layer thickness (Δz); absorption coefficient (μ_a); and reduced scattering coefficient (μ'_s).

note that the magnitude of the μ_a background values, which are as high as about 0.01 mm^{-1} , are not consistent with the μ_a contributions that one would expect from physiological concentrations of any of these three candidates (collagen, melanin, and CCO). Finally, variations in the extinction spectra used for O, D, W, and L, as reflected in different results from the literature were considered [141], but this also could not explain the need to introduce the μ_a background. Therefore, it was concluded that additional chromophores or errors in the extinction spectra of the considered chromophores would not account for the μ_a background.

Next, systematic errors associated with uncertainties in the source-detector distances and in the scattering spectrum determined from SC FD-NIRS (due to the use of calibration-free methods, systematic errors that may come from calibration procedures are excluded) were examined. Errors in ρ_s would be expected to be tissue independent, but different μ_a background values were found on different tissues. Additionally, the nominal distances were varied ($\pm 5 \text{ mm}$) when analysing the data, and the background artifact was still observed in the fits. An error in the extrapolated scattering was also considered by varying the scattering spectrum within the errors in the measurements at 2λ with SC FD-NIRS. This also failed to impact the recovered μ_a background from the fits. It is also observed that the μ'_s non-linearly combines with the μ_a coefficient to result

in the measured R , thus a systematic scattering error is not expected to result in a spectrally constant artifact. From these considerations, systematic distance and scattering errors were ruled out as the source of background μ_a .

Finally, approximations in the model used were interrogated. The heart of the analysis is the diffusion theory model for a homogeneous semi-infinite medium with extrapolated boundary conditions (Appendix A). Different boundary conditions (zero-boundary) and a different geometry (cylindrical) [142] consistent with a curved tissue boundary, were considered. But neither was able to account for the large background μ_a artifact.

In summary, all of the above potential sources of the observed μ_a background were ruled out, thus confirming that tissue heterogeneity is the most likely reason for the deviation of the measured μ_a spectra from a linear combination of μ_a contributions from O, D, W, and L.

10.1.4.C Meaning of Spectrally Obtained Effective Concentrations

The main result of Blaney *et alia* Applied Optics (2021) [8] is that the μ_a spectrum measured in heterogeneous media cannot be accurately reproduced by a linear combination of the extinction spectra of the chromophores that are in-homogeneously distributed in the medium. In some sense, this is an obvious result (why

would one expect to accurately model an inhomogeneous medium with a homogeneous distribution of absorbers?), but it is an important one given that effectively homogeneous chromophore distributions are routinely measured in the field of diffuse optics. It is stressed that there are other potential reasons for the inaccuracy of the spectral measurements, but after considering them it was concluded that the spatial heterogeneity of the chromophores distribution is the dominant one. The question then becomes: what is the relationship between these effectively homogeneous distributions of the chromophores and their actual spatially dependent concentrations? The answer to this question must depend on the methods used for the spectral measurements (ρ_s , Single-Distance (SD) or MD approaches, CW versus FD versus Time-Domain (TD), discrete λ_s or the range of λ_s used, *et cetera*) and on the specific chromophores and their spatial distribution in the medium. The results of this work allows for the answer for the slope-based measurements used by DS at ρ_s of 25 mm and 35 mm, and for tissues consisting of an adipose layer and underlying muscle (given the relatively long ρ_s and the slope method used, contributions from the superficial skin layer are neglected). In these conditions, a two-layered distribution of the chromophores is a significantly better representation of reality than a homogeneous distribution.

Focusing on the physical tissues measured, the *in vivo* measurements were performed on tissues that, beyond the thin superficial skin layer, featured subcutaneous fat (adipose tissue) and underlying skeletal muscle. The greater hemoglobin concentration observed in the bottom-layer with respect to the top-layer is consistent with the greater blood perfusion of muscle tissue versus more superficial adipose tissue (Figure 10.5 and Table 10.5). This tissue dependence of chromophore concentrations is inline with literature [135]. With regards to scattering properties, the μ'_s at 690 nm and 830 nm, and the power of scattering λ dependence consistently show a smaller scattering and smaller power for the top-layer versus the bottom-layer. While data from the literature shows a weaker λ dependence of scatter-

ing in adipose versus muscle [135], in agreement with the results for the top- versus bottom-layer, the μ'_s at 690 nm and 830 nm was reported to be greater in fat versus muscle after extrapolation of scattering values at 500 nm [135]. The reliability of the assessment of scattering properties in the 2 layers with this spectral method is a point that will require further investigations and may be limited by the discrete λ_s used herein for FD.

Examining some of the notable results, in the case of a thick top layer ($z_{top} > 12$ mm: the chest for Subject C, abdomen, and thigh; Table 10.1), the tissue is close to being effectively homogeneous, the background μ_a is negligible, and the homogeneous fits with and without background are similar to each other and yield chromophore concentrations and scattering parameters that are close to those of the first layer in the two-layer analysis (Tables 10.4&10.5). In this case, the optical measurements are mostly sensitive to the top-layer and a homogeneous model accurately describes the measured spectra.

Conversely, in the case of a thinner top-layer ($z_{top} < 12$ mm: forearm, arm, chest for Subjects A and B, and calf; Table 10.1) the situation is more complicated. The effectively homogeneous chromophore concentrations obtained from fits that include the background are always in between the values recovered for the each of the 2 layers in the two-layer analysis (Tables 10.4&10.5). This result is somewhat intuitive, and may be summarized by stating that the apparent homogeneous recovered chromophore concentrations (Yes Bck) take the meaning of an effective average of the concentrations in the 2 layers. In fact, measurements of effectively homogeneous concentrations are commonly interpreted in exactly this way, as an effective average of spatially distributed chromophores within the region of optical sensitivity. On the other hand, the results for the spectral fits that do not include the apparent μ_a background (No Bck) are particularly interesting. Compared to Yes Bck, they yield essentially the same W and L concentrations (Figure 10.5(c)(d) and Table 10.4), whereas they yield O and D concentrations that are much closer to those of the bottom layer (Figure 10.5(a)(b) and Tables 10.4&10.5). The much

smaller impact of the μ_a background on the recovered **W** and **L** concentrations, compared to the **O** and **D** concentrations, is due to the fact that the μ_a contributions from **O** and **D** are relevant in the entire spectral range considered (about 600 nm to 1064 nm), whereas the μ_a contributions from **W** and **L** are only relevant above 900 nm. The fact that the **O** and **D** concentrations recovered with No Bck, despite the worse quality of the fit compared to the Yes Bck case, provide better estimates of the **O** and **D** concentrations in the bottom layer can be a desirable feature in non-invasive applications that target underlying tissue. These applications include brain measurements, in which case the top-layer comprises scalp and skull, and skeletal muscle measurements (such as described here), in which case the top-layer comprises skin and adipose tissue. While, as already mentioned, these latter results are specific to the slope method, ρ_s , spectral range, and two-layered chromophore distribution considered here, it is important to always consider the question of the meaning of measured effectively homogeneous concentrations in relation to the actual spatial distribution of chromophores in the tissue.

10.2 In-Silico Spectra of Two-Layer Tissue

Due to the heavy effect that a heterogeneous medium appeared to have on measurements of absolute spectral absorption coefficient (μ_a) in the previous section and Blaney *et alia* Applied Optics (2021) [8] a more extensive investigation of the two-layer model applied to spectral measurements was done in Blaney *et alia* Journal of Innovative Optical Health Sciences (2022) [9]. Therefore in Blaney *et alia* Journal of Innovative Optical Health Sciences (2022) [9] we investigated the relationship between chromophore concentrations in two-layered scattering media and the apparent chromophore concentrations measured with broadband optical spectroscopy, primarily the Self-Calibrating (SC) Frequency-Domain (FD) Near-InfraRed Spectroscopy (NIRS) / Dual-Slope (DS) Continuous-

Wave (CW) broadband Diffuse Reflectance Spectroscopy (bDRS) method.

10.2.1 Motivation to Understand the Partial Volume Effect

Biomedical diffuse optics typically utilizes a simplified model to analyze data collected from a complex medium. That complex medium being biological tissue, which has a heterogeneous distribution of optical properties, and that simplified model often being the semi-infinite homogeneous model seen in Appendix A [143]. Therefore, recovered optical properties are said to be effective homogeneous properties. This meaning that a homogeneous medium with these properties would replicate the behavior of the data. When the measurement of a single region is sought (discussed in Part I), such as the brain [32], muscle [30], or breast lesions [29], these heterogeneous effects on homogeneous recovered data are considered partial-volume confounds [144]. Therefore, an understanding of how heterogeneous properties are related to effective homogeneous properties may help with data interpretation.

Simulations of optically diffuse media offer a method for generating forward model data where the actual optical properties within the medium are known and may be varied. This allows one to generate forward data from a complex medium and then invert the data using a homogeneous model as one would with experimental data, to compare the actual simulated medium to the recovered values. Highly complex heterogeneous media may be simulated with Monte Carlo methods. These methods may simulate voxelized or meshed media with computationally efficient parallel computations of photon propagation [145]. Monte Carlo simulations have the advantage of being able to simulate complex media but these methods do not match analytical expressions in terms of speed. Due to how fast analytical expressions may be evaluated, many media of differing properties to be simulated in a short computation time by repeating the analytical evaluation. However, the media analytical methods simulate must be simpler com-

pared to Monte Carlo. It may be said that the simplest heterogeneous medium is the two-layer medium for which analytical expressions for the complex Reflectance (\tilde{R}) exist [142]. In Blaney *et alia* Journal of Innovative Optical Health Sciences (2022) [9], analytical expressions from diffusion theory for the \tilde{R} in a two-layer medium was used to generate forward data (Appendix A) and expressions for a semi-infinite homogeneous medium is used to invert data (Appendix B&D).

10.2.2 Description of Two-Layer Simulations

10.2.2.A Simulation Parameters

The parameters describing these optically diffuse tow-layer media can be split into 2 categories, those affecting the μ_a and those affecting the reduced scattering coefficient (μ'_s) [17]. Absorption parameters are related to chromophore concentration of Oxy-hemoglobin (O), Deoxy-hemoglobin (D), Water (W), and Lipid (L). Scattering on the other-hand can be described by a power-law containing two parameters, an amplitude^a and the reduced scattering power coefficient (b) (Equations 9.2&9.3 and Appendix A). These parameters are both inputs to the two-layer forward models (with the parameters possibly being different in different layers; Appendix A) and the out puts of the full inversion (Appendices B&D)

To generate forward data the SC FD NIRS / DS CW NIRS was simulated. The FD portion measured \tilde{R}_S with a modulation frequency (f_{mod}) of 140.625 MHz 2 discrete optical wavelengths (λ_S) of 690 nm and 830 nm. The CW portion measured Reflectances (R_S) at a broadband range of λ_S (650 nm to 1024 nm spaced by 0.5 nm). Both the FD \tilde{R} and CW R were simulated at two source-detector distances (ρ_S) of 25 mm and 35 mm. Therefore, the simulated instrument outputs:

- 4 FD \tilde{R} ($\tilde{R}(\lambda, \rho)$; two λ_S and two ρ_S).

^aThe scattering amplitude is expressed as the value of the reduced scattering coefficient (μ'_s) at a single optical wavelength (λ).

- 1498 CW R ($R(\lambda, \rho)$; 749 λ_S and two ρ_S).

based on the expressions for a two-layer medium in Appendix A.

The two-layer forward model (Appendix A) used expressions derived from diffusion theory to simulated a two-layer medium and both \tilde{R} and R . The input of the model described chromophore concentrations and reduced scattering parameters in the 2 layers as well as the thickness, these 13 parameters are as follows:

1. Total-hemoglobin (T) concentration in the top layer (T_{top}).
2. T concentration in the bottom layer (T_{bot}).
3. Tissue oxygen Saturation (S) in the top layer (S_{top}).
4. S in the bottom layer (S_{bot}).
5. W volume fraction in the top layer (W_{top}).
6. W volume fraction in the bottom layer (W_{bot}).
7. L volume fraction in the top layer (L_{top}).
8. L volume fraction in the bottom layer (L_{bot}).
9. The μ'_s at 830 nm in the top layer ($\mu'_{s,top}(830\text{nm})$).
10. The μ'_s at 830 nm in the bottom layer ($\mu'_{s,bot}(830\text{nm})$).
11. The b in the top layer (b_{top}).
12. The b in the bottom layer (b_{bot}).
13. The thickness of the top layer (z_{top}).

10.2.2.B Simulation Procedure for Recovered Effective Absolute Properties

The first step of the model was to calculate the μ_a spectrum^b for each layer from the absorption parameters. These layer-dependent absorption

^bThe full spectral simulation accounted for all 749 Continuous-Wave (CW) and two Frequency-Domain (FD) optical wavelengths (λ_S).

spectra were calculated as a linear combination of known extinction coefficient (ϵ) as shown in Appendix A [120, 121, 123]. The μ'_s spectrum was calculated for each layer using a power law as shown in Appendix A.

The analytical two-layer model for diffuse reflectance [142] (Appendix A) took the μ_a and μ'_s spectra for each layer and z_{top} as input with a final unmentioned parameter of index of refraction (n) which was assumed to be fixed at 1.4 for both layers. Both \tilde{R} and R is output given the above input parameters for each ρ and λ .

Using these \tilde{R} and R the recovery of absolute optical properties was achieved using a iterative method described in Appendix B. This output effective homogeneous absolute complex effective attenuation coefficient ($\tilde{\mu}_{eff}$) for the FD λ_s , and effective homogeneous absolute effective attenuation coefficient (μ_{eff}) for the CW λ_s (Appendix F). As shown in Appendix B $\tilde{\mu}_{eff}$ is converted to μ_a and μ'_s for the FD λ_s . Then the full μ_a spectrum is retrieved from μ_{eff} at all CW λ using Equations 9.1-9.3.

Finally, the recovered μ_a over CW λ_s is converted to effective homogeneous^c recovered T, S, W, and L using the methods in Appendix D.

Therefore, the output of these *in silico* experiments was the absorption and scattering parameters necessary to describe an equivalent homogeneous medium:

1. Recovered effective homogeneous T concentration (T_{rec}).
2. Recovered effective homogeneous S (S_{rec}).
3. Recovered effective homogeneous W volume fraction (W_{rec}).
4. Recovered effective homogeneous L volume fraction (L_{rec}).
5. Recovered effective homogeneous μ'_s at 830 nm ($\mu'_{srec}(830\text{ nm})$).
6. Recovered effective homogeneous b (b_{rec}).

^cThe effective homogeneous properties recovered are also dependent on the specific instrument simulated, particularly the source-detector distances (ρ_s) and optical wavelengths (λ_s).

Equivalent homogeneous medium meaning, given the two-layer properties modeled and the ρ_s and λ_s simulated, these effective homogeneous properties give the same \tilde{R} and R as the two-layered case (Appendix F).

10.2.2.C Sensitivity in a Two-Layer Medium

Sensitivities to changes in absorption parameters in each layer of a two-layer medium were also considered in Blaney *et alia* Journal of Innovative Optical Health Sciences (2022) [9].^d These sensitivities were calculated as numerical derivatives, where an independent variable^e was changed by a small amount^f and the dependent variable's^g change was retrieved. The ratio of the change in the dependent variable divided by the independent variable was considered the sensitivity of the dependent variable to a change in the independent variable. In all cases μ'_s recovered from FD was fixed at the baseline value when recovering the small change in the dependent variable. Thus only changes in absorption parameters were considered, and importantly cross-talk between absorption parameters and scattering parameters was ignored. In practice this would be equivalent to making only one FD measurement at the beginning of an experiment and then measuring absorption dynamics with only CW, therefore assuming constant scattering during an experiment.

Sensitivities could take the form of any pair between independent and dependent variables described in previous sections. These sensitivities were split into two categories, first co-sensitivities

^dThese sensitivities to changes in absorption parameters are not the same as Sensitivity to absorption change (S) as S is more specific. S is only concerned with $\Delta\mu_a$ directly, while the sensitivity in this section is more general and concerned with changes in chromophore concentrations.

^eInputs to the two-layer forward model are considered independent variables.

^fThe small amount used to calculate the numerical derivative was the baseline value of the parameter multiplied by 10^{-6} .

^gDependent variables are the outputs of the homogeneous inverse model.

which are between like parameters^h and second cross-sensitivities which are between differing parameters.ⁱ Taking the example of the co-sensitivity between top layer Total-hemoglobin (T) and recovered T or $\delta T/\delta T_{top}$, this should be interpreted as how much a change in the top layer T will effect the effective homogeneous recovered T . These sensitivity values also are affected by the baseline properties, therefore this dependence was also investigated by recalculating sensitivities for various values of baseline two-layer absorption parameters.

10.2.3 In-Silico Results for a Two-Layer Model and Effective Homogeneous Recovery

10.2.3.A Recovery of Effective Homogeneous Absolute Values

10.2.3.A.a Baseline Model Two-Layer
Table 10.7 shows the baseline absorption model and the recovered baseline absorption properties for said model. Table 10.8 shows scattering values for this same baseline model. Unsurprisingly, in this case the recovered parameters take values between the actual values of the 2 layers. However, the dominant layer is different for different parameters, for example recovered T is closer to the actual bottom-layer value but recovered W is approximately the average of the top- and bottom-layers.

10.2.3.A.b Variation of Two-Layer Model Parameters Starting with the baseline two-layer model parameters stated in Tables 10.7&10.8, each parameter was individually varied.^j For every new set of two-layer forward model absorption and scattering properties the recovered values were then found.

^hAn example of a co-sensitivity would be between top layer Total-hemoglobin (T) and recovered T or $\delta T/\delta T_{top}$.

ⁱAn example of a cross-sensitivity would be between top layer Water (W) and recovered Total-hemoglobin (T) or $\delta T/\delta W_{top}$.

^jParameters were varied without co-variation, meaning while one input parameter varied all other input parameters were kept fixed to their baseline value.

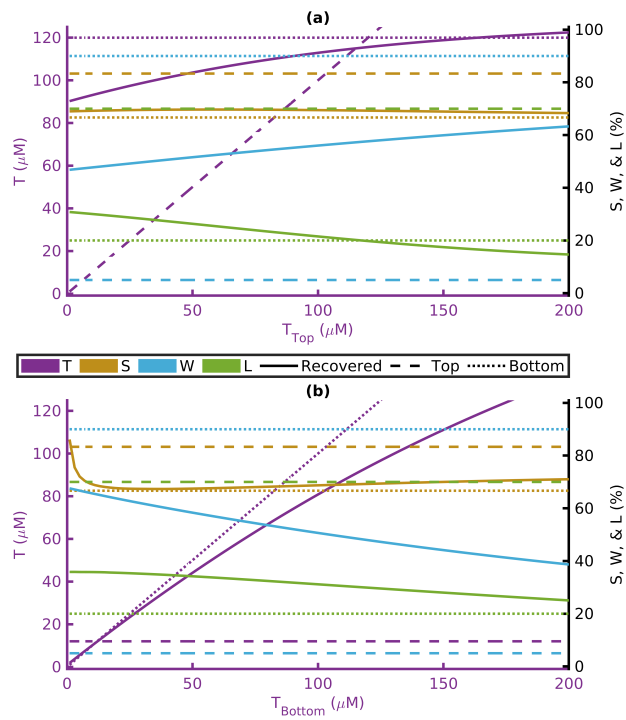


Figure 10.7: Recovered values versus actual top- (a) or bottom-layer (b) T fixing others to Tables 10.7&10.8.

Note 1: This figure can be found as Figure 1 in Blaney *et alia* Journal of Innovative Optical Health Sciences (2022) [9].

Acronyms: Total-hemoglobin (T); tissue oxygen Saturation (S); Water (W); and Lipid (L).

Figures 10.7-10.10 show this computational experiment for the absorption parameters with Figures 10.7, 10.8, 10.9,&10.10 varying T , S , W , and L , respectively. In each of these, the variation of the top-layer parameter is shown in subplot (a) and the variation of the bottom-layer in (b). Solid lines show the recovered value of the parameter while dashed or dotted lines show the actual top or bottom parameter values, respectively. By examining these plots one may determine how close a recovered parameter is to the actual value in a particular layer^k as a function of one of the absorption parameters. For example, Figure 10.7(a) shows that the recovered value for T is always closer to bottom layer T regardless

^kDetermination of how close a recovered value is to the actual is done by comparing the solid lines to the dashed or dotted lines.

Table 10.7: Actual and recovered absorption parameters for baseline two-layer medium in Blaney *et alia* Journal of Innovative Optical Health Sciences (2022) [9] with a top-layer thickness of 5 mm.

	T (μM)	S (%)	W (%)	L (%)	μ_a (650 nm) (mm ⁻¹)	μ_a (775 nm) (mm ⁻¹)	μ_a (900 nm) (mm ⁻¹)	μ_a (1024 nm) (mm ⁻¹)
Top actual	12	83	5	70	0.003	0.003	0.007	0.007
Bottom actual	120	67	90	20	0.042	0.026	0.034	0.042
Recovered	94	69	48	30	0.027	0.020	0.027	0.030

Note 1 This table can be found as Table 1 in Blaney *et alia* Journal of Innovative Optical Health Sciences (2022) [9].

Acronyms and Symbols Total-hemoglobin (T); tissue oxygen Saturation (S); Water (W); Lipid (L); and absorption coefficient (μ_a).

Table 10.8: Actual and recovered absorption parameters for baseline two-layer medium in Blaney *et alia* Journal of Innovative Optical Health Sciences (2022) [9] with a top-layer thickness of 5 mm.

	μ'_s (830 nm) (mm ⁻¹)	b	μ'_s (690 nm) (mm ⁻¹)
Top actual	0.60	0.1	0.61
Botton actual	0.40	1.5	0.53
Recovered	0.42	0.9	0.50

Note 1 This table can be found as Table 2 in Blaney *et alia* Journal of Innovative Optical Health Sciences (2022) [9].

Acronyms and Symbols Reduced scattering coefficient (μ'_s); and reduced scattering power coefficient (b).

of the value of top layer T.^l

Scattering parameters have a somewhat more complex effect on the recovered values. This is seen in Figures 10.11&10.12 for μ'_s and b, respectively. These figures display the recovered absorption parameters while varying top-layer (a) or bottom-layer (c) scattering properties as well as the recovered scattering parameters while varying top-layer (b) or bottom-layer (d) scattering properties. An example of the aforementioned complex effects can be seen in Figure 10.11(b) where the recovered value of b may take values not in-between top layer b and bottom layer b for large values of top layer μ'_s at 830 nm.

Finally, Figure 10.13 displays the results from the computational experiment where z_{top} was varied. In this case, the recovered parameters can

^lThis result can only be said to be true for the instrument simulated and baseline parameters used.

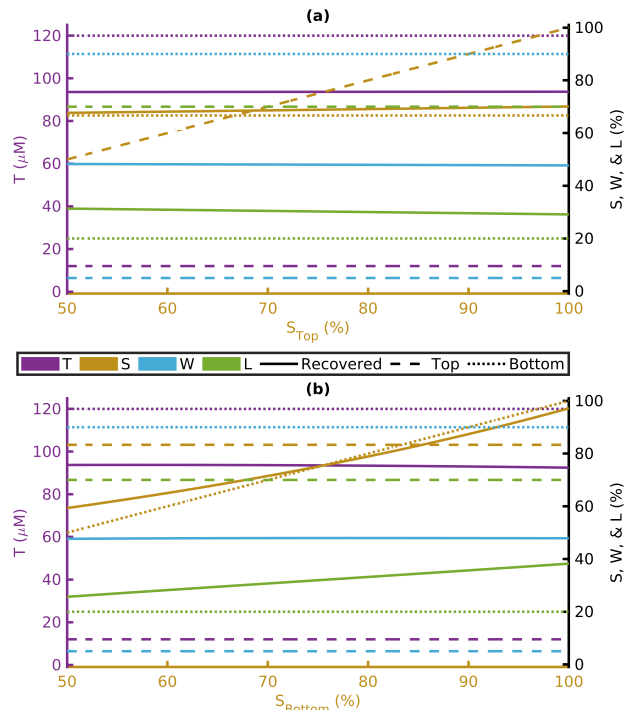


Figure 10.8: Recovered values versus actual top-(a) or bottom-layer (b) S fixing others to Tables 10.7&10.8.

Note 1: This figure can be found as Figure 2 in Blaney *et alia* Journal of Innovative Optical Health Sciences (2022) [9].

Acronyms: Total-hemoglobin (T); tissue oxygen Saturation (S); Water (W); and Lipid (L).

be seen to start closer to the actual values for the bottom-layer when z_{top} is thin and move closer to the actual top-layer value as z_{top} increases, with the curves following a sigmoid like shape. Some interesting results include the dominance of bottom layer S and top layer μ'_s at 830 nm on the

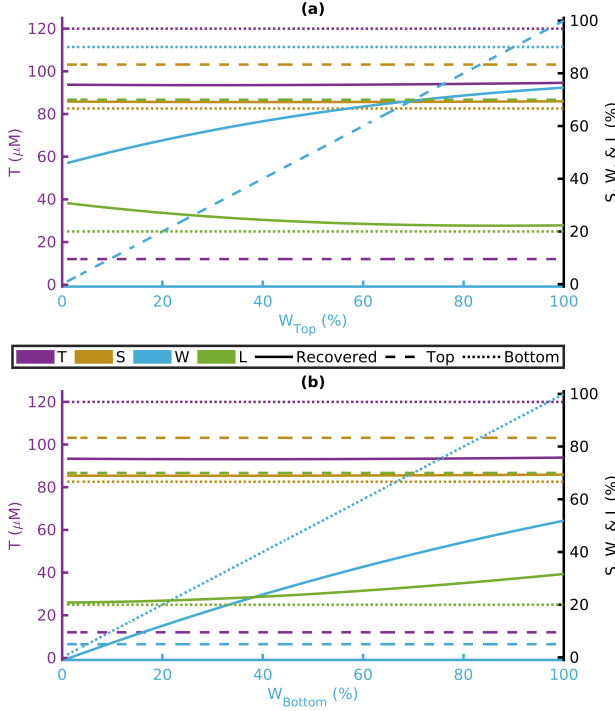


Figure 10.9: Recovered values versus actual top- (a) or bottom-layer (b) **W** fixing others to Tables 10.7&10.8.

Note 1: This figure can be found as Figure 3 in Blaney *et alia* Journal of Innovative Optical Health Sciences (2022) [9].

Acronyms: Total-hemoglobin (T); tissue oxygen Saturation (S); Water (W); and Lipid (L).

recovered value even for thick z_{top} , considering that end value of z_{top} in the plots is deeper than most of the sensitivity region for these optical measurements [3].

10.2.3.B Sensitivity to Absorption Parameters in a Two-Layered Medium

Table 10.9: Co-sensitivities for a two-layer medium with the baseline optical properties of Tables 10.7&10.8.

	$\delta T / \delta T_{lay}$	$\delta S / \delta S_{lay}$	$\delta W / \delta W_{lay}$	$\delta L / \delta L_{lay}$
Top	0.33	0.058	0.48	0.31
Bottom	0.62	0.63	0.41	0.58

Note 1 This table can be found as Table 3 in Blaney *et alia* Journal of Innovative Optical Health Sciences (2022) [9].

Acronyms and Symbols Total-hemoglobin (T); tissue oxygen Saturation (S); Water (W); and Lipid (L).

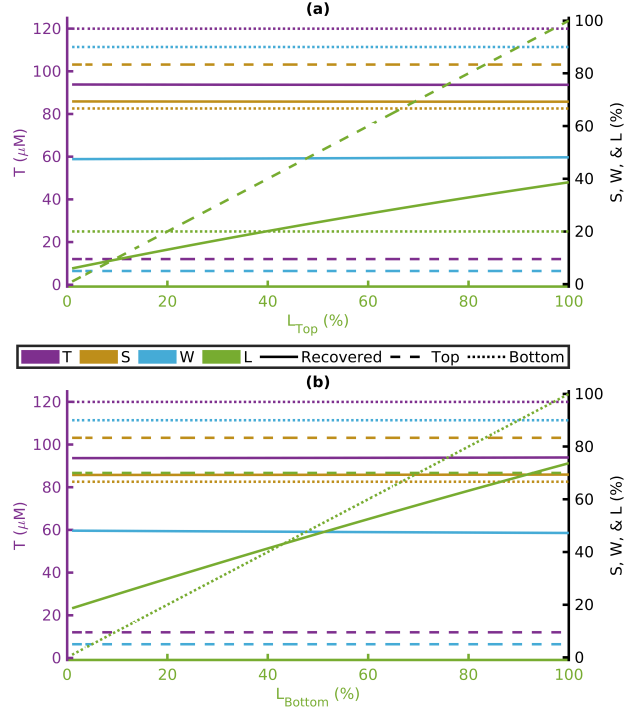


Figure 10.10: Recovered values versus actual top- (a) or bottom-layer (b) **L** fixing others to Tables 10.7&10.8.

Note 1: This figure can be found as Figure 4 in Blaney *et alia* Journal of Innovative Optical Health Sciences (2022) [9].

Acronyms: Total-hemoglobin (T); tissue oxygen Saturation (S); Water (W); and Lipid (L).

10.2.3.B.a Baseline Model Sensitivities

Using the values in Tables 10.7&10.8 as baseline, co-sensitivities^m were calculated (Table 10.9). From this it can be seen that recovered dynamic changes in **T**, **L**, and especially **S** are more sensitive to bottom-layer dynamics of the like chromophore. Conversely, recovered **W** dynamics are more sensitive to changes in the top-layer. Here it is emphasized that these values are only strictly actual for the particular baseline model chosen, and this consideration will be addressed in the following section.

Table 10.10 shows the full set of sensitivities displayed as fractions for the baseline model. In this case the co-sensitivities (Table 10.9) can be

^mSensitivities between like parameters are dubbed co-sensitivities, between recovered **T** and top layer **T** for example.

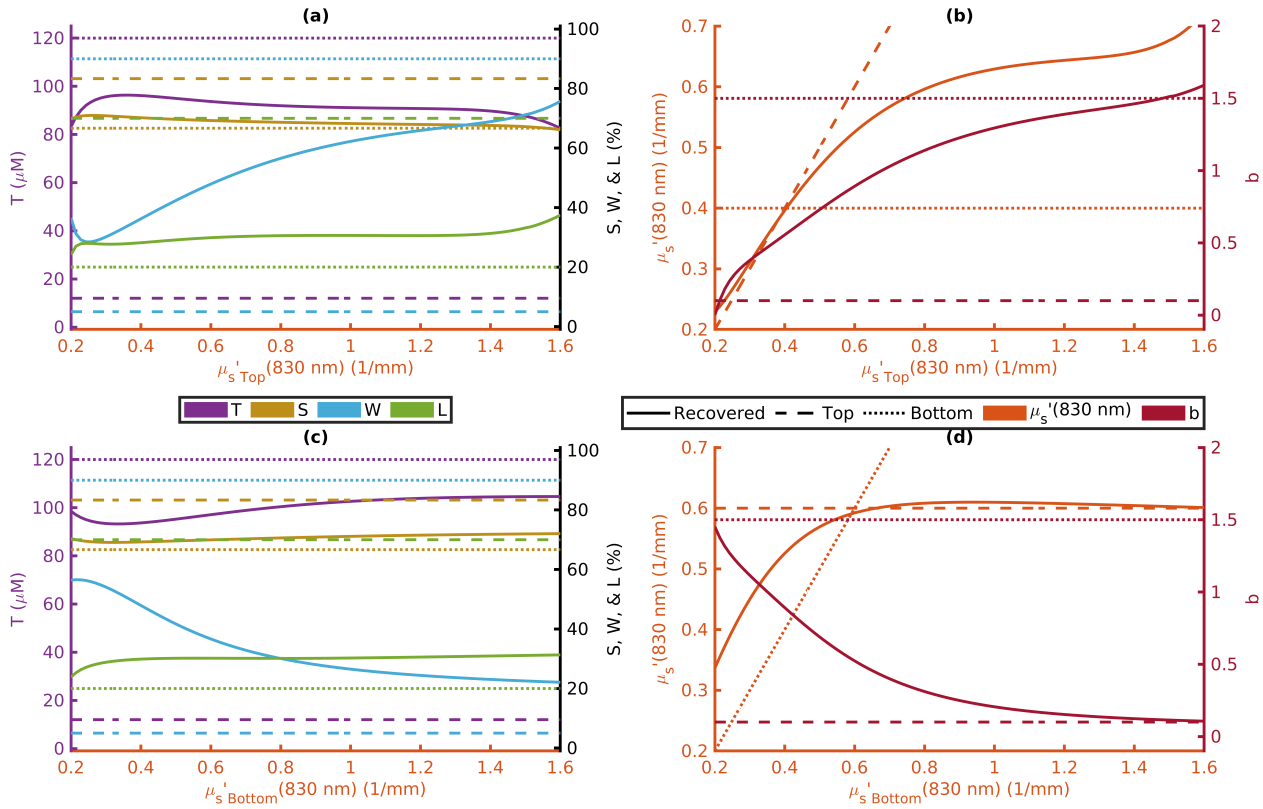


Figure 10.11: Absorption (a)&(c) and scattering (b)&(d) recovered values versus actual top- (a)&(b) or bottom-layer (c)&(d) μ_s' fixing others to Tables 10.7&10.8.

Note 1: This figure can be found as Figure 5 in Blaney *et alia* Journal of Innovative Optical Health Sciences (2022) [9].

Acronyms: Total-hemoglobin (T); tissue oxygen Saturation (S); Water (W); Lipid (L); reduced scattering coefficient (μ_s'); and reduced scattering power coefficient (b).

found in the diagonal of the upper and lower sub-tables and all off-diagonal elements are cross-sensitivitiesⁿ which can be thought of as cross-talk between parameters. Examining the cross-sensitivities in Table 10.10, it appears that there is little cross-talk between parameters, with the only parameter displaying notable cross-talking being the recovered changes in L . In the case of measuring recovered L dynamics, its value may be affected by changes in top layer W , bottom layer S , and bottom layer W . Again, all values are valid only for the particular baseline model. However, since little cross-sensitivity was

observed^o overall, the following section will neglect cross-sensitivity for brevity.

10.2.3.B.b Variation of Sensitivities as a Result of Varying Two-Layer Model Parameters In this section the two-layer absolute properties are varied and co-sensitivities calculated allowing for insight about how these sensitivities are affected by the absolute values of the parameters in a two-layer medium. In all cases parameters were not co-varied and unvaried parameters were held at the values of the baseline model (Tables 10.7&10.8), simply stated, only one parameter was varied at a time.

ⁿSensitivities between dis-similar parameters are cross-sensitivities, for example between recovered T and top layer W .

^oLittle cross-sensitivity except in the case of recovered L changes, which typically is assumed to not have dynamics.

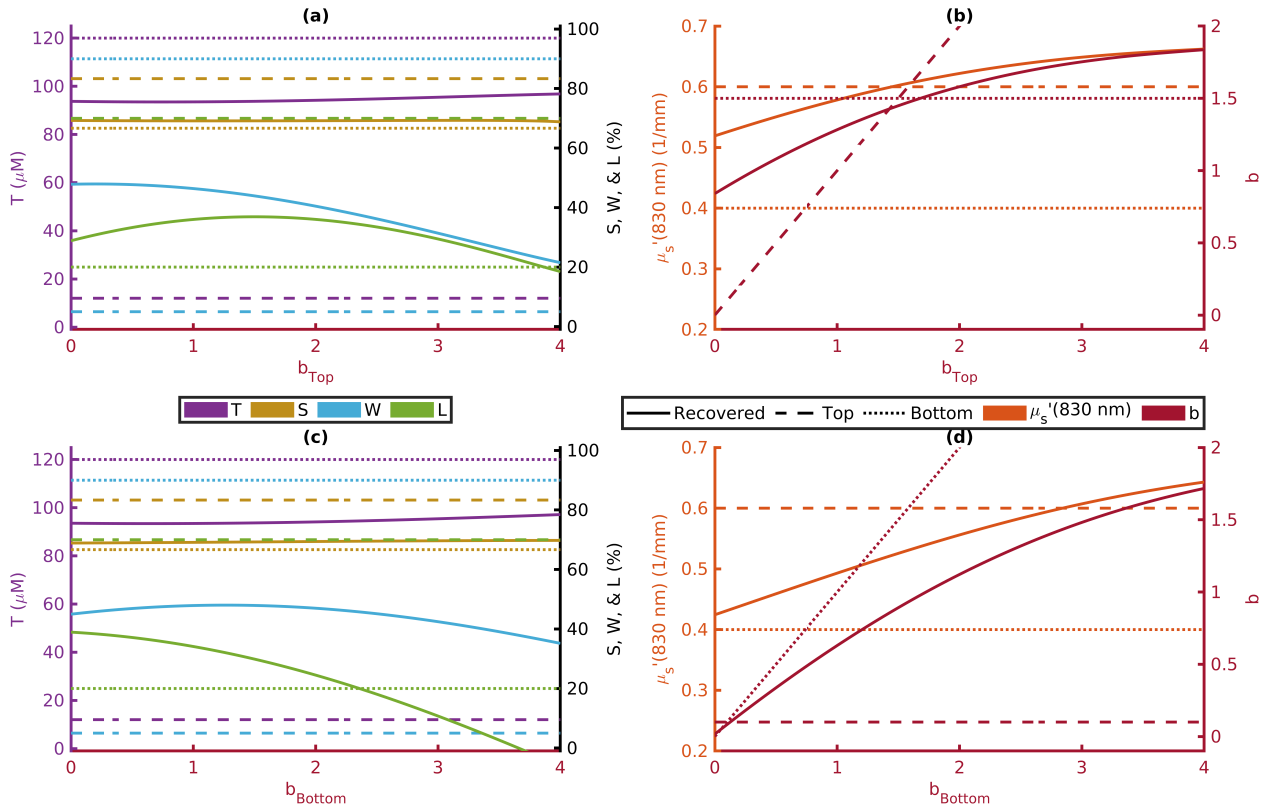


Figure 10.12: Absorption (a)&(c) and scattering (b)&(d) recovered values versus actual top- (a)&(b) or bottom-layer (c)&(d) b fixing others to Tables 10.7&10.8.

Note 1: This figure can be found as Figure 6 in Blaney *et alia* Journal of Innovative Optical Health Sciences (2022) [9].

Acronyms: Total-hemoglobin (T); tissue oxygen Saturation (S); Water (W); Lipid (L); reduced scattering coefficient (μ_s'); and reduced scattering power coefficient (b).

These results are displayed in Figure 10.14 where each sub-plot contains dual y -axes and dual x -axes. Which y -axis a curve belongs to is designated by the line type, which is specified in square brackets of the axis title. All solid lines correspond to T sensitivities, dashed lines to S sensitivities, dotted lines to W sensitivities, and dash-dotted lines to L sensitivities. Which x -axis a curve belongs to is signified by color, which is the same as the color of the variable in the axis title. All yellow lines show the sensitivity while varying the absolute value of S , blue lines while varying the absolute value of W , green lines while varying the absolute value of L , and purple lines while varying the absolute value of T . Each row of subplots examines differing combinations of which layer the sensitivity is to and

which layer the absolute value is being varied.

Despite the plethora of information in Figure 10.14 the story in most subplots is quite simple. This is because the absolute value of a given parameter does not affect many of the sensitivities in a given subplot. For example, in Figure 10.14(a) the sensitivities of recovered T or S to top-layer changes as a function of actual absolute top-layer properties is plotted. In this case it is immediately obvious that only the purple curves significantly change. This means that the sensitivities of recovered T or S to top-layer changes are not affected by the absolute value of top layer S , top layer W , or top layer L . However, since the purple line does change, the T sensitivity to the top-layer decreases and the S sensitivity to the top-layer increases each with greater top

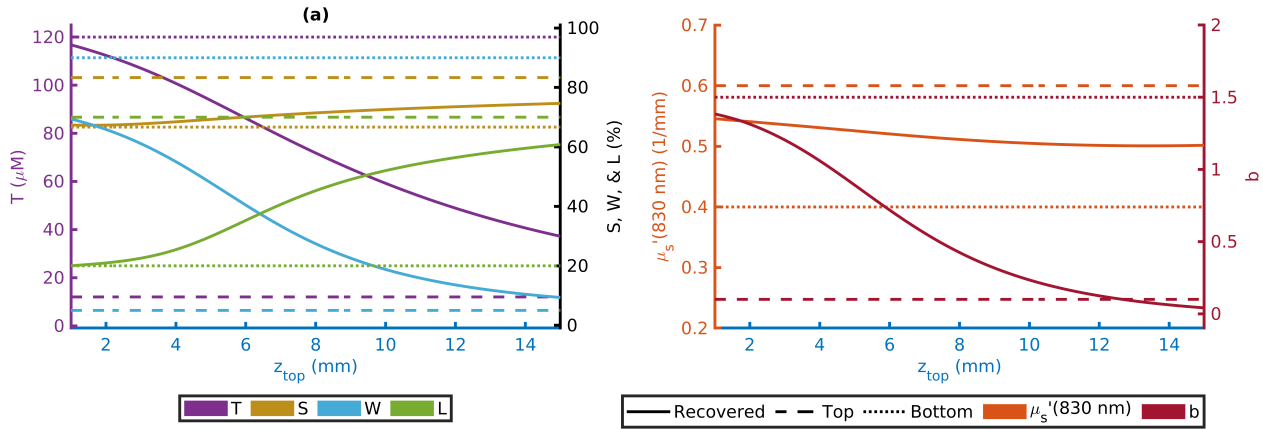


Figure 10.13: Absorption (a) and scattering (b) recovered values versus z_{top} fixing others to Tables 10.7&10.8.

Note 1: This figure can be found as Figure 7 in Blaney *et alia* Journal of Innovative Optical Health Sciences (2022) [9].

Acronyms: Total-hemoglobin (T); tissue oxygen Saturation (S); Water (W); Lipid (L); reduced scattering coefficient (μ'_s); reduced scattering power coefficient (b); and top layer thickness (z_{top}).

Table 10.10: All sensitivities for a two-layer medium with the baseline optical properties of Tables 10.7&10.8.

	δT (μM)	δS	δW	δL
δT_{Top} (μM)	0.33	$0.000\ 10\ \mu\text{M}^{-1}$	$0.000\ 92\ \mu\text{M}^{-1}$	$-0.0011\ \mu\text{M}^{-1}$
δS_{Top}	$-0.048\ \mu\text{M}$	0.058	0.0017	-0.020
δW_{Top}	$-1.0\ \mu\text{M}$	-0.0077	0.48	-0.21
δL_{Top}	$0.058\ \mu\text{M}$	$-0.000\ 85$	0.0074	0.31
δT_{Bottom} (μM)	0.62	$0.000\ 43\ \mu\text{M}^{-1}$	$-0.0011\ \mu\text{M}^{-1}$	$-0.000\ 16\ \mu\text{M}^{-1}$
δS_{Bottom}	$0.48\ \mu\text{M}$	0.63	-0.036	0.16
δW_{Bottom}	$2.0\ \mu\text{M}$	0.010	0.41	0.17
δL_{Bottom}	$0.20\ \mu\text{M}$	0.0014	-0.0089	0.58

Note 1 This table can be found as Table 4 in Blaney *et alia* Journal of Innovative Optical Health Sciences (2022) [9].

Note 2 Each element is the value of a numerical partial derivative with numerator corresponding to the top row labels and denominator corresponding to the left column labels.

Note 3 Co-sensitivities are diagonal elements of the top and bottom sub-tables and are restated in Table 10.9, off-diagonal elements are cross-sensitivities.

Note 4 All values are fractions none are represented in percent.

Acronyms and Symbols Total-hemoglobin (T); tissue oxygen Saturation (S); Water (W); and Lipid (L).

layer T .

Examining Figure 10.14 as a whole, some general trends are observed. In the left column the curves show that T and S sensitivities are not affected by the actual absolute values of W or L ,

but are somewhat affected by the actual value of S and are strongly effected by the actual value of T . The right column concerns that sensitivities of W and L which appear to be more heavily affected by the actual absolute value of all pa-

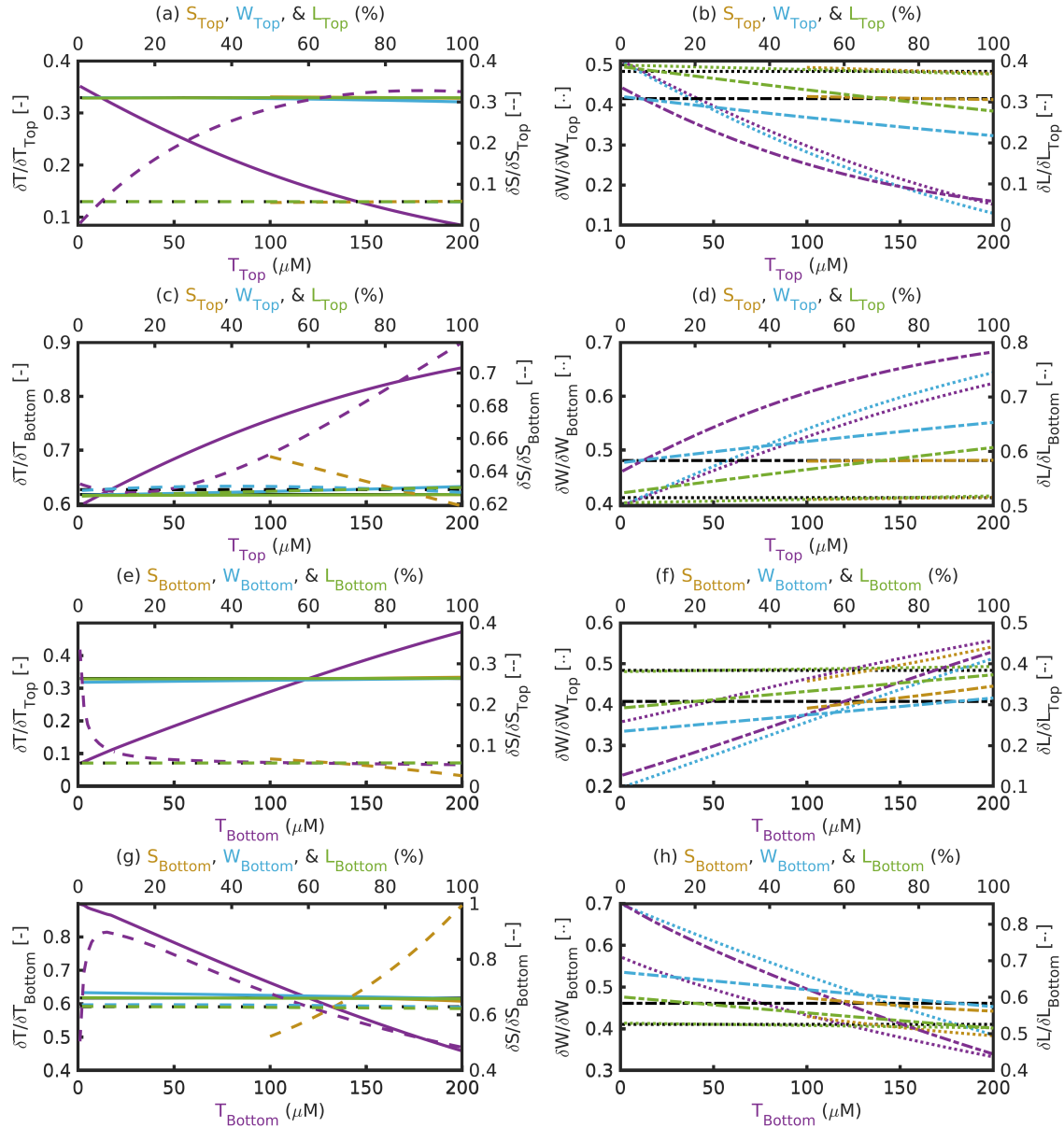


Figure 10.14: Co-sensitivities of recovered absorption parameters to actual changes in the top- or bottom-layer as a function of the absolute value of actual two-layer absorption parameters. (a),(c),(e),&(g) T and S sensitivities. (b),(d),(f),&(h) W and L sensitivities. (a)-(b) Top-layer sensitivities versus top-layer absolute values. (c)-(d) Bottom-layer sensitivities versus top-layer absolute values. (e)-(f) Top-layer sensitivities versus bottom-layer absolute values. (g)-(h) Bottom-layer sensitivities versus bottom-layer absolute values. Absolute values were varied without co-variation, and baseline model parameters are found in Tables 10.7&10.8, and z_{top} was 5 mm. Black lines show the co-sensitivities of the baseline model (Table 10.9).

Note 1: This figure can be found as Figure 8 in Blaney *et alia* Journal of Innovative Optical Health Sciences (2022) [9].

Note 2: x -axes: Curves belong to the x -axis of like color. Purple curves correspond to the bottom x -axes and show the variation of the actual absolute value of T . Yellow, blue, and green curves correspond to the top x -axes and show the variation of the actual absolute value of S , W , and L , respectively.

Note 3: y -axes: Curves belong to the y -axis of designated symbol which is shown in square brackets. Solid, dashed, dotted, and dash-dotted lines correspond to sensitivities of T , S , W , and L , respectively.

Acronyms: Total-hemoglobin (T); tissue oxygen Saturation (S); Water (W); Lipid (L); and top layer thickness (z_{top}).

rameters but to a lesser extent on S . The actual absolute value of T has the most effect on these sensitivities, closely followed by the actual absolute value of W . Finally, the actual absolute value of L does not affect the W sensitivity, but the opposite is not true.

Again, it is noted that all these results are specific to the model in question. Despite the parameters in this experiment being varied, they were not co-varied, scattering or thickness were not varied at all.

10.3 Discussion of Two-Layer *in-Silico* Simulations

The work in Blaney *et alia* Journal of Innovative Optical Health Sciences (2022) [9] sought to investigate how actual properties from a two-layer model are related to the properties retrieved from methods that utilize a Dual-Slope (DS) instrument and semi-infinite homogeneous model at their core. Arguably the two-layer model is the simplest heterogeneous model one can have, and yet its interactions with a homogeneous inversion model are still complex. Examining this simple pair of mismatched forward and inverse models may help provide insight into the meaning of retrieved optical properties from tissues, which are in-fact much more complex and heterogeneous than even a two-layer model.

First, the case of recovery of effective absolute homogeneous optical properties was considered. General trends observed in those simulations are:

- (a) Recovered Total-hemoglobin (T) is dominated by top layer T (Table 10.7 and Figure 10.7(b)).
- (b) Recovered tissue oxygen Saturation (S) is dominated by bottom layer S (Table 10.7 and Figure 10.8).
- (c) Recovered Water (W) and Lipid (L) are not dominated by either the top- or bottom-layer value alone (Table 10.7 and Figures 10.9-10.10).

- (d) Actual scattering properties have little effect on recovered T and S but do effect recovered W and L (Figures 10.11(a)(c)&10.12(a)(c)).
- (e) Recovered reduced scattering power coefficient (b) can take values outside of the range between actual top layer b and bottom layer b (Figure 10.12(b)).
- (f) Recovered reduced scattering coefficient (μ'_s) is dominated by the actual top-layer value (Figure 10.13(b)).

As a whole these results provide some valuable insights. For example, a goal in biomedical diffuse optics is to measure the chromophore concentrations of deep tissues. Points (a) and (b) suggest that for this model and measurement method the goal is feasible, at least for a similar z_{top} to the ones studied. Additionally, point (e) may provide some insight into apparent b s that are outside of the range of what is physically possible.^p Finally, these results show that each individual recovered property is not representative of the same region as the others. For example, point (f) suggests that recovered μ'_s is dominated by the top layer but point (a) suggests that the opposite is true for T . Since the recovered μ'_s resulted from the Frequency-Domain (FD) measurement and absorption coefficient (μ_a) from Continuous-Wave (CW), this may be evidence that FD exhibits more superficial sensitivity compared to CW. This is consistent with the idea that at increasing modulation frequencies sensitivity to optical property changes becomes more superficial [58]. However, this effect only occurs at frequencies above 500 MHz, therefore it is likely that this is not the effect here. Thus, this observed effect is likely simply due to the μ'_s measurement being dominated by superficial layers.

The results for sensitivity tell a similar story to those of absolute properties, but with the additional focus on dynamic changes in absorption while assuming scattering is constant. Again, a list of general observations follows:

^pThe range of physically possible reduced scattering power coefficient (b) is between 0 and 4 (Appendix A).

- (g) Recovered dynamics in absorption parameters are significantly affected by each layer except for **S** whose dynamics are dominated by the bottom-layer (Table 10.10).
- (h) There is little cross-talk in dynamics of different parameters except for **L** which has significant cross-talk with top-layer **W**, bottom-layer **S**, and bottom-layer **W** (Table 10.10).
- (i) The actual absolute value of **T** or **W** affects the sensitivity of almost every parameter (Figure 10.14).
- (j) The actual absolute value of **S** has little effect, for the most part, on the sensitivity of almost every parameter except the sensitivity recovered **S** to bottom-layer **S** (Figure 10.14(c)(g)).
- (k) The actual absolute value of **L** only has significant effect on **L** sensitivity (Figure 10.14(b)(d)(f)(h)).

As may be expected in most cases, sensitivities are affected by the absolute value of multiple parameters within a two-layer medium. However, point (h) may be a significant result. This being that **L** dynamics will have significant cross-talk with **W** and **S** dynamics due to the high cross-sensitivity (Table 10.10). Therefore, caution is recommended when allowing **L** to dynamically change in analysis, especially for the optical wavelength (λ) range examined here. This confound may not be a significant issue since **L** is not typically expected to dynamically change, thus it is reasonable and, likely safer due to the cross-talk, to assume no **L** changes from baseline during one's analysis.

These results should be considered when interpreting certain recovered properties or dynamic changes in a heterogeneous medium. Furthermore, since the particular results are dependent on instrumental setup, it may be helpful for one to repeat such simulations for one's own instrument, thus aiding in the interpretation of data from said instrument. The two-layer medium is much simpler than the complex heterogeneous one that is reality within biological tissue, but

the model does provide insight into how different instruments and methods behave when measuring heterogeneity.

Appendices

Appendix A

Forward Models

A.1 Diffuse Reflectance and Fluence

A.1.1 Diffuse Reflectance from A Semi-Infinite Homogeneous Medium

Considering a semi-infinite medium with extrapolated-boundary conditions, the complex Reflectance (\tilde{R}), defined as the net optical flux exiting the tissue per unit source power, may be written as [17, 143]:

$$\tilde{R} = \frac{1}{4\pi} \left(\tilde{C}_2 e^{-\tilde{\mu}_{eff} \|\vec{r}_1\|} + \tilde{C}_2 e^{-\tilde{\mu}_{eff} \|\vec{r}_2\|} \right) \quad (\text{A.1})$$

$$\tilde{C}_1 = z_0 \left(\frac{1 + \tilde{\mu}_{eff} \|\vec{r}_1\|}{\|\vec{r}_1\|^3} \right) \quad (\text{A.2})$$

$$\tilde{C}_2 = -z'_0 \left(\frac{1 + \tilde{\mu}_{eff} \|\vec{r}_2\|}{\|\vec{r}_2\|^3} \right) \quad (\text{A.3})$$

$$\vec{r}_1 = \vec{r}_{det} - \vec{r}_{src} \quad (\text{A.4})$$

$$\vec{r}_2 = \vec{r}_{det} - \vec{r}_{src'} \quad (\text{A.5})$$

$$\vec{r}_{src} = \vec{r}_{pencil} + z_0 \hat{z} \quad (\text{A.6})$$

$$\vec{r}_{src'} = \vec{r}_{pencil} + z'_0 \hat{z} \quad (\text{A.7})$$

$$\vec{r}_{det} = \rho \hat{x} \quad (\text{A.8})$$

$$\vec{r}_{pencil} = \vec{0} \quad (\text{A.9})$$

where z_0 is the depth of the real isotropic source (at \vec{r}_{src}):

$$z_0 = \frac{1}{\mu'_s} \quad (\text{A.10})$$

z'_0 is the height of the imaginary isotropic source (at $\vec{r}_{src'}$):

$$z'_0 = -z_0 + 2z_b \quad (\text{A.11})$$

z_b is the extrapolated boundary height:

$$z_b = -\frac{2A}{3(\mu'_s + \mu_a)} \quad (\text{A.12})$$

\vec{r}_{det} is the detector position and \vec{r}_{pencil} is the position of the pencil beam source on the surface of the semi-infinite medium. Here the pencil beam is assumed to be at the origin and the detector source-detector distance (ρ) away along the x axis, in general they can be anywhere on the surface and ρ is the distance between the pencil beam and the detector. The surface of the medium is at $z = 0$ with positive pointing into the medium, this implies the pencil beam must have a z coordinate of 0 and points in the positive z direction. The geometry of these vectors is shown in Figure A.1.

Next we express complex effective attenuation coefficient ($\tilde{\mu}_{eff}$):

$$\tilde{\mu}_{eff} = \sqrt{3(\mu'_s + \mu_a) \left(\mu_a - \frac{\omega n_{in} i}{c} \right)} \quad (\text{A.13})$$

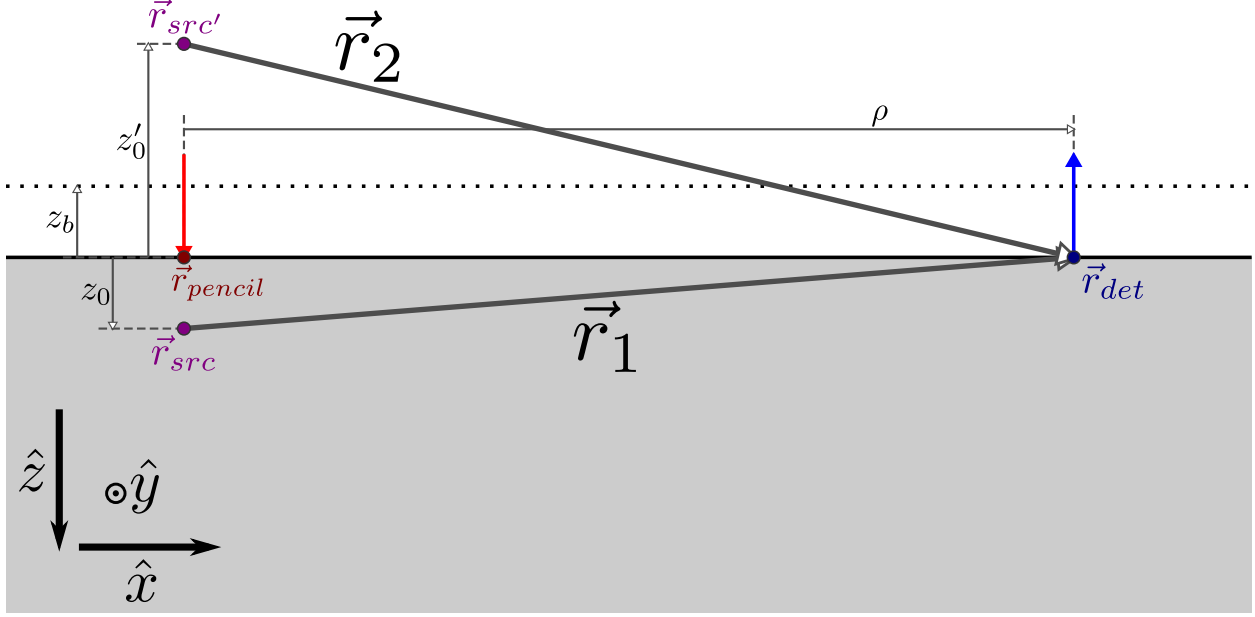


Figure A.1: Diagram of geometry and position vectors (\vec{r} s) in Equations A.1&A.15. The pencil beam source (red) impinges on the medium's surface at \vec{r}_{pencil} and light is detected (blue) at \vec{r}_{det} . The distance between the pencil source and detector on the surface is the source-detector distance (ρ). Isotropic sources are placed at \vec{r}_{src} and $\vec{r}_{src'}$ (purple), the former being the real source and the latter being the image source. z_0 is the real source depth, z_b is the boundary (dotted black) height, and z'_0 is the image source height. Notice that the real and image sources are symmetric about the boundary.

speed of light in vacuum (c) divided by n_{in} is describing the speed of light inside the medium (Equation A.16) and angular modulation frequency (ω) is expressed in terms of the Frequency-Domain (FD) modulation frequency (f_{mod}):

$$\omega = 2\pi f_{mod} \quad (\text{A.14})$$

The reflection parameter (A) describes the mismatch between index of refraction (n) inside (n_{in}) and outside of the medium (n_{out}) [143, 146]. For a typical mismatch of $n_{in} = 1.4$ and $n_{out} = 1$, $A = 2.949$, code to generate this parameter value is found in Listing A.1 [3]. The chief optical properties are absorption coefficient (μ_a) and reduced scattering coefficient (μ'_s) which may be considered the inputs to the \tilde{R} forward model. The expression for \tilde{R} is implemented in Listing A.2.

Reflectance (R) from Continuous-Wave (CW) may also be obtained from Equation A.1 by us-

ing effective attenuation coefficient (μ_{eff}) in the above expressions. The non-complex version of μ_{eff} is obtained by setting ω to zero, making all above variables real instead of complex and resulting in R instead of \tilde{R} . In FD one is often concerned with the Intensity (I) and phase (ϕ). For FD what is referred to as I is the amplitude of \tilde{R} ($|\tilde{R}|$) and similarly ϕ is the angle of \tilde{R} ($\angle \tilde{R}$).

Equation A.1 is derived from the extrapolated boundary condition ($z_b \neq 0$). The expression may be simplified using the zero boundary condition which assume a completely absorbing surface by setting $z_b = 0$. The consequence of this is that $\|\vec{r}_1\| = \|\vec{r}_2\|$ and Equation A.1 becomes one exponential instead of the sum of two. Further assumptions about ρ being larger than z_0 and μ_a being smaller than μ'_s lead us to the typical statement that linearized Intensity ($\ln(\rho^2 I)$) is linear with ρ . It is these assumptions that lead to the linear slopes method in Appendix B

while the iterative recovery method in said Appendix does not use these assumptions and works directly with Equation A.1.

A.1.2 Fluence in a Semi-Infinite Homogeneous Medium

Instead of describing the photons exiting the diffuse medium as with \tilde{R} we may also describe the distribution of photons within the medium with the complex fluence rate ($\tilde{\Phi}$). Using the same variables defined above for the expression of \tilde{R} we can define the Green's function for $\tilde{\Phi}$:

$$\tilde{\Phi} = \frac{3\mu'_s}{4\pi} \left(\frac{e^{-\|\vec{r}_1\|/\tilde{\mu}_{eff}}}{\|\vec{r}_1\|} - \frac{e^{-\|\vec{r}_2\|/\tilde{\mu}_{eff}}}{\|\vec{r}_2\|} \right) \quad (\text{A.15})$$

Here the same vector notation is used as Equation A.1 above, but now \vec{r}_{det} can be anywhere within the medium and the retrieved value for $\tilde{\Phi}$ is the $\tilde{\Phi}$ at \vec{r}_{det} . This can be imagined by examining Figure A.1 where now \vec{r}_{det} position is inside the medium instead of on the surface.

As with other complex variables, fluence rate (Φ) for CW can be obtained by setting ω to zero and using the same expression. The expression for $\tilde{\Phi}$ is implemented in Listing A.3.

A.1.3 Diffuse Reflectance from a Layered Cylindrical Medium

The following diffusion theory derived expressions describe \tilde{R} from a two layered cylinder with source at the center of the flat surface and \tilde{R} measured on the same flat surface [142]. As with the previous section, R may be obtained by setting ω or f_{mod} to zero. To emphasize that the main independent variables are the ρ , μ_a , μ'_s , and the thickness of the top layer (z_{top}), the dependent variables in these expressions are shown as functions of them. Other variables are in-fact independent but are not included in this notation. Examples of de-emphasized independent variables are n and ω . Furthermore, for brevity, this function notation is only used on the left-hand-side of the following expressions.

First, the following values are defined. The speed of light within the medium (v) in terms of

c and n :

$$v = \frac{c}{n} \quad (\text{A.16})$$

where, c taken to be $2.997\,924\,58 \times 10^{11} \text{ mm s}^{-1}$. ω is defined in terms of f_{mod} in Equation A.14. Next, the diffusion coefficient (\mathcal{D}) is:

$$\mathcal{D}(\mu'_{s,top/bot}) = \frac{1}{3\mu'_{s,top/bot}} \quad (\text{A.17})$$

where, the subscript of μ'_s tells whether the variable belongs to the top (*top*) or bottom (*bot*) layer. The approximate depth of the isotropic source (z_0) is redefined from the above section, now in terms of the top layer μ'_s :

$$z_0(\mu'_{s,top}) = \frac{1}{\mu'_{s,top}} \quad (\text{A.18})$$

The approximate extrapolated boundary height (z_b) is also redefined in this way:

$$z_b(\mu'_{s,top}) = 2A\mathcal{D}_{top} \quad (\text{A.19})$$

where, A is the index of refraction mismatch parameter from the previous section [143, 146].

Next, various coefficients are defined as a function of the k^{th} zero of the 0^{th} order Bessel function of the first kind. First, the optical attenuation parameter (\tilde{a}_k):

$$\tilde{a}_k(\mu_{a,top/bot}, \mu'_{s,top/bot}) = \sqrt{\frac{\mu_{a,top/bot}}{\mathcal{D}_{top/bot}} + \left(\frac{j_{0,k}}{B}\right)^2 + \frac{\omega}{v\mathcal{D}_{top/bot}}i} \quad (\text{A.20})$$

where, the subscript of μ_a tells whether the variable belongs to the top (*top*) or bottom (*bot*) layer, $j_{0,k}$ is the k^{th} zero of the 0^{th} order Bessel function of the first kind, B is the radius of the two-layer cylinder (for which the source is in the center; B is typically assumed to be 150 mm). Then, the ρ parameter (Q_k) is written:

$$Q_k(\rho) = \frac{J_0\left(\frac{\rho j_{0,k}}{B}\right)}{J_1(j_{0,k})^2} \quad (\text{A.21})$$

Now the reflectance for the case when the isotropic source is in the first layer (\tilde{R}_1) can be

expressed:

$$\begin{aligned} \tilde{R}_1(\rho, \mu_{a,top}, \mu'_{s,top}, z_{top}, \mu_{a,bot}, \mu'_{s,bot}) = & \frac{1}{\pi B^2} \sum_{k=1}^{\infty} \left\{ \left[\right. \right. \\ & \frac{e^{-\tilde{a}_{top,k}z_0} + e^{-\tilde{a}_{top,k}(z_0+2z_b)}}{e^{\tilde{a}_{top,k}(z_{top}+z_b)}} \\ & + \frac{\cosh(\tilde{a}_{top,k}z_0) \times \sinh(\tilde{a}_{top,k}(z_0+2z_b))}{e^{\tilde{a}_{top,k}(z_{top}+z_b)}} \\ & \times \left(\mathcal{D}_{top}\tilde{a}_{top,k} - \mathcal{D}_{bot}\tilde{a}_{bot,k} \right) \quad (\text{A.22}) \\ & \left. \left. \times \left(\mathcal{D}_{top}\tilde{a}_{top,k} \cosh(\tilde{a}_{top,k}(z_{top}+z_b)) \right. \right. \right. \\ & \left. \left. \left. + \mathcal{D}_{bot}\tilde{a}_{bot,k} \sinh(\tilde{a}_{top,k}(z_{top}+z_b)) \right) \right] Q_k \right\} \end{aligned}$$

where, z_{top} is the thickness of the top layer. For computation, infinite sums were typically done over 10^3 terms.

To express the reflectance when the isotropic source is in the second layer (\tilde{R}_2) additional coefficients are defined to simplify the expression:

$$\tilde{\alpha}_{1,k}(\mu_{a,top}, \mu'_{s,top}) = e^{-\tilde{a}_{top,k}z_b} \quad (\text{A.23})$$

$$\tilde{\alpha}_{2,k}(\mu_{a,top}, \mu'_{s,top}, z_{top}) = n^2 e^{\tilde{a}_{top,k}z_{top}} \quad (\text{A.24})$$

$$\begin{aligned} \tilde{\alpha}_{3,k}(\mu_{a,top}, \mu'_{s,top}, z_{top}) = & \quad (\text{A.25}) \\ \tilde{\alpha}_{3,k}\tilde{\alpha}_{2,k}\mathcal{D}_{top}e^{\tilde{a}_{top,k}z_{top}} & \end{aligned}$$

$$\tilde{\beta}_{1,k}(\mu_{a,top}, \mu'_{s,top}) = e^{\tilde{a}_{top,k}z_b} \quad (\text{A.26})$$

$$\tilde{\beta}_{2,k}(\mu_{a,top}, \mu'_{s,top}, z_{top}) = n^2 e^{-\tilde{a}_{top,k}z_{top}} \quad (\text{A.27})$$

$$\begin{aligned} \tilde{\beta}_{3,k}(\mu_{a,top}, \mu'_{s,top}, z_{top}) = & \quad (\text{A.28}) \\ -\tilde{\alpha}_{top,k}\mathcal{D}_{top}e^{-\tilde{a}_{top,k}z_{top}} & \end{aligned}$$

$$\tilde{\gamma}_{2,k}(z_{top}, \mu_{a,bot}, \mu'_{s,bot}) = -n^2 e^{-\tilde{a}_{bot,k}z_{top}} \quad (\text{A.29})$$

$$\begin{aligned} \tilde{\gamma}_{3,k}(z_{top}, \mu_{a,bot}, \mu'_{s,bot}) = & \quad (\text{A.30}) \\ \tilde{\alpha}_{bot,k}\mathcal{D}_{bot}e^{-\tilde{a}_{bot,k}z_{top}} & \end{aligned}$$

$$\begin{aligned} \tilde{\zeta}_{2,k}(\mu'_{s,top}, z_{top}, \mu_{a,bot}, \mu'_{s,bot}) = & \quad (\text{A.31}) \\ -\frac{n^2 e^{-\tilde{a}_{bot,k}(z_{top}-z_0)}}{2\tilde{a}_{bot,k}\mathcal{D}_{bot}} & \end{aligned}$$

$$\begin{aligned} \tilde{\zeta}_{3,k}(\mu'_{s,top}, z_{top}, \mu_{a,bot}, \mu'_{s,bot}) = & \quad (\text{A.32}) \\ -\frac{e^{\tilde{a}_{bot,k}(z_{top}-z_0)}}{2} & \end{aligned}$$

Then combinations of these coefficients are defined.

$$\begin{aligned} \tilde{\Xi}_k(\mu_{a,top}, \mu'_{s,top}, z_{top}, \mu_{a,bot}, \mu'_{s,bot}) = & \quad (\text{A.33}) \\ \tilde{\alpha}_{1,k}\tilde{\beta}_{2,k}\tilde{\gamma}_{3,k} - \tilde{\alpha}_{1,k}\tilde{\beta}_{3,k}\tilde{\gamma}_{2,k} \\ - \tilde{\alpha}_{2,k}\tilde{\beta}_{1,k}\tilde{\gamma}_{3,k} + \tilde{\alpha}_{3,k}\tilde{\beta}_{1,k}\tilde{\gamma}_{2,k} & \end{aligned}$$

$$\begin{aligned} \tilde{\Upsilon}_k(\mu_{a,top}, \mu'_{s,top}, z_{top}, \mu_{a,bot}, \mu'_{s,bot}) = & \quad (\text{A.34}) \\ -\frac{\tilde{\beta}_{1,k}(\tilde{\gamma}_{2,k}\tilde{\zeta}_{3,k} - \tilde{\gamma}_{3,k}\tilde{\zeta}_{2,k})}{\tilde{\Xi}_k} & \end{aligned}$$

$$\begin{aligned} \tilde{\Psi}_k(\mu_{a,top}, \mu'_{s,top}, z_{top}, \mu_{a,bot}, \mu'_{s,bot}) = & \quad (\text{A.35}) \\ \frac{\tilde{\alpha}_{1,k}(\tilde{\gamma}_{2,k}\tilde{\zeta}_{3,k} - \tilde{\gamma}_{3,k}\tilde{\zeta}_{2,k})}{\tilde{\Xi}_k} & \end{aligned}$$

Given all these coefficients the reflectance when the isotropic source is in the second layer (\tilde{R}_2) can now be expressed:

$$\begin{aligned} \tilde{R}_2(\rho, \mu_{a,top}, \mu'_{s,top}, z_{top}, \mu_{a,bot}, \mu'_{s,bot}) = & \quad (\text{A.36}) \\ \frac{1}{\pi B^2} \sum_{k=1}^{\infty} \left\{ \left[\mathcal{D}_{top}\tilde{a}_{top,k}(\tilde{\Upsilon}_k - \tilde{\Psi}_k) \right] Q_k \right\} & \end{aligned}$$

where, as before, the sum was typically done over 10^3 terms.

Finally, the piece-wise expression for \tilde{R} from a two-layer medium may be expressed:

$$\begin{aligned} \tilde{R}(\rho, \mu_{a,top}, \mu'_{s,top}, z_{top}, \mu_{a,bot}, \mu'_{s,bot}) = & \quad (\text{A.37}) \\ \begin{cases} \tilde{R}_1 & z_0 < z_{top} \\ \tilde{R}_2 & z_0 \geq z_{top} \end{cases} & \end{aligned}$$

As with Equation A.1 R may be obtained by setting ω to zero.

A.2 Optical Properties

A.2.1 Absorption Coefficient

The absorption coefficient (μ_a) is modeled as a linear combination of extinction coefficient (ϵ) weighted by the chromophore concentrations. For one optical wavelength (λ), μ_a can be expressed as follows:

$$\mu_a = \sum_{k=1}^{N_{chrom}} C_k \epsilon_{Ck} \quad (\text{A.38})$$

where N_{chrom} is the number of chromophores, C_k is the concentration of chromophore k , and ϵ_{Ck} is the extinction of chromophore k . However, ϵ is λ dependent, thus μ_a is also and the above equation is true for a continuum of λ s. Therefore, the system can be written as follows:

$$\begin{bmatrix} \mu_a(\lambda_1) \\ \vdots \\ \mu_a(\lambda_{N_{lam}}) \end{bmatrix} = \begin{bmatrix} \epsilon_{C1}(\lambda_1) & \dots & \epsilon_{C_{N_{chrom}}}(\lambda_1) \\ \vdots & \ddots & \vdots \\ \epsilon_{C1}(\lambda_{N_{lam}}) & \dots & \epsilon_{C_{N_{chrom}}}(\lambda_{N_{lam}}) \end{bmatrix} \times \begin{bmatrix} C_1 \\ \vdots \\ C_{N_{chrom}} \end{bmatrix} \quad (\text{A.39})$$

or after introducing matrix of extinction coefficients (\mathbf{E}):

$$\vec{\mu}_a = \mathbf{E} \vec{C} \quad (\text{A.40})$$

Similarly if absorption coefficient change ($\Delta\mu_a$) and chromophore concentration changes (ΔC) are considered:

$$\Delta\vec{\mu}_a = \mathbf{E} \Delta \vec{C} \quad (\text{A.41})$$

These expressions are general for N_{lam} λ s and N_{chrom} chromophores.

These expressions can be formulated in various ways for various scenarios. Considering the case where only Oxy-hemoglobin (O) and Deoxy-hemoglobin (D) are chromophores we have:

$$\vec{\mu}_a = [\bar{\epsilon}_O \quad \bar{\epsilon}_D] \begin{bmatrix} O \\ D \end{bmatrix} \quad (\text{A.42})$$

or for Oxy-hemoglobin concentration change (ΔO) and Deoxy-hemoglobin concentration change (ΔD):

$$\Delta\vec{\mu}_a = [\bar{\epsilon}_O \quad \bar{\epsilon}_D] \begin{bmatrix} \Delta O \\ \Delta D \end{bmatrix} \quad (\text{A.43})$$

Also the chromophores Water (W) and Lipid (L) can be added:

$$\vec{\mu}_a = [\bar{\epsilon}_O \quad \bar{\epsilon}_D \quad \bar{\epsilon}_W \quad \bar{\epsilon}_L] \begin{bmatrix} O \\ D \\ W \\ L \end{bmatrix} \quad (\text{A.44})$$

and even reformulated in terms of Total-hemoglobin (T) and tissue oxygen Saturation (S) instead of O and D:

$$\vec{\mu}_a = [\bar{\epsilon}_O \quad \bar{\epsilon}_D \quad \bar{\epsilon}_W \quad \bar{\epsilon}_L] \begin{bmatrix} ST \\ (1-S)T \\ W \\ L \end{bmatrix} \quad (\text{A.45})$$

since:

$$O = ST \quad (\text{A.46})$$

$$D = (1 - S)T \quad (\text{A.47})$$

This suits to shows the the linear combination of chromophores can be used to model the λ dependence of μ_a . In Appendix D these expressions are inverted to give a way to convert a measured μ_a to a chromophore concentration.

A.2.2 Reduced Scattering Coefficient

The reduced scattering coefficient (μ'_s) can be modeled as a decreasing power law dependence with λ . This is because in the λ range and types of media considered in diffuse optics there is a plethora of different types of scattering events occurring that roughly have different power law dependencies with λ .^a Since diffuse optics is concerned with average behavior and primarily μ'_s

^aThe reduced scattering coefficient (μ'_s) may have an oscillatory dependence on optical wavelength (λ) in addition to a power law, however, considering the range of λ s and scattering particle sizes considered in this work only the power law dependence is considered.

the overall λ dependence is modeled with reduced scattering power coefficient (b) as follows:

$$\mu'_s(\lambda) = \mu'_s(\lambda_0) \left(\frac{\lambda}{\lambda_0} \right)^{-b} \quad (\text{A.48})$$

The scattering dependence can be thought of as a mixture of Mie scattering, which is not strongly λ dependent and Rayleigh scattering, which is strongly λ dependent. b typically takes values between 0 to 4 with the upper limit set based on the Rayleigh scattering dependence. In biological tissue a typical b value may be roughly between 1 to 2, however, this should not be considered a guideline for a typical b value since the retried value may be dependent on exact measurement methodology.

Listings

Listing A.1: MathWorks MATrix LABoratory [Natick, MA USA] (MATLAB) code for index of refraction (n) mismatch parameter (A)

```

1 function A = n2A(nin, nout)
2 % A = n2A(nin, nout)
3 % Inputs:
4 %     nin – Index of refraction inside medium
5 %     nout – Index of refraction outside medium
6 % Output:
7 %     A – Index of refraction mismatch parameter
8
9 if nargin==0
10     dan12=1.4;
11 else
12     dan12=nin/nout;
13 end
14
15 if dan12>1
16     A=504.332889–2641.00214*dan12+...
17         5923.699064*dan12.^2–7376.355814*dan12^3+...
18             5507.53041*dan12^4–2463.357945*dan12^5+...
19                 610.956547*dan12^6–64.8047*dan12^7;
20 elseif dan12<1
21     A=3.084635–6.531194*dan12+...
22         8.357854*dan12^2–5.082751*dan12^3+1.171382*dan12^4;
23 else
24     A=1;
25 end
26
27 end

```

Available at:

<https://github.com/DOIT-Lab/DOIT-Public/tree/master/Dissertations/GilesBlaney2022/code>

Listing A.2: MathWorks MATrix LABoratory [Natick, MA USA] (MATLAB) code for complex Reflectance (\tilde{R}) which is capable of computing for a vector of positions

```

1 function [R] = complexReflectance(rs, rd, omega, optProp)
2 % Giles Blaney Spring 2019
3 % [R] = complexReflectance(rs, rd, omega, optProp)
4 % Inputs:
5 %     rs – Source coordinates. (mm)
6 %     rd – Detector coordinates. (mm)
7 %     omega – (OPTIONAL, default=2*pi*1.40625e8 rad/sec) Angular modulation
8 %             frequency. (rad/sec)
9 %     optProp – (OPTIONAL) Struct of optical properties with the following
10 %               fields:
11 %                   nin – (default=1.4) Index of refraction inside. (–)
12 %                   nout – (default=1) Index of refraction outside. (–)
13 %                   musp – (default=1.2 1/mm) Reduced scattering. (1/mm)
14 %                   mua – (default=0.01 1/mm) Absorption. (1/mm)
15 % Outputs:
16 %     R – Complex reflectance. (1/mm^2)

```

```

17
18 if nargin<=2
19     fmod=1.40625e8; %Hz
20     omega=2*pi*fmod; %rad/sec
21
22     optProp.nin=1.4;
23     optProp.nout=1;
24     optProp.musp=1.2; %1/mm
25     optProp.mua=0.01; %1/mm
26
27     warning(['Default optical properties used, this may be inconsistent',...
28             ' with the musp used for source depth']);
29 end
30
31
32 if size(rs, 1)>1 && size(rd, 1)>1
33     error('Can not use multiple sources and multiple detectors');
34 end
35
36 x0=rs(:, 1); %mm
37 y0=rs(:, 2); %mm
38 z0=rs(:, 3); %mm
39
40 c=2.99792458e11; %mm/sec
41 v=c/optProp.nin;
42
43 A=n2A(optProp.nin, optProp.nout);
44 D=1/(3*optProp.musp); %mm
45 zb=-2*A*D; %mm
46
47 mueff=sqrt(optProp.mua/D-1i*omega/(v*D)); %1/mm
48
49 rsp=[x0, y0, -z0+2*zb]; %mm
50
51 r1=vecnorm(rd-rs, 2, 2);
52 r2=vecnorm(rd-rsp, 2, 2);
53
54 R=(z0./(r1+mueff).*exp(-mueff.*r1)./(r1.^2)+...
55     (z0-2*zb).*(1./r2+mueff).*exp(-mueff.*r2)./(r2.^2))/...
56     (4*pi);
57
end

```

Available at:

<https://github.com/DOIT-Lab/DOIT-Public/tree/master/Dissertations/GilesBlaney2022/code>

Listing A.3: MathWorks MATrix LABoratory [Natick, MA USA] (MATLAB) code for complex fluence rate ($\tilde{\Phi}$) which is capable of computing for a vector of positions

```

1 function [PHI] = complexFluence(rs, rd, omega, optProp)
2 % Giles Blaney Spring 2019
3 % [PHI] = complexFluence(rs, rd, omega, optProp)
4 % Inputs:
5 %   rs      -- Source coordinates. (mm)
6 %   rd      -- Detector coordinates. (mm)
7 %   omega   -- (OPTIONAL, default=2*pi*1.40625e8 rad/sec) Angular modulation

```

```

8 %          frequency. (rad/sec)
9 % optProp - (OPTIONAL) Struct of optical properties with the following
10 % fields:
11 %      nin - (default=1.4) Index of refraction inside. (-)
12 %      nout - (default=1) Index of refraction outside. (-)
13 %      musp - (default=1.2 1/mm) Reduced scattering. (1/mm)
14 %      mua - (default=0.01 1/mm) Absorption. (1/mm)
15 % Outputs:
16 % PHI    - Complex fluence. (1/mm^2)
17
18 if nargin<=2
19     fmod=1.40625e8; %Hz
20     omega=2*pi*fmod; %rad/sec
21
22     optProp.nin=1.4;
23     optProp.nout=1;
24     optProp.musp=1.2; %1/mm
25     optProp.mua=0.01; %1/mm
26
27     warning(['Default optical properties used, this may be inconsistent',...
28             ' with the musp used for source depth']);
29 end
30
31 if size(rs, 1)>1 && size(rd, 1)>1
32     error('Can not use multiple sources and multiple detectors');
33 end
34
35 x0=rs(:, 1); %mm
36 y0=rs(:, 2); %mm
37 z0=rs(:, 3); %mm
38
39 c=2.99792458e11; %mm/sec
40 v=c/optProp.nin;
41
42 A=n2A(optProp.nin, optProp.nout);
43 D=1/(3*optProp.musp); %mm
44 zb=-2*A*D; %mm
45
46 mueff=sqrt(optProp.mua/D-1i*omega/(v*D)); %1/mm
47
48 rsp=[x0, y0, -z0+2*zb]; %mm
49
50 r1=vecnorm(rd-rs, 2, 2);
51 r2=vecnorm(rd-rsp, 2, 2);
52
53 PHI=(exp(-mueff.*r1)./r1-exp(-mueff.*r2)./r2)/(4*pi*D);
54 end

```

Available at:

<https://github.com/DOIT-Lab/DOIT-Public/tree/master/Dissertations/GilesBlaney2022/code>

Appendix B

Measurement of Absolute Optical Properties

B.1 Iterative Method

The iterative method of absolute optical property recovery seeks to linearize Equation A.1 directly without making further assumptions. For this method to work the spatial dependence of complex Reflectance (\tilde{R}) or Reflectance (R) versus source-detector distance (ρ) must be measured. Multi-Distance (MD), Self-Calibrating (SC), and Dual-Slope (DS) all achieve this. A typical Frequency-Domain (FD) instrument will output Intensity (I) (*id est* amplitude) and phase (ϕ) from which R can be expressed as follows:

$$\tilde{R} = I e^{i\phi} \quad (\text{B.1})$$

In the following, we first describe the analysis of \tilde{R} across multiple ρ s to retrieve complex effective attenuation coefficient ($\tilde{\mu}_{eff}$) and then absorption coefficient (μ_a) and reduced scattering coefficient (μ'_s). When working with R data the same expressions can be used and the property retrieved will be effective attenuation coefficient (μ_{eff}) which can converted to μ_a assuming μ'_s is known (Equation 9.1).

To yield a linear relationship Equation A.1 can be rewritten as:

$$\ln \left[\frac{4\pi \tilde{R}}{\tilde{C}_1 + \tilde{C}_1 e^{\tilde{\mu}_{eff}(\|\vec{r}_1\| - \|\vec{r}_2\|)}} \right] = -\tilde{\mu}_{eff} \|\vec{r}_1\| \quad (\text{B.2})$$

where the meanings of the variables is described in Appendix A for Equation A.1. For simplicity the left-hand-side of this expression is renamed \tilde{y} and noting these variables' dependencies on μ_a ,

μ'_s , and ρ we can write:

$$\tilde{y}(\mu_a, \mu'_s, \rho) = -\tilde{\mu}_{eff}(\mu_a, \mu'_s) \|\vec{r}_1(\mu'_s, \rho)\| \quad (\text{B.3})$$

This expression has optical properties on both the left- and right-hand-sides, therefore it can not simply be solved. Therefore, a iterative solution is used with iteration number k :

$$\begin{aligned} \tilde{y}(\mu_{a,k-1}, \mu'_{s,k-1}, \rho) &= \\ -\tilde{\mu}_{eff}(\mu_{a,k}, \mu'_{s,k}) \|\vec{r}_1(\mu'_{s,k-1}, \rho)\| + b_k & \end{aligned} \quad (\text{B.4})$$

where a complex linear fit is repeated over multiple iterations to find the slope of \tilde{y} versus $\|\vec{r}_1\|$. The variable b_k has been added to not force the linear fit to pass through the origin and absorb instrumental factors. An initial guess for μ_a and μ'_s must be used to start the iteration, for this guess the linear slopes method is used to estimate the optical properties. After just a few iterations $\tilde{\mu}_{eff}$ typically stops changing significantly and the fit is said to have converged.

The $\tilde{\mu}_{eff}$ may be converted to the optical properties μ_a and μ'_s . This also must be done each iteration so that the values may be used as the $k-1$ value for the next iteration. To do this, first total reduced attenuation coefficient (μ_t') is found:

$$\mu_t' = \frac{-2c\Re[\tilde{\mu}_{eff}]\Im[\tilde{\mu}_{eff}]}{3n\omega} \quad (\text{B.5})$$

using the known and assumed angular modulation frequency (ω), speed of light in vacuum (c), and index of refraction (n). Then μ_a is found:

$$\mu_a = \frac{\Re[\tilde{\mu}_{eff}]^2 - \Im[\tilde{\mu}_{eff}]^2}{3\mu_t'} \quad (\text{B.6})$$

and finally μ'_s :

$$\mu'_s = \mu'_t - \mu_a \quad (\text{B.7})$$

This method was implemented in MathWorks MATrix LABoratory [Natick, MA USA] (MATLAB) for Self-Calibrating (SC)/Dual-Slope (DS) data in Listing B.1 for FD and Listing B.2 for Continuous-Wave (CW) data assuming μ'_s is known and relying on Equation 9.1 as in Part III, Blaney *et alia* Applied Sciences (2021) [7], Blaney *et alia* Applied Optics (2021) [8], and Blaney *et alia* Journal of Innovative Optical Health Sciences (2022) [9].

B.2 Linear Slopes Method

The linear slope method for absolute optical property recovery utilizes the zero-boundary version of the diffuse reflection from Appendix A. Additionally, assumptions are made to assume linearized Intensity ($\ln(\rho^2 I)$) is linear with source-detector distance (ρ). These assumptions are summed up by the following requirement expressed as an inequality [55]:

$$\rho \sqrt{3\mu_a\mu'_s} >> 1 \quad (\text{B.8})$$

Since this condition is not defined strict enough, it is unclear in which situations it is met (mainly because of the use of $>>$ which is not a specific requirement). Therefore, this linear slope method is not preferred. However, it is still used due to its simplicity and as an initial guess in the iterative recovery method in the previous section. In-fact this method is implemented in MathWorks MATrix LABoratory [Natick, MA USA] (MATLAB) in lines 103-129 of Listing B.1 to provide the initial guess for the iterative method.

Considering that Frequency-Domain (FD) Near-InfraRed Spectroscopy (NIRS) measures Intensity (I) (*id est* the amplitude) and phase (ϕ) and that both $\ln(\rho^2 I)$ and ϕ is considered to be linear with ρ , the slopes of these data can be fit. These slopes are expressed as $Sl_{\ln(\rho^2 I)}$ and Sl_ϕ for $\ln(\rho^2 I)$ versus ρ and ϕ versus ρ , respectively. These are the slopes from Self-Calibrating (SC)/Dual-Slope (DS) or calibrated Single-Slope

(SS)/Multi-Distance (MD) measurements. Using these slopes, angular modulation frequency (ω), speed of light in vacuum (c), and index of refraction (n) the optical properties absorption coefficient (μ_a) and reduced scattering coefficient (μ'_s) are simply expressed as [2, 55]:

$$\mu_a = \frac{n\omega}{2c} \left(\frac{Sl_\phi}{Sl_{\ln(\rho^2 I)}} - \frac{Sl_{\ln(\rho^2 I)}}{Sl_\phi} \right) \quad (\text{B.9})$$

$$\mu'_s = \frac{Sl_{\ln(\rho^2 I)}^2 - Sl_\phi^2}{3\mu_a} - \mu_a \quad (\text{B.10})$$

In the case that μ'_s is assumed or known and only $\ln(\rho^2 I)$ is measured in Continuous-Wave (CW), this method may also be used to find μ_a [55]:

$$\mu_a = \frac{Sl_{\ln(\rho^2 I)}^2}{3\mu'_s} \quad (\text{B.11})$$

In-fact this is also seen in MATLAB code in lines 80-92 of Listing B.2 where it is used as the initial guess for the iterative recovery of μ_a from CW data assuming μ'_s .

Listings

Listing B.1: MathWorks MATrix LABoratory [Natick, MA USA] (MATLAB) code of absolute optical property recovery using Frequency-Domain (FD) data from a Dual-Slope (DS) set

```

1  function [mua, musp, iter]=DSR2muamuspEB_iterRecov(rhos, RR, opts)
2  % [mua, musp, iter]=DSR2muamuspEB_iterRecov(rhos, RR, opts)
3  % Giles Blaney Fall 2020
4  % Assumes extrapolated-boundary condition
5  % Expects DS set made of 4 SD measurements
6  % Inputs:
7  %     rhos      – 1 x 4 array of source-detector distances in the
8  %                  following format: [S1, L1, S2, L2] (mm)
9  %     RR       – Complex relectance data in a 1 x 4 array containing data
10 %                  in the following format: [S1, L1, S2, L2]
11 %     opts      – (Optional) Structure containing options as feilds:
12 %                  – mua0: mua to use at for first iteration (1/mm)
13 %                  – musp0: musp to use at for first iteration (1/mm)
14 %                  – mueff_tol: Change in mueff stoping criteria (1/mm)
15 %                  – abs(mueff(n)-mueff(n-1))< mueff_tol => Stop
16 %                  – n_max: Maximum iteration number stoping criteria
17 %                  – n>=n_max => Stop
18 %                  – omega: Modulation frequency (rad/sec)
19 %                  – v: Speed of light in tissue (mm/sec)
20 %                  – nin: Index of refraction inside medium
21 %                  – nout: Index of refraction outside medium
22 % Output:
23 %     mua      – mua found (1/mm)
24 %     mua      – musp found (1/mm)
25 %     iter     – Structure containing information about iterations as
26 %                  feilds:
27 %                  – n: Number of iterations
28 %                  – mueff_all: History of mueff during iterations
29 %                  – mua_all: History of mua during iterations
30 %                  – musp_all: History of musp during iterations
31
32 %% Parse Input
33 if nargin<=2
34     mu0Bool=true;
35     mueff_tol=1e-4; %1/mm
36     n_max=10;
37     omega=2*pi*140.625e6; %rad/sec
38     nin=1.4;
39     v=2.99792458e11/nin; %mm/sec
40     nout=1;
41 else
42     if isfield(opts, 'mua0')
43         mua0=opts.mua0;
44         musp0=opts.musp0;
45         mu0Bool=false;
46     else
47         mu0Bool=true;
48     end
49     mueff_tol=opts.mueff_tol;

```

```

50      n_max=opts.n_max;
51      omega=opts.omega;
52      v=opts.v;
53      nin=opts.nin;
54      nout=opts.nout;
55  end
56
57 if length(rhos)<4
58     rhos=[rhos, rhos];
59 end
60
61 rho1=rhos(1:2);
62 rho2=rhos(3:4);
63 R1=RR(1:2);
64 R2=RR(3:4);
65
66 if angle(R1(1))>angle(R1(2))
67     R1(2)=abs(R1(2))*exp(1i*(angle(R1(2))+2*pi));
68 end
69
70 if angle(R2(1))>angle(R2(2))
71     R2(2)=abs(R2(2))*exp(1i*(angle(R2(2))+2*pi));
72 end
73
74 %% Find mua0
75 if mu0Bool
76     I1=abs(R1);
77     I2=abs(R2);
78     P1=angle(R1);
79     P2=angle(R2);
80
81     SSI10=(log(rho1(2)^2*I1(2))-log(rho1(1)^2*I1(1)))/...
82             (rho1(2)-rho1(1));
83     SSI20=(log(rho2(2)^2*I2(2))-log(rho2(1)^2*I2(1)))/...
84             (rho2(2)-rho2(1));
85
86     SSP10=wrapToPi(P1(2)-P1(1))/...
87             (rho1(2)-rho1(1));
88     SSP20=wrapToPi(P2(2)-P2(1))/...
89             (rho2(2)-rho2(1));
90
91     DSI0=(SSI10+SSI20)/2;
92     DSP0=(SSP10+SSP20)/2;
93
94     mua0=(omega/(2*v))*(DSP0./DSI0-DSI0./DSP0);
95     musp0=(DSI0.^2-DSP0.^2).',...
96             (3*mua0)-mua0;
97 end
98
99 %% Iterative mua Recovery
100 n=1;
101 stopBool=false;
102 mua=mua0; %1/mm
103 musp=musp0; %1/mm

```

```

104    mueff0=sqrt(3*(mua0-li*omega/v)*(musp0+mua0));
105    A=n2A(nin, nout);
106    mueff=mueff0;
107    while ~stopBool
108        z0=1/musp(n);
109        zb=-2*A/(3*(musp(n)+mua(n)));
110        z0p=-z0+2*zb;
111        r1_1=sqrt(rho1.^2+z0.^2);
112        r1_2=sqrt(rho2.^2+z0.^2);
113        r2_1=sqrt(rho1.^2+z0p.^2);
114        r2_2=sqrt(rho2.^2+z0p.^2);
115
116        C1_1=z0.* (1./r1_1+mueff(n))./(r1_1.^2);
117        C1_2=z0.* (1./r1_2+mueff(n))./(r1_2.^2);
118        C2_1=-z0p.* (1./r2_1+mueff(n))./(r2_1.^2);
119        C2_2=-z0p.* (1./r2_2+mueff(n))./(r2_2.^2);
120
121        y_1=log(4*pi*R1./...
122            (C1_1+C2_1.*exp(mueff(n).*(r1_1-r2_1)))); 
123        y_2=log(4*pi*R2./...
124            (C1_2+C2_2.*exp(mueff(n).*(r1_2-r2_2)))); 
125
126        SSR1=diff(y_1)/diff(r1_1);
127        SSR2=diff(y_2)/diff(r1_2);
128
129        DSR=(SSR1+SSR2)/2;
130
131        n=n+1;
132
133        mueff(n)=-DSR;
134
135        a=real(mueff(n));
136        b=imag(mueff(n));
137        mutp=-2*a*b*v/(3*omega);
138        mua(n)=(a^2-b^2)/(3*mutp);
139        musp(n)=(mutp-mua(n));
140
141        if n>=n_max
142            warning('Max iterations reached.');
143            stopBool=true;
144        elseif abs(mueff(end)-mueff(end-1))<mueff_tol
145            stopBool=true;
146        end
147    end
148
149    %% Package Output
150    iter.n=n;
151    iter.mueff_all=mueff;
152    iter.mua=mua;
153    iter.musp=musp;
154
155    mua=mua(end);
156    musp=musp(end);
157

```

158 | end

Available at:

<https://github.com/DOIT-Lab/DOIT-Public/tree/master/Dissertations/GilesBlaney2022/code>

Listing B.2: MathWorks MATrix LABoratory [Natick, MA USA] (MATLAB) code of absolute absorption recovery assuming known reduced scattering using Continuous-Wave (CW) data from a Dual-Slope (DS) set

```

1 function [mua, iter]=DSI2muaEB_iterRecov(rhos, II, musp, opts)
2 % [mua, iter]=DSI2muaEB_iterRecov(rhos, II, musp, opts)
3 % Giles Blaney Fall 2020
4 % Assumes extrapolated-boundary condition
5 % Expects DS set made of 4 SD measurements
6 % Inputs:
7 %     dis      - 1 x 4 array of source-detector distances in the
8 %                  following format: [S1, L1, S2, L2] (mm)
9 %     II       - DC data in a 1 x 4 array containing data in the
10 %                  following format: [S1, L1, S2, L2]
11 %     musp    - Assumed musp (1/mm)
12 %     opts     - (Optional) Structure containing options as feilds:
13 %                  - mua0: mua to use at for first iteration (1/mm)
14 %                  - mueff_tol: Change in mueff stoping criteria (1/mm)
15 %                  - abs(mueff(n)-mueff(n-1))<mueff_tol => Stop
16 %                  - n_max: Maximum iteration number stoping criteria
17 %                  n>=n_max => Stop
18 %                  - nin: Index of refraction inside medium
19 %                  - nout: Index of refraction outside medium
20 % Output:
21 %     mua      - mua found (1/mm)
22 %     iter     - Structure containing information about iterations as
23 %                  feilds:
24 %                  - n: Number of iterations
25 %                  - mueff_all: History of mueff during iterations
26
27 %% Parse Input
28 if nargin<=3
29     mua0Bool=true;
30     mueff_tol=1e-4; %1/mm
31     n_max=10;
32     nin=1.4;
33     nout=1;
34 else
35     if isfield(opts, 'mua0')
36         mua0=opts.mua0;
37         mua0Bool=false;
38     else
39         mua0Bool=true;
40     end
41     mueff_tol=opts.mueff_tol;
42     n_max=opts.n_max;
43     nin=opts.nin;
44     nout=opts.nout;
45 end
46

```

```

47 if length(rhos)<4
48     rhos=[rhos, rhos];
49 end
50
51 rho1=rhos(1:2);
52 rho2=rhos(3:4);
53 I1=II(1:2);
54 I2=II(3:4);
55
56 %% Find mua0
57 if mua0Bool
58     SSI10=(log(rho1(2)^2*I1(2))-log(rho1(1)^2*I1(1)))/...
59         (rho1(2)-rho1(1));
60     SSI20=(log(rho2(2)^2*I2(2))-log(rho2(1)^2*I2(1)))/...
61         (rho2(2)-rho2(1));
62
63     DSI0=(SSI10+SSI20)/2;
64
65     mua0=DSI0^2/(3*musp);
66 end
67
68 %% Iterative mua Recovery
69 z0=1/musp;
70 r1_1=sqrt(z0^2+rho1.^2);
71 r1_2=sqrt(z0^2+rho2.^2);
72
73 n=1;
74 stopBool=false;
75 mua=mua0; %1/mm
76 mueff0=sqrt(3*mua0*(musp+mua0));
77 A=n2A(nin, nout);
78 mueff=mueff0;
79 while ~stopBool
80     zb=-2*A/(3*(musp+mua(n)));
81     z0p=z0+2*zb;
82     r2_1=sqrt(rho1.^2+z0p.^2);
83     r2_2=sqrt(rho2.^2+z0p.^2);
84
85     C1_1=z0.*((1./r1_1)+mueff(n))./(r1_1.^2);
86     C1_2=z0.*((1./r1_2)+mueff(n))./(r1_2.^2);
87     C2_1=-z0p.*((1./r2_1)+mueff(n))./(r2_1.^2);
88     C2_2=-z0p.*((1./r2_2)+mueff(n))./(r2_2.^2);
89
90     y_1=log(4*pi*I1./...
91         (C1_1+C2_1.*exp(mueff(n).*(r1_1-r2_1))));
92     y_2=log(4*pi*I2./...
93         (C1_2+C2_2.*exp(mueff(n).*(r1_2-r2_2))));
94
95     SSI1=diff(y_1)/diff(r1_1);
96     SSI2=diff(y_2)/diff(r1_2);
97
98     DSI=(SSI1+SSI2)/2;
99
100    n=n+1;

```

```
101
102     mueff(n)=~DSI;
103     mua(n)=sqrt(musp^2/4+mueff(n)^2/3)~musp/2;
104
105     if n>=n_max
106         warning('Max iterations reached.');
107         stopBool=true;
108     elseif abs(mueff(end)-mueff(end-1))<mueff_tol
109         stopBool=true;
110     end
111 end
112
113 %% Package Output
114 iter.n=n;
115 iter.mueff_all=mueff;
116 iter.mua=mua;
117
118 mua=mua(end);
119
120 end
```

Available at:

<https://github.com/DOIT-Lab/DOIT-Public/tree/master/Dissertations/GilesBlaney2022/code>

Appendix C

Measuring Changes in the Absorption Coefficient

Here we describe six different methods for measuring absorption changes with the data collected in Near-InfraRed Spectroscopy (NIRS) [3]:

- Single-Distance (SD) Intensity (I): Capable in Continuous-Wave (CW) and Frequency-Domain (FD) with only one source and detector pair.
- SD phase (ϕ): Measurable in FD with only one source and detector pair.
- Single-Slope (SS) I : Feasible in CW and FD with measurement at multiple source-detector distances (ρ s).
- SS ϕ : Afforded by a FD with measurement at multiple ρ s.
- Dual-Slope (DS) I : Realizable in CW and FD using a DS set (Chapter 3).
- DS ϕ : Possible in FD using a DS set (Chapter 3).

Each of these methods yields a time trace of effective absorption coefficient change ($\Delta\mu_a$), which may then be converted into time traces of Oxy-hemoglobin concentration change (ΔO) and Deoxy-hemoglobin concentration change (ΔD) (Appendix D).

C.1 Generalized Total Optical Path-Length

Before we can discuss ways to calculate absorption coefficient change ($\Delta\mu_a$) we must first define

general complex total optical path-length ($\langle \tilde{L} \rangle$) which is utilized to determine various coefficients in the following sections. Using the complex Reflectance (\tilde{R}) from Equation A.1 and its accompanying definitions of variables we can write $\langle \tilde{L} \rangle$ for a semi-infinite medium with extrapolated boundary:

$$\langle \tilde{L} \rangle = \frac{3\mu'_s}{8\pi\tilde{R}} \times \left(\frac{z_0 e^{-\|\vec{r}_1\| \tilde{\mu}_{eff}}}{\|\vec{r}_1\|} - \frac{z'_0 e^{-\|\vec{r}_2\| \tilde{\mu}_{eff}}}{\|\vec{r}_2\|} \right) \quad (\text{C.1})$$

which primarily depends on absorption coefficient (μ_a), reduced scattering coefficient (μ'_s), and source-detector distance (ρ) (through the position vectors (\vec{r} s) and \tilde{R}). In following sections total optical path-length ($\langle L \rangle$) is written to depend on the spatial position of the source and detector, this is because following sections are more general than the semi-infinite medium. Here where the semi-infinite medium is considered only the ρ along the surface is of importance. Code for the $\langle \tilde{L} \rangle$ can be found in Listing C.1.

$\langle L \rangle$ can be of various data-types such as Frequency-Domain (FD) Intensity (I) (*id est* amplitude) or FD phase (ϕ) ($\langle L \rangle_I$ or $\langle L \rangle_\phi$) which are obtained from:

$$\langle L \rangle_I = \Re [\langle \tilde{L} \rangle] \quad (\text{C.2})$$

$$\langle L \rangle_\phi = \Im [\langle \tilde{L} \rangle] \quad (\text{C.3})$$

In the case of the $\langle L \rangle$ for Continuous-Wave (CW) I ($\langle L \rangle_{CW}$), the above expressions may still be used simply by setting angular modulation frequency (ω) or modulation frequency (f_{mod}) to zero. This will result in a real instead of complex $\langle L \rangle$ which is itself $\langle L \rangle_{CW}$. Unlike $\langle L \rangle_I$ or $\langle L \rangle_\phi$, $\langle L \rangle_\phi$ has a clear physical meaning which is, the average length of the path of a photon that travels from the source to be detected by the detector. The meaning is no longer clear in FD since we now consider the phase and amplitude of photon density waves and $\langle \tilde{L} \rangle$ is complex. For this reason, we name $\langle \tilde{L} \rangle$ the *general* path-length since it is not clear that it represents a physical path despite having the units of length.

C.2 Absorption Changes Measured with Single-Distance Intensity or Phase

Intensity (I) changes measured with Single-Distance (SD) can be converted to changes in absorption using the modified Beer-Lambert Law (mBLL) and the Differential Path-length Factor (DPF) [147] (denoted here with DPF_I to highlight its use in conjunction with intensity measurements). One may introduce a similar, generalized DPF concept for SD phase (ϕ) (denoted as DPF_ϕ). In the following expressions we also utilize total optical path-lenth ($\langle L \rangle$) for I or ϕ ($\langle L \rangle_I$ or $\langle L \rangle_\phi$) in-place of DPF which result in more concise expressions since they do not require source-detector distance (ρ).

Considering a baseline SD I or SD ϕ (SDI_0 or $SD\phi_0$), absorption coefficient change ($\Delta\mu_a$) may be expressed as follows:

$$\begin{aligned}\Delta\mu_{a,SDI} &= \frac{\ln(\frac{SDI_0}{SDI})}{\langle L \rangle_I} = \frac{\ln(\frac{SDI_0}{SDI})}{\rho DPF_I} \\ &\approx -\frac{\left(\frac{SDI - SDI_0}{SDI_0}\right)}{\rho DPF_I} = -\frac{\left(\frac{SDI - SDI_0}{SDI_0}\right)}{\langle L \rangle_I}\end{aligned}\quad (C.4)$$

$$\begin{aligned}\Delta\mu_{a,SD\phi} &= -\frac{SD\phi - SD\phi_0}{\langle L \rangle_\phi} \\ &= -\frac{SD\phi - SD\phi_0}{\rho DPF_\phi}\end{aligned}\quad (C.5)$$

Since for optical data (\mathcal{Y}):

$$DPF_{\mathcal{Y}} = \frac{\langle L \rangle_{\mathcal{Y}}}{\rho} \quad (C.6)$$

Example values of $\langle L \rangle$ and DPF for various optical properties can be found in the supplementary material of Blaney *et alia* Journal of Biophotonics (2020) [3].

C.3 Absorption Changes Measured with Intensity or Phase Slopes

Changes in slopes measured with Single-Slope (SS) can also be converted into absorption coefficient change ($\Delta\mu_a$). In the case of Intensity (I), the slope refers to the slope of linearized Intensity ($\ln(\rho^2 I)$) on source-detector distance (ρ) (SSI), while for phase (ϕ) the slope is of ϕ on ρ ($SS\phi$), and we introduce baseline slopes (SSI_0 or $SS\phi_0$). For slope methods we also introduce the Differential Slope Factor (DSF) which is a proportionality constant to convert to $\Delta\mu_a$ similar to Differential Path-length Factor (DPF).

For $\Delta\mu_a$ from SS we have:

$$\Delta\mu_{a,SSI} = -\frac{SSI - SSI_0}{DSF_I} \quad (C.7)$$

$$\Delta\mu_{a,SS\phi} = -\frac{SS\phi - SS\phi_0}{DSF_\phi} \quad (C.8)$$

Considering optical data (\mathcal{Y}) which can be either I or ϕ we can define DSF:

$$DSF_{\mathcal{Y}} = \frac{\sum_{i=1}^{N_{SD}} (\rho_i - \bar{\rho}) \langle L \rangle_{\mathcal{Y}} [\vec{r}_{src}, \vec{r}_{det,i}]}{\sum_{i=1}^{N_{SD}} (\rho_i - \bar{\rho})^2} \quad (C.9)$$

where we note that total optical path-lenth ($\langle L \rangle$) is a function of the source and detector position (\vec{r}_{src} and \vec{r}_{det}). Here, N_{SD} refers to the number of Single-Distance (SD) measurements in the SS set which is being considered. Additionally, \vec{r}_{det} is indexed by i since the expression assumes a common source and multiple detectors in the SS set, if the opisite is true the index would be on the source position. In general the sum is over

the various SD sets that make up the SS and $\langle L \rangle$ depends on the spatial positions of the source and detector in the SD set. Next we will define the various ρ variables in the above expression:

$$\rho_i = \|\vec{r}_{src} - \vec{r}_{det,i}\| \quad (C.10)$$

$$\bar{\rho} = \frac{\sum_{i=1}^{N_{SD}} \rho_i}{N_{SD}} \quad (C.11)$$

where the detector was chosen to be indexed as before, but this can be adapted depending on the particular SS arrangement.

Finally, we can define the $\Delta\mu_a$ for a Dual-Slope (DS) set. Considering a DS set made of SSs SS_1 and SS_2 with corresponding DSFs for those SS sets of $DSF_{y,1}$ and $DSF_{y,2}$ we can write $\Delta\mu_a$ for DS:

$$\Delta\mu_{a,DSI} = -\frac{\{SSI - SSI_0\}_{SS_1} + \{SSI - SSI_0\}_{SS_2}}{DSF_{I,1} + DSF_{I,2}} \quad (C.12)$$

$$\Delta\mu_{a,DS\phi} = -\frac{(SS\phi - SS\phi_0)_{SS_1} + (SS\phi - SS\phi_0)_{SS_2}}{DSF_{\phi,1} + DSF_{\phi,2}} \quad (C.13)$$

for both DS I and DS ϕ .

Example values of DSF for various optical properties can be found in the supplementary material of Blaney *et alia* Journal of Biophotonics (2020) [3].

Listings

Listing C.1: MathWorks MATrix LABoratory [Natick, MA USA] (MATLAB) code for generation of general complex total optical path-length ($\langle \tilde{L} \rangle$) given a vector of positions

```

1 function [L, R] = complexTotPathLen(rs, rd, omega, optProp)
2 % Giles Blaney Spring 2019
3 % [L, R] = complexTotPathLen(rs, rd, omega, optProp)
4 % Inputs:
5 %   rs      — Source coordinates. (mm)
6 %   rd      — Detector coordinates. (mm)
7 %   omega   — (OPTIONAL, default=2*pi*1.40625e8 rad/sec) Angular modulation
8 %             frequency. (rad/sec)
9 %   optProp — (OPTIONAL) Struct of optical properties with the following
10 %             fields:
11 %                 nin — (default=1.4) Index of refraction inside. (-)
12 %                 nout — (default=1) Index of refraction outside. (-)
13 %                 musp — (default=1.2 1/mm) Reduced scattering. (1/mm)
14 %                 mua  — (default=0.01 1/mm) Absorption. (1/mm)
15 % Outputs:
16 %   L      — Complex total pathlength. (mm)
17 %   R      — Complex reflectance. (1/mm^2)
18
19 if nargin<=2
20     fmod=1.40625e8; %Hz
21     omega=2*pi*fmod; %rad/sec
22
23     optProp.nin=1.4;
24     optProp.nout=1;
25     optProp.musp=1.2; %1/mm
26     optProp.mua=0.01; %1/mm
27
28     warning(['Default optical properties used, this may be inconsistent',...
29             ' with the musp used for source depth']);
30 end
31
32 if size(rs, 1)>1 && size(rd, 1)>1
33     error('Can not use multiple sources and multiple detectors');
34 end
35
36 x0=rs(:, 1); %mm
37 y0=rs(:, 2); %mm
38 z0=rs(:, 3); %mm
39
40 c=2.99792458e11; %mm/sec
41 v=c/optProp.nin;
42
43 A=n2A(optProp.nin, optProp.nout);
44 D=1/(3*optProp.musp); %mm
45 zb=-2*A*D; %mm
46
47 mueff=sqrt(optProp.mua/D-1i*omega/(v*D)); %1/mm
48
49 rsp=[x0, y0, -z0+2*zb]; %mm

```

```
50
51 r1=vecnorm(rd-rs, 2, 2);
52 r2=vecnorm(rd-rsp, 2, 2);
53
54 R=complexReflectance(rs, rd, omega, optProp);
55
56 L=((z0./r1).*exp(-mueff.*r1)+((z0-2.*zb)./r2).*exp(-mueff.*r2))./...
57     (8*pi*D*R);
58 end
```

Available at:

<https://github.com/DOIT-Lab/DOIT-Public/tree/master/Dissertations/GilesBlaney2022/code>

Appendix D

Recovery of Chromophore Concentrations

Methods in Appendix B retrieve the absolute absorption coefficient (μ_a) and methods in Appendix C retrieve an absorption coefficient change ($\Delta\mu_a$). Typically we wish to convert these measurement to either absolute or dynamic changes (for μ_a or $\Delta\mu_a$) in chromophore concentrations. This is done by inverting Equation A.40 or Equation A.41. This relies on N_{lam} measurements of μ_a from different optical wavelengths (λ_s). Considering that we wish to retrieve N_{chrom} chromophores, we must measure enough λ_s to satisfy:

$$N_{lam} \geq N_{chrom} \quad (\text{D.1})$$

For example if Oxy-hemoglobin (O) and Deoxy-hemoglobin (D) wish to be measured, we need at least 2 measures of μ_a at two different λ_s .

In practice the inversion of Equation A.40 or Equation A.41 can be done in various ways. In the case of $N_{lam} = N_{chrom}$ there is a single solution, while in the case of $N_{lam} > N_{chrom}$ the inversion is in-fact a linear fit. Regardless of the case, we utilize the `mldivide` MathWorks Matrix LABoratory [Natick, MA USA] (MATLAB) function to achieve the inversion (solution or fit). Naming the MATLAB matrix of extinction coefficients (\mathbf{E}) E , vector of chromophore concentrations (\vec{C}) C , and vector of absorption coefficients ($\vec{\mu}_a$) μ_a we can write the inversion in MATLAB code:

```
1 C=E\mu_a;
```

Or in the case of vector of absorption coefficient changes ($\Delta\vec{\mu}_a$) as $d\mu_a$ and vector of chromophore concentration changes (\vec{C}) \vec{C} we write:

mophore concentration changes ($\Delta\vec{C}$) as dC we write:

```
1 dC=E\dmu_a;
```

MATLAB's `mldivide` divide function utilizes various numerical solvers depending on if the inverted matrix (\mathbf{E} or E in this case) is square, non-square, *et cetera* [65]. For our case we can consider two cases:

- If $N_{lam} > N_{chrom}$ MATLAB will utilize `qr` decomposition to invert \mathbf{E} .
- If $N_{lam} = N_{chrom}$ MATLAB will use some numerical method to find \mathbf{E}^{-1} .

For `qr` decomposition we write \mathbf{E} as:

$$\mathbf{E} = \mathbf{QR} = [\mathbf{Q}_1 \quad \mathbf{Q}_2] \begin{bmatrix} \mathbf{R}_1 \\ \mathbf{0} \end{bmatrix} \quad (\text{D.2})$$

where \mathbf{Q}_1 and \mathbf{Q}_2 have orthogonal columns and \mathbf{R}_1 is upper right triangular. Now give the two cases ($N_{lam} > N_{chrom}$ or $N_{lam} = N_{chrom}$) and using `qr` in the first case we can write the piecewise function for finding \vec{C} from $\vec{\mu}_a$:

$$\vec{C} = \begin{cases} \mathbf{R}_1^{-1} (\mathbf{Q}_1^T \vec{\mu}_a) & N_{lam} > N_{chrom} \\ \mathbf{E}^{-1} \vec{\mu}_a & N_{lam} = N_{chrom} \end{cases} \quad (\text{D.3})$$

or finding $\Delta\vec{C}$ from $\Delta\vec{\mu}_a$:

$$\Delta\vec{C} = \begin{cases} \mathbf{R}_1^{-1} (\mathbf{Q}_1^T \Delta\vec{\mu}_a) & N_{lam} > N_{chrom} \\ \mathbf{E}^{-1} \Delta\vec{\mu}_a & N_{lam} = N_{chrom} \end{cases} \quad (\text{D.4})$$

As an example of when $N_{lam} = N_{chrom}$, lets now consider finding Oxy-hemoglobin concentration change (ΔO) and Deoxy-hemoglobin concentration change (ΔD) from $\Delta\mu_a$ at λs of 690 nm and 830 nm. For this we will use the following **E** of extinction coefficient (ϵ):

$$\mathbf{E} = \begin{bmatrix} \epsilon_O(690 \text{ nm}) & \epsilon_D(690 \text{ nm}) \\ \epsilon_O(830 \text{ nm}) & \epsilon_D(830 \text{ nm}) \end{bmatrix} \quad (\text{D.5})$$

which we will write as **E_OD** in MATLAB using **ext** followed by the chromophore name and **λ** to represent the various ϵ . Considering that we have measured $\Delta\mu_a$ at 690 nm and 830 nm written as **dmua690** and **dmua830**, we can find ΔO and ΔD (**dO** and **dD**) using the following code:

```

1 E_OD=[ext0690, extD690; ...
2     ext0830, extD830];
3 dC_OD=E_OD\dmua690; dmua830];
4 dO=dC_OD(1);
5 dD=dC_OD(2);

```

Notice that even though there is a solution to the inversion, we still use **mldivide** since it is more general and concise in code.

Finally as an example of $N_{lam} > N_{chrom}$, we may consider finding **O** (**O**), **D** (**D**), **Water** (**W**) (**W**), and **Lipid** (**L**) (**L**) using 1000 λs . In this case lets say we measured $\vec{\mu}_a$ called **mua** such that it has **size(mua)** equal to [1000,1], and we have ϵ vectors ($\vec{\epsilon}$) for **O** (**ext0**), **D** (**extD**), **W** (**extW**), and **L** (**extL**) which also all have **size()** equal to [1000,1].

```

1 E_ODWL=[ext0, extD, extW, extL];
2 C_ODWL=E_ODWL\mua;
3 O=C_ODWL(1);
4 D=C_ODWL(2);
5 W=C_ODWL(3);
6 L=C_ODWL(4);

```

Therefore, regardless of the number and type of chromophores, dynamic or absolute, and number of wavelengths the **mldivide** function may be used to invert Equation A.40 or Equation A.41.

Appendix E

Generation of Sensitivity Maps

Equation 2.1 shows the physical meaning of Sensitivity to absorption change (\mathcal{S}) in terms of a measured and actual local absorption coefficient change ($\Delta\mu_a$). However, Equation 2.1 is not how \mathcal{S} is computed. We instead utilize expressions for general complex total optical path-length ($\langle \tilde{L} \rangle$) from Equation C.1 and general complex partial optical path-length ($\langle \tilde{\ell} \rangle$) to generate \mathcal{S} . \mathcal{S} maps can be generated for any of the methods to measure $\Delta\mu_a$ from Appendix C. These \mathcal{S} values may be used to create a matrix of sensitivity to absorption change (\mathcal{S}) for imaging applications (Chapter 5), to generate \mathcal{S} maps (Chapters 2&3) or for simulation of dynamic measurements as discussed in Appendix F.

E.1 Generalized Partial Optical Path-Length

Similar general complex total optical path-length ($\langle \tilde{L} \rangle$) in Equation C.1 which describes the path of all photons in a semi-infinite homogeneous diffusion medium, we can also consider the general complex partial optical path-length ($\langle \tilde{\ell} \rangle$) which is concerned with the path through some localized region within the diffuse medium. To do this we must introduce the following position vector (\vec{r}):

- The position of the isotropic source of \vec{r}_{src} (this is typically $\vec{r}_{src} = \frac{1}{\mu_s} \hat{z}$ for a pencil beam at the origin).
- The position of the detector of \vec{r}_{det} (this is typically $\vec{r}_{det} = \rho \hat{x}$ for a detector at source-detector distance (ρ) along the x-axis).

- The position of the localized absorption perturbation of \vec{r}_{pert} with volume of V .

Using these positions we find that the $\langle \tilde{\ell} \rangle$ for the perturbation at \vec{r}_{pert} with volume V is:

$$\langle \tilde{\ell} \rangle = \frac{\tilde{\Phi}[\vec{r}_{src}, \vec{r}_{pert}] \tilde{R}[\vec{r}_{pert}, \vec{r}_{det}]}{\tilde{R}[\vec{r}_{src}, \vec{r}_{det}]} V \quad (\text{E.1})$$

where $\tilde{\Phi}[\vec{r}_{src}, \vec{r}_{pert}]$ is the complex fluence rate ($\tilde{\Phi}$) at \vec{r}_{pert} given a isotropic source at \vec{r}_{src} , $\tilde{R}[\vec{r}_{pert}, \vec{r}_{det}]$ is the complex Reflectance (\tilde{R}) detected at \vec{r}_{det} given a isotropic source at \vec{r}_{pert} , and $\tilde{R}[\vec{r}_{src}, \vec{r}_{det}]$ is the \tilde{R} detected at \vec{r}_{det} given a isotropic source at \vec{r}_{src} . The expressions for \tilde{R} and $\tilde{\Phi}$ can be found in Appendix A as Equations A.1&A.15. This equation of partial optical path-length ($\langle \tilde{\ell} \rangle$) is implemented in Listing E.1.

As with other complex variables, the Continuous-Wave (CW) version of $\langle \ell \rangle$, named $\langle \ell \rangle_{CW}$, can be found by setting angular modulation frequency (ω) to zero in the expressions for \tilde{R} and $\tilde{\Phi}$ to get Reflectance (R) and fluence rate (Φ) instead. Just like total optical path-length ($\langle L \rangle$) in Appendix C, $\langle \ell \rangle$ has a physical meaning (while $\langle \tilde{\ell} \rangle$'s meaning is less clear thus leading to the name *general* path-length). The physical interpretation for $\langle \ell \rangle$ is the average path-length that a photon from \vec{r}_{src} and detected at \vec{r}_{det} spends inside a region centered at \vec{r}_{pert} with volume V .

As with $\langle L \rangle$ in Appendix C, the $\langle \ell \rangle$ for Frequency-Domain (FD) data-types Intensity (I) (*id est* amplitude) and phase (ϕ) can be defined:

$$\langle \ell \rangle_I = \Re[\langle \tilde{\ell} \rangle] \quad (\text{E.2})$$

$$\langle \ell \rangle_\phi = \Im \left[\langle \tilde{\ell} \rangle \right] \quad (\text{E.3})$$

The following sections utilize these $\langle \ell \rangle$ s combined with $\langle L \rangle$ to express Sensitivity to absorption change (S) for various data-types. It is important to note that $\langle \ell \rangle$ controls the perturbation in question for S both in terms of its location (\vec{r}_{pert}) and volume (V). Typically, $\langle \ell \rangle$ is found for very small voxels, $1 \text{ mm} \times 1 \text{ mm} \times 1 \text{ mm}$ or smaller, and then summed to find $\langle \ell \rangle$ for a larger perturbation of some specific shape.

E.2 Sensitivity to Local Absorption Perturbation

First lets consider the Single-Distance (SD) set with total optical path-lenth ($\langle L \rangle$) and its Sensitivity to absorption change (S) to a perturbation with partial optical path-lenth ($\langle \ell \rangle$). The expression for SD S can be written as follows for optical data (\mathcal{Y}) which can be either Intensity (I) or phase (ϕ):

$$S_{SDY} = \frac{\langle \ell \rangle_{\mathcal{Y}}}{\langle L \rangle_{\mathcal{Y}}} \quad (\text{E.4})$$

where, $\langle \ell \rangle$ is written above and $\langle L \rangle$ can be found in Appendix C.

Next lets consider a Single-Slope (SS) set made of N_{SD} SD sets with a single source at position vector (\vec{r}) of \vec{r}_{src} and N_{SD} detectors indexed by i at \vec{r} s of $\vec{r}_{src,det}$. Remembering the notation of Differential Slope Factor (DSF) from Appendix C, we can express the SS S to a perturbation with $\langle \ell \rangle$:

$$S_{SSY} = \frac{\sum_{i=1}^{N_{SD}} (\rho_i - \bar{\rho}) \langle \ell \rangle_{\mathcal{Y}} [\vec{r}_{src}, \vec{r}_{det,i}]}{\sum_{i=1}^{N_{SD}} (\rho_i - \bar{\rho}) \langle L \rangle_{\mathcal{Y}} [\vec{r}_{src}, \vec{r}_{det,i}]} \quad (\text{E.5})$$

noting that we write the $\langle \ell \rangle$ a and $\langle L \rangle$ as functions of \vec{r}_{src} and $\vec{r}_{det,i}$ since they are important for the sum. They are of course functions of other variables which are omitted for brevity. Additionally, it should be noted that for simplicity the expression is written assuming one source and multiple detectors, however, in general the sum is over all the SDs in the SS set.

Finally, lets consider a Dual-Slope (DS) set made of two SS sets named SS_1 and SS_2 . Using the numerator and denominator of Equation E.5 surrounded by curly brackets to represent the encompassed expression for a given SS, we can write the S to a perturbation with $\langle \ell \rangle$ for DS as:

$$\begin{aligned} S_{DSY} = & \left(\left\{ \sum_{i=1}^{N_{SD}} (\rho_i - \bar{\rho}) \langle \ell \rangle_{\mathcal{Y}} [\vec{r}_{src}, \vec{r}_{det,i}] \right\}_{SS_1} \right. \\ & + \left. \left\{ \sum_{i=1}^{N_{SD}} (\rho_i - \bar{\rho}) \langle \ell \rangle_{\mathcal{Y}} [\vec{r}_{src}, \vec{r}_{det,i}] \right\}_{SS_2} \right) \\ & \div \left(\left\{ \sum_{i=1}^{N_{SD}} (\rho_i - \bar{\rho}) \langle L \rangle_{\mathcal{Y}} [\vec{r}_{src}, \vec{r}_{det,i}] \right\}_{SS_1} \right. \\ & + \left. \left\{ \sum_{i=1}^{N_{SD}} (\rho_i - \bar{\rho}) \langle L \rangle_{\mathcal{Y}} [\vec{r}_{src}, \vec{r}_{det,i}] \right\}_{SS_2} \right) \end{aligned} \quad (\text{E.6})$$

where we note that for a symmetric DS set, the DS S is simply the average of the two SS S s within the set. This is because the denominator of Equation A.1 and the DSFs are the same for the two SSs in a symmetric DS set.

A key property of S regardless of data-type is that the sum over perturbations everywhere in the medium is one. This is the same as saying that if the absorption coefficient change ($\Delta\mu_a$) occurs everywhere the apparent measured $\Delta\mu_a$ and actual $\Delta\mu_a$ will be the same. Caution should be taken however, since if overlapped perturbations are simulated when calculating S then one should no longer expect the sum of all S to be one.

E.2.1 Computational Methods to Generate Sensitivity Maps

Listing E.2 shows the MathWorks MATrix LABoratory [Natick, MA USA] (MATLAB) code for generation of S maps. This code is supported by the functions for complex Reflectance (\tilde{R}), complex fluence rate ($\tilde{\Phi}$), general complex total optical path-lenth ($\langle L \rangle$), and general complex partial optical path-lenth ($\langle \ell \rangle$) in Listings A.2,A.3,C.1,&E.1. The key to efficient generation of S maps in Listing E.2 is the calcula-

tion of $\langle \tilde{\ell} \rangle$ and other values for every voxel in the medium simultaneously. This is done by carefully writing the supporting functions so that they could process a vector of voxel positions instead of one at a time. Lines 179-180 show a simple way to get a list of all voxel positions within the medium, and lines 190-191 show an example of where $\langle \ell \rangle$ is computed for all positions simultaneously for particular source-detector pair.

After the code generates all of the \mathcal{S} values for each voxel, where the voxels are considered to be small, \mathcal{S} is found for larger perturbations by sums. For example to get layered \mathcal{S} the fine voxelized \mathcal{S} is summed in all x and y dimensions. Also to generate maps for larger perturbations convolution with the perturbation shape is preformed (for example lines 351-354 in Listing E.2), however it should be noted that the output shows the results with overlap. Therefore, if overlap is simulated the sum of all \mathcal{S} in the medium is no longer one.

E.3 Extension of Sensitivity to Signal-to-Noise

Using the Sensitivity to absorption change (\mathcal{S}), we can calculate a Signal-to-Noise Ratio (SNR) associated with each perturbation within the medium. To this aim, we define the noise equivalent absorption change as the change in absorption that results from a change in the signal at the level of the noise in that signal. We start by writing the noise equivalent absorption change (σ_{μ_a}) for the three methods (Single-Distance (SD), Single-Slope (SS),) and optical data (\mathcal{Y}) (either Intensity (I) or phase (ϕ)):

$$\sigma_{\mu_a, SDY} = \frac{\sigma_Y}{\langle L \rangle_Y} \quad (\text{E.7})$$

$$\sigma_{\mu_a, SSY} = \frac{\sigma_Y \sqrt{\sum_{i=1}^{N_{SD}} (\rho_i - \bar{\rho})^2}}{\sum_{i=1}^{N_{SD}} (\rho_i - \bar{\rho}) \langle L \rangle_Y [\vec{r}_{src}, \vec{r}_{det,i}]} \quad (\text{E.8})$$

$$\sigma_{\mu_a, DSY} = \frac{\sqrt{\sigma_{\mu_a, SSY1}^2 + \sigma_{\mu_a, SSY2}^2}}{2} \quad (\text{E.9})$$

where, in this case we have *only derived the expression for Dual-Slope (DS)* for a symmetric DS set. σ_Y is the noise of \mathcal{Y} . For I this is in units of a fraction compared to baseline and for ϕ the units are simply rad. Now that we have σ_{μ_a} for the various data-types we can write the SNR both in terms of the apparent measured absorption coefficient change ($\Delta\mu_a$) and the actual $\Delta\mu_a$ of the perturbation in question:

$$SNR = \frac{\Delta\mu_{a,apparent}}{\sigma_{\mu_a}} = \frac{\mathcal{S}\Delta\mu_{a,actual}}{\sigma_{\mu_a}} \quad (\text{E.10})$$

note that this SNR is dependent not only on the analysis method, data type (with associated noise), and probe geometry, but also on the assumed true absorption perturbation and its size.

Listings

Listing E.1: MathWorks MATrix LABoratory [Natick, MA USA] (MATLAB) code for generation of general complex partial optical path-length ($\langle \ell \rangle$) given a vector of positions

```

1 function [l] = complexPartPathLen(rs, r, rd, V, omega, optProp)
2 % Giles Blaney Spring 2019
3 % [l] = complexPartPathLen(rs, rd, omega, optProp)
4 % Inputs:
5 % rs      — Source coordinates. (mm)
6 % r       — Center coordinate of volume. (mm)
7 % rd      — Detector coordinates. (mm)
8 % V       — Volume. (mm^3)
9 % omega   — (OPTIONAL, default=2*pi*1.40625e8 rad/sec) Angular modulation
10 %          frequency. (rad/sec)
11 % optProp — (OPTIONAL) Struct of optical properties with the following
12 %            fields:
13 %              nin — (default=1.4) Index of refraction inside. (-)
14 %              nout — (default=1) Index of refraction outside. (-)
15 %              musp — (default=1.2 1/mm) Reduced scattering. (1/mm)
16 %              mua  — (default=0.01 1/mm) Absorption. (1/mm)
17 % Outputs:
18 % l      — Complex partial pathlength. (mm)
19
20 if nargin<=4
21     fmod=1.40625e8; %Hz
22     omega=2*pi*fmod; %rad/sec
23
24     optProp.nin=1.4;
25     optProp.nout=1;
26     optProp.musp=1.2; %1/mm
27     optProp.mua=0.01; %1/mm
28 end
29
30 PHIrs_r=complexFluence(rs, r, omega, optProp);
31 Rr_rd=complexReflectance(r, rd, omega, optProp);
32 Rrs_rd=complexReflectance(rs, rd, omega, optProp);
33
34 l=(PHIrs_r.*Rr_rd.*V)./Rrs_rd;
35 end

```

Available at:

<https://github.com/DOIT-Lab/DOIT-Public/tree/master/Dissertations/GilesBlaney2022/code>

Listing E.2: MathWorks MATrix LABoratory [Natick, MA USA] (MATLAB) code for generation of Sensitivity to absorption change (\mathcal{S}) maps

```

1 function [SD, SS, DS, params] = makeSenMaps(armt, pert, geo, optProp, opts)
2 % [SD, SS, DS, params] = makeSenMaps(armt, pert, geo, optProp, opts)
3 %
4 % Giles Blaney Summer 2019
5 %
6 % NOTE: All units are in mm or 1/mm.
7 %
8 % Coordinate system used by this code assumes z axis (3rd index) is normal

```

```

9 % to the surface of the medium and positive into the medium.
10 %
11 % All inputs optional, defaults will be used with no inputs.
12 %
13 % Inputs:
14 %   armt -- Arrangement structure with the following feilds:
15 %     rSrc -- Coordinates of sources (number of sources X 3) {mm}
16 %           [x1, y1, z1; x2, y2, z2; ... ; xn, yn, zn]
17 %     rDet -- Coordinates of detectors (same structure as rSrc)
18 %           {mm}
19 %     SDprs -- Single distance pairs (number of pairs X 2)
20 %           [sInd1, dInd1; sInd2, dInd2; ... ;sIndn, dIndn]
21 %     SSprs -- Single slope pairs (number of distances X 2 X
22 %           number of pairs)
23 %           SSprs(:, :, n)=[sInd1, dInd1; sInd2, dInd2]
24 %     DSprs -- Dual slope pairs (number of distances X 2 X
25 %           number of slopes X number of pairs)
26 %           DSprs(:, :, 1, n)=[sInd11, dInd11; sInd12, dInd12]
27 %           DSprs(:, :, 2, n)=[sInd21, dInd21; sInd22, dInd22]
28 %
29 %   pert -- Perturbation structure with the following feilds:
30 %     partSz -- Size of perturbation volume in voxels (1 X 3)
31 %           [nx, ny, nz]
32 %     dmua -- Change in the absorption coefficient of
33 %           perturbation {1/mm}
34 %
35 %   geo -- Geometry structure with the following feilds:
36 %     xMar -- Margin in x direction of full volume, volume will
37 %           extend from -xMar to +xMar along the x axis {mm}
38 %     yMar -- Margin in y direction of full volume, volume will
39 %           extend from -yMar to +yMar along the y axis {mm}
40 %     zMax -- Maximum z of full volume, volume will extend from 0
41 %           to +zMax {mm}
42 %     dr -- Voxel size in three dimentions {mm}
43 %           [dx, dy, dz]
44 %
45 %   optProp -- Optical properties structure with the following feilds:
46 %     nin -- Index of refraction inside the medium
47 %     nout -- Index of refraction outside the medium
48 %     musp -- Baseline scattering coefficient within medium {1/mm}
49 %     mua -- Baseline absorption coefficient within medium {1/mm}
50 %
51 %   opts -- Options structure with the following feilds:
52 %     fmod -- Modulation frequency {Hz}
53 %     PhN -- Noise in phase measurement {deg}
54 %     InN -- Noise in intensity measurement {percent}
55 %
56 % Outputs:
57 %   SD -- Single distnace structure with the following feilds:
58 %     S_Ph -- Phase sensitivity map (voxels in x X voxels in y X
59 %           voxels in z)
60 %     S_In -- Intensity sensitivity map (same structure as S_Ph)
61 %     S_PhN -- Noise equivalent sensitivity for phase
62 %     S_InN -- Noise equivalent sensitivity for intensity

```

```

63 %
64 % SS      — Single slope structure with the same feilds as SD
65 %
66 % DS      — Dual slope structure with the same feilds as SD
67 %
68 % params — Parameters structure with the following feilds:
69 %           armt   — Arrangement structure same as input
70 %           geo    — Geometry structure same as input with the following
71 %                   additional feilds:
72 %             X — Meshgird for x axis (voxels in x X
73 %                   voxels in y X voxels in z) {mm}
74 %             Y — Meshgird for y axis (same structure as X)
75 %                   {mm}
76 %             Z — Meshgird for z axis (same structure as X)
77 %                   {mm}
78 %             x — x axis coordinates (1 X voxels in x) {mm}
79 %             y — y axis coordinates (1 X voxels in y) {mm}
80 %             z — z axis coordinates (1 X voxels in z) {mm}
81 %           optProp — Optical properties structure same as input
82 %           opts   — Options structure same as input
83
84 %% Unpackage Input
85 if nargin<=0
86     armt.rSrc=[...
87         -30, 0, 0; ...
88         30, 0, 0]; %mm
89     armt.rDet=[...
90         -5, 0, 0; ...
91         5, 0, 0]; %mm
92
93     %[sInd1, dInd1; ...; sIndn, dIndn]
94     armt.SDprs=[...
95         1, 2];
96
97     %SSprs(:, :, n)=[sInd1, dInd1; sInd2, dInd2]
98     armt.SSprs(:, :, 1)=[...
99         1, 1; ...
100        1, 2];
101
102     %SSprs(:, :, SSInd, n)=[sInd1, dInd1; sInd2, dInd2]
103     armt.DSprs(:, :, 1, 1)=[...
104         1, 1; ...
105         1, 2];
106     armt.DSprs(:, :, 2, 1)=[...
107         2, 2; ...
108         2, 1];
109 end
110 if nargin<=1
111     pert.partSz=[20, 20, 4]; %Num Voxels [x, y, z]
112     pert.dmuA=0.003; %1/mm
113 end
114 if nargin<=2
115     geo.xMar=45; %mm
116     geo.yMar=45; %mm

```

```

117      geo.zMax=25; %mm
118      geo.dr=[0.5, 0.5, 0.5]; %mm
119  end
120  if nargin<=3
121      optProp.nin=1.4;
122      optProp.nout=1;
123      optProp.musp=1.2; %1/mm
124      optProp.mua=0.01; %1/mm
125
126  end
127  if nargin<=4
128      opts.fmod=1.40625e8; %Hz
129      opts.PhN=0.06; %deg
130      opts.InN=0.4; %Percent
131  end
132
133 rSrc_true=armt.rSrc; %mm
134 rDet=armt.rDet; %mm
135 SDprs=armt.SDprs; %[sInd1, dInd1; ...; sIndn, dIndn]
136 SSprs=armt.SSprs; %SSprs(:, :, n)=[sInd1, dInd1; sInd2, dInd2]
137 DSprs=armt.DSprs; %SSprs(:, :, SSInd, n)=[sInd1, dInd1; sInd2, dInd2]
138
139 xMar=geo.xMar; %mm
140 yMar=geo.yMar; %mm
141 zMax=geo.zMax; %mm
142 dx=geo.dr(1); %mm
143 dy=geo.dr(2); %mm
144 dz=geo.dr(3); %mm
145
146 partSz(1)=pert.partSz(2); %Num Voxels [y, x, z]
147 partSz(2)=pert.partSz(1);
148 partSz(3)=pert.partSz(3);
149 dmua=pert.dmua; %1/mm
150
151 musp=optProp.musp; %1/mm
152
153 omega=2*pi*opts.fmod; %rad/sec
154 PhN=opts.PhN*pi/180; %rad
155 InN=opts.InN/100; %Frac
156
157 rSrc=rSrc_true+[0, 0, 1/musp];
158
159 %% Calculate Pathlengths
160 initVar=NaN(size(rSrc, 1), size(rDet, 1));
161 L=initVar;
162 LIn=initVar;
163 LPh=initVar;
164 R=initVar;
165 for sInd=1:size(rSrc, 1)
166     for dInd=1:size(rDet, 1)
167         [L(sInd, dInd), R(sInd, dInd)]=...
168             complexTotPathLen(rSrc(sInd, :), rDet(dInd, :), omega, optProp);
169
170     LIn(sInd, dInd)=real(L(sInd, dInd));

```

```

171      LPh(sInd, dInd)=imag(L(sInd, dInd));
172    end
173  end
174
175  x=xMar:dx:xMar;
176  y=yMar:dy:yMar;
177  z=0:dz:zMax;
178
179 [X, Y, Z]=meshgrid(x, y, z);
180 r=[X(:, ), Y(:, ), Z(:, )];
181
182 V=dx*dy*dz;
183
184 initVar=NaN(size(r, 1), size(rSrc, 1), size(rDet, 1));
185 l=initVar;
186 lIn=initVar;
187 lPh=initVar;
188 for sInd=1:size(rSrc, 1)
189   for dInd=1:size(rDet, 1)
190     l(:, sInd, dInd)=complexPartPathLen(...%
191       rSrc(sInd, :, ), r, rDet(dInd, :, ), V, omega, optProp);
192
193     lIn(:, sInd, dInd)=real(l(:, sInd, dInd));
194     lPh(:, sInd, dInd)=imag(l(:, sInd, dInd));
195   end
196 end
197 lIn(isnan(lIn))=0;
198 lPh(isnan(lPh))=0;
199
200 %% Sen
201 % SD
202 if ~isempty(SDprs)
203   initVar=NaN(size(r, 1), size(SDprs, 1));
204   S_SDIn=initVar;
205   S_SDPh=initVar;
206   for pInd=1:size(SDprs, 1)
207     sInd=SDprs(pInd, 1);
208     dInd=SDprs(pInd, 2);
209     if dInd==0 || sInd==0
210       continue;
211     end
212
213     S_SDIn(:, pInd)=lIn(:, sInd, dInd)./LIn(sInd, dInd);
214     S_SDPh(:, pInd)=lPh(:, sInd, dInd)./LPh(sInd, dInd);
215   end
216 end
217
218 % SS
219 if ~isempty(SSprs)
220   initVar=NaN(size(r, 1), size(SSprs, 3));
221   S_SSIn=initVar;
222   S_SSPh=initVar;
223   S_SSIn_num=initVar;
224   S_SSPh_num=initVar;

```

```

225     S_SSIn_den=initVar;
226     S_SSPh_den=initVar;
227     for pInd=1:size(SSprs, 3)
228         sInds=SSprs(:, 1, pInd);
229         dInds=SSprs(:, 2, pInd);
230         if sum(dInds==0)>0 || sum(sInds==0)>0
231             continue;
232         end
233
234         rsd=vecnorm((rDet(dInds, :)-rSrc(sInds, :))');
235         rsd_avg=mean(rsd);
236         rsd_diff=rsd-rsd_avg;
237
238         S_SSIn_num(:, pInd)=0;
239         S_SSPh_num(:, pInd)=0;
240         S_SSIn_den(:, pInd)=0;
241         S_SSPh_den(:, pInd)=0;
242         for rInd=1:length(rsd_diff)
243             S_SSIn_num(:, pInd)=S_SSIn_num(:, pInd)+...
244                 (rsd_diff(rInd).*lIn(:, sInds(rInd), dInds(rInd)));
245             S_SSIn_den(:, pInd)=S_SSIn_den(:, pInd)+...
246                 (rsd_diff(rInd).*LIn(sInds(rInd), dInds(rInd)));
247
248             S_SSPh_num(:, pInd)=S_SSPh_num(:, pInd)+...
249                 (rsd_diff(rInd).*lPh(:, sInds(rInd), dInds(rInd)));
250             S_SSPh_den(:, pInd)=S_SSPh_den(:, pInd)+...
251                 (rsd_diff(rInd).*LPh(sInds(rInd), dInds(rInd)));
252         end
253         S_SSIn(:, pInd)=S_SSIn_num(:, pInd)./S_SSIn_den(:, pInd);
254         S_SSPh(:, pInd)=S_SSPh_num(:, pInd)./S_SSPh_den(:, pInd);
255     end
256
257
258 % DS
259 if ~isempty(DSprs)
260     initVar=NaN(size(r, 1), size(DSprs, 4));
261     S_DSIn=initVar;
262     S_DSPh=initVar;
263     for SInd=1:size(DSprs, 4)
264         DS_SSprs=DSprs(:, :, :, SInd);
265
266         initVar=NaN(size(r, 1), size(DS_SSprs, 3));
267         S_DS_SSIn=initVar;
268         S_DS_SSPh=initVar;
269         S_DS_SSIn_num=initVar;
270         S_DS_SSPh_num=initVar;
271         S_DS_SSIn_den=initVar;
272         S_DS_SSPh_den=initVar;
273         for pInd=1:size(DS_SSprs, 3)
274             sInds=DS_SSprs(:, 1, pInd);
275             dInds=DS_SSprs(:, 2, pInd);
276             if sum(dInds==0)>0 || sum(sInds==0)>0
277                 continue;
278             end

```

```

279
280     rsd=vecnorm((rDet(dInds, :) - rSrc(sInds, :))');
281     rsd_avg=mean(rsd);
282     rsd_diff=rsd-rsd_avg;
283
284     S_DS_SSIn_num(:, pInd)=0;
285     S_DS_SSPh_num(:, pInd)=0;
286     S_DS_SSIn_den(:, pInd)=0;
287     S_DS_SSPh_den(:, pInd)=0;
288     for rInd=1:length(rsd_diff)
289         S_DS_SSIn_num(:, pInd)=S_DS_SSIn_num(:, pInd)+...
290             (rsd_diff(rInd).*lIn(:, sInds(rInd), dInds(rInd)));
291         S_DS_SSIn_den(:, pInd)=S_DS_SSIn_den(:, pInd)+...
292             (rsd_diff(rInd).*LIn(sInds(rInd), dInds(rInd)));
293
294         S_DS_SSPh_num(:, pInd)=S_DS_SSPh_num(:, pInd)+...
295             (rsd_diff(rInd).*lPh(:, sInds(rInd), dInds(rInd)));
296         S_DS_SSPh_den(:, pInd)=S_DS_SSPh_den(:, pInd)+...
297             (rsd_diff(rInd).*LPh(sInds(rInd), dInds(rInd)));
298     end
299     S_DS_SSIn(:, pInd)=S_DS_SSIn_num(:, pInd). / S_DS_SSIn_den(:, pInd);
300     S_DS_SSPh(:, pInd)=S_DS_SSPh_num(:, pInd). / S_DS_SSPh_den(:, pInd);
301 end
302
303 warning('Only valid for symmetric DS sets');
304 S_DSIn(:, SInd)=mean(S_DS_SSIn, 2, 'omitnan');
305 S_DSPh(:, SInd)=mean(S_DS_SSPh, 2, 'omitnan');
306 end
307 end
308
309 %% Make Maps
310 % SD
311 if ~isempty(SDprs)
312     initVar=NaN(size(X, 1), size(X, 2), size(X, 3), size(SDprs, 1));
313     S_SDIn_Map=initVar;
314     S_SDPH_Map=initVar;
315     for pInd=1:size(SDprs, 1)
316         S_SDIn_Map(:, :, :, pInd)=reshape(S_SDIn(:, pInd), size(X));
317         S_SDPH_Map(:, :, :, pInd)=reshape(S_SDPH(:, pInd), size(X));
318     end
319 end
320
321 % SS
322 if ~isempty(SSprs)
323     initVar=NaN(size(X, 1), size(X, 2), size(X, 3), size(SSprs, 3));
324     S_SSIn_Map=initVar;
325     S_SSPh_Map=initVar;
326     for pInd=1:size(SSprs, 3)
327         S_SSIn_Map(:, :, :, pInd)=reshape(S_SSIn(:, pInd), size(X));
328         S_SSPh_Map(:, :, :, pInd)=reshape(S_SSPh(:, pInd), size(X));
329     end
330 end
331
332 % DS

```

```

333 if ~isempty(DSprs)
334     initVar=NaN(size(X, 1), size(X, 2), size(X, 3), size(DSprs, 4));
335     S_DSIn_Map=initVar;
336     S_DSPh_Map=initVar;
337     for pInd=1:size(DSprs, 4)
338         S_DSIn_Map(:, :, :, pInd)=reshape(S_DSIn(:, pInd), size(X));
339         S_DSPh_Map(:, :, :, pInd)=reshape(S_DSPh(:, pInd), size(X));
340     end
341 end
342
343 %% Convolve Volume
344 % SD
345 if ~isempty(SDprs)
346     initVar=NaN(size(S_SDIn_Map));
347     S_SDIn_Map_vol=initVar;
348     S_SDPh_Map_vol=initVar;
349     for pInd=1:size(SDprs, 1)
350         H=ones(partSz);
351         S_SDIn_Map_vol(:, :, :, pInd)=convn(...
352             S_SDIn_Map(:, :, :, pInd), H, 'same');
353         S_SDPh_Map_vol(:, :, :, pInd)=convn(...
354             S_SDPh_Map(:, :, :, pInd), H, 'same');
355     end
356 end
357
358 % SS
359 if ~isempty(SSprs)
360     initVar=NaN(size(S_SSIn_Map));
361     S_SSIn_Map_vol=initVar;
362     S_SSPh_Map_vol=initVar;
363     for pInd=1:size(SSprs, 3)
364         H=ones(partSz);
365         S_SSIn_Map_vol(:, :, :, pInd)=convn(...
366             S_SSIn_Map(:, :, :, pInd), H, 'same');
367         S_SSPh_Map_vol(:, :, :, pInd)=convn(...
368             S_SSPh_Map(:, :, :, pInd), H, 'same');
369     end
370 end
371
372 % DS
373 if ~isempty(DSprs)
374     initVar=NaN(size(S_DSIn_Map));
375     S_DSIn_Map_vol=initVar;
376     S_DSPh_Map_vol=initVar;
377     for pInd=1:size(DSprs, 4)
378         H=ones(partSz);
379         S_DSIn_Map_vol(:, :, :, pInd)=convn(...
380             S_DSIn_Map(:, :, :, pInd), H, 'same');
381         S_DSPh_Map_vol(:, :, :, pInd)=convn(...
382             S_DSPh_Map(:, :, :, pInd), H, 'same');
383     end
384 end
385
386 %% Calc Noise

```

```

387 % SD
388 if ~isempty(SDprs)
389     initVar=NaN(size(SDprs, 1), 1);
390     S_SDInN=initVar;
391     S_SDPhN=initVar;
392     for pInd=1:size(SDprs, 1)
393         sInd=SDprs(pInd, 1);
394         dInd=SDprs(pInd, 2);
395         if dInd==0 || sInd==0
396             continue;
397         end
398
399         S_SDInN(pInd)=InN/(LIn(sInd, dInd)*dmua);
400         S_SDPhN(pInd)=PhN/(LPh(sInd, dInd)*dmua);
401     end
402 end
403
404 % SS
405 if ~isempty(SSprs)
406     initVar=NaN(size(SSprs, 3), 1);
407     S_SSInN=initVar;
408     S_SSPhN=initVar;
409     for pInd=1:size(SSprs, 3)
410         sInds=SSprs(:, 1, pInd);
411         dInds=SSprs(:, 2, pInd);
412         if sum(dInds==0)>0 || sum(sInds==0)>0
413             continue;
414         end
415
416         rsd=vecnorm((rDet(dInds, :)-rSrc(sInds, :))');
417         rsd_avg=mean(rsd);
418         rsd_diff=rsd-rsd_avg;
419
420         initVar=NaN(size(rsd_diff));
421         LInVec=initVar;
422         LPhVec=initVar;
423         for rInd=1:length(rsd_diff)
424             LInVec(rInd)=LIn(sInds(rInd), dInds(rInd));
425             LPhVec(rInd)=LPh(sInds(rInd), dInds(rInd));
426         end
427
428         S_SSInN(pInd)=(InN*sqrt(sum(rsd_diff.^2)))/...
429             (dmua*dot(rsd_diff, LInVec));
430         S_SSPhN(pInd)=(PhN*sqrt(sum(rsd_diff.^2)))/...
431             (dmua*dot(rsd_diff, LPhVec));
432
433     end
434 end
435
436 % DS
437 if ~isempty(DSprs)
438     initVar=NaN(size(DSprs, 4), 1);
439     S_DSInN=initVar;
440     S_DSPhN=initVar;

```

```

441     for SInd=1:size(DSpRs, 4)
442         DS_SSPrs=DSpRs(:, :, :, SInd);
443
444         initVar=NaN(size(DS_SSPrs, 3), 1);
445         S_DS_SSInN=initVar;
446         S_DS_SSPhN=initVar;
447         for pInd=1:size(DS_SSPrs, 3)
448             sInds=DS_SSPrs(:, 1, pInd);
449             dInds=DS_SSPrs(:, 2, pInd);
450             if sum(dInds==0)>0 || sum(sInds==0)>0
451                 continue;
452             end
453
454             rsd=vecnorm((rDet(dInds, :)-rSrc(sInds, :))');
455             rsd_avg=mean(rsd);
456             rsd_diff=rsd-rsd_avg;
457
458             initVar=NaN(size(rsd_diff));
459             LInVec=initVar;
460             LPhVec=initVar;
461             for rInd=1:length(rsd_diff)
462                 LInVec(rInd)=LIn(sInds(rInd), dInds(rInd));
463                 LPhVec(rInd)=LPh(sInds(rInd), dInds(rInd));
464             end
465
466             S_DS_SSInN(pInd)=(InN*sqrt(sum(rsd_diff.^2)))/...
467                             (dmua*dot(rsd_diff, LInVec));
468             S_DS_SSPhN(pInd)=(PhN*sqrt(sum(rsd_diff.^2)))/...
469                             (dmua*dot(rsd_diff, LPhVec));
470         end
471
472         S_DSInN(SInd)=sqrt(sum(S_DS_SSInN.^2, 'omitnan'))/length(S_DS_SSInN);
473         S_DSPhN(SInd)=sqrt(sum(S_DS_SSPhN.^2, 'omitnan'))/length(S_DS_SSPhN);
474     end
475 end
476
477 %% Package Output
478 geo.X=X;
479 geo.Y=Y;
480 geo.Z=Z;
481 geo.x=x;
482 geo.y=y;
483 geo.z=z;
484
485 params.armt=armt;
486 params.geo=geo;
487 params.optProp=optProp;
488 params.opts=opts;
489
490 if ~isempty(SDprS)
491     SD.S_Ph=S_SDPh_Map_vol;
492     SD.S_In=S_SDIn_Map_vol;
493     SD.S_PhN=S_SDPhN;
494     SD.S_InN=S_SDInN;

```

```
495 else
496     SD=[];
497 end
498
499 if ~isempty(SSprs)
500     SS.S_Ph=S_SSPh_Map_vol;
501     SS.S_In=S_SSIn_Map_vol;
502     SS.S_PhN=S_SSPhN;
503     SS.S_InN=S_SSInN;
504 else
505     SS=[];
506 end
507
508 if ~isempty(DSpres)
509     DS.S_Ph=S_DSPH_Map_vol;
510     DS.S_In=S_DSIn_Map_vol;
511     DS.S_PhN=S_DSPH_N;
512     DS.S_InN=S_DSInN;
513 else
514     DS=[];
515 end
516 end
```

Available at:

<https://github.com/DOIT-Lab/DOIT-Public/tree/master/Dissertations/GilesBlaney2022/code>

Appendix F

Simulation of Apparent Measurements

In general we simulate a given measurement by generating forward data with a forward model and then analyzing that data. The analysis process may be considered an inverse model which is in turn based on a forward model itself. Therefore these simulations are interesting to the extent that the forward model used to generate data and inverse model do not match.

F.1 Simulation of Measurements of Dynamic Changes

When analyzing data for absorption coefficient change ($\Delta\mu_a$) the analysis methods are those found in Appendix C. These methods are based on retrieving $\Delta\mu_a$ as if the change occurred everywhere in a semi-infinite homogeneous medium. Therefore if the change is localized, what is measured will not be the same as the actual $\Delta\mu_a$. This relationship depends on analysis method and perturbation location which is the meaning of Sensitivity to absorption change (\mathcal{S}) maps (Appendix E). Therefore, these simulations are done using \mathcal{S} as the forward model and Appendix C as the inverse.

Assume a medium is voxelized into N_{vox} voxels *without overlap*. Then using the methods in Appendix E, a $N_{vox} \times 1$ vector of \mathcal{S} ($\vec{\mathcal{S}}$) can be created for whichever datatype one wishes to simulate. Now for the same voxels we can simulate a actual $\Delta\mu_a$ $N_{vox} \times 1$ vector ($\Delta\vec{\mu}_a,_{actual}$). Rearranging Equation 2.1 and summing over all voxels we can calculate the apparent measured $\Delta\mu_a$ ($\Delta\mu_a,_{apparent}$):

$$\Delta\mu_a,_{apparent} = \vec{\mathcal{S}}^T \Delta\vec{\mu}_a,_{actual} \quad (\text{F.1})$$

It is emphasized that this method only works if the \mathcal{S} values correspond to voxels which *do not overlap*, and of course the order of the voxels in the two vectors must be the same.

Now lets look at this implementation in MathWorks MATrix LABoratory [Natick, MA USA] (MATLAB). The code in Listing E.2 can be used to generate \mathcal{S} maps. To do the type of simulation we wish we must not have overlap. This is achieved by setting the `pert.partSz` input to `[1,1,1]`. Now the function will retrieve the \mathcal{S} for each individual voxel without using convolution. Lets utilize a specific example to demonstrate the next steps. Say we want to simulate a Single-Distance (SD) set with source-detector distance (ρ) of 35 mm, the default medium optical properties (Listing E.2), and a actual vector of absorption coefficient changes ($\Delta\vec{\mu}_a$) (`dmua_actual`) of 0.001 mm^{-1} at all voxels with $z \geq 10 \text{ mm}$. The following code will retrieve the apparent measured $\Delta\mu_a$ with SD Intensity (I) (`dmua_apparent`) using $\vec{\mathcal{S}}$ (`Svec`) from Listing E.2:

```

1 armt.rSrc=[-35/2, 0, 0]; %mm
2 armt.rDet=[35/2, 0, 0]; %mm
3 armt.SDprs=[1, 1];
4
5 pert.partSz=[1, 1, 1];
6 %pert.dmua not used in this example
7 pert.dmua=NaN;
8
9 [SD, ~, ~, params]=...
10           makeSenMaps(armt, pert);
11 Svec=SD.S_In(:);
12
13 dmua_actual=...

```

```

14     (params.geo.Z(:)>=10)*...
15     0.001; %1/mm
16
17 dmua_apparent=Svec'*dmua_actual;

```

This method can be expanded to different actual $\Delta\mu_a$ in different voxels allowing one to simulate measurements from regions with different $\Delta\mu_a$ dynamics.

Using the above equation and code we can simulate a apparent measured $\Delta\mu_a$ given localized actual $\Delta\mu_a$. However, often we to simulate Oxy-hemoglobin concentration change (ΔO) and Deoxy-hemoglobin concentration change (ΔD). This turns out to be simple, the forward model for $\Delta\mu_a$ from Appendix A can be used to find actual $\Delta\mu_a$ at every voxel from the actual ΔO and ΔD at each voxel. Then the above simulation methods find apparent $\Delta\mu_a$ which can be converted to apparent ΔO and ΔD with Appendix D. If this is done, the simulation needs to be run at two or more optical wavelengths (λ s).

Furthermore, if one wishes to simulate Oxy-hemoglobin phasor (\tilde{O}) and Deoxy-hemoglobin phasor (\tilde{D}) the same methods can also be applied. The forward models to retrieve $\Delta\mu_a$ from Appendix A will accept complex numbers which represent \tilde{O} and \tilde{D} and will result the absorption coefficient (μ_a) phasors. Then the S methods will also work with complex numbers to give the apparent μ_a phasor, and finally these complex μ_a phasors can be input into the methods in Appendix D to result in apparent \tilde{O} and \tilde{D} .

Therefore, using S maps one can simulate various types of $\Delta\mu_a$ s (including phasors) and receive the apparent measured $\Delta\mu_a$ s. However, one should note that what is simulated is dependent in the absolute μ_a and reduced scattering coefficient (μ'_s), which is also assumed to be homogeneous in the S expressions used here. Additionally, the S theory assumes $\Delta\mu_a$ is small compared to μ_a . This simplification is not realistic and should be noted using S simulations. But certain types of simulations are still valuable, such as comparing what different data-types measure from the same medium with simulated $\Delta\mu_a$.

F.2 Simulation of Measurements of Absolute Optical Properties

As stated above, the simulations in this appendix are primarily concerned with testing mismatched forward and inverse models. In the case of the measurement of absolute optical properties, the inverse model is the one in Appendix B which is based on the semi-infinite homogeneous medium. Most of the interest in testing this inversion comes from generating forward data from heterogeneous media. This was done extensively in Part III.

Our inverse model for absolute optical properties (Appendix B) takes measurements of complex Reflectance (\tilde{R}) at two source-detector distance (ρ) as input. Therefore any forward model which calculates \tilde{R} as a function of ρ may be used to generate forward data for the inverse model. The first such forward model is the two-layer forward model in Appendix A which gives \tilde{R} from a medium with two layers having different absorption coefficient (μ_a) and reduced scattering coefficient (μ'_s). Another forward model that may be used is Monte Carlo which can simulate even more complex distributions of μ_a and μ'_s to generate \tilde{R} which also can be inverted with the methods in Appendix B.

In practice this is quite simple. Any forward model you like is used to generate \tilde{R} at at least two ρ s. Then this \tilde{R} is input into the methods in Appendix B to result in the effective homogeneous μ_a and μ'_s . The result from this computational experiment is called *effective homogeneous* because the inverse model has found a homogeneous medium with μ_a and μ'_s that would result in a similar or even the same behavior in \tilde{R} as the more complex forward model. Studying how effective homogeneous optical properties are related to actual heterogeneous optical properties is complex, in part because it is likely that different heterogeneous optical properties may result in the same effective homogeneous optical properties.

Appendix G

Phasor Analysis

A phasor represents the phase and amplitude of a given signal at a given frequency. Some sort of time-frequency transform is used to convert a time (t) series say $x(t)$ to its phasor $\tilde{x}(f)$ at frequency f . If a time resolved phasor analysis is used, a time-frequency map of phasors may be generated ($\tilde{x}(t, f)$) where each pixel is a complex value representing the amplitude and phase of said signal at that time and frequency.

G.1 Wavelet Phasor Analysis

We conduct wavelet phasor analysis using the **Continuous Wavelet Transform (CWT)** of the signal of interest ($x(t)$ for example) which results in the phasor $\tilde{x}(t, f)$, which we write as a function of t and f since this method does result in time-resolved phasors. We utilize the analytic Morlet mother wavelet for the **CWT**, which is the default of the **MathWorks MATrix LABoratory [Natick, MA USA] (MATLAB)** `wcoherence` used in coherence analysis (Appendix H). Here we note that the **CWT** does not truly output phasors as a function of f but instead as a function of wavelet scale, however for the Morlet mother wavelet it is reasonable to assume that f is the inverse of the wavelet scale.

In general the wavelet transform can be written as [65]:

$$\tilde{x}(t, f) = \int_{-\infty}^{\infty} x(t') f \psi^*(f(t' - t)) dt' \quad (\text{G.1})$$

where $\psi(t)$ is the mother wavelet and we are approximating the f as the inverse of the scale.

Computationally to take the **CWT** we utilize the **MATLAB** `cwtft` function to match the ver-

sion of **wcoherence** we utilize for coherence (Appendix H). This function computes the **CWT** of a time series using the Fast-Fourier Transform (FFT) algorithm for efficiency.

G.1.1 Coherent Hemodynamics Spectroscopy Phasor Ratio Vectors

In **Coherent Hemodynamics Spectroscopy (CHS)** the chief phasors of interest are Oxy-hemoglobin phasor (\tilde{O}), Deoxy-hemoglobin phasor (\tilde{D}), and Arterial blood pressure phasor (\tilde{A}). We determine each of these using the **CWT**. To interpret these phasors we take their ratio vectors which represent the amplitude ratio and phase difference between the two phasors in the ratio.

The two common **CHS** phasor ratio vectors are phasor ratio vector between Total-hemoglobin and Arterial blood pressure phasor ($\overrightarrow{T/A}$) and phasor ratio vector between Deoxy-hemoglobin and Oxy-hemoglobin ($\overrightarrow{D/O}$) which can simply be found by the division of the two phasors for each time-frequency pixel. Appendix H examples how regions of significant **Coherence (C)** are found between these phasors. The maps of $\overrightarrow{T/A}$ or $\overrightarrow{D/O}$ are masked by significant **C** (throwing away areas without significant **C**) to determine time and frequency regions of significantly coherent $\overrightarrow{T/A}$ or $\overrightarrow{D/O}$.

Finally to produce $\overrightarrow{T/A}$ or $\overrightarrow{D/O}$ at a given frequency, averaging is done across time, only considering pixels with significant **C**. The averaging is also done over a frequency bandwidth, where the bandwidth is determined by the **Full-Width Half-Max (FWHM)** of the power-spectral density of the **CWT** of a synthetic sinusoidal signal. Af-

ter this averaging a single $\overrightarrow{T/A}$ or $\overrightarrow{D/O}$ is output for every frequency of interest, which represents the transfer function between the two signals in the pair by only considering times and frequencies where the pair is coherent.

Appendix H

Determination of Coherence

We identify times and frequencies of significant coherence between two signals in a wavelet scalogram by comparing the measured coherence to a threshold generated with random surrogate data (Chapter 7). This is especially important in **Coh**erent Hemodynamics Spectroscopy (CHS) analysis which focuses on signals pairs involving **Oxy**-hemoglobin concentration change (ΔO), **Deoxy**-hemoglobin concentration change (ΔD), and **Ar**terial blood pressure change (ΔA). However, in general, these methods can be applied to any pair of signals for which you wish to find times and frequencies where they are significantly coherent.

H.1 Coherence

Coherence (\mathfrak{C}) is a metric used to examine the relationship between two signals. Take the two signals $x(t)$ and $y(t)$ which are a function of time (t). Given these two signals we can discuss the \mathfrak{C} between them, written as $\mathfrak{C}(\tilde{x}(f), \tilde{y}(f))$, where $\tilde{x}(f)$ and $\tilde{y}(f)$ are the phasors of $x(t)$ and $y(t)$, respectively at frequency f .

Depending on the methods utilized to find the signal's phasors, \mathfrak{C} may be a function of frequency (f , corresponding to the phasor frequency) or both f and t (if the analysis allows for time resolved phasors). Values of coherence are bounded by 0 and 1 ($\mathfrak{C} \in [0, 1]$) taking the value of 0 if x and y have no linear relationship whatsoever and 1 if they are related by a perfect linear system. For example take the time domain transfer function (*id est* impulse response) $h(t)$, then we can

write the following:

$$\mathfrak{C}(\tilde{x}(f), \tilde{y}(f)) = \begin{cases} 1 & y(t) = h(t) \otimes x(t) \\ \in [0, 1] & \text{otherwise} \end{cases} \quad (\text{H.1})$$

which is equivalent to:

$$\mathfrak{C}(\tilde{x}(f), \tilde{y}(f)) = \begin{cases} 1 & \tilde{y}(f) = \tilde{h}(f) \times \tilde{x}(f) \\ \in [0, 1] & \text{otherwise} \end{cases} \quad (\text{H.2})$$

However, in reality two signals are not related with a *perfect* linear system, therefore realistically $\mathfrak{C} \in [0, 1]$ for real world measurements.

As mentioned above if the phasors are time resolved such as in a spectrogram or wavelet scalogram, the \mathfrak{C} is also time resolved (as well as frequency resolved). Additionally, depending on the specific analysis methods are parameters the actual meaning of the value of \mathfrak{C} may be difficult to interpret.

H.1.1 Wavelet Coherence

We utilize a modified version of the **MathWorks MATrix LABoratory [Natick, MA USA] (MATLAB)** `wcoherence` function to determine the \mathfrak{C} between two signals (say $x(t)$ and $y(t)$). Wavelet analysis enables the time and frequency resolved phasors of the signals ($\tilde{x}(t, f)$ and $\tilde{y}(t, f)$). Thus, in this section (unlike previous) we show when values are functions of both time (t) and (f) to highlight this feature of wavelet analysis.

First we obtain the $\tilde{x}(t, f)$ and $\tilde{y}(t, f)$ phasors from the **Continuous Wavelet Transform (CWT)**

as shown in Appendix G. Using these phasors we can write the wavelet \mathfrak{C} [65]:

$$\frac{\mathfrak{C}(\tilde{x}(t, f), \tilde{y}(t, f)) =}{\mathfrak{S}[\tilde{x}^*(t, f)\tilde{y}(t, f)]^2}{\mathfrak{S}[|\tilde{x}(t, f)|^2]\mathfrak{S}[|\tilde{y}(t, f)|^2]} \quad (\text{H.3})$$

where \mathfrak{S} is a time-frequency smoothing operator. In the case of our modified `wcoherence` function, \mathfrak{S} only smooths in time (to preserve frequency resolution) and the smoothing window is a Gaussian that scales with the wavelet scale (same as the MATLAB default for `wcoherence`).

Examining Equation H.3 we see that the numerator is the squared magnitude of the cross-spectrum, and the denominator is the squared magnitude of the two signals phasor's multiplied together. Therefore, \mathfrak{C} may be thought of as a normalized cross-spectral density. Some insight may now also be gained about the limiting values of \mathfrak{C} now. If the signals are completely coherent and the \mathfrak{C} equal to 1, then the cross-spectral density is equal to the power-spectral densities of the two signals multiplied together. This is one way of saying that all of the power from the two signals is coupled together. Conversely if \mathfrak{C} is 0, then the cross-spectral density is also 0 which means none of the power between the signals is coupled.

Besides that idea that higher \mathfrak{C} means a more coupled signals, the interpretation of the actual value of \mathfrak{C} is difficult. This is in-part because the value of \mathfrak{C} is dependent on analysis parameters and importantly \mathfrak{S} . As the window size of \mathfrak{S} becomes smaller \mathfrak{C} becomes biased to larger values, and if no smoothing is applied (\mathfrak{S} having a window of one time-frequency pixel) \mathfrak{C} will be 1. Therefore there is a trade-off between time-frequency resolution and the ease of interpretation of \mathfrak{C} .

H.2 Coherence Thresholding

Since the interpretation of the actual value of Coherence (\mathfrak{C}) is difficult, we opt to make a statement about the significance. To do this we do a test for significance at each time-frequency pixel in the wavelet scalogram. The threshold for 95 %

significance is found using the method in Chapter 7. Then this threshold map is compared to the \mathfrak{C} map for the two signals of interest. Regions where the \mathfrak{C} is above threshold are considered to be times and frequencies of significant coherence. Only these significant coherence regions are used in further analysis.

H.2.1 Coherent Hemodynamics Spectroscopy Thresholding

In Coherent Hemodynamics Spectroscopy (CHS) the region of significant coherence is determined for Coherence between Total-hemoglobin and Arterial blood pressure phasor ($\mathfrak{C}(\tilde{T}, \tilde{A})$), Coherence between Oxy-hemoglobin and Arterial blood pressure phasor ($\mathfrak{C}(\tilde{O}, \tilde{A})$), and Coherence between Deoxy-hemoglobin and Arterial blood pressure phasor ($\mathfrak{C}(\tilde{D}, \tilde{A})$) since Arterial Blood Pressure (ABP) is assumed to be the chief hemodynamic driver. This is with the goal of finding time-frequency regions for the analysis of phasor ratio vector between Total-hemoglobin and Arterial blood pressure phasor (\tilde{T}/\tilde{A}) and phasor ratio vector between Deoxy-hemoglobin and Oxy-hemoglobin (\tilde{D}/\tilde{O}). For \tilde{T}/\tilde{A} only areas in time-frequency where $\mathfrak{C}(\tilde{T}, \tilde{A})$ is significant are used for analysis. While for \tilde{D}/\tilde{O} only times-frequency areas where $\mathfrak{C}(\tilde{O}, \tilde{A})$ and $\mathfrak{C}(\tilde{D}, \tilde{A})$ is significant is used for analysis. This selection of only coherent phasor ratio vectors is the reason for the *coherent* name of CHS.

Postface

Current and Future Work

As is typical in research, this dissertation by no means represents the final conclusions of the research within. Any of the chapters may be expanded upon in the future. At the time of writing, we have various directions in which we want to expand this work.

Regarding the work with **Sensitivity to absorption change (\mathcal{S})**, we wish to explore how sensitivity maps change when the medium is heterogeneous. Specifically, how this effects the net region of \mathcal{S} exhibited by **Dual-Slope (DS)**. To do this we are employing Monte Carlo simulations to derive the **partial optical path-lengths ($\langle \ell \rangle$ s)** from heterogeneous media and then generating \mathcal{S} maps. Further, we are interested in expanding on the idea of \mathcal{S} . As defined now \mathcal{S} is essentially a Jacobian, meaning it only represents changes in optical properties (we can also get a similar concept for reduced scattering coefficient (μ'_s) instead of absorption coefficient (μ_a)). We are exploring the idea of expanding sensitivity to absolute measurements. This would allow for visualization of which parts of a medium affect absolute measurements and possibly lead to better ways to reconstruct images of absolute optical properties.

On the instrumentation side, we are interested in optimizing the **phase (ϕ)** measurements in **Frequency-Domain (FD) Near-Infrared Spectroscopy (NIRS)**. This is because of indications that **DS** ϕ has promise for measurements of deep hemodynamics. However, the struggle with ϕ is the noise. There are indications that the **Contrast-to-Noise Ratio (CNR)** for ϕ will increase at higher **modulation frequency (f_{mod})** than the one currently used of 140.625 MHz. Therefore, we are in the process of constructing a **FD NIRS** instrument better optimized for higher f_{mod} and dynamic ϕ measurement. With this project, we are also experimenting with differ-

ent sampling methods (*id est* heterodyne, direct sampling, *et cetera*) to find the best method for our situation.

Concerning the expansion of **DS** imaging and **Coherence (\mathfrak{C})** analysis, we are considering methods which combine our \mathfrak{C} analysis methods developed with **Coherent Hemodynamics Spectroscopy (CHS)** to image reconstruction and \mathcal{S} maps between different **DS** sets.

Finally, to expand on the spectroscopy work we are moving in two directions. We are working to increase the sampling rate of the spectroscopy system. This would allow for dynamic hemodynamic measurements. When this is realized we will attempt to target **Cytochrome-C-Oxidase (CCO)** as a chromophore in the brain that relates to cellular metabolism. Doing so will likely require more advanced spectroscopic analysis techniques such as derivative spectroscopy. The second spectroscopy direction continues to focus on calibration-free absolute measurements. We wish to apply the **DS** geometry to a small volume allowing for quantitative measurements of absolute optical properties with small sample size and no calibration.

All of this current and future work is only written from the prospective I have at the time of authoring this dissertation. Of course these ideas may be expanded upon, go in a different directions, or be abandoned. However, I do think it is likely that we will begin to see **DS** or similar methods applied more in the field of diffuse optics, if not just for its suppression of coupling factors and instrumental drifts.

Acknowledgments

I have chosen to write this acknowledgments section in a slightly unusual way. Specifically, it is separated into sections. This is for two reasons, first so acknowledged people's names are placed in the table of contents instead of being buried within the acknowledgments. Second, a section encourages me to write a personal statement for each. I am doing it this way because I wish to write how each of these people have assisted in my journey to this point.

Family

First is my family who gave me the encouragement and opportunities to be who I am today. What led me to the pursuit of a **Doctor of Philosophy (Ph.D.)** is a long story that starts when I was a young child. Pursuing science and engineering is something I've known I wanted to do since I can remember, and a **Ph.D.** has been my goal since I knew what it was. I am the first in my immediate family to pursue such a high degree, and everyone around me has supported me every step along the way.

Carolyn Blaney

Carolyn Blaney is my mother who has worked so hard to raise my brother (George Blaney) and I. She has always encouraged us to pursue whatever interested us while keeping us safe. From a young age I knew that I had a passion for science and exploring the world. She would let George and I explore the woods in the backyard, dig holes to see what we could uncover, and do crazy experiments both inside and outside the house. All of these things led to more work for her, in this way she poured so much of herself into raising us without compromising our potential. When

I was young I was rather misbehaved in school, not wanting to listen to teachers. She had to bear the brunt of the work resulting from this, going to meetings with teachers and finding ways to compromise. I can not imagine how much work this must have been for her. Despite all of this, she never discouraged us (George or I) and has led us to be the people we are today; with the same passion for science and exploration that we had when we were young children.

Gary Blaney

Gary Blaney is my father who has done much to provide for George and I, as well as, provide as many resources as he could for us to explore our passions. Being a mechanical engineer I followed in his footsteps during my undergraduate degree, but at no point did he push or even suggest that I do so. He has always said I should do whatever I want, and he would help in whatever way he could. For example, when I was very little I found my father's machinists handbook and would insist he explain a page to me before I went to sleep, which he gladly did despite knowing that I would not understand at such a young age. Growing up I had access to various tools which he taught me how to use and always let me borrow for any of my crazy projects. When I was young and dreamed of having my own laboratory, he even built a shed in our backyard which I could call my lab. My dad's encouragement and willingness to help sent me on a path to follow what I am passionate in.

George Blaney

George Blaney is my younger brother who is graduating with his undergraduate degree at the same time I am finishing graduate school. Grow-

ing up we were both very strong minded and stubborn which led to many conflicts. But as we matured, we grew to realize that we had so many interests and ways of thinking in common. We share a love of science, knowledge, and learning. Because of our similarities, we are able to have long in-depth conversations and because of our differences those conversations are on interesting topics and always ends with one or both of us learning something. George is different from me in so many ways, but the same in just as many. Because of this I feel that our relationship has grown in a way that both of us has gained from over the years.

John & Virginia Michaud

John and Virginia Michaud are my maternal grandparents (Carolyn Blaney's parents). They have always been supportive of me and have helped my parents raise me. When I was younger I would visit there house almost every-other weekend where I would help John do various projects around the house or watch some of my favorite television shows with Virginia. Helping John around the house taught me much about work ethic and how difficult it really is to plant a tree or shingle a house. While, Virginia taught me to always speak my mind and stand-up for what I believe in. They have always been very supportive of me giving me many opportunities and resources to help me grow, for that I am very grateful.

Phillip & Marjorie Blaney

Phillip (Phil) and Marjorie (Margie) Blaney are my paternal grandparents (Gary Blaney's parents). Just with my other grandparents, they have supported and helped raise me. The other half of the weekends when I wasn't at my maternal grandparents' house I was at Phil and Margie's. They taught me to engage my mind by teaching me various card and board-games which they were always willing to play with me. This was rather important to me, as it lead me to become more interested in problem solving and applications of mathematics. Phil was a machinist

and a teacher, both professions that I really admire. Being a machinist he had a machine shop in his garage that I remember being fascinated by. They have also been very supportive of me my whole life and have helped me grow to who I am today.

Mary Drabik

Mary Drabik is my great-grandmother on my maternal grandparents side (Virginia Michaud's mother). Before I was old enough to go to school everyday, I would spend most of my day with her. She taught me two hobbies which I still enjoy today, cooking and gardening. Both of these scratched my engineering itch to make something, and cooking taught me to experiment. Learning how to cook and experiment with ingredients at a young age was so much fun for me. I started by trying to bake every type of baked good I could think of, which she happily helped me do. Cooking has had a great influence on my life and is still my favorite pastime, it is a great combination of science and creativity. Cooking so much with Mary also had an impact on her, as in her last years one of the things she would remind me of when I saw her was how I used to come over her house and cook.

Ernst & Gail von Metzsch

Ernst and Gail von Metzsch are my great-aunt and uncle (Gail von Metzsch is John Michaud's sister). Aside from being supportive family members my whole life, they were also enormously financially supportive when I went to college. They have always promised to pay for any of their family members to go to college, which included me. Therefore, thanks to them I was able to receive my undergraduate degree without acquiring any debt. I have been so privileged to have this opportunity which so many people do not have. In-fact I simply do not think I would have been able to go to my undergraduate university without their support and as a result would likely not be in the position I am today. The opportunity they so generously have given me has allowed me to pursue my passion for science and

higher learning. I have tried to make sure this opportunity does not go to waste.

Anjelica Molnar-Fenton

Anjelica Molnar-Fenton has been my romantic partner during the entire time I've been pursuing a Ph.D.. On a day to day basis she has supported me the most over the past 5 yr. She listens to me talk about my day, gives me advice on how to handle situations personal and professional, and has helped me when I have become stressed from assignments or deadlines. Furthermore, since she has a scientific background she has been able to listen to me explain things I am working on for my research. Anjelica has stayed and supported me through both good times and bad, I could not ask for more, and can only hope that she would say I've done the same for her.

Mentors and Colleagues

Now are my mentors and colleagues who have guided me and given me the resources to bring me to where I am now. I have been very fortunate to have so many great people who have helped me along the way. I truly think I have been fortunate.

Profs. Sergio Fantini & Angelo Sassaroli

Professor (Prof.) Sergio Fantini is my Doctor of Philosophy (Ph.D.) advisor and the director of the Diffuse Optical Imaging of Tissue (DOIT) lab. Prof. Angelo Sassaroli is Sergio's long time collaborator and a research professor in the DOIT lab. Both have provided valuable guidance during my time in the Ph.D. program. Imagine all of the negative stereotypes of a graduate school advisor, Sergio has the opposite of all of them. He is always understanding about time and what is reasonable. But, despite this, he will push you to do your best work and provide ample room for you to learn. Meanwhile, Angelo is always there to teach advanced concepts and is patient enough to make sure you fully understand a

concept before moving on. Both Sergio and Angelo are also open to any new idea or project that I've wished to work on, giving me opportunities to pursue my interests. Between Sergio providing professional and big picture mentor-ship and Angelo providing technical mentor-ship, I have felt like I've had more than enough resources to succeed in the DOIT lab.

Cristianne Fernandez, Leon Wang, & Thao Pham

Cristianne (Cristy) Fernandez, Leon Wang, and Thao Pham Ph.D. are or were all Ph.D. candidates at Tufts University at the same time as me, with both Cristy and Thao being in the DOIT lab and Leon in a collaborator's lab. Cristy has become one of the best friends I've made during graduate school and has provided both personal and professional support during the time that we've overlapped in the lab. We regularly do activities outside of work such as board games or barbecues with friends. Thao was also a lab member during most of my time in the DOIT lab, and we became friends during that time. We worked very closely together on technical aspects of our work, but also found time to do many things outside of work such as going out for a bite to eat after our weekly lab group meetings. Finally, Leon has become a close collaborator of mine in the last year or two. During that time we have also become friends and regularly relax over beer and brain-store work ideas or just talk. All of these relationships that I have developed with my fellow graduate students have been very important both in terms of professional collaboration and developing friendships.

Prof. Charles DiMarzio

Prof. Charles (Chuck) DiMarzio was one of my closest mentors at my undergraduate university, Northeastern. He took interest in my simply because I expressed interest in research. Chuck quickly began meeting with me weekly to discuss research and found a small project I could work on to gain experience. He was very generous with his time, more than I could have asked. In do-

ing so, he really put me on the path to graduate school that I had always dreamed of. When it was time to apply to graduate school, he worked with me very closely to choose labs to apply. We would go over papers from various labs week by week so that I could understand what kind of research was out there. Chuck introduced me to Sergio during this search. Without Chuck's guidance I simply would not be in the position I am today.

Blair Cochran

Blair Cochran was my high-school physics teacher. Often you will hear stories about the one teacher that really inspired and encouraged someone, this is what Blair was to me. To this day after about 10 yr of higher education, when someone asks which teachers I've had that really made a difference and inspired me I mention Blair. I really do talk about how he made physics interesting, straightforward, and fun to learn when I start talking about my past learning experiences. Blair's physics class included so many interesting projects intertwined with the actual lectures about physics. These included everything from a robotics competition, to an egg drop, to a trip to an amusement park to study roller coasters. His physics class really was fun, well thought out, and so well organized. But aside from how influential his class was to me, Blair also allowed me to have opportunities outside of class. I would often hang around in his classroom after school where he even let me play around with the lab equipment. When a group of students, including myself, expressed interest in science trivia competitions he enabled us to do it. Also, very importantly from an academic sense, when we expressed interest in taking advanced placement physics, despite the class not being offered, he made it happen. This gave me a leg up when I joined my undergraduate university. Blair even allowed me to be a pseudo-teaching-assistant in my senior year, giving me even more exposure to physics and science education. Blair really cared about the success of all his students, and I saw him provide so many valuable opportunities. I am so thankful and lucky to have had

him as a teacher in high-school.

Funding

All of the research herein has been funded by National Institutes of Health (NIH) grants with Professor (Prof.) Sergio Fantini as the principle investigator. The NIH grant numbers are as follows:

- R01-NS095334
- R21-EB020347
- R01-EB029414

Bibliography

- ¹K. Khaksari, G. Blaney, A. Sassaroli, N. Krishnamurthy, T. Pham, and S. Fantini, “Depth dependence of coherent hemodynamics in the human head”, *Journal of Biomedical Optics* **23**, 121615 (2018).
- ²Blaney, Sassaroli, Pham, Krishnamurthy, and Fantini, “Multi-distance frequency-domain optical measurements of coherent cerebral hemodynamics”, *Photonics* **6**, 83 (2019).
- ³G. Blaney, A. Sassaroli, T. Pham, C. Fernandez, and S. Fantini, “Phase dual-slopes in frequency-domain near-infrared spectroscopy for enhanced sensitivity to brain tissue: First applications to human subjects”, *Journal of Biophotonics* **13**, e201960018 (2020).
- ⁴G. Blaney, A. Sassaroli, and S. Fantini, “Dual-slope imaging in highly scattering media with frequency-domain near-infrared spectroscopy”, *Optics Letters* **45**, 4464–4467 (2020).
- ⁵G. Blaney, A. Sassaroli, and S. Fantini, “Design of a source-detector array for dual-slope diffuse optical imaging”, *Review of Scientific Instruments* **91**, 093702 (2020).
- ⁶G. Blaney, A. Sassaroli, and S. Fantini, “Algorithm for determination of thresholds of significant coherence in time-frequency analysis”, *Biomedical Signal Processing and Control* **56**, 101704 (2020).
- ⁷G. Blaney, R. Donaldson, S. Mushtak, H. Nguyen, L. Vignale, C. Fernandez, T. Pham, A. Sassaroli, and S. Fantini, “Dual-slope diffuse reflectance instrument for calibration-free broadband spectroscopy”, *Applied Sciences* **11**, edited by J. Kiefer, 1757 (2021).
- ⁸G. Blaney, P. Curtsmith, A. Sassaroli, C. Fernandez, and S. Fantini, “Broadband absorption spectroscopy of heterogeneous biological tissue”, *Applied Optics* **60**, 7552–7562 (2021).
- ⁹G. Blaney, M. Bottone, A. Sassaroli, C. Fernandez, and S. Fantini, “Broadband diffuse optical spectroscopy of two-layered scattering media containing oxyhemoglobin, deoxyhemoglobin, water, and lipids”, *Journal of Innovative Optical Health Sciences In Press*, 10 . 1142 / S1793545822500201 (2022).
- ¹⁰G. P. Blaney, N. Krishnamurthy, A. Sassaroli, T. T. Pham, and S. Fantini, “Comparison of spontaneous and induced coherent hemodynamics in the human brain”, in *Optical Tomography and Spectroscopy of Tissue XIII*, edited by S. Fantini, P. Taroni, B. J. Tromberg, and E. M. Sevick-Muraca (Mar. 2019), p. 108741I.
- ¹¹G. Blaney, A. Sassaroli, T. Pham, C. Fernandez, and S. Fantini, “Dual-slope imaging in frequency-domain near-infrared spectroscopy”, in *Biophotonics Congress: Biomedical Optics* (Apr. 2020), JTh2A.9.
- ¹²G. Blaney, A. Sassaroli, T. T. Pham, C. Fernandez, and S. Fantini, “Towards functional dual-slope imaging: methods to design, evaluate, and construct a source-detector array”, in *Optical Tomography and Spectroscopy of Tissue XIV*, edited by S. Fantini and P. Taroni (Mar. 2021), 116390T.
- ¹³G. Blaney, A. Sassaroli, C. Fernandez, and S. Fantini, “Functional brain mapping with dual-slope frequency-domain near-infrared spectroscopy”, in *Neural Imaging and Sensing*, edited by Q. Luo, J. Ding, and L. Fu (2022), p. 1194602.
- ¹⁴G. Blaney, R. Donaldson, S. Mushtak, H. Nguyen, L. Vignale, C. Fernandez, A. Sassaroli, T. T. Pham, and S. Fantini, “Broadband absorption spectroscopy in tissue: combining dual-slope continuous-wave and self-calibrating frequency-domain measurements”, in *Optical Tomography and Spectroscopy of Tissue XIV*, edited by S. Fantini and P. Taroni (Mar. 2021), 116390H.

- ¹⁵G. Blaney, A. Sassaroli, P. Curtsmith, C. Fernandez, T. Pham, and S. Fantini, “Dual-slope broadband diffuse reflectance spectrometer for absolute absorption spectra of turbid media”, in *Diffuse Optical Spectroscopy and Imaging VIII* (Dec. 2021), p. 119200V.
- ¹⁶S. Fantini and A. Sassaroli, “Frequency-Domain Techniques for Cerebral and Functional Near-Infrared Spectroscopy”, *Frontiers in Neuroscience* **14**, 300 (2020).
- ¹⁷I. J. Bigio and S. Fantini, *Quantitative Biomedical Optics: Theory, Methods, and Applications* (Cambridge: Cambridge University Press, 2016).
- ¹⁸F. Scholkmann, S. Kleiser, A. J. Metz, R. Zimmermann, J. Mata Pavia, U. Wolf, and M. Wolf, “A review on continuous wave functional near-infrared spectroscopy and imaging instrumentation and methodology”, *NeuroImage* **85**, 6–27 (2014).
- ¹⁹Y. Ozaki, W. F. McClure, and A. A. Christy, eds., *Near-Infrared Spectroscopy in Food Science and Technology* (John Wiley & Sons, 2006).
- ²⁰J. B. Johnson, “An overview of near-infrared spectroscopy (NIRS) for the detection of insect pests in stored grains”, *Journal of Stored Products Research* **86**, 101558 (2020).
- ²¹H. I. Kademi, B. H. Ulusoy, and C. Hecer, “Applications of miniaturized and portable near infrared spectroscopy (NIRS) for inspection and control of meat and meat products”, *Food Reviews International* **35**, 201–220 (2019).
- ²²M. Razuc, A. Graña, L. Gallo, M. V. Ramírez-Rigo, and R. J. Romañach, “Near-infrared spectroscopic applications in pharmaceutical particle technology”, *Drug Development and Industrial Pharmacy* **45**, 1565–1589 (2019).
- ²³S. Stranzinger, D. Markl, J. G. Khinast, and A. Paudel, “Review of sensing technologies for measuring powder density variations during pharmaceutical solid dosage form manufacturing”, *TrAC Trends in Analytical Chemistry* **135**, 116147 (2021).
- ²⁴P. L. K. Trant, S. M. Kristiansen, and S. M. Sindbæk, “Visible near-infrared spectroscopy as an aid for archaeological interpretation”, *Archaeological and Anthropological Sciences* **12**, 280 (2020).
- ²⁵S. Tsuchikawa and H. Kobori, “A review of recent application of near infrared spectroscopy to wood science and technology”, *Journal of Wood Science* **61**, 213–220 (2015).
- ²⁶Z. Chen, A. Gu, X. Zhang, and Z. Zhang, “Authentication and inference of seal stamps on Chinese traditional painting by using multivariate classification and near-infrared spectroscopy”, *Chemometrics and Intelligent Laboratory Systems* **171**, 226–233 (2017).
- ²⁷F. Lange and I. Tachtsidis, “Clinical Brain Monitoring with Time Domain NIRS: A Review and Future Perspectives”, *Applied Sciences* **9**, 1612 (2019).
- ²⁸N. F. Agbangla, M. Audiffren, and C. T. Albinet, “Use of near-infrared spectroscopy in the investigation of brain activation during cognitive aging: A systematic review of an emerging area of research”, *Ageing Research Reviews* **38**, 52–66 (2017).
- ²⁹D. Grosenick, H. Rinneberg, R. Cubeddu, and P. Taroni, “Review of optical breast imaging and spectroscopy”, *Journal of Biomedical Optics* **21**, 091311 (2016).
- ³⁰S. Perrey and M. Ferrari, “Muscle Oximetry in Sports Science: A Systematic Review”, *Sports Medicine* **48**, 597–616 (2018).
- ³¹T. J. Barstow, “Understanding near infrared spectroscopy and its application to skeletal muscle research”, *Journal of Applied Physiology* **126**, 1360–1376 (2019).

- ³²M. Ferrari and V. Quaresima, “A brief review on the history of human functional near-infrared spectroscopy (fNIRS) development and fields of application”, *NeuroImage* **63**, 921–935 (2012).
- ³³M. Caldwell, F. Scholkmann, U. Wolf, M. Wolf, C. Elwell, and I. Tachtsidis, “Modelling confounding effects from extracerebral contamination and systemic factors on functional near-infrared spectroscopy”, *NeuroImage* **143**, 91–105 (2016).
- ³⁴I. Tachtsidis and F. Scholkmann, “False positives and false negatives in functional near-infrared spectroscopy: issues, challenges, and the way forward”, *Neurophotonics* **3**, 031405 (2016).
- ³⁵F. Herold, P. Wiegel, F. Scholkmann, and N. Müller, “Applications of Functional Near-Infrared Spectroscopy (fNIRS) Neuroimaging in Exercise–Cognition Science: A Systematic, Methodology-Focused Review”, *Journal of Clinical Medicine* **7**, 466 (2018).
- ³⁶H. B. Nielsen, “Systematic review of near-infrared spectroscopy determined cerebral oxygenation during non-cardiac surgery”, *Frontiers in Physiology* **5**, 93 (2014).
- ³⁷A. la Cour, G. Greisen, and S. Hyttel-Sørensen, “In vivo validation of cerebral near-infrared spectroscopy: a review”, *Neurophotonics* **5**, 040901 (2018).
- ³⁸T. Funane, H. Atsumori, T. Katura, A. N. Obata, H. Sato, Y. Tanikawa, E. Okada, and M. Kiguchi, “Quantitative evaluation of deep and shallow tissue layers’ contribution to fNIRS signal using multi-distance optodes and independent component analysis”, *NeuroImage* **85**, 150–165 (2014).
- ³⁹Q. Zhang, E. N. Brown, and G. E. Strangman, “Adaptive filtering for global interference cancellation and real-time recovery of evoked brain activity: a Monte Carlo simulation study”, *Journal of Biomedical Optics* **12**, 044014 (2007).
- ⁴⁰L. Gagnon, M. A. Yücel, D. A. Boas, and R. J. Cooper, “Further improvement in reducing superficial contamination in NIRS using double short separation measurements”, *NeuroImage* **85**, 127–135 (2014).
- ⁴¹R. Saager and A. Berger, “Measurement of layer-like hemodynamic trends in scalp and cortex: implications for physiological baseline suppression in functional near-infrared spectroscopy”, *Journal of Biomedical Optics* **13**, 034017 (2008).
- ⁴²M. Kacprzak, P. Sawosz, W. Weigl, D. Milej, A. Gerega, and A. Liebert, “Frequency analysis of oscillations in cerebral hemodynamics measured by time domain near infrared spectroscopy”, *Biomedical Optics Express* **10**, 761–771 (2019).
- ⁴³S. Fantini, “Dynamic model for the tissue concentration and oxygen saturation of hemoglobin in relation to blood volume, flow velocity, and oxygen consumption: Implications for functional neuroimaging and coherent hemodynamics spectroscopy (CHS)”, *NeuroImage* **85**, 202–221 (2014).
- ⁴⁴J. M. Kainerstorfer, A. Sassaroli, B. Hallacoglu, M. L. Pierro, and S. Fantini, “Practical Steps for Applying a New Dynamic Model to Near-Infrared Spectroscopy Measurements of Hemodynamic Oscillations and Transient Changes”, *Academic Radiology* **21**, 185–196 (2014).
- ⁴⁵M. Reinhard, E. Wehrle-Wieland, D. Grabiak, M. Roth, B. Guschlauer, J. Timmer, C. Weiller, and A. Hetzel, “Oscillatory cerebral hemodynamics—the macro- vs. microvascular level”, *Journal of the Neurological Sciences* **250**, 103–109 (2006).
- ⁴⁶R. Cheng, Y. Shang, D. Hayes, S. P. Saha, and G. Yu, “Noninvasive optical evaluation of spontaneous low frequency oscillations in cerebral hemodynamics”, *NeuroImage* **62**, 1445–1454 (2012).
- ⁴⁷V. Chernomordik, F. Amyot, K. Kenney, E. Wassermann, R. Diaz-Arrastia, and A. Gandjbakhche, “Abnormality of low frequency cerebral hemodynamics oscillations in TBI population”, *Brain Research* **1639**, 194–199 (2016).

- ⁴⁸T. Peng, P. N. Ainslie, J. D. Cotter, C. Murrell, K. Thomas, M. J. Williams, K. George, R. Shave, A. B. Rowley, and S. J. Payne, “The effects of age on the spontaneous low-frequency oscillations in cerebral and systemic cardiovascular dynamics”, *Physiological Measurement* **29**, 1055–1069 (2008).
- ⁴⁹F. Scholkmann, U. Gerber, M. Wolf, and U. Wolf, “End-tidal CO₂: An important parameter for a correct interpretation in functional brain studies using speech tasks”, *NeuroImage* **66**, 71–79 (2013).
- ⁵⁰M. A. Franceschini, S. Fantini, L. A. Paunescu, J. S. Maier, and E. Gratton, “Influence of a superficial layer in the quantitative spectroscopic study of strongly scattering media”, *Applied Optics* **37**, 7447–7458 (1998).
- ⁵¹M. Doulgerakis-Kontoudis, A. T. Eggebrecht, and H. Dehghani, “Information rich phase content of frequency domain functional Near Infrared Spectroscopy”, in *Neural Imaging and Sensing*, Vol. 10865, edited by Q. Luo, J. Ding, and L. Fu (2019), pp. 20–25.
- ⁵²D. Contini, L. Spinelli, A. Torricelli, A. Pifferi, and R. Cubeddu, “Novel method for depth-resolved brain functional imaging by time-domain NIRS”, in *European Conferences on Biomedical Optics* (2007), 6629_7.
- ⁵³A. Abdalmalak, D. Milej, M. Diop, M. Shokouhi, L. Naci, A. M. Owen, and K. St. Lawrence, “Can time-resolved NIRS provide the sensitivity to detect brain activity during motor imagery consistently?”, *Biomedical Optics Express* **8**, 2162–2172 (2017).
- ⁵⁴D. Milej, A. Abdalmalak, P. McLachlan, M. Diop, A. Liebert, and K. St. Lawrence, “Subtraction-based approach for enhancing the depth sensitivity of time-resolved NIRS”, *Biomedical Optics Express* **7**, 4514–4526 (2016).
- ⁵⁵S. Fantini, D. Hueber, M. A. Franceschini, E. Gratton, W. Rosenfeld, P. G. Stubblefield, D. Maulik, and M. R. Stankovic, “Non-invasive optical monitoring of the newborn piglet brain using continuous-wave and frequency-domain spectroscopy”, *Physics in Medicine and Biology* **44**, 1543–1563 (1999).
- ⁵⁶V. Toronov, A. Webb, J. H. Choi, M. Wolf, L. Safanova, U. Wolf, and E. Gratton, “Study of local cerebral hemodynamics by frequency-domain near-infrared spectroscopy and correlation with simultaneously acquired functional magnetic resonance imaging”, *Optics Express* **9**, 417–427 (2001).
- ⁵⁷E. Gratton, V. Toronov, U. Wolf, M. Wolf, and A. Webb, “Measurement of brain activity by near-infrared light”, *Journal of Biomedical Optics* **10**, 011008 (2005).
- ⁵⁸A. Sassaroli, G. Blaney, and S. Fantini, “Dual-slope method for enhanced depth sensitivity in diffuse optical spectroscopy”, *J. Opt. Soc. Am. A* **36**, 1743–1761 (2019).
- ⁵⁹S. Fantini, G. Blaney, and A. Sassaroli, “Transformational change in the field of diffuse optics: From going bananas to going nuts”, *Journal of Innovative Optical Health Sciences* **13**, 1930013 (2019).
- ⁶⁰P. Sawosz and A. Liebert, “Method to improve the depth sensitivity of diffuse reflectance measurements to absorption changes in optically turbid medium”, *Biomedical Optics Express* **10**, 5031–5041 (2019).
- ⁶¹D. M. Hueber, S. Fantini, A. E. Cerussi, and B. B. Barbieri, “New optical probe designs for absolute (self-calibrating) NIR tissue hemoglobin measurements”, in *Optical Tomography and Spectroscopy of Tissue III*, Vol. 3597 (July 1999), pp. 618–631.

- ⁶²V. Toronov, E. D'Amico, D. Hueber, E. Gratton, B. Barbieri, and A. Webb, "Optimization of the signal-to-noise ratio of frequency-domain instrumentation for near-infrared spectro-imaging of the human brain", *Optics Express* **11**, 2717–2729 (2003).
- ⁶³R. Penrose, "A generalized inverse for matrices", *Mathematical Proceedings of the Cambridge Philosophical Society* **51**, 406–413 (1955).
- ⁶⁴M. Doulgerakis, A. T. Eggebrecht, and H. Dehghani, "High-density functional diffuse optical tomography based on frequency-domain measurements improves image quality and spatial resolution", *Neurophotonics* **6**, 035007 (2019).
- ⁶⁵MathWorks, *MATLAB Help*, <https://www.mathworks.com/help/matlab/>, 2020.
- ⁶⁶B. Hallacoglu, A. Sassaroli, E. Guerrero-Berroa, M. Schnaider Beeri, V. Haroutunian, M. Shaul, I. H. Rosenberg, A. Toren, and S. Fantini, "Absolute measurement of cerebral optical coefficients, hemoglobin concentration and oxygen saturation in old and young adults with near-infrared spectroscopy", *Journal of Biomedical Optics* **17**, 081406 (2012).
- ⁶⁷X. Xiao, X. Yu, Z. Zhang, Y. Zhao, Y. Jiang, Z. Li, Y. Yang, and C. Zhu, "Transcranial brain atlas", *Science Advances* **4**, eaar6904 (2018).
- ⁶⁸H. Lu, L. C. W. Lam, and Y. Ning, "Scalp-to-cortex distance of left primary motor cortex and its computational head model: Implications for personalized neuromodulation", *CNS Neuroscience & Therapeutics* **25**, 1270–1276 (2019).
- ⁶⁹P. F. Fox, T. Uniacke-Lowe, P. L. H. McSweeney, and J. A. O'Mahony, *Dairy Chemistry and Biochemistry*, Second (Springer, Cham, 2015).
- ⁷⁰T. Katura, N. Tanaka, A. Obata, H. Sato, and A. Maki, "Quantitative evaluation of interrelations between spontaneous low-frequency oscillations in cerebral hemodynamics and systemic cardiovascular dynamics", *NeuroImage* **31**, 1592–1600 (2006).
- ⁷¹G. Taga, Y. Konishi, A. Maki, T. Tachibana, M. Fujiwara, and H. Koizumi, "Spontaneous oscillation of oxy- and deoxy- hemoglobin changes with a phase difference throughout the occipital cortex of newborn infants observed using non-invasive optical topography", *Neuroscience Letters* **282**, 101–104 (2000).
- ⁷²H. Watanabe, Y. Shitara, Y. Aoki, T. Inoue, S. Tsuchida, N. Takahashi, and G. Taga, "Hemoglobin phase of oxygenation and deoxygenation in early brain development measured using fNIRS", *Proceedings of the National Academy of Sciences* **114**, E1737–E1744 (2017).
- ⁷³H. Obrig, M. Neufang, R. Wenzel, M. Kohl, J. Steinbrink, K. Einhäupl, and A. Villringer, "Spontaneous Low Frequency Oscillations of Cerebral Hemodynamics and Metabolism in Human Adults", *NeuroImage* **12**, 623–639 (2000).
- ⁷⁴M. L. Pierro, A. Sassaroli, P. R. Bergethon, B. L. Ehrenberg, and S. Fantini, "Phase-amplitude investigation of spontaneous low-frequency oscillations of cerebral hemodynamics with near-infrared spectroscopy: A sleep study in human subjects", *NeuroImage* **63**, 1571–1584 (2012).
- ⁷⁵M. Reinhard, F. K. Schumacher, S. Rutsch, M. Oeinck, J. Timmer, I. Mader, B. Schelter, C. Weiller, and C. P. Kaller, "Spatial mapping of dynamic cerebral autoregulation by multichannel near-infrared spectroscopy in high-grade carotid artery disease", *Journal of Biomedical Optics* **19**, 097005 (2014).
- ⁷⁶R. Aaslid, M. Blaha, G. Sviri, C. M. Douville, and D. W. Newell, "Asymmetric Dynamic Cerebral Autoregulatory Response to Cyclic Stimuli", *Stroke* **38**, 1465–1469 (2007).

- ⁷⁷J. A. Claassen, A. S. Meel-van den Abeelen, D. M. Simpson, and R. B. Panerai, “Transfer function analysis of dynamic cerebral autoregulation: A white paper from the International Cerebral Autoregulation Research Network”, *Journal of Cerebral Blood Flow & Metabolism* **36**, 665–680 (2016).
- ⁷⁸A. H. E. A. van Beek, J. Lagro, M. G. M. Olde-Rikkert, R. Zhang, and J. A. H. R. Claassen, “Oscillations in cerebral blood flow and cortical oxygenation in Alzheimer’s disease”, *Neurobiology of Aging* **33**, 428.e21–428.e31 (2012).
- ⁷⁹A. Sassaroli, X. Zang, K. T. Tgavalekos, and S. Fantini, “Induced and spontaneous hemodynamic oscillations in cerebral and extracerebral tissue for coherent hemodynamics spectroscopy”, in *Optical Tomography and Spectroscopy of Tissue XII*, Vol. 10059, edited by B. J. Tromberg, A. G. Yodh, E. M. Sevick-Muraca, and R. R. Alfano (2017), pp. 138–145.
- ⁸⁰J. M. Kainerstorfer, A. Sassaroli, K. T. Tgavalekos, and S. Fantini, “Cerebral Autoregulation in the Microvasculature Measured with Near-Infrared Spectroscopy”, *Journal of Cerebral Blood Flow & Metabolism* **35**, 959–966 (2015).
- ⁸¹M. L. Pierro, J. M. Kainerstorfer, A. Civiletto, D. E. Weiner, A. Sassaroli, B. Hallacoglu, and S. Fantini, “Reduced speed of microvascular blood flow in hemodialysis patients versus healthy controls: a coherent hemodynamics spectroscopy study”, *Journal of Biomedical Optics* **19**, 026005 (2014).
- ⁸²K. Tgavalekos, T. Pham, N. Krishnamurthy, A. Sassaroli, and S. Fantini, “Frequency-resolved analysis of coherent oscillations of local cerebral blood volume, measured with near-infrared spectroscopy, and systemic arterial pressure in healthy human subjects”, *PLoS ONE* **14**, edited by M. M. Bachschmid, e0211710 (2019).
- ⁸³T. Takahashi, Y. Takikawa, R. Kawagoe, S. Shibuya, T. Iwano, and S. Kitazawa, “Influence of skin blood flow on near-infrared spectroscopy signals measured on the forehead during a verbal fluency task”, *NeuroImage* **57**, 991–1002 (2011).
- ⁸⁴E. Kirilina, A. Jelzow, A. Heine, M. Niessing, H. Wabnitz, R. Brühl, B. Ittermann, A. M. Jacobs, and I. Tachtsidis, “The physiological origin of task-evoked systemic artefacts in functional near infrared spectroscopy”, *NeuroImage* **61**, 70–81 (2012).
- ⁸⁵A. Sassaroli, K. Tgavalekos, and S. Fantini, “The meaning of “coherent” and its quantification in coherent hemodynamics spectroscopy”, *Journal of Innovative Optical Health Sciences* **11**, 1850036 (2018).
- ⁸⁶T. Pham, K. Tgavalekos, A. Sassaroli, G. Blaney, and S. Fantini, “Quantitative measurements of cerebral blood flow with near-infrared spectroscopy”, *Biomedical Optics Express* **10**, 2117–2134 (2019).
- ⁸⁷J. M. Kainerstorfer, A. Sassaroli, and S. Fantini, “Optical oximetry of volume-oscillating vascular compartments: contributions from oscillatory blood flow”, *Journal of Biomedical Optics* **21**, 101408 (2016).
- ⁸⁸R. Zhang, J. H. Zuckerman, C. A. Giller, and B. D. Levine, “Transfer function analysis of dynamic cerebral autoregulation in humans”, *American Journal of Physiology-Heart and Circulatory Physiology* **274**, H233–H241 (1998).
- ⁸⁹R. B. Panerai, P. J. Eames, and J. F. Potter, “Multiple coherence of cerebral blood flow velocity in humans”, *American Journal of Physiology-Heart and Circulatory Physiology* **291**, H251–H259 (2006).

- ⁹⁰L. Faes, G. Pinna, A. Porta, R. Maestri, and G. Nollo, “Surrogate Data Analysis for Assessing the Significance of the Coherence Function”, *IEEE Transactions on Biomedical Engineering* **51**, 1156–1166 (2004).
- ⁹¹R. B. Panerai, V. J. Haunton, M. F. Hanby, A. S. M. Salinet, and T. G. Robinson, “Statistical criteria for estimation of the cerebral autoregulation index (ARI) at rest”, *Physiological Measurement* **37**, 661–672 (2016).
- ⁹²F. Tian, T. Tarumi, H. Liu, R. Zhang, and L. Chalak, “Wavelet coherence analysis of dynamic cerebral autoregulation in neonatal hypoxic–ischemic encephalopathy”, *NeuroImage: Clinical* **11**, 124–132 (2016).
- ⁹³A. Grinsted, J. C. Moore, and S. Jevrejeva, “Application of the cross wavelet transform and wavelet coherence to geophysical time series”, *Nonlinear Processes in Geophysics* **11**, 561–566 (2004).
- ⁹⁴J. H. Miles, “Estimation of signal coherence threshold and concealed spectral lines applied to detection of turbofan engine combustion noise”, *The Journal of the Acoustical Society of America* **129**, 3068–3081 (2011).
- ⁹⁵C. Buragohain and S. Suri, “Quantiles on Streams”, in *Encyclopedia of Database Systems*, edited by L. Liu and M. T. Özsü (Springer US, Boston, MA, 2009), pp. 2235–2240.
- ⁹⁶G. S. Manku, S. Rajagopalan, and B. G. Lindsay, “Approximate medians and other quantiles in one pass and with limited memory”, in *SIGMOD*, Vol. 27 (June 1998), pp. 426–435.
- ⁹⁷M. Greenwald and S. Khanna, “Space-efficient online computation of quantile summaries”, *ACM SIGMOD Record* **30**, 58–66 (2001).
- ⁹⁸N. Shrivastava, C. Buragohain, D. Agrawal, and S. Suri, “Medians and beyond”, in *SenSys* (2004), pp. 239–249.
- ⁹⁹P. Berens, “CircStat: A MATLAB Toolbox for Circular Statistics”, *Journal of Statistical Software* **31**, 1–21 (2009).
- ¹⁰⁰A. Sassaroli, M. Pierro, P. R. Bergethon, and S. Fantini, “Low-Frequency Spontaneous Oscillations of Cerebral Hemodynamics Investigated With Near-Infrared Spectroscopy: A Review”, *IEEE Journal of Selected Topics in Quantum Electronics* **18**, 1478–1492 (2012).
- ¹⁰¹H. Gu, H. Lu, F. Q. Ye, E. A. Stein, and Y. Yang, “Noninvasive quantification of cerebral blood volume in humans during functional activation”, *NeuroImage* **30**, 377–387 (2006).
- ¹⁰²J. Hua, P. Liu, T. Kim, M. Donahue, S. Rane, J. J. Chen, Q. Qin, and S.-G. Kim, “MRI techniques to measure arterial and venous cerebral blood volume”, *NeuroImage* **187**, 17–31 (2019).
- ¹⁰³S. N. Krieger, M. N. Streicher, R. Trampel, and R. Turner, “Cerebral Blood Volume Changes during Brain Activation”, *Journal of Cerebral Blood Flow & Metabolism* **32**, 1618–1631 (2012).
- ¹⁰⁴V. Toronov, S. Walker, R. Gupta, J. H. Choi, E. Gratton, D. Hueber, and A. Webb, “The roles of changes in deoxyhemoglobin concentration and regional cerebral blood volume in the fMRI BOLD signal”, *NeuroImage* **19**, 1521–1531 (2003).
- ¹⁰⁵T. Durduran, R. Choe, W. B. Baker, and A. G. Yodh, “Diffuse optics for tissue monitoring and tomography”, *Reports on Progress in Physics* **73**, 076701 (2010).
- ¹⁰⁶S. L. Jacques and B. W. Pogue, “Tutorial on diffuse light transport”, *Journal of Biomedical Optics* **13**, 041302 (2008).

- ¹⁰⁷J. B. Fishkin and E. Gratton, “Propagation of photon-density waves in strongly scattering media containing an absorbing semi-infinite plane bounded by a straight edge”, *Journal of the Optical Society of America A* **10**, 127–140 (1993).
- ¹⁰⁸S. Fantini, M. A. Franceschini, and E. Gratton, “Semi-infinite-geometry boundary problem for light migration in highly scattering media: a frequency-domain study in the diffusion approximation”, *JOSA B* **11**, 2128–2138 (1994).
- ¹⁰⁹P. Lanka, P. Lanka, A. Segala, A. Segala, A. Farina, A. Farina, S. K. V. Sekar, E. Nisoli, A. Valerio, P. Taroni, P. Taroni, R. Cubeddu, R. Cubeddu, A. Pifferi, and A. Pifferi, “Non-invasive investigation of adipose tissue by time domain diffuse optical spectroscopy”, *Biomedical Optics Express* **11**, 2779–2793 (2020).
- ¹¹⁰S. Vasudevan, F. Forghani, C. Campbell, S. Bedford, and T. D. O’Sullivan, “Method for Quantitative Broadband Diffuse Optical Spectroscopy of Tumor-Like Inclusions”, *Applied Sciences* **10**, 1419 (2020).
- ¹¹¹G Ganesan, R. V. Warren, A Leproux, M Compton, K Cutler, S Wittkopp, G Tran, T O’Sullivan, S Malik, P. R. Galassetti, and B. J. Tromberg, “Diffuse optical spectroscopic imaging of subcutaneous adipose tissue metabolic changes during weight loss”, *International Journal of Obesity* **40**, 1292–1300 (2016).
- ¹¹²S. Konugolu Venkata Sekar, A. Dalla Mora, I. Bargigia, E. Martinenghi, C. Lindner, P. Farzam, M. Pagliazzi, T. Durduran, P. Taroni, A. Pifferi, and A. Farina, “Broadband (600–1350 nm) Time-Resolved Diffuse Optical Spectrometer for Clinical Use”, *IEEE Journal of Selected Topics in Quantum Electronics* **22**, 406–414 (2016).
- ¹¹³T. D. O’Sullivan, A. E. Cerussi, D. J. Cuccia, and B. J. Tromberg, “Diffuse optical imaging using spatially and temporally modulated light”, *Journal of Biomedical Optics* **17**, 0713111 (2012).
- ¹¹⁴I. Tachtsidis, L. Gao, T. S. Leung, M. Kohl-Bareis, C. E. Cooper, and C. E. Elwell, “A Hybrid Multi-Distance Phase and Broadband Spatially Resolved Spectrometer and Algorithm for Resolving Absolute Concentrations of Chromophores in the Near-Infrared Light Spectrum”, in *Oxygen Transport to Tissue XXXI*, edited by E. Takahashi and D. F. Bruley, Advances in Experimental Medicine and Biology (2010), pp. 169–175.
- ¹¹⁵F. Bevilacqua, A. J. Berger, A. E. Cerussi, D. Jakubowski, and B. J. Tromberg, “Broadband absorption spectroscopy in turbid media by combined frequency-domain and steady-state methods”, *Applied Optics* **39**, 6498–6507 (2000).
- ¹¹⁶P. Di Ninni, F. Martelli, and G. Zaccanti, “The use of India ink in tissue-simulating phantoms”, *Optics Express* **18**, 26854 (2010).
- ¹¹⁷F. Martelli and G. Zaccanti, “Calibration of scattering and absorption properties of a liquid diffusive medium at NIR wavelengths. CW method”, *Optics Express* **15**, 486–500 (2007).
- ¹¹⁸B. Cugmas, P. Naglič, S. P. M. Menachery, F. Pernuš, and B. Likar, “Poor optical stability of molecular dyes when used as absorbers in water-based tissue-simulating phantoms”, in *Design and Quality for Biomedical Technologies XII*, Vol. 10870, edited by R. Liang and J. Hwang (2019), pp. 56–65.
- ¹¹⁹R. M. Pope and E. S. Fry, “Absorption spectrum (380–700 nm) of pure water II Integrating cavity measurements”, *Applied Optics* **36**, 8710–8723 (1997).
- ¹²⁰L. Kou, D. Labrie, and P. Chylek, “Refractive indices of water and ice in the 0.65- to 2.5-Mm spectral range”, *Applied Optics* **32**, 3531–3540 (1993).

- ¹²¹R. L. P. van Veen, H. J. C. M. Sterenborg, A. Pifferi, A. Torricelli, and R. Cubeddu, “Determination of VIS- NIR absorption coefficients of mammalian fat, with time- and spatially resolved diffuse reflectance and transmission spectroscopy”, in *Biomedical Topical Meeting* (2004), SF4.
- ¹²²D. Geraskin, H. Boeth, and M. Kohl-Bareis, “Optical measurement of adipose tissue thickness and comparison with ultrasound, magnetic resonance imaging, and callipers”, *Journal of Biomedical Optics* **14**, 044017 (2009).
- ¹²³S. Prahl, *Tabulated Molar Extinction Coefficient for Hemoglobin in Water*, <https://omlc.org/spectra/hemoglobin/summary.html>, 1998.
- ¹²⁴P. Taroni, D. Comelli, A. Pifferi, A. Torricelli, and R. Cubeddu, “Absorption of collagen: effects on the estimate of breast composition and related diagnostic implications”, *Journal of Biomedical Optics* **12**, 014021 (2007).
- ¹²⁵G. Bale, C. E. Elwell, and I. Tachtsidis, “From Jöbsis to the present day: a review of clinical near-infrared spectroscopy measurements of cerebral cytochrome-c-oxidase”, *Journal of biomedical optics* **21**, 091307 (2016).
- ¹²⁶E. L. Hull, M. G. Nichols, and T. H. Foster, “Quantitative broadband near-infrared spectroscopy of tissue-simulating phantoms containing erythrocytes”, *Physics in Medicine and Biology* **43**, 3381–3404 (1998).
- ¹²⁷S. J. Matcher, M. Cope, and D. T. Delpy, “Use of the water absorption spectrum to quantify tissue chromophore concentration changes in near-infrared spectroscopy”, *Physics in Medicine and Biology* **39**, 177–196 (1994).
- ¹²⁸M. Diop, E. Wright, V. Toronov, T.-Y. Lee, and K. S. Lawrence, “Improved light collection and wavelet de-noising enable quantification of cerebral blood flow and oxygen metabolism by a low-cost, off-the-shelf spectrometer”, *Journal of Biomedical Optics* **19**, 057007 (2014).
- ¹²⁹H. Z. Yeganeh, V. Toronov, J. T. Elliott, M. Diop, T.-Y. Lee, and K. S. Lawrence, “Broadband continuous-wave technique to measure baseline values and changes in the tissue chromophore concentrations”, *Biomedical Optics Express* **3**, 2761–2770 (2012).
- ¹³⁰H. Dehghani, F. Leblond, B. W. Pogue, and F. Chauchard, “Application of spectral derivative data in visible and near-infrared spectroscopy”, *Physics in Medicine and Biology* **55**, 3381–3399 (2010).
- ¹³¹A. Pifferi, A. Torricelli, P. Taroni, and R. Cubeddu, “Reconstruction of absorber concentrations in a two-layer structure by use of multidistance time-resolved reflectance spectroscopy”, *Optics Letters* **26**, 1963–1965 (2001).
- ¹³²O. Pucci, V. Toronov, and K. S. Lawrence, “Measurement of the optical properties of a two-layer model of the human head using broadband near-infrared spectroscopy”, *Applied Optics* **49**, 6324–6332 (2010).
- ¹³³B. Hallacoglu, A. Sassaroli, and S. Fantini, “Optical Characterization of Two-Layered Turbid Media for Non-Invasive, Absolute Oximetry in Cerebral and Extracerebral Tissue”, *PLOS ONE* **8**, e64095 (2013).
- ¹³⁴J. D. Veesa and H. Dehghani, “Hyper-spectral Recovery of Cerebral and Extra-Cerebral Tissue Properties Using Continuous Wave Near-Infrared Spectroscopic Data”, *Applied Sciences* **9**, 2836 (2019).
- ¹³⁵S. L. Jacques, “Optical properties of biological tissues: a review”, *Physics in Medicine and Biology* **58**, R37–R61 (2013).

- ¹³⁶A. Liemert and A. Kienle, “Light diffusion in a turbid cylinder. I. Homogeneous case”, *Optics Express* **18**, 9456–9473 (2010).
- ¹³⁷S. Jacques, *Melanosome Absorption Coefficient*, <https://omlc.org/spectra/melanin/mua.html>, 1998.
- ¹³⁸R. R. Anderson and J. A. Parrish, “Optical Properties of Human Skin”, in *The Science of Photomedicine*, edited by J. D. Regan and J. A. Parrish, Photobiology (Springer US, Boston, MA, 1982), pp. 147–194.
- ¹³⁹P. Oltulu, B. Ince, N. Kokbudak, S. Findik, and F. Kilinc, “Measurement of epidermis, dermis, and total skin thicknesses from six different body regions with a new ethical histometric technique”, *Turkish Journal of Plastic Surgery* **26**, 56 (2018).
- ¹⁴⁰A. Matas, M. G. Sowa, G. Taylor, and H. H. Mantsch, “Melanin as a confounding factor in near infrared spectroscopy of skin”, *Vibrational Spectroscopy* **28**, 45–52 (2002).
- ¹⁴¹Y. Zhao, L. Qiu, Y. Sun, C. Huang, and T. Li, “Optimal hemoglobin extinction coefficient data set for near-infrared spectroscopy”, *Biomedical Optics Express* **8**, 5151–5159 (2017).
- ¹⁴²A. Liemert and A. Kienle, “Light diffusion in a turbid cylinder. II. Layered case”, *Optics Express* **18**, 9266–9279 (2010).
- ¹⁴³D. Contini, F. Martelli, and G. Zaccanti, “Photon migration through a turbid slab described by a model based on diffusion approximation. I. Theory”, *Applied Optics* **36**, 4587–4599 (1997).
- ¹⁴⁴M. Dehaes, L. Gagnon, F. Lesage, M. Péligrini-Issac, A. Vignaud, R. Valabrégue, R. Grebe, F. Wallois, and H. Benali, “Quantitative investigation of the effect of the extra-cerebral vasculature in diffuse optical imaging: a simulation study”, *Biomedical Optics Express* **2**, 680–695 (2011).
- ¹⁴⁵Q. Fang, “Mesh-based Monte Carlo method using fast ray-tracing in Plücker coordinates”, *Biomedical Optics Express* **1**, 165–175 (2010).
- ¹⁴⁶F. Martelli, D. Contini, A. Taddeucci, and G. Zaccanti, “Photon migration through a turbid slab described by a model based on diffusion approximation II Comparison with Monte Carlo results”, *Applied Optics* **36**, 4600–4612 (1997).
- ¹⁴⁷A. Sassaroli and S. Fantini, “Comment on the modified Beer–Lambert law for scattering media”, *Physics in Medicine and Biology* **49**, N255–N257 (2004).